



NASA CR-159,332

NASA CONTRACTOR REPORT 159332

NASA-CR-159332
19840020666

Results of Design Studies and Wind Tunnel Tests of High-Aspect-Ratio Supercritical Wings for an Energy Efficient Transport

Doris K. Steckel, John A. Dahlin, and Preston A. Henne

McDonnell Douglas Corporation
Douglas Aircraft Company
Long Beach, California 90846

LIBRARY COPY

NOV 25 1980

CONTRACT NAS1-14744
OCTOBER 1980

LANGLEY RESEARCH CENTER
LIBRARY, NASA
HAMPTON, VIRGINIA

~~FOR EARLY DOMESTIC DISSEMINATION~~

~~Because of its significant early commercial potential, this information which has been developed under a U. S. Government contract is being disseminated within the United States in advance of general publication. This information may be duplicated and used by the recipient with the express limitation that it not be published. Release of this information to other domestic parties by the recipient shall be made subject to these limitations. Foreign release may be made only with prior NASA approval and appropriate export licenses. This legend shall be marked on any reproduction of this information in whole or in part.~~

~~REVIEW FOR GENERAL RELEASE ON AUGUST 31, 1984~~

NASA
National Aeronautics and
Space Administration
Langley Research Center
Hampton, Virginia 23665



NASA CONTRACTOR REPORT 159332

Results of Design Studies and Wind Tunnel Tests of High-Aspect-Ratio Supercritical Wings for an Energy Efficient Transport

Doris K. Steckel, John A. Dahlin, and Preston A. Henne
McDonnell Douglas Corporation
Long Beach, California

Prepared for
Langley Research Center
under Contract NAS1-14744

NASA

National Aeronautics and
Space Administration

Langley Research Center
Hampton, Virginia 23665

781-71495*#

This Page Intentionally Left Blank

FOREWORD

This document presents the results of a contract study performed for the National Aeronautics and Space Administration (NASA) by Douglas Aircraft Company, of McDonnell Douglas Corporation. This work was part of Phase I of the Energy Efficient Transport (EET) project of the Aircraft Energy Efficiency (ACEE) program. Specifically, the study was one task in the contract on Selected Advanced Aerodynamic and Active Control Concepts Development. The activity included the design and testing of several high-aspect-ratio supercritical wings suitable for an advanced medium-range, wide-body transport. The effects of nacelles and pylons, flap support fairings, and ailerons were also studied.

Acknowledgements for their support and guidance are given to the NASA technical monitor for the contract, Mr. D.L. Maiden of the Energy Efficient Transport Project Office at the Langley Research Center and Mr. J.R. Tulinius, the on-site NASA representative; also, to Dr. R.T. Whitcomb of Langley Research Center for his creativity in providing industry with the versatile and practical concept that has been successfully demonstrated by tests and fuel-efficiency studies of the supercritical wing. Acknowledgement is also given to the Director and staff of the Ames Research Center, at which facility the extensive test program was conducted.

The Douglas personnel who made significant contributions to this work were:

M. Klotzsche	ACEE Program Manager
A.B. Taylor	EET Project Manager
D.K. Steckel	Task Manager, Aerodynamic Design (Report author)
J.T. Callaghan	Aerodynamic Project Engineer - EET
J.A. Dahlin	Aerodynamic Design (Report author)
P.A. Henne	Aerodynamic Design (Report author)
D.G. MacWilkinson	Aerodynamic Design

D.L. McDowell	Aerodynamic Design
C.C. Peavey	Aerodynamic Design
N.F. Wasson	Aerodynamic Design
J.D. Cadwell et al.	Aerodynamics Wind Tunnel Model Group
C.H. Bengel	Aerodynamic Administration

CONTENTS

	Page
SUMMARY	1
SYMBOLS	3
INTRODUCTION.	7
RESULTS OF SYSTEM STUDIES	13
High-Lift Systems.	13
Selection of Basic Wing Parameters	13
WING CONFIGURATION DEVELOPMENT.	25
TEST PLAN AND MODEL DESCRIPTION.	31
ANALYSIS.	51
Basic Data	51
Drag Rise Characteristics.	51
Buffet Boundary.	60
Interference Effects	68
Tail-on Characteristics.	76
Trim Drag.	77
Wake Rake Results.	82
Aileron Effectiveness.	86
COMPARISON OF DATA WITH ESTIMATION METHODS.	89
CONCLUSIONS AND RECOMMENDATIONS	97
REFERENCES.	103
APPENDIX - PLOTTED FORCE AND MOMENT DATA	A-1

This Page Intentionally Left Blank

ILLUSTRATIONS

Figure		Page
1	DC-X-200 General Arrangement	14
2	DC-X-200 Wing Planform and High-Lift System.	15
3	Improvements in Low-Speed Performance for Advanced Technology Configuration.	15
4	Factors Weighed in Determining Optimum Cruise Speed.	16
5	Wing Area Study Results.	17
6	Effects of Aspect Ratio and Fuel Cost Assumption on Various Economic Parameters	18
7	Effects of Aspect Ratio on Noise and Block Fuel.	19
8	Effects of Wing Sweep on Direct Operating Cost	20
9	Comparison of Thickness and Cruise Lift Coefficients - Conventional Transport (DC-10-10) and DC-X-200.	20
10	Improvement in Cruise Lift-to-Drag Ratio for Advanced High-Aspect-Ratio Wing.	21
11	Comparative Characteristics.	21
12	Relative Fuel Burned	22
13	Relative Direct Operating Costs for Conventional and Advanced Configurations	22
14	Advanced Features Economic Assessment.	23
15	Wing Configurations Matrix Evaluated Using the 3-D Douglas-Jameson Transonic Program	26
16	Computational Effect of Inboard Leading Edge Glove	27
17	Comparison of Study Baseline and Configuration W ₃ Upper Surface Pressure Distributions (Cruise Conditions).	28
18	Wing Planforms, Wings W ₃ and W ₄	29
19	Comparison of Upper Surface Chordwise Pressure Distributions, Wings W ₃ and W ₄	29
20	Airfoil Modifications for Alternate Wing Configuration, W ₅ . .	30

Figure	Page
21 Model Three View	32
22 Model Installation in ARC 11-Ft Transonic Wind Tunnel - Side View	33
23 Horizontal Stabilizer H_{1A} Diagram.	38
24 Vertical Stabilizer V_{1A} Diagram.	39
25 Comparison of Tested Wing Geometries	40
26 Pressure Orifice Locations	41
27 Wing Line Diagram - W_3	42
28 Wing Line Diagram - W_4, W_5, W_7, W_8	43
29 Nacelle/Pylon Assembly	43
30 Vertical Traverse Arm - Wake Rake.	47
31 Model and Rake Installation in ARC 11-Ft Transonic Wind Tunnel - Side View.	48
32 Model and Rake Installation in ARC 11-Ft Transonic Wind Tunnel - Top View	49
33 Drag Rise Characteristics in the Cruise Regime for EET Wings Tested in ARC 11-ft Wind Tunnel	53
34 Comparison Between Theoretical Spanwise Variations of Sectional Lift.	54
35 Comparison Between Measured and Performance Target Drag-Rise Characteristics	54
36 Effect of Spanwise Lift Distribution on Drag-Rise Characteristics	56
37 Comparison Between W_3 and W_4 Experimental Variation in Sectional Lift Coefficient, $M = .50$	57
38 Spanwise Distribution of Local Normal Mach Number into the Shock.	57
39 Effect of Leading Edge Radius on Drag-Rise Characteristics Max Camber = 2.1%	58
40 Effect of Leading Edge Radius on Drag-Rise Characteristics Max Camber = 2.5%	58

Figure	Page
41 Effect of Aft Camber on Drag-Rise Characteristics Leading Edge Radius = 1.59% C.	59
42 Trailing Edge Pressures for Wing W ₅ at 60-Percent Semispan.	60
43 Combined Effect of Camber and Leading Edge Radius on Drag-Rise Characteristics.	61
44 Buffet Boundary by Various Criteria - Wing W ₃	63
45 Buffet Boundary by Various Criteria - Wing W ₄	63
46 Buffet Boundary by Various Criteria - Wing W ₅	64
47 Buffet Boundary by Various Criteria - Wing W ₈	64
48 Trailing Edge Pressure Characteristics.	65
49 Comparison of Buffet Boundaries for Tested Wings.	66
50 Effect of Nacelles and Pylons on Wing-Body Lift Curve	68
51 Effect of Nacelles and Pylons on Spanwise Lift Distribution	69
52 Effect of Nacelles and Pylons on Wing Pressures	70
53 Effect of Nacelles and Pylons on Wing Pressures near Pylon at Constant Angle of Attack (Interpolated Data)	72
54 Calculated Effects of Nacelles and Pylons on Spanwise Distribution of Lift	73
55 Nacelle/Pylon Installed Drag Increment Without Flap Linkage Fairings	73
56 Nacelle/Pylon Installed Drag Increment with Flap Linkage Fairings Installed	75
57 Effects of Nacelles, Pylons, and Flap Linkage Fairings on Drag Divergence Mach Number	75
58 Effect of Nacelles and Pylons on the Tail-off Pitching Moments.	76
59 Nacelle and Pylon Installation Effects on the Configuration Pitching Moment (Tail-off)	77
60 Estimated Effect of Static Margin on Drag	78
61 Estimated Change in Spanwise Distribution of Downwash on Horizontal Tail Due to Sting	80

Figure	Page
62 Trim Drag Characteristics of Wing W_4	81
63 Cruise Trim Drag	81
64 LB-488 W_8 with Wake Rake Installed in Wind Tunnel	83
65 Typical Wing Wake Pressure Profiles	84
66 Spanwise Variation of Profile Drag	84
67 Wake Rake Wing Profile Drag Polars	85
68 Comparison of Experimental Compressibility Drag Increments	86
69 Effect of Transition Configuration on Wing Profile Drag Polars	87
70 Aileron Effectiveness at High Mach Number	88
71 Aileron Effectiveness Versus Mach Number	88
72 Comparison of Calculated and Experimental Chordwise Pressure Distributions, $M = 0.50$	90
73 Comparison of Calculated and Experimental Chordwise Pressure Distributions, $M = 0.75$	91
74 Comparison of Calculated and Experimental Chordwise Pressure Distributions, $M = 0.80$	92
75 Effect of Fuselage on Spanwise Variation of Mach Number	93
76 Comparison of Calculated and Experimental Lift Curves	94
77 Comparison of Calculated and Experimental Compressibility Drag Increments at Test Reynolds Number and Transition Conditions	95

TABLES

Table		Page
1	Configuration Notation	34
2	Dimensional Data	44
3	Summary of Plotted Force and Moment Data	52

SUMMARY

This report presents the results of the design, fabrication, and wind-tunnel testing of models of a fuel-efficient advanced technology aircraft derived from detailed system studies of a medium-range wide-body transport. The primary emphasis of the study was on the design of a high-aspect-ratio supercritical wing which, in conjunction with an advanced high-lift system, could meet the design goals of the aircraft in terms of cruise drag, buffet boundary, and off-design performance. Five wing configurations were tested to determine the effects of leading and trailing edge geometry, and span loading on these characteristics. Nacelles and pylons, flap support fairings, ailerons, and tail surfaces were also tested with selected configurations. The results of the study indicate that significant reductions can be achieved in fuel burned and direct operating cost by the use of high-aspect-ratio supercritical wing technology. The study further shows that to achieve these advantages, the effects of the many wing design variables on the aerodynamic performance must be known and selected in such a way as to benefit the complete airplane system.

This Page Intentionally Left Blank

SYMBOLS

All dimensional values presented in this report are given both in the International System of Units (SI)¹ and in U.S. Customary Units, the principal measurements and calculations having used the latter system. Longitudinal and lateral aerodynamic characteristics are referenced to the aircraft stability axes. Force and moment data are nondimensionalized by trapezoidal wing area and presented in coefficient form.

Symbols and coefficients used in this report are defined as follows:

AR	wing aspect ratio, based on adjusted wing area (trapezoidal referenced area, exposed glove area, plus area of exposed trailing-edge extensions)
B _{3A}	model fuselage
CAM	camber
C _D	aircraft drag coefficient
C _L	aircraft lift coefficient
C _{Lmax}	aircraft maximum lift coefficient
C _ℓ	aircraft rolling moment coefficient
C _{ℓδ_a}	aircraft rolling moment coefficient due to aileron deflection
C _m	aircraft pitching moment coefficient
C _{m_{ac}}	aircraft pitching moment coefficient about wing aerodynamic center
C _p	pressure coefficient
CG	center of gravity
DOC	direct operating cost
FRP	fuselage reference plane
H _{1A}	model horizontal tail
HRP	horizontal reference plane

L.E.	leading edge
LER	leading-edge radius
M	Mach number
M_{CR}	cruise Mach number
M_D	aircraft dive Mach number
M_{DIV}	drag divergence Mach number
M_N	normal Mach number
MAC	mean aerodynamic chord
N _{5A}	model nacelle
P _{2B}	model pylon
Re	Reynolds number
$Re_{\bar{c}}$	Reynolds number based on mean aerodynamic chord
S	wing planform area
T ₁ , etc.	boundary-layer transition configuration
T.E.	trailing edge
V _{1A}	model vertical tail
V _x	horizontal velocity component
V _z	vertical velocity component
W ₃ , etc.	defined wing geometry
W _{3A} , etc.	model wing constructed for testing of defined geometry
WRP	wing reference plane
X _{2A} , etc.	model wing-fuselage fillet
b	wing span
b _{F3A}	model flap linkage fairing
c	airfoil chord or local wing chord
\bar{c}	length of mean aerodynamic chord

c_l	section lift coefficient
i_H	horizontal stabilizer incidence angle, positive for trailing edge down
t/c	thickness-to-chord ratio
Γ	dihedral angle
ΔC_{DC}	compressibility drag increment
Λ	sweep angle
α	angle of attack
α_F	fuselage angle of attack
δ_a	aileron deflection angle, positive for trailing edge down
δ_F	flap deflection angle
ϵ	downwash angle
λ	wing taper ratio (trapezoidal)
η	fractional distance along wing semispan
ϕ	local flow-field angle

This Page Intentionally Left Blank

INTRODUCTION

The research accomplished over the past few years on supercritical wings has shown conclusively that there is a definite performance advantage to be obtained from the use of this technology. However, the manner in which this advantage is used and the magnitude of the gains are functions of many variables and difficult to assess without detailed studies that realistically evaluate the airplane as a total integrated system fulfilling current social, operational, and economic needs.

At the time the EET program was initiated, Douglas Aircraft Company was studying the DC-X-200, a 200-plus passenger, wide-body, medium-range transport. The environment in which these studies were being made was one of rapidly rising inflation, concern over fuel prices and availability, and increasingly stringent noise regulations. The influences of these factors on the new design were:

- (1) Due to the increased cost of producing a new aircraft, advanced technologies would be needed to design and build an aircraft which could, from the standpoint of economics, compete with, let alone be better than, today's transports.
- (2) Concern over fuel meant that this new design must be more fuel-efficient and hence the new technologies most probably could not be used to improve the level of comfort or significantly increase speed.
- (3) Greater aerodynamic efficiency in terms of low-speed lift/drag would be needed to supplement engine technology in meeting new noise requirements.

In light of these factors, and because preliminary systems studies had shown the benefit of applying the supercritical technology advantage to a combination of increased thickness and higher aspect ratio, the decision was made to study the thick, high-aspect-ratio, supercritical wing in

detail as part of the Douglas EET effort. Although the generalized characteristics, which pointed to this advanced technology as worthy of further pursuit, were correct in principle, the application of such technology in the detail design phase can often lead to problems which can significantly limit the gains, or even make its application impractical. This study therefore examined the high-aspect-ratio supercritical wing as an integrated technology on a design which fulfills today's economic and environmental needs, and which involves all of the interfaces in order to optimize the structural and aerodynamic characteristics for efficient aircraft operation throughout the flight envelope.

Some of the primary variables which influence the wing design are:

- (1) Choice of High-Lift System Technology - Assuming that the aircraft's wing area is sized by a low-speed requirement, for example, approach speed, this area can vary by hundreds of square feet, depending on whether a simple or advanced high-lift system is used. If an advanced high-lift system is assumed, the wing area will be relatively smaller and, while benefiting from a significant weight advantage, will also present additional problems, not the least of which is the integration of the wing with the fuselage. A small, high-aspect-ratio wing has a relatively small root chord which requires a significant extension in order to house the landing gear. This problem is aggravated by the addition of another advanced technology, relaxed static stability, which moves the gear further aft relative to the wing. Accommodating these requirements results in a large trailing-edge extension which unsweeps a significant portion of the inboard wing and makes the job of the designer more difficult in terms of eliminating root effect and maintaining sweep effectiveness.

The smaller chords also tend to aggravate the interference problems since items of fixed size, such as nacelles, must be integrated on a smaller wing chord which structurally offers less potential for optimum positioning.

For a given takeoff gross weight, the airfoils of the small high-aspect-ratio wing are required to operate at higher lift coefficients

than those required for a larger wing of more conventional aspect ratio; hence, more design ingenuity is required to achieve a satisfactory buffet boundary without incurring a weight penalty (i.e., thinning the airfoils).

The wing chosen for this study was sized by a combination of approach speed and initial cruise altitude and employs an advanced high-lift system; hence, the study addresses the above problems.

- (2) Choice of Wing Parameters - To use supercritical wing technology in the optimum manner from the standpoint of fuel efficiency, it is applied to increasing wing thickness (approximately 20 to 25 percent thicker than today's transports) which, in turn, offsets the weight of the higher-aspect-ratio wing. Within these ground rules, however, many other design variables must be considered which, almost without exception, have both favorable and unfavorable effects on the total airframe system. Some of these are discussed below:

Spanwise distribution of lift, or span loading. Although an elliptical span loading offers the lowest induced drag, the optimum loading, considering the combined aerodynamic and structural characteristics, usually has some degree of washout. Since, at cruise Mach number, the initial separation which determines buffet onset usually occurs on the outboard wing panel, it is undesirable to allow the local velocities in this region to become too high. Thinning the outboard wing can alleviate this situation, but at the expense of a penalty in weight. In the final analysis, the choice of span loading is a function of wing weight, low-speed and high-speed clean wing separation characteristics (e.g., stall progression and buffet boundary) as well as induced drag.

Spanwise distribution of thickness. Since thickness and lift are somewhat interchangeable for a given upper surface velocity distribution, the decisions on the distribution of lift must be made in conjunction with the decisions on thickness. On the

inboard wing, the thickness near the root is affected by such considerations as the depth required for the landing gear and the volume needed for fuel. In addition, the choice of the spanwise distribution of thickness considers not only the combination of lift and thickness required to meet the cruise performance, but also the impact of the distribution on low-speed performance in both the clean and high-lift modes. Since, for a given planform, the weight of the wing box is largely a function of the lift and the thickness-to-chord ratio, the aerodynamic and weight characteristics must be considered in unison before a final decision can be reached.

Airfoil characteristics. The choice of chordwise and spanwise airfoil characteristics introduces many other variables. For the basic outboard airfoil, decisions must be made regarding the leading-edge radius and the amount of aft camber. Blunt leading edges are desirable from the standpoint of supercritical development at cruise, and maximum lift at low speeds. They are undesirable from the standpoint of drag creep. Highly aft-cambered airfoils are desirable from the standpoint of achieving good characteristics at high-lift coefficients, but they have high negative pitching moments which, for some configurations, can result in excessively high trim drag. Low-lift-coefficient (dive) characteristics at very high Mach numbers can also be unacceptable with too much aft camber, particularly where outboard lateral control devices are used. The spanwise distribution of aft camber also presents a design challenge as it is difficult to carry a large amount of lift aft on the chord near the root and at the same time counteract the root effect to maintain satisfactory inboard isobar characteristics.

The wing geometry configuration was developed through a combination of supercritical wing technology and DC-X-200 system studies. The supercritical wing technology included both Douglas and NASA contributions. The geometry development utilized application of existing experimental data and theoretical methods. Available experimental results included

two-dimensional, high-Reynolds-number data from the NAE 5-foot wind tunnel as well as three-dimensional data from the NASA-Ames 11-foot, the Rockwell International 7-foot, and the NASA-Langley 8-foot wind tunnels. Theoretical analyses included considerable use of the Douglas versions of the two-dimensional Bauer, Garabedian, and Korn program² (Program H), the two-dimensional Tranen program³, and the three-dimensional Jameson program⁴ (FL022).

In the following sections of this report, the results of the system studies which led to the basic configuration used in this task are discussed, as well as the wing design studies which resulted in the wind tunnel test configurations. Test results and analyses of these results are presented and, where appropriate, compared to the theoretical methods used in the design phase.

This Page Intentionally Left Blank

RESULTS OF SYSTEM STUDIES

The in-house system studies, from which the basic configurations tested in Phase I were derived, had as their objective the design of a medium-range wide-body transport capable of replacing the narrow-body aircraft of the B707/DC-8 generation. The design goals for this aircraft were lower fuel consumption, greater economy, reduced noise, and expanded cargo capability from today's transports. The principal advanced technology incorporated in this design was a high-aspect-ratio supercritical wing; other advanced technologies included an advanced high-lift system consisting of a variable camber Krueger and two-segment flap, longitudinal stability augmentation with relaxed static stability, use of composite structure for selected components, a short core-cowl nacelle for the wing-mounted engines, and significant advances in various digital and electronic systems. A three view of the aircraft, the DC-X-200, which was designed to use DC-10 fuselage components, is shown in Figure 1.

For these studies, aerodynamic characteristics of the high-aspect-ratio supercritical wings were estimated using both two- and three-dimensional test data and transonic theory. Since no satisfactory high-aspect-ratio supercritical wing data were available prior to the tests reported herein, optimistic levels for drag-rise characteristics and buffet boundaries were derived assuming that close to the full two-dimensional potential of the supercritical wing could be obtained. This appeared to be an achievable if somewhat ambitious goal based on theory and on three-dimensional data for lower-aspect-ratio supercritical wings.

High-Lift Systems - The advanced high-lift system, which is the subject of another task of the EET Phase I Studies, is shown in Figure 2. The improvement in low-speed performance over the DC-10-10 is shown in Figure 3.

Selection of Basic Wing Parameters - Early in the study, cruise speeds of $M = 0.78$ and $M = 0.80$ were chosen, the former to reduce fuel burned and the latter, the Mach number for minimum direct operating cost. Figure 4

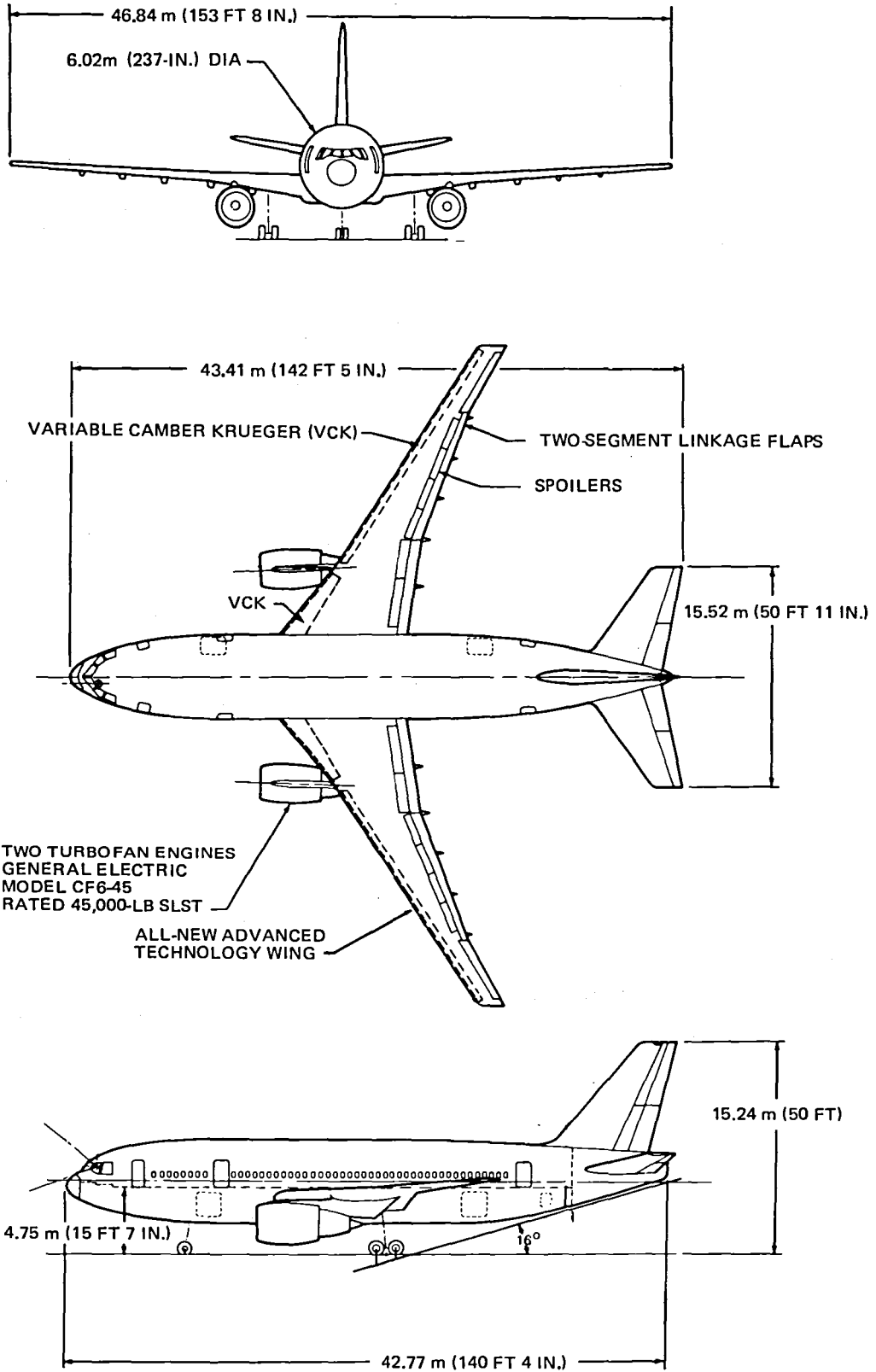


FIGURE 1. DC-X-200 GENERAL ARRANGEMENT

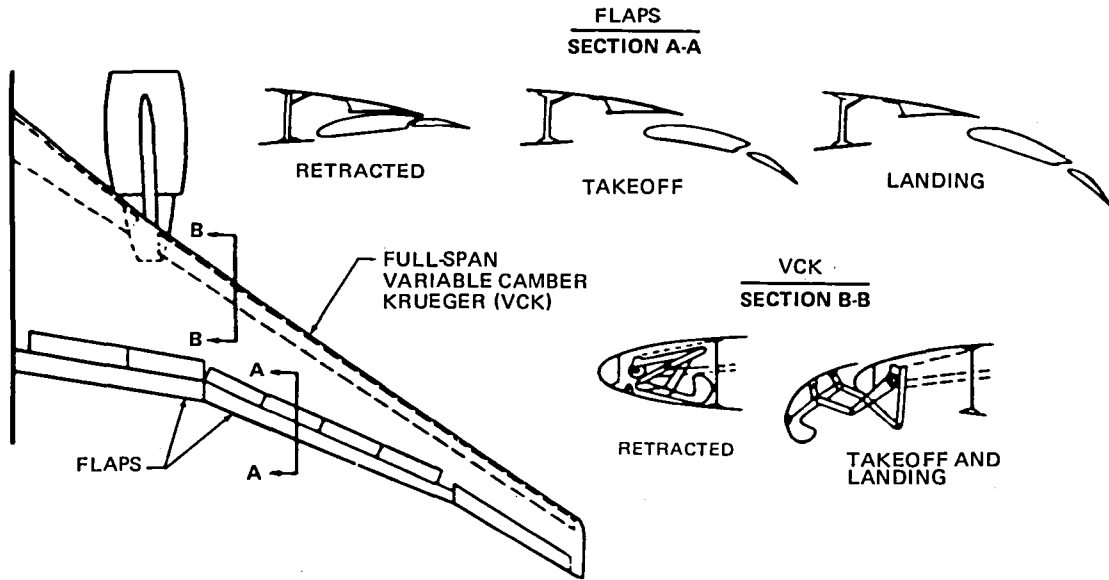


FIGURE 2. DC-X-200 WING PLANFORM AND HIGH-LIFT SYSTEM

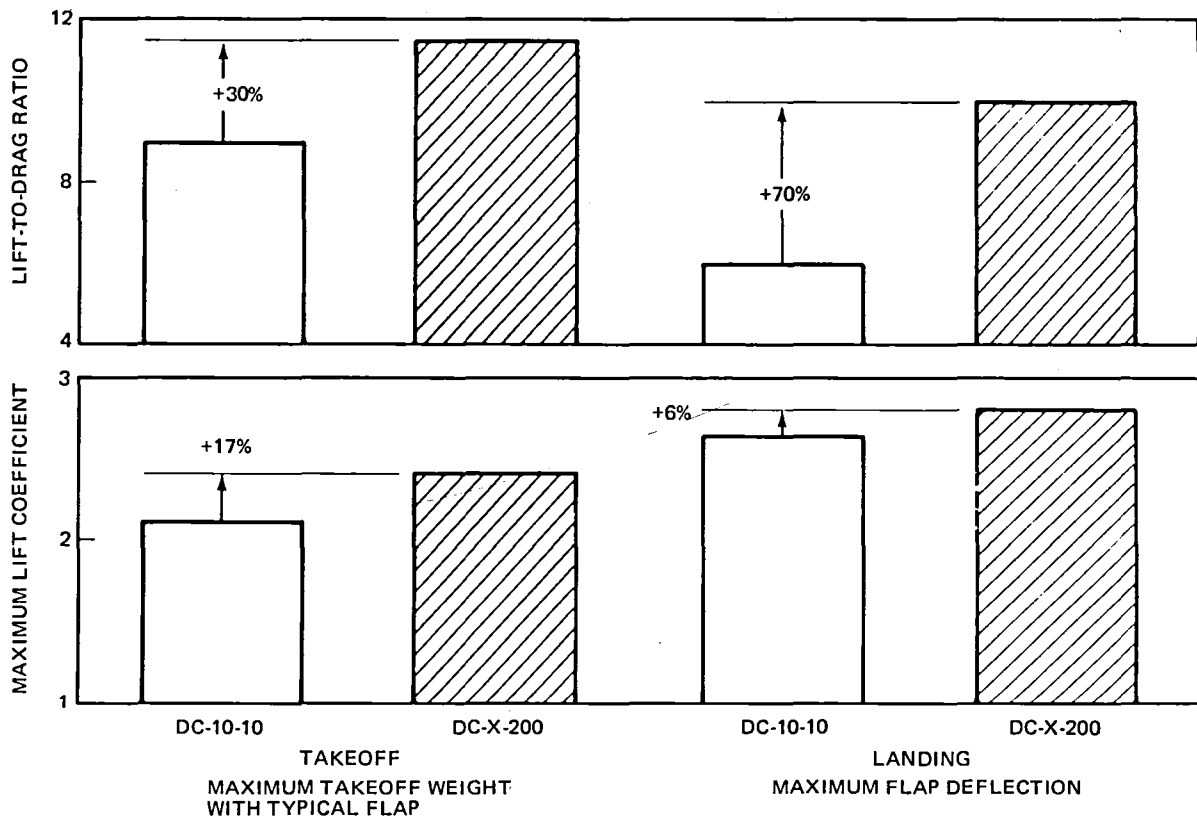


FIGURE 3. IMPROVEMENTS IN LOW-SPEED PERFORMANCE FOR ADVANCED TECHNOLOGY CONFIGURATION

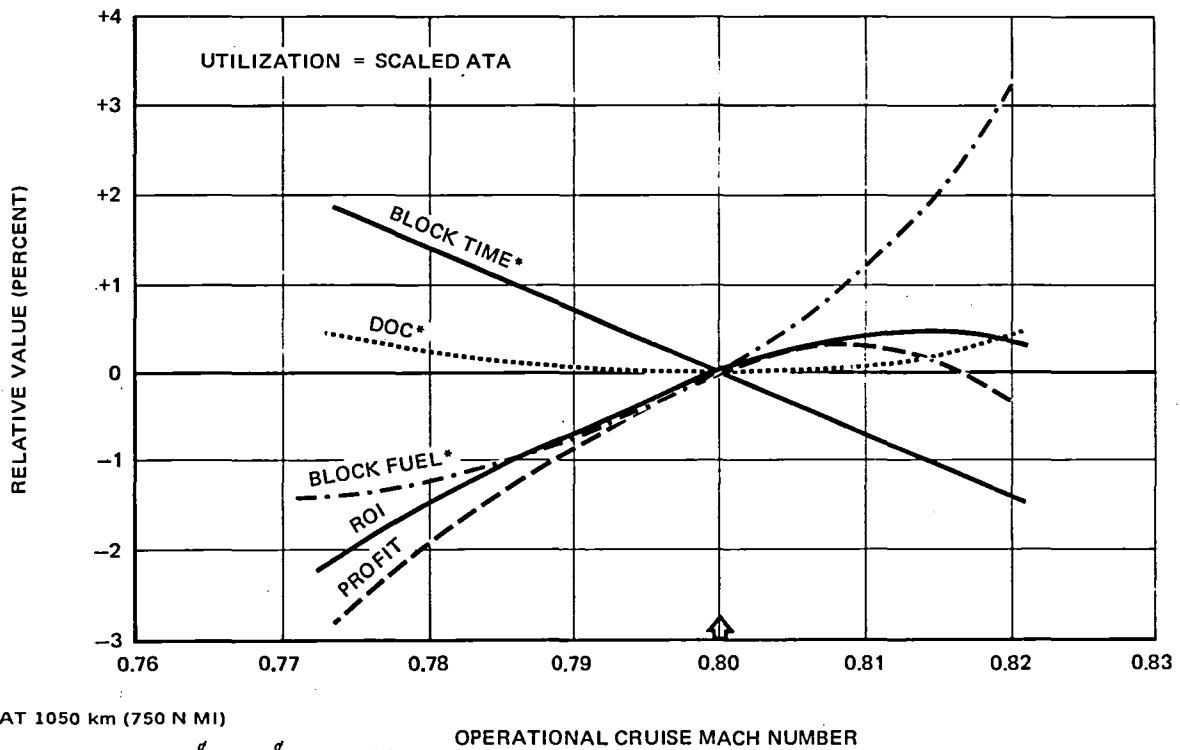


FIGURE 4. FACTORS WEIGHED IN DETERMINING OPTIMUM CRUISE SPEED

illustrates the trends in some important operational parameters with cruise Mach number for an assumed fuel cost of 16.5 cents per kilogram, or 50 cents per gallon (1977 dollars). While the direct operating cost (DOC) tends to "bucket" in the region of $M = 0.79$ to 0.81 , the block fuel burned levels off below $M = 0.78$. These two considerations were given the most weight in selecting the cruise Mach number for the aircraft. The other operational and economic indicators were also taken into account, to a lesser extent.

The basic wing geometry was selected after studying the effects of wing area and aspect ratio on the fuel burned and on various other economic indicators. The effects of wing area on some of the more important parameters are shown in Figure 5.

For compatibility with airport terminals, it was desirable that the wing span for the high-aspect-ratio wing not exceed that of the DC-10-10. This requirement, together with fuel usage and direct operating cost, resulted

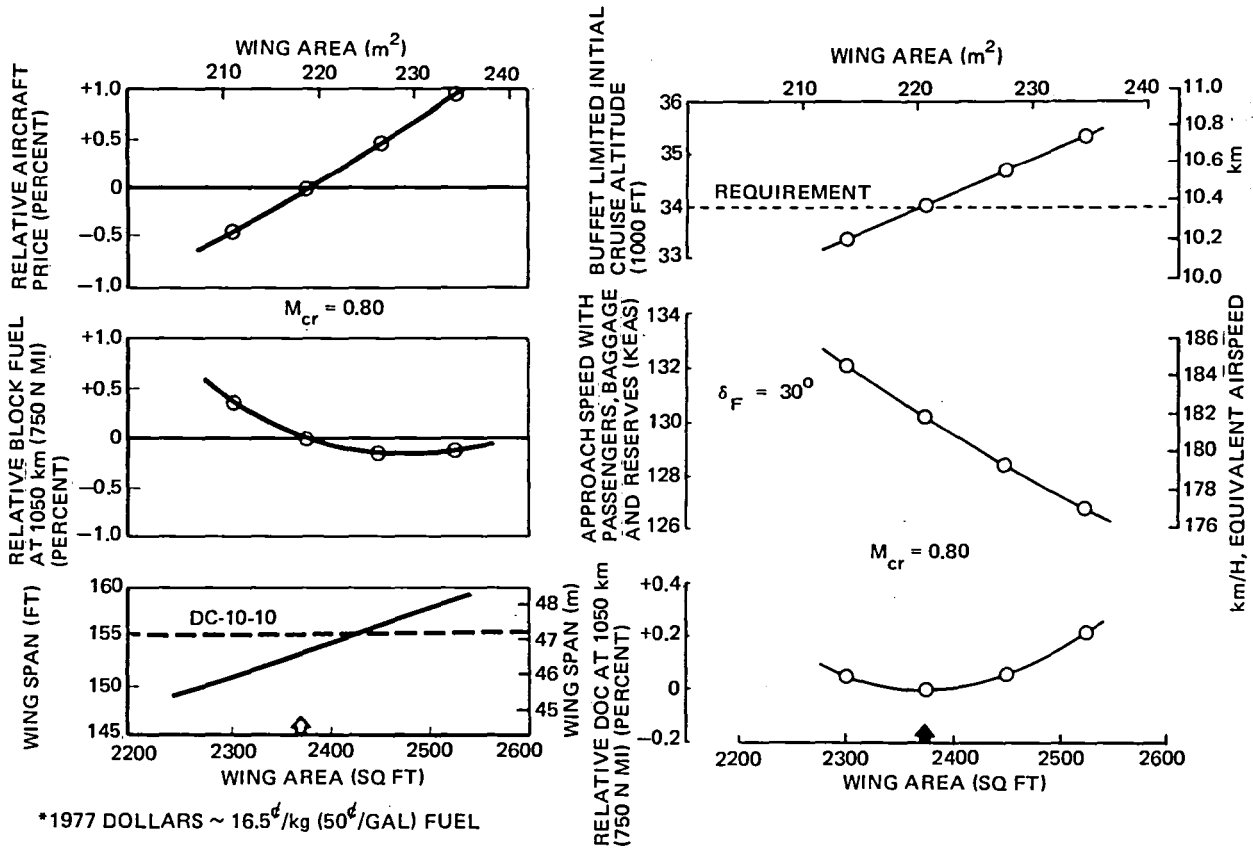
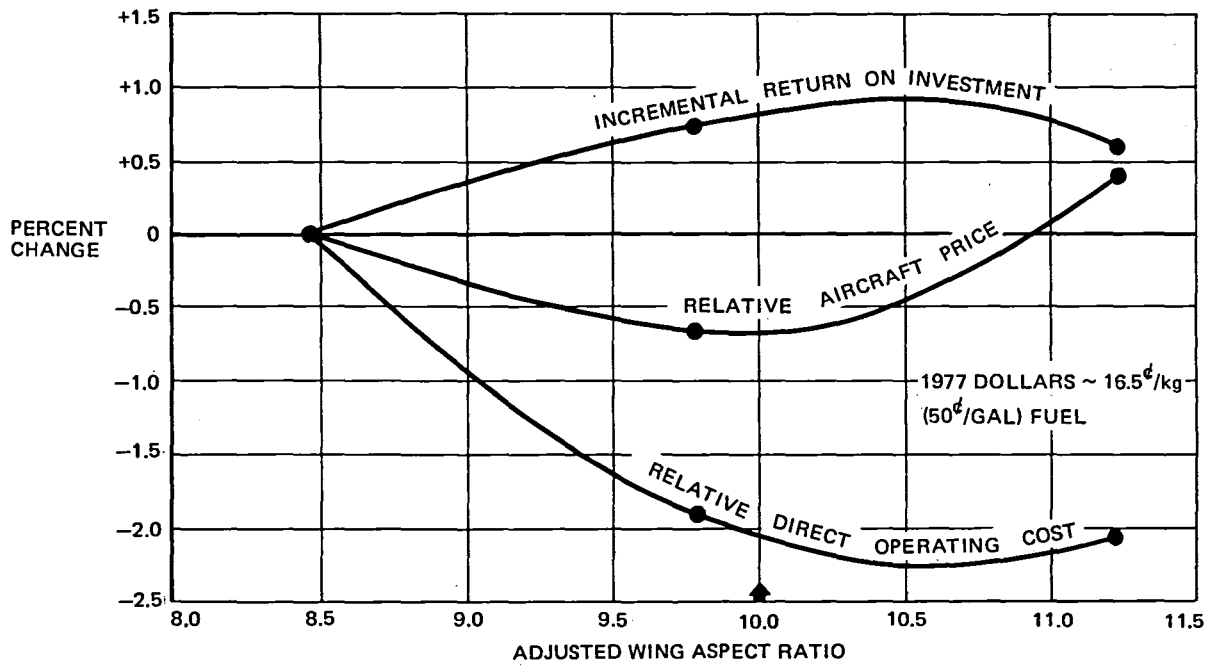


FIGURE 5. WING AREA STUDY RESULTS

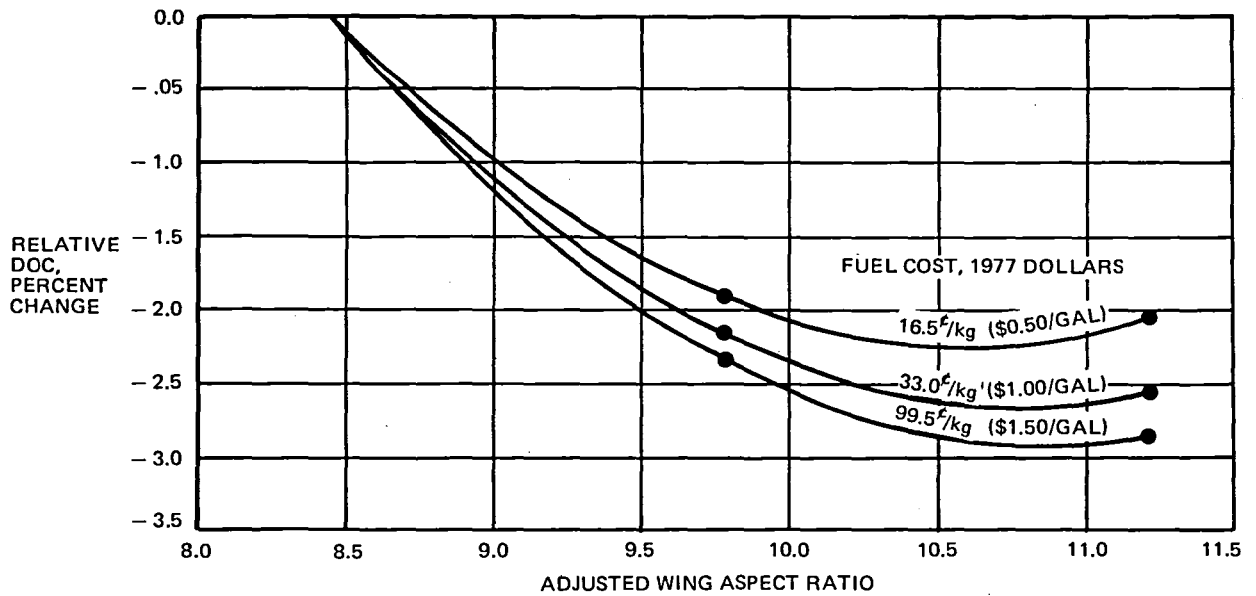
in a wing area slightly under 220 square meters (2400 square feet). This area was compatible with an initial cruise altitude of 10,400 meters (34,000 feet) and an approach speed of 182 km/h (130 knots).

The effects of aspect ratio are shown in Figures 6 and 7. In Figure 6a, the relative change with aspect ratio is shown for three economic parameters. In each case, the optimum aspect ratio is 10 or higher. In Figure 6b, the effect of aspect ratio on DOC is shown again, for three different fuel cost assumptions. In Figure 7, the effects of aspect ratio on noise and fuel burned are shown, and again the higher aspect ratios show significant improvements.

After considering the results of these studies and the incorporation of the relatively small, high-aspect-ratio wing with the fuselage and other aircraft components, an aspect ratio of 10.0, based on adjusted wing area, was selected. This corresponds to an aspect ratio of 10.8, based on wing trapezoidal reference area. (Adjusted wing area includes the exposed area



a. EFFECT OF ASPECT RATIO ON ECONOMIC PARAMETERS – FIXED FUEL COST



b. EFFECT OF ASPECT RATIO ON RELATIVE DOC FOR VARIOUS FUEL COSTS

FIGURE 6. EFFECTS OF ASPECT RATIO AND FUEL COST ASSUMPTION ON VARIOUS ECONOMIC PARAMETERS

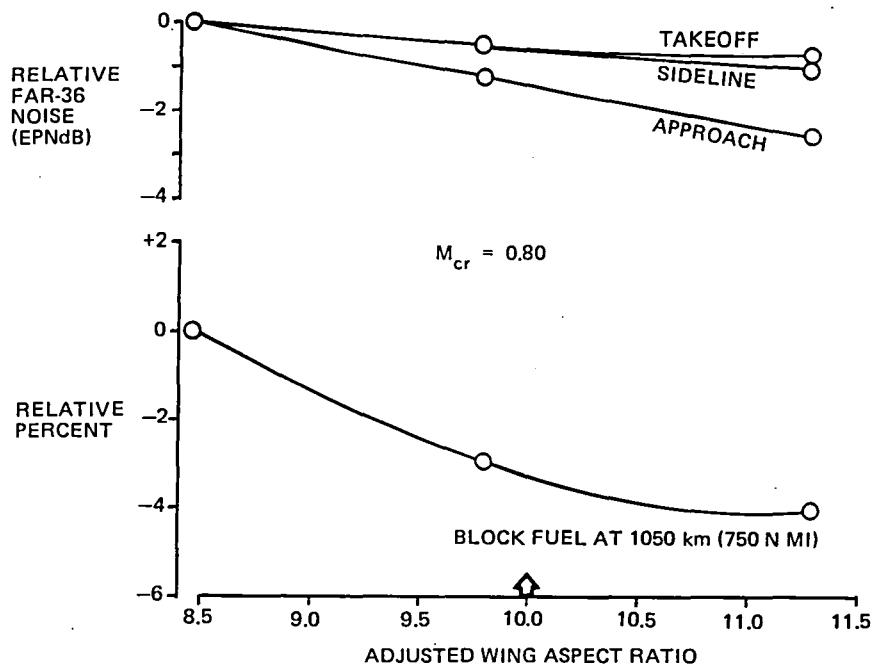


FIGURE 7. EFFECTS OF ASPECT RATIO ON NOISE AND BLOCK FUEL

of the leading-edge glove and trailing-edge extensions in addition to the trapezoidal reference area.)

Thickness and sweep studies done concurrently with the studies discussed above resulted in a quarter-chord sweep of approximately 30 degrees and an average thickness-to-chord ratio of approximately 0.125. The effect of sweep on DOC is shown in Figure 8.

The increased thickness and design lift coefficient for the high-aspect-ratio wing compared with the DC-10-10 are shown in Figure 9. The improved cruise efficiency, in terms of lift-to-drag ratio, compared with the DC-10-10 is shown in Figure 10.

In order to evaluate the impact of the advanced technologies on the fuel burned and the direct operating cost, a comparison of the advanced airplane was made with existing operational aircraft. The comparable characteristics of the airplanes evaluated are shown in Figure 11.

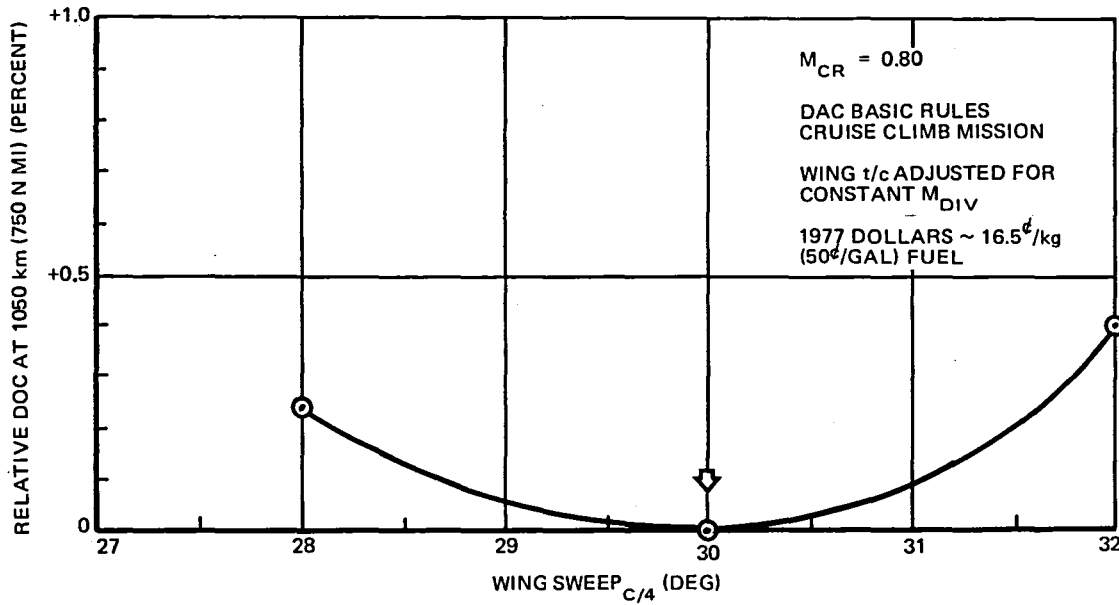


FIGURE 8. EFFECTS OF WING SWEEP ON DIRECT OPERATING COST

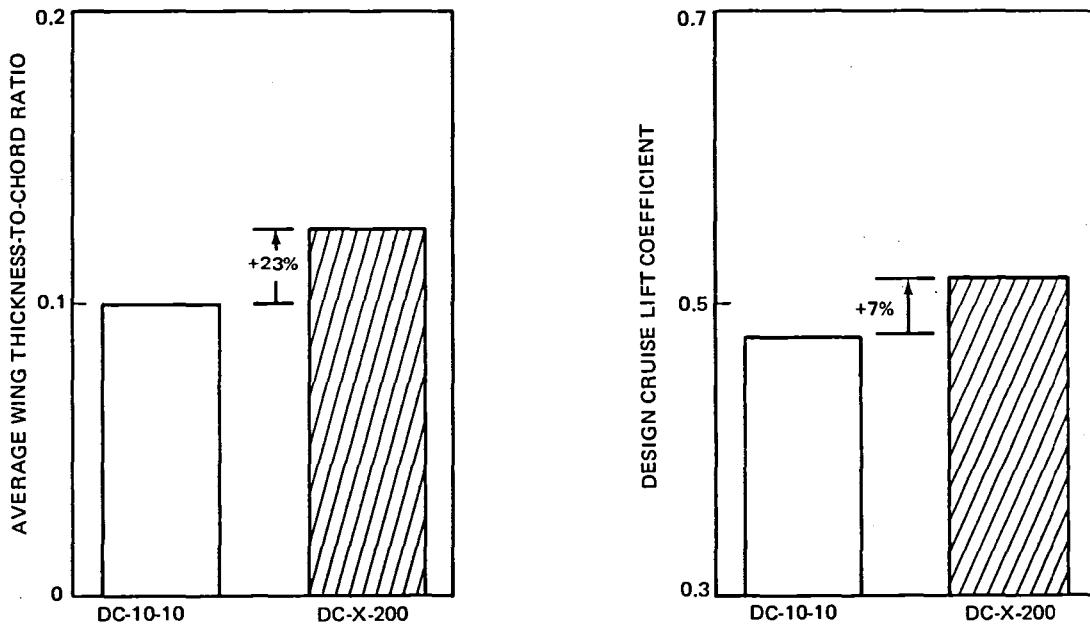


FIGURE 9. COMPARISON OF THICKNESS AND CRUISE LIFT COEFFICIENTS ~ CONVENTIONAL TRANSPORT (DC-10-10) AND DC-X-200

The relative fuel burned per seat-mile as a function of fuel burned per mile is shown in Figure 12. The DC-10-10 is used as the basis for comparison.

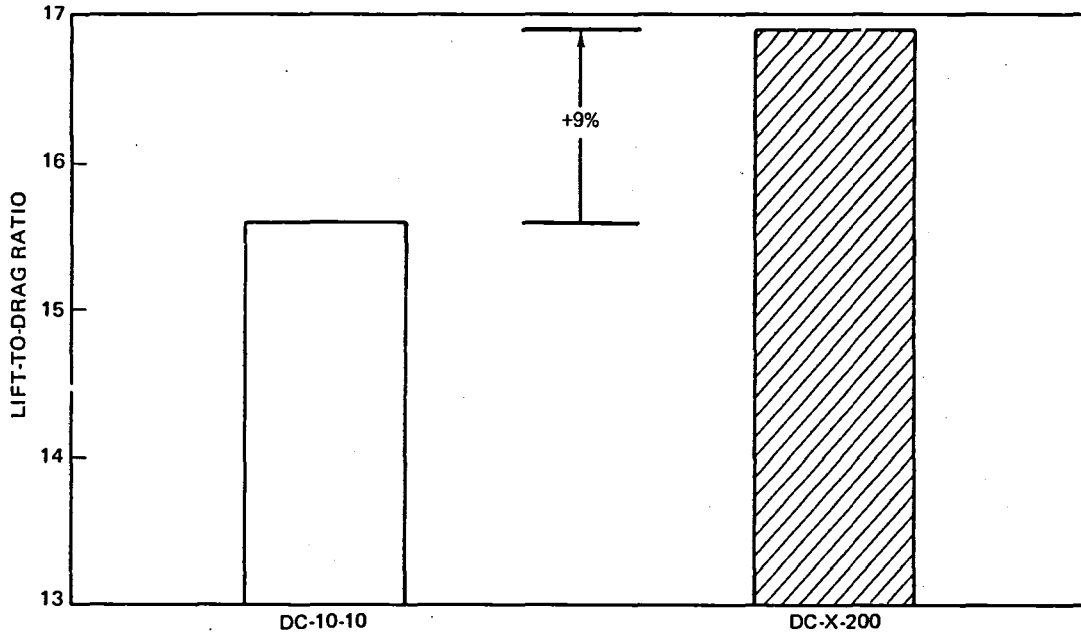


FIGURE 10. IMPROVEMENT IN CRUISE LIFT-TO-DRAG RATIO FOR ADVANCED HIGH-ASPECT-RATIO WING

	<u>B727-200 ADV</u>	<u>DC-X-200 (N-21)</u>	<u>A300B-4</u>	<u>DC-10-10</u>
ENGINES: NUMBER AND TYPE	3, JT8D-15	2, CF6-45	2, CF6-50C	3, CF6-6D
THRUST PER ENGINE, KN (LB)	68.95 (15,500)	200.17 (45,000)	226.86 (51,000)	178.37 (40,100)
NUMBER OF MIXED CLASS SEATS	140	230	257	295
CARGO VOLUME, M ³ (CU FT)	32.31 (1,141)	94.97 (3,354)	105.5 (3,725)	130.77 (4,618)
WING AREA, M ² (SQ FT)	149.6 (1,610)	220.2 (2,370)	245.7 (2,645)	343.3 (3,695)
MAXIMUM TAKEOFF WEIGHT, KG (LB)	86,409 (190,500)	132,902 (293,000)	150,002 (330,700)	195,044 (430,000)
OPERATOR'S EMPTY WEIGHT, KG (LB)	47,368 (104,430)	79,038 (174,250)	90,945 (200,500)	110,236 (243,030)
DESIGN RANGE, KM (N MI)	2,769 (1,980)	3,636 (2,600)	2,769 (1,980)	4,349 (3,110)
CRUISE MACH NUMBER	0.81	0.80	0.80	0.83
TAKEOFF FIELD LENGTH, MTOGW, SL, 29°C (84°F), M (FT)	2,630 (8,630)	2,173 (7,130)	2,103 (6,900)	2,825 (9,270)
APPROACH SPEED WITH FULL PSGR, BAGGAGE AND RESERVES, KM/H EQUIV (KEAS)	182 (130)	183 (131)	183 (131)	182 (130)
PAYLOAD FROM DEN→JFK, 33°C (92°F) DAY, AIRLINE RULES (PSGR/KG (LB) CARGO)	84/0	230/3,946 (8,700)	169/0	246/0
FUEL BURNED AT 1389 KM (750 N MI), KG (LB)	7,902 (17,420)	8,160 (17,990)	11,122 (24,520)	12,374 (27,280)
RELATIVE AIRCRAFT STUDY PRICE (PERCENT)	38	79	85	100*

*1977 \$30.4M

FIGURE 11. COMPARATIVE CHARACTERISTICS

Direct operating costs for different configurations per 1050-km (750-n-mi) trip and per seat are shown in Figure 13.

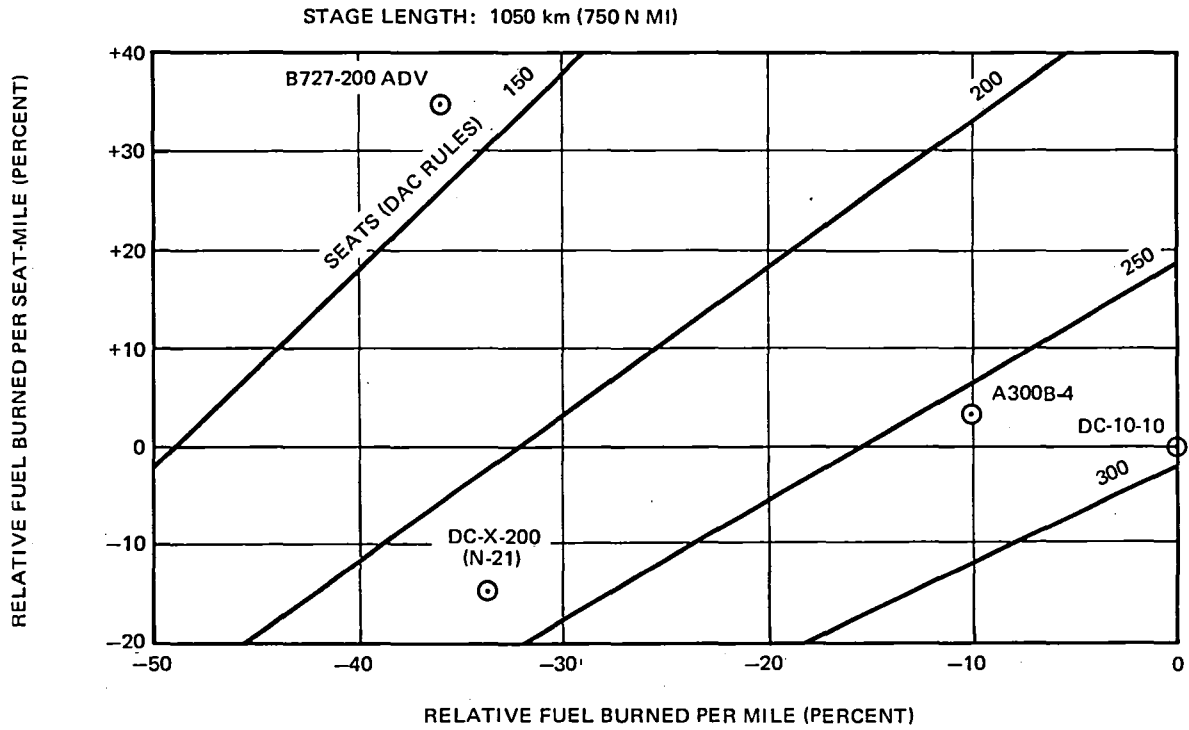


FIGURE 12. RELATIVE FUEL BURNED

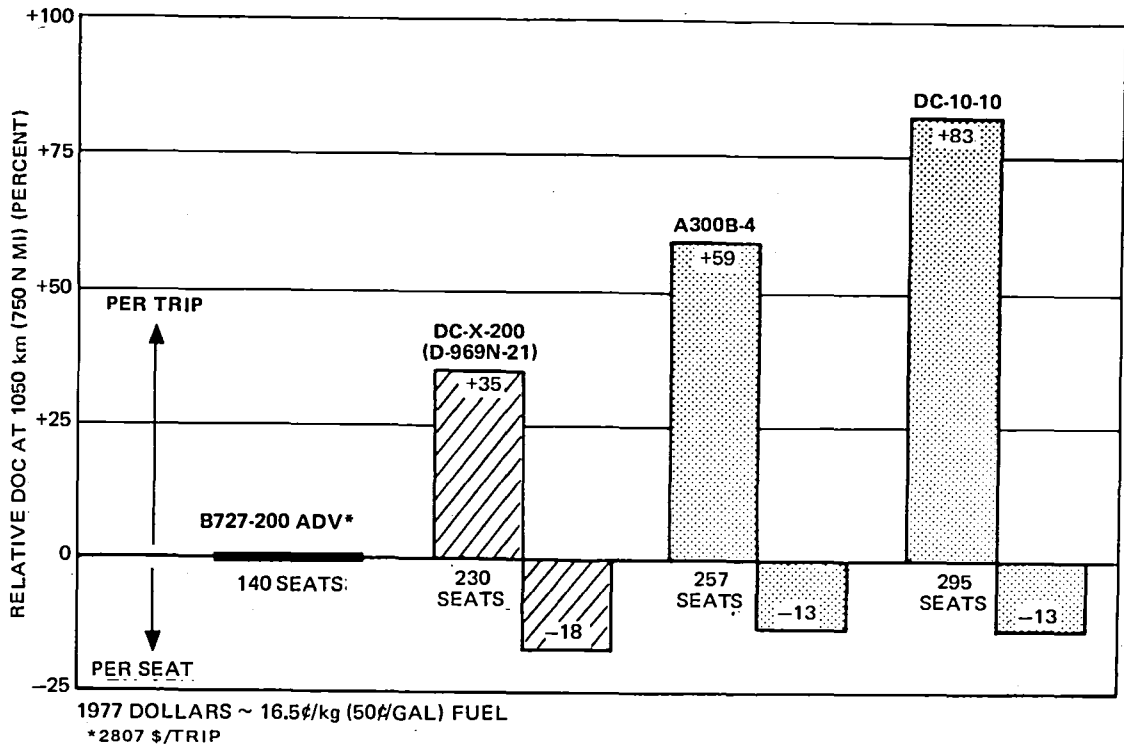


FIGURE 13. RELATIVE DIRECT OPERATING COSTS FOR CONVENTIONAL AND ADVANCED CONFIGURATIONS

Since these figures include the effects of several advanced technologies, a breakdown of the approximate impact of the individual technologies on direct operating cost is shown in Figure 14. Of the total reduction of 9.6 percent, over half is due to the high-aspect-ratio supercritical wing. It is estimated that the reduction in fuel due to this technology, for the mission studied, would be approximately 6 percent.

<u>ADVANCED FEATURE</u>	<u>DOC (%)</u>	<u>INCREMENTAL* OPERATIONAL PROFIT (%)</u>
SUPERCritical WING (CONSTANT AR)	-3.5	+58
HIGH-ASPECT-RATIO WING	-2.0	+10
VARIABLE CAMBER KRUEGER	-1.9	+32
LONGITUDINAL STABILITY AUGMENTATION	-0.5	+5
COMPOSITE FLOOR BEAMS AND STRUTS	-0.2	+1
COMPOSITE CONTROL SURFACES/FAIRINGS/WING FIXED TRAILING EDGE	-0.2	+2
AUTOMATIC REVERSE THRUST	-0.2	+2
ELECTRICALLY SIGNALLED SPOILERS	-0.1	+2
SHORTENED ENGINE CORE COWL (NO PRIMARY REV)	-0.7	+10
DIGITAL FLIGHT GUIDANCE AND CONTROL	-0.3	+6
TOTALS	-9.6	+130

*RELATIVE TO ALTERNATIVE INVESTMENTS AT 8.5% ANNUAL INTEREST

FIGURE 14. ADVANCED FEATURES ECONOMIC ASSESSMENT

This Page Intentionally Left Blank

WING CONFIGURATION DEVELOPMENT

In the development of the wing geometry, heavy reliance was placed on two- and three-dimensional test data generated by both Douglas and NASA as well as on advanced computational methods. The test data were used to determine broad design criteria while the transonic computational methods (i.e., Program H, Tranen, and Jameson) were used to accomplish the many detailed designs analyzed before the final five wings were selected.

Figure 15 presents the matrix of wing geometries that was examined during the development of wings W_3 , W_4 , and W_5 . Each planform and its associated annotation represents a different wing geometry which was analyzed using the three-dimensional Jameson program. The abbreviations, defined in the legend, identify configuration changes for each geometry. Variations in geometric characteristics included changes in twist distribution and planform as well as changes in defining airfoil sections. Asterisks are included to indicate configurations modified to observe aircraft system constraints.

The baseline configuration, W_A , was a high-aspect-ratio wing with a large inboard trailing-edge extension to house the landing gear. This wing was swept 30 degrees at the quarter-chord of the trapezoidal wing. W_A closely resembled the previously developed high-aspect-ratio configurations W_1 and W_2 , which had been wind tunnel tested prior to the contract activities. The test data and theoretical analyses of these configurations indicated an undesirable transonic flow development as a result of the large trailing-edge extensions and inboard airfoil sections.

The present development study was initiated by examining geometric perturbations from W_A . The most significant changes were then incorporated and further analyzed. The investigations which eventually led to W_X included significant changes in the planform. The effect of a small inboard leading-edge extension or glove was found to be quite favorable in reducing the inboard shock strength at transonic conditions. This effect

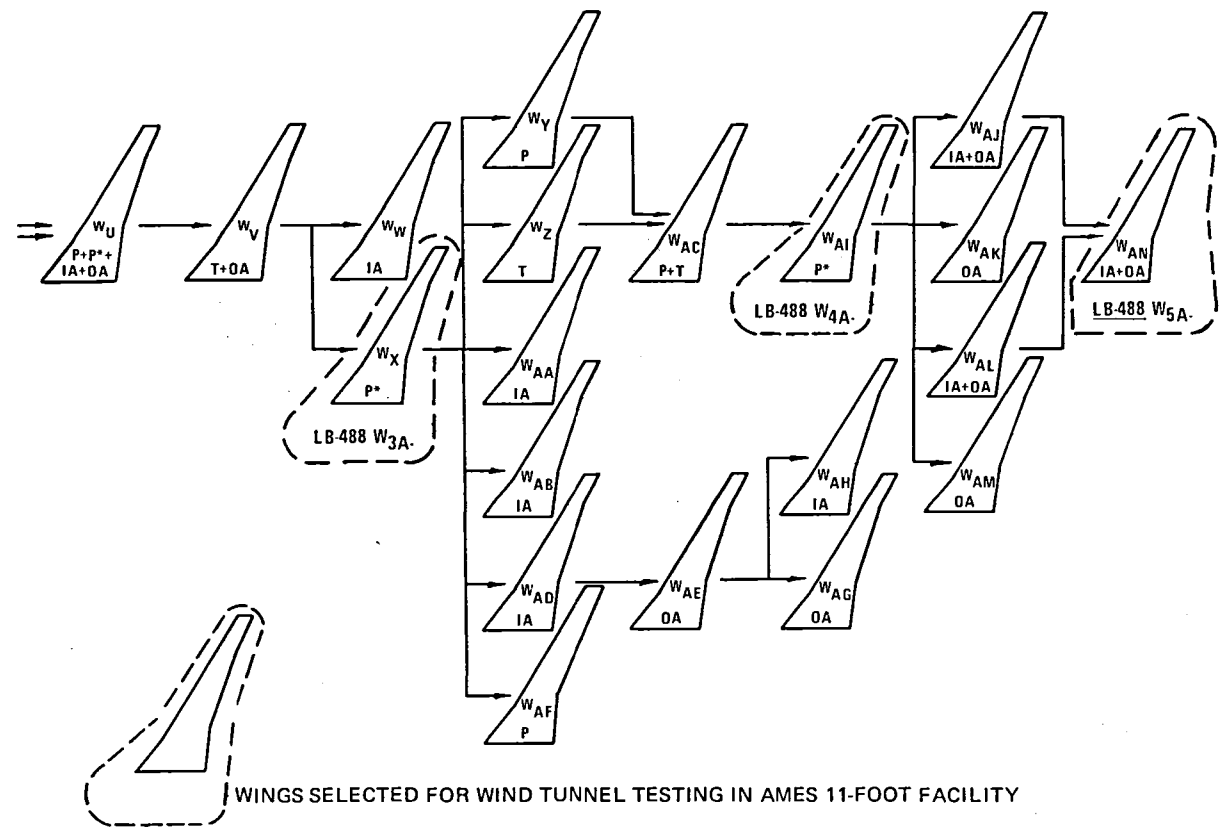
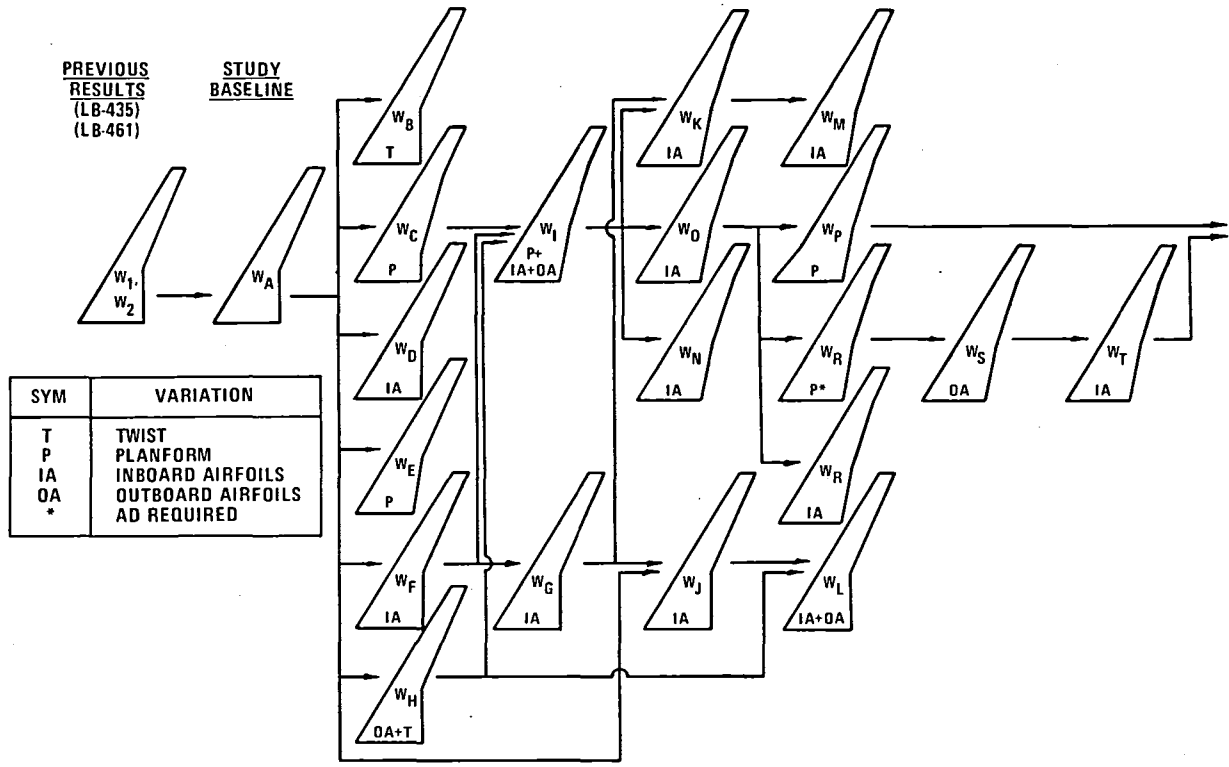


FIGURE 15. WING CONFIGURATIONS MATRIX EVALUATED USING THE 3-D DOUGLAS-JAMESON TRANSONIC PROGRAM

is shown in Figure 16. The upper surface isobars for the glove-off configuration illustrate a concentration of lines representing a shock wave near the midchord of the wing. Reduction of the shock sweep is evident at the wing root. With the leading-edge glove added, the shock is nearly eliminated.

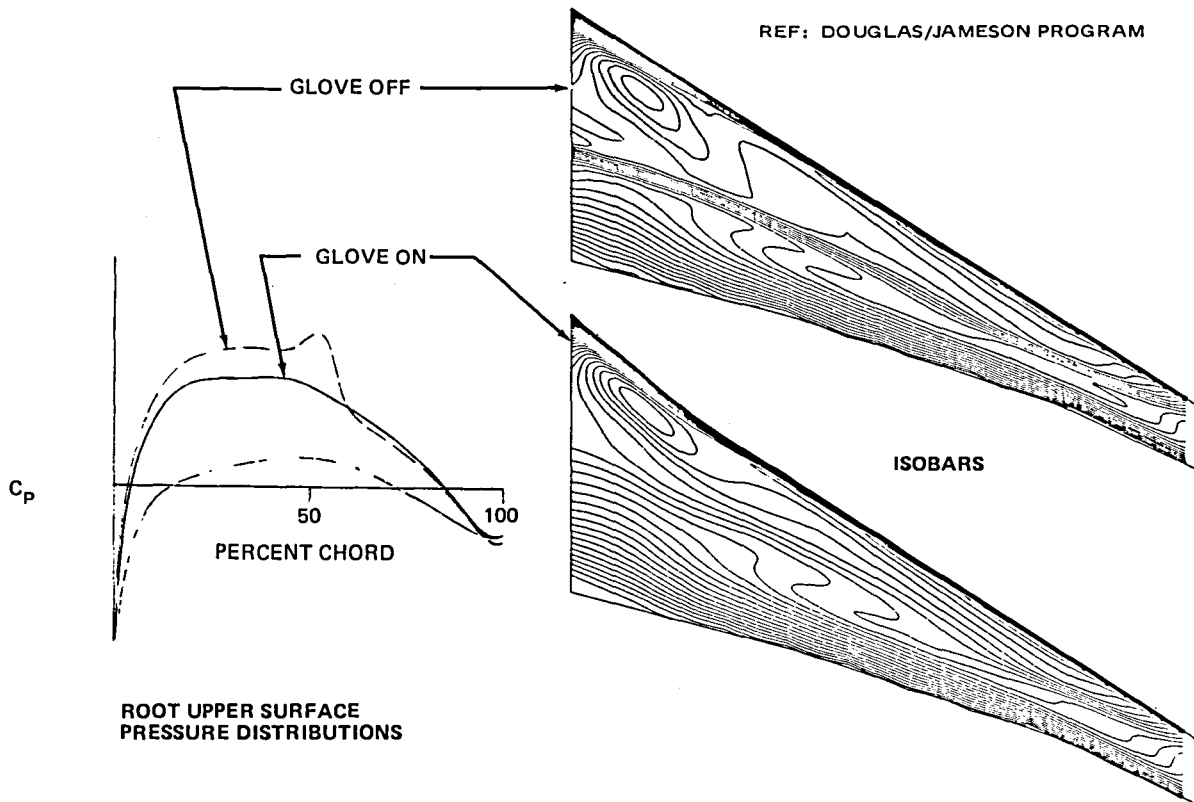


FIGURE 16. COMPUTATIONAL EFFECT OF INBOARD LEADING EDGE GLOVE

Configuration W_x was selected as the first wind tunnel model wing W_3 . The improvement in the calculated upper surface pressure distributions at transonic conditions is shown in Figure 17. The strong aft shock evident in the W_A pressure distributions has been suppressed and brought further forward. The major changes incorporated in W_3 are the addition of the leading-edge glove, the introduction of a second trailing-edge break to soften the effect of the inboard trailing-edge extension, and modification of defining airfoil sections. These modifications included changes in both camber and leading-edge radius on the outboard sections as well as redefinition of the inboard sections to accommodate the planform change.

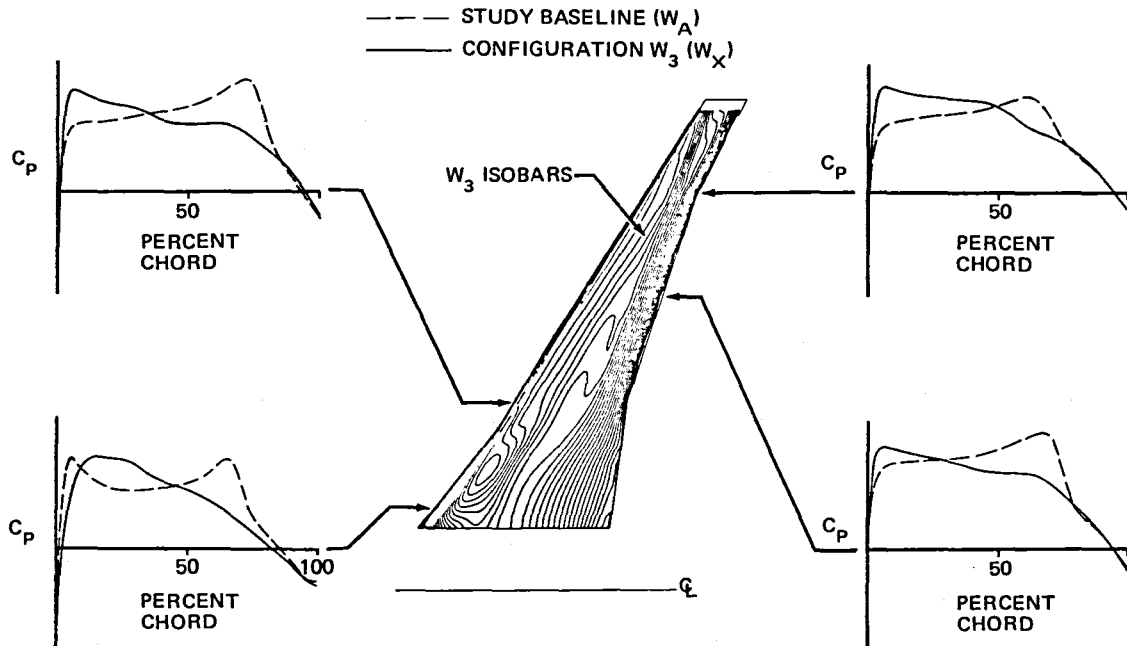


FIGURE 17. COMPARISON OF STUDY BASELINE AND CONFIGURATION W_3 UPPER SURFACE PRESSURE DISTRIBUTIONS (CRUISE CONDITIONS)

After the W_3 definition was completed, a more detailed analysis at off-design conditions was accomplished. This analysis indicated that buffet C_L could be improved with a planform and twist modification designed to lower the local lift coefficients on the outboard wing where flow separation was predicted to start. These changes were used to develop wind tunnel test configuration W_4 (W_{A1} in Figure 15). The planform variation is shown in Figure 18.

Figure 19 presents a comparison of calculated upper surface pressure distributions at an outboard span station for W_3 and W_4 .

The predicted buffet C_L improvement for W_4 over W_3 is the result of improving the flow over the outboard panel of the wing. The Mach number ahead of the shock is suppressed and the shock is further forward at the same free-stream Mach number and C_L conditions. These two effects provide more favorable conditions for boundary-layer recovery at the airfoil trailing edge.

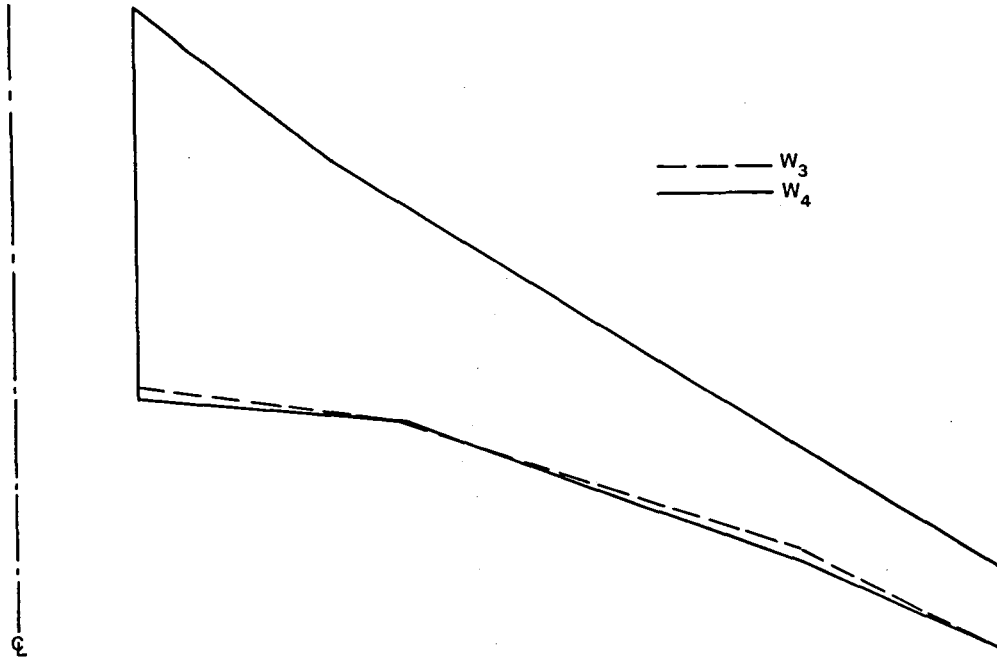


FIGURE 18. WING PLANFORMS, WINGS W_3 AND W_4

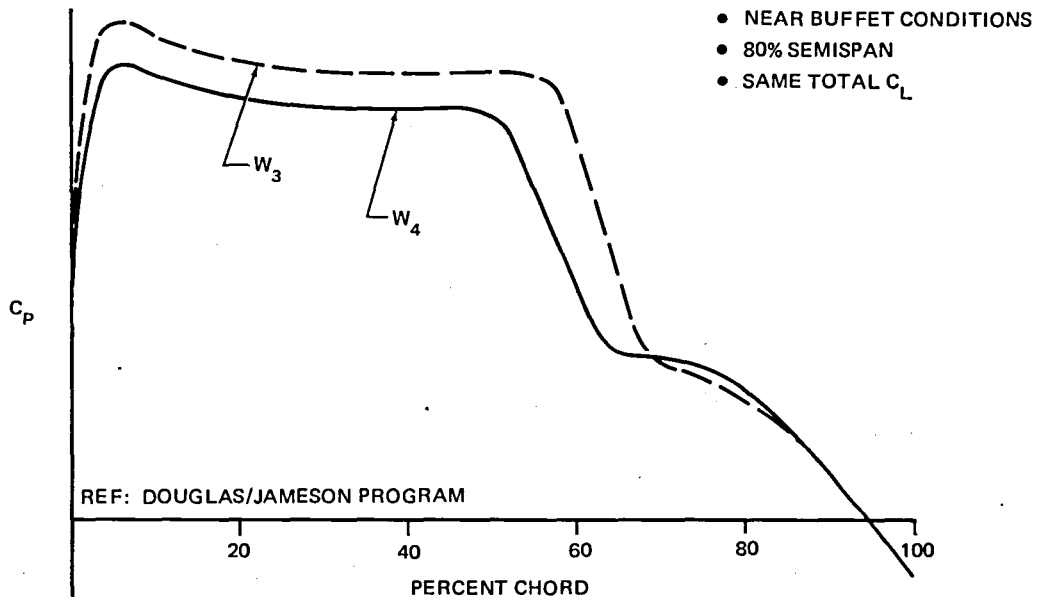


FIGURE 19. COMPARISON OF UPPER SURFACE CHORDWISE PRESSURE DISTRIBUTIONS, WINGS W_3 AND W_4

Further analysis of the defining airfoils used in W_3 and W_4 identified the areas of potential performance improvements. Reduced leading-edge radius addresses a possible premature drag creep before drag divergence. Increased aft camber improves the buffet C_L provided viscous effects do not cause excessive performance losses. These two variations, shown in Figure 20, were used to define test configuration W_5 . W_4 and W_5 have the same planform and were designed so that the leading edge and the aft camber variations do not overlap. Models for W_4 and W_5 were built with separate leading and trailing edges and provide four different wing geometries by using all combinations of the components. Hence, the effects of the leading-edge and trailing-edge modifications could be evaluated separately as well as together. The leading edge of W_4 and the trailing edge of W_5 were defined as W_7 , while the trailing edge of W_4 and the leading edge of W_5 were defined as W_8 .

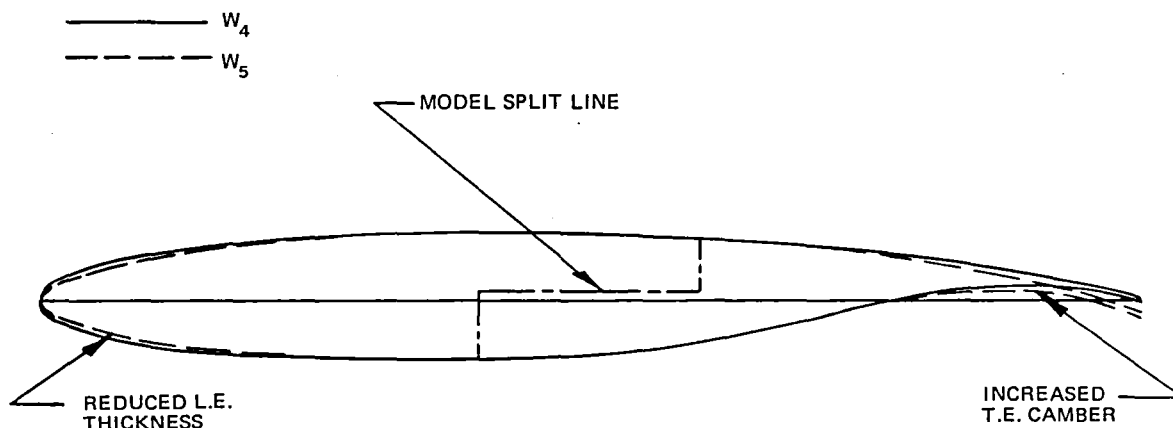


FIGURE 20. AIRFOIL MODIFICATIONS FOR ALTERNATE WING CONFIGURATION, W_5

TEST PLAN AND MODEL DESCRIPTION

Four wind tunnel tests were conducted between 4 April 1978 and 18 May 1979 to aid in the evaluation of the candidate high-aspect-ratio supercritical wing configurations. The wide-body configuration D-969N-21 was tested with the five wings, W_{3A}, W_{4A}, W_{5A}, W_{7A}, and W_{8A}. In all four tests, six-component force and moment data and wing pressure data were collected. Some flow-visualization photographs and wing wake pressure profile data were also obtained.

The first test, designated LB-488A, obtained data on wing W_{3A} and W_{4A}. Throughout this test, a lack of repeatability of the data was evident. For that reason, most of the test was repeated in the second entry, LB-488C, with much improved reliability. In LB-488C, the same configurations were tested at additional conditions and several wing surface flow visualization photographs were also taken. Therefore, the results of LB-488C will be presented in this report instead of those of LB-488A.

Test LB-488B followed in which four wings (W_{4A}, W_{5A}, W_{7A}, and W_{8A}) were tested. Force and pressure data were obtained on the wing-body configurations. Additionally, wing W_{4A} was tested with nacelles and pylons, flap linkage fairings, and empennage. Oil flow photographs were taken of selected configurations.

The final test of the series, LB-488D, was a test of the W₈ wing with a wake rake to obtain wake pressure profiles. The W₈ wing was also tested with the right aileron deflected up and down to evaluate outboard lateral control devices at cruise and dive Mach numbers.

The tests were conducted in the NASA-Ames Research Center 11-foot transonic wind tunnel. This tunnel facility is equipped for sting-mounting of complete aircraft models and for collection of six-component force and moment data as well as pressure data from an instrumented model. The tunnel provided a range of Mach numbers from 0.5 to 0.925, with Reynolds numbers from 6.5 million per foot to 8.0 million per foot.

The model tested was a 4.0-percent scale model of the DC-X-200 aircraft configuration. This included a wide-body fuselage, five high-aspect-ratio supercritical wing configurations with accompanying wing-body fillets, tail surfaces, and a set of nacelles, pylons, and flap linkage fairings for one of the wings. Each of the wings was instrumented with static pressure orifices. The model is shown in three-view in Figure 21, and sting-mounted in Figure 22.

DIMENSIONS IN CENTIMETERS (INCHES) MODEL SCALE

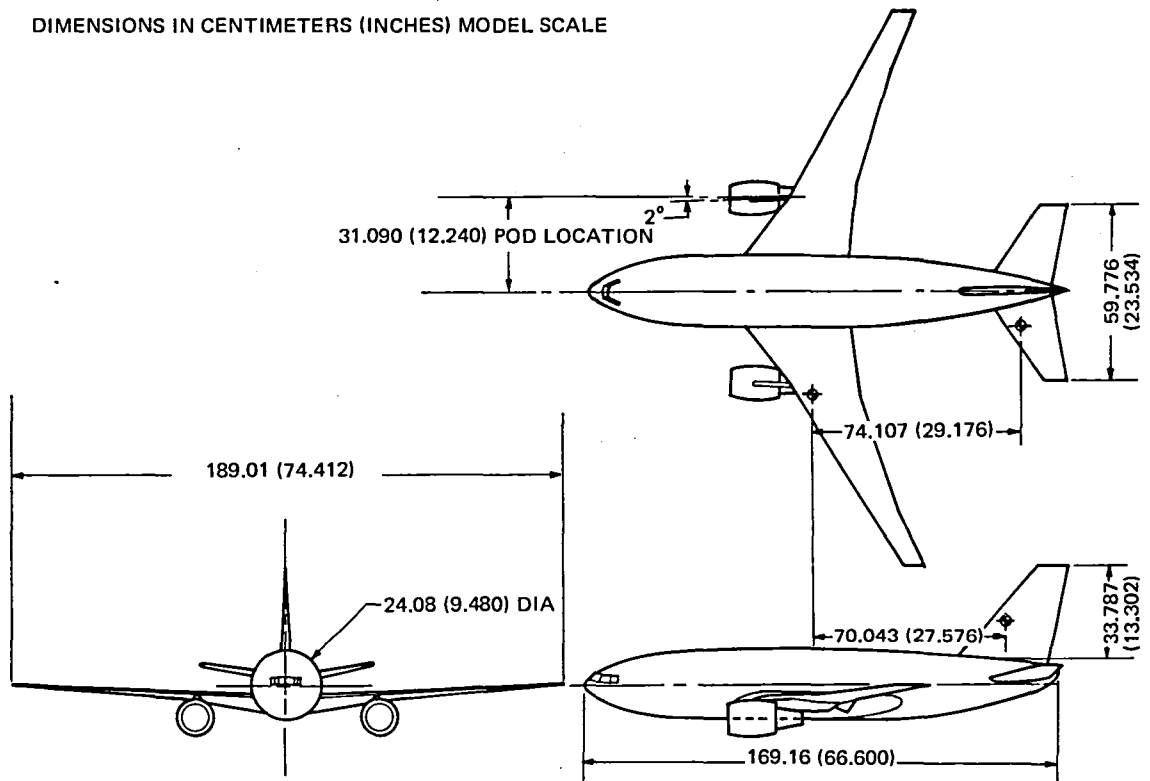


FIGURE 21. MODEL THREE VIEW

Boundary-layer transition location was controlled during the test by the application of glass beads to the various surfaces. The different transition schemes are identified together with the other test configuration notation in Table 1.

The B_{3A} fuselage represented the D-969N-21 configuration except for the hole in the aft fuselage necessary for the support sting. Housed within the fuselage were the dynamic damper, scanvalve assemblies, electrolytic alignment bubbles, and spirit levels for pitch and roll referencing. The

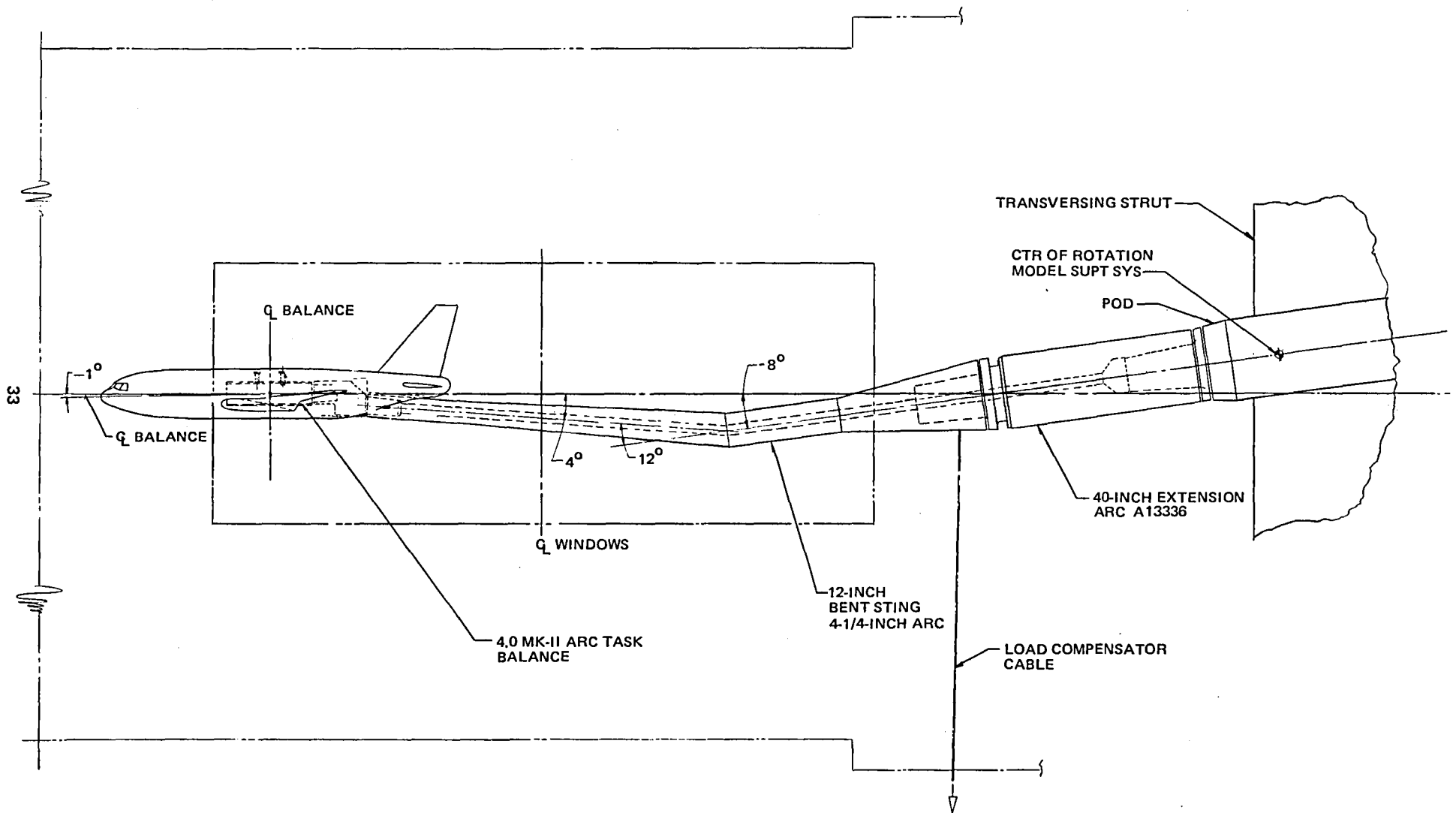


FIGURE 22. MODEL INSTALLATION IN ARC 11-FT TRANSONIC WIND TUNNEL – SIDE VIEW

TABLE 1

CONFIGURATION NOTATION

B _{3A}	Model DC-X-200 fuselage. Full-scale dimensions: Length = 42.29 m (1665 in.); constant-section diameter = 6.02 m (237 in.). The aft fuselage is modified to permit entry of the support sting.
b _{F3A}	Set of 10 flap mechanism fairings for the W _{4A} wing that are minimum enclosures for the current linkage motion system.
H _{1A}	Model DC-X-200 variable incidence horizontal stabilizer. Full-scale dimensions: S = 58.768 m ² (632.58 sq ft); b = 14.944 m (588.35 in.). $\Gamma = 10^\circ$. Slab surfaces.
N _{5A}	Set of two flow-through, short core-cowl nacelles for the G.E. CF6-45 engine.
P _{2B}	Pylons for N _{5A} on wing W _{4A} . The pylons are symmetrical and are cut back 3-1/4 percent of chord from the wing leading edge.
V _{1A}	Slab vertical stabilizer of Model DC-X-200. Full-scale dimensions: S = 44.6 m ² (480.0 sq ft); b = 8.447 m (332.554 in.).
W _{3A}	Model DC-X-200 wing. Full-scale dimensions: S = 212.603 m ² (2288.457 sq ft); b = 47.2521 m (1860.320 in.); AR = 10.0; $\lambda = 0.1407$; MAC = 5.351 m (210.655 in.). The model wing differs from the airplane static wing in that the dihedral and twist are increased so that these increases plus the deflection under load at M = 0.80, Re = 8 million, and C _L = 0.57 result in a simulated deflection for 1-g loading. The model wing consists of forward and aft segments with the spanwise joint at approximately 60-percent chord on the upper surface and 40-percent chord on the lower surface. The left-hand panel is instrumented with four chordwise rows of pressure orifices and an oil dispensing strip near

TABLE 1

CONFIGURATION NOTATION (Continued)

	the leading edge on the upper surface. The right-hand panel is instrumented with three chordwise rows of pressure orifices and an oil dispensing strip near the leading edge of the lower surface.
W _{4A}	DC-X-200 candidate wing with the same airfoils as W _{3A} but with a different planform. Full-scale dimensions: $S = 212.605 \text{ m}^2$ (2288.48 sq ft); $b = 47.252 \text{ m}$ (1860.320 in.); $AR = 10.0$; $\lambda = 0.2034$; $MAC = 5.15655 \text{ m}$ (203.014 in.). Other details are the same as in wing W _{3A} .
W _{5A}	DC-X-200 candidate wing with the same features as W _{4A} but with different airfoils. Does not have oil dispensing strips.
W _{7A}	The forward segments of the W _{4A} wing combined with the aft segments of the W _{5A} wing.
W _{8A}	The forward segments of the W _{5A} wing combined with the aft segments of the W _{4A} wing.
W _{8C}	Same as W _{8A} except for the addition of a deflectable outboard aileron in the right wing.
X _{2A}	Wing-fuselage fillet for B _{3A} W _{3A} adapted from the DC-10 X ₄₀ fillet.
X _{3A}	Same as X _{2A} except for B _{3A} with W _{4A} , W _{5A} , W _{7A} , and W _{8A} .
α_F	Angle of attack, in degrees, of the fuselage reference plane relative to the equivalent free airstream. Nose-up is positive.
i_H	Horizontal stabilizer incidence angle. Trailing-edge down is positive.

TABLE 1

CONFIGURATION NOTATION (Continued)

δ_a	Aileron deflection angle. Trailing-edge down is positive.
T_1	Glass beads on fuselage nose. 0.058 mm (0.0023 in.) dia. located 31.8 mm (1.25 in.) aft of nose.
T_3	$T_1 + 0.069$ -mm (0.0027-in.) dia. beads on upper wing surface, in a 3.2-mm (1/8-in.) wide band from 13 mm (1/2 in.) aft of L.E. at fuselage to 25 mm (1 in.) at L.E. break, constant 25 mm (1 in.) to outboard T.E. break to 13 mm (1/2 in.) at tip. All dimensions streamwise.
T_4	$T_1 + 0.069$ -mm (0.0027-in.) dia. beads on both sides of tail surfaces 25 mm (1 in.) aft of leading edge (streamwise).
T_5	$T_1 + 0.081$ -mm (0.0032-in.) dia. beads on upper wing surface in a 3.2-mm (1/8-in.) wide band. From 25 mm (1/2 in.) aft of leading edge at fuselage to 66 mm (2.6 in.) at inboard T.E. break to 41 mm (1.6 in.) at outboard T.E. break to 25 mm (1/2 in.) at tip.
T_5 (flap track fairings - bf_{3A})	3.2-mm (1/8-in.) wide band of 0.058-mm (0.0023-in.) dia. beads around each fairing 8 mm (0.3 in.) aft of leading edge.
T_5 (pylons - P_{2B})	3.2-mm (1/8-in.) wide band of 0.058-mm (0.0023-in.) dia. beads on both sides of pylon 3 mm (0.1 in.) aft of leading edge (normal to L.E.)
T_5 (nacelles - N_{5A})	fan cowl - 3.2-mm (1/8-in.) wide band of 0.058-mm (0.0023-in.) dia. beads on

TABLE I

CONFIGURATION NOTATION (Concluded)

inside and outside of fan cowl 5 mm (0.2 in.) aft of leading edge (normal to L.E.)

core cowl- 3.2-mm (1/8-in.) wide band of 0.058-mm (0.0023-in.) dia. beads on inside and outside of core cowl 8 mm (0.3 in.) aft of leading edge (normal to L.E.)

core plug- 3.2-mm (1/8-in.) wide band of 0.058-mm (0.0023-in.) dia. beads around plug 8 mm (0.03 in.) aft of leading edge

support blades - 3.2-mm (1/8-in.) wide band of 0.058-mm (0.0023-in.) dia. beads on both sides of all blades 8 mm (0.3 in.) aft of leading edge (normal to L.E.)

T₆ T₁ + 0.081-mm (0.0032-in.) dia. beads on both wing surfaces, 8 mm (0.3 in.) aft of leading edge.

R₂ spanwise traversing wing wake survey rake

NASA ARC Task 4.0 Mk. II internal strain gauge balance was housed in the fuselage midsection. Portions of the nose and midsection were removable to allow access to the instrumentation and to allow changing of the wing-body fillets. The aft fuselage had provisions for mounting tail surfaces. Line diagrams of the slab tail surfaces are shown in Figures 23 and 24. The

$S_H = 0.09403 \text{ m}^2 (1.0121 \text{ SQ FT})$
 $AR = 3.80$
 $\lambda = 0.350$
 $\text{SWEEP } C_H/4 = 30^\circ$
 $\Gamma = 10.0^\circ$

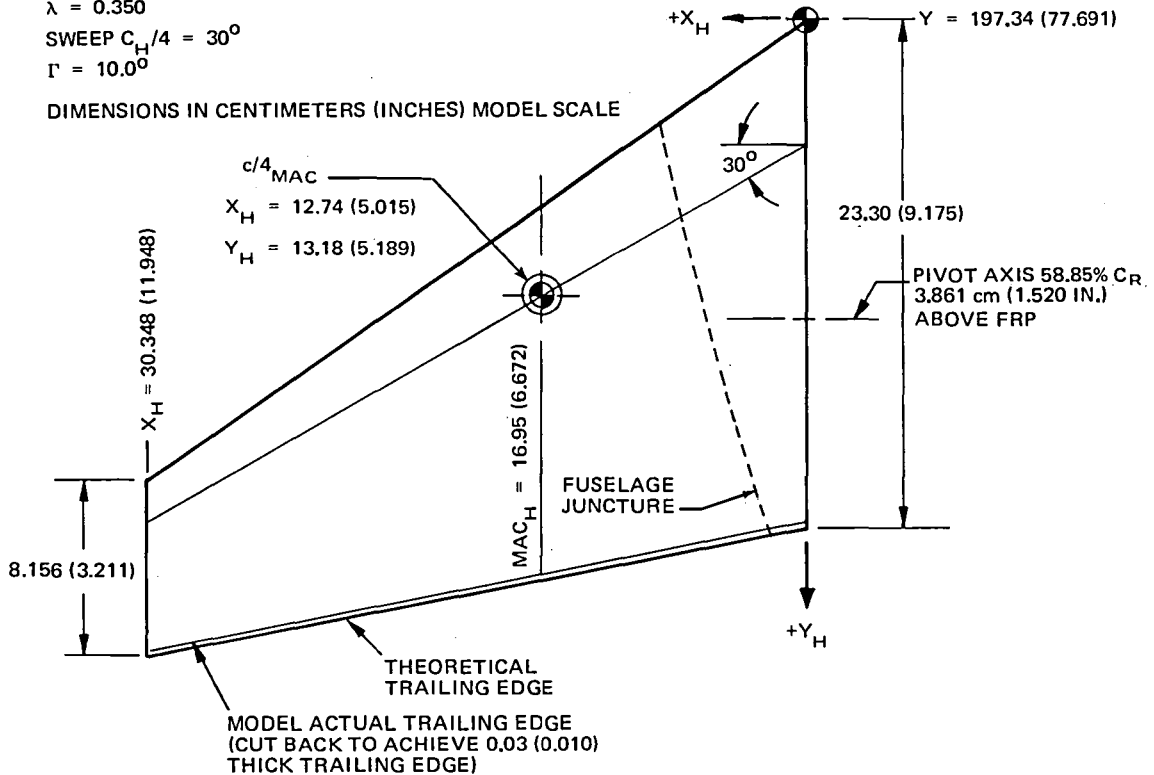


FIGURE 23. HORIZONTAL STABILIZER H_{1A} DIAGRAM

horizontal stabilizer was trunnion-mounted to allow changes in the incidence angle. The tail surfaces were replaceable by filler blocks for tail-off tests. The sting cavity was instrumented with 16 static pressure orifices to yield data to correct for the effects of the opening on the aerodynamic data.

The wings consisted of two panels (left and right), each of which were constructed of two halves (forward and aft), as shown in Figure 25. Wings W_{7A} and W_{8A} were created by interchanging the forward and aft portions of W_{4A} and W_{5A} . Wing W_{8A} was modified by the installation of an aileron of 25-percent chord from 80-percent to 98.4-percent semispan, and a row of pressure orifices at 92.5-percent semispan over the aft portion of the chord. This wing, designated W_{8C} , was tested in LB-488D.

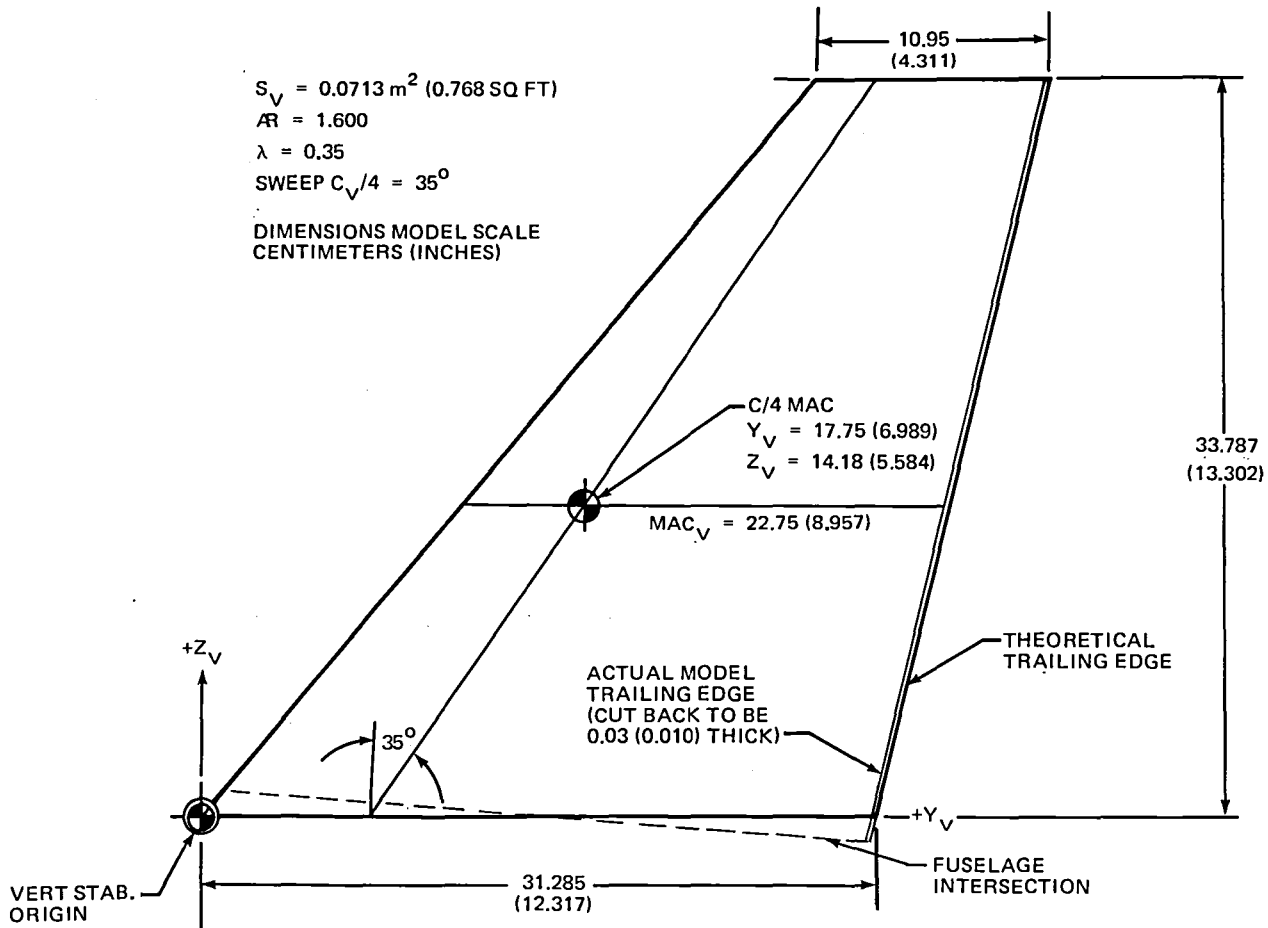


FIGURE 24. VERTICAL STABILIZER V_{1A} DIAGRAM

Each of the other wings was instrumented with seven rows of pressure orifices, as shown in Figure 26. The wing line diagrams are shown in Figures 27 and 28.

A pair of symmetrical pylons and flow-through nacelles and a set of flap hinge fairings were available for wing W_{4A} . The nacelles represented the short core-cowl configuration for the G.E. CF6-45 engine. The pylons were symmetrical and were cut back 3-1/4 percent from the wing leading edge. The nacelle/pylon assembly is shown in Figure 29.

The model dimensional data are tabulated in Table 2.

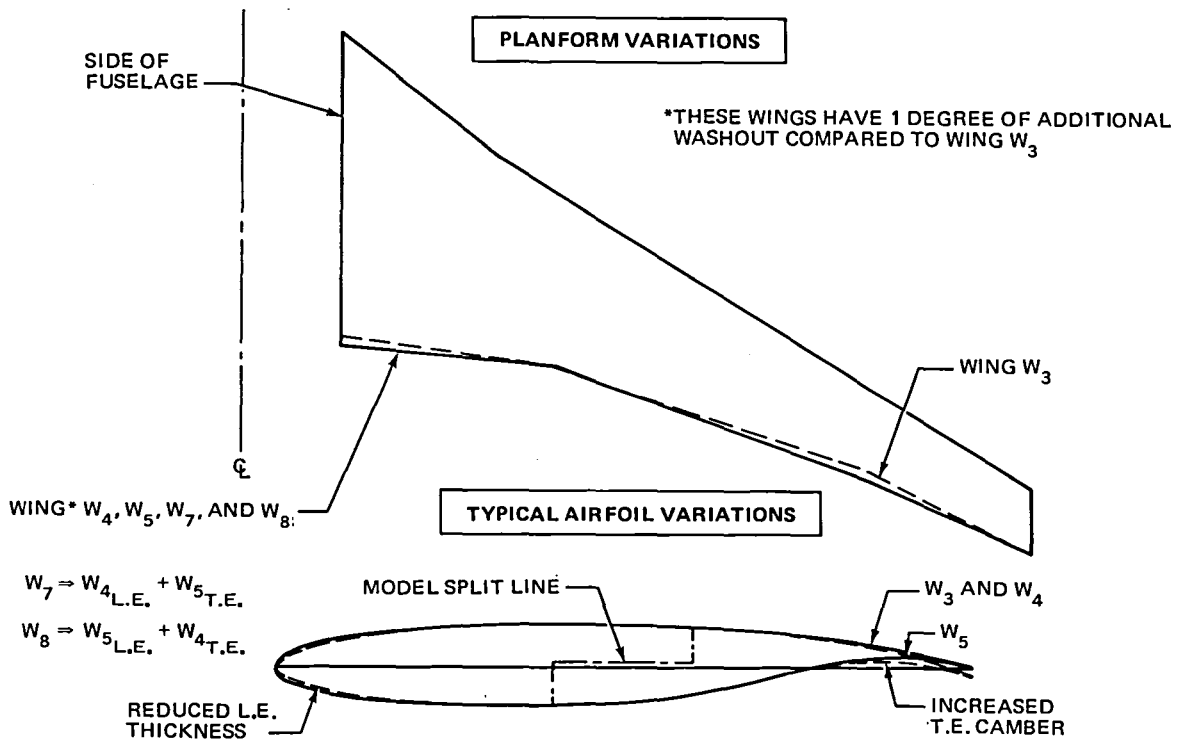
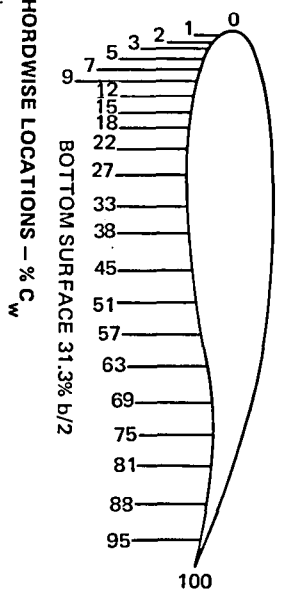
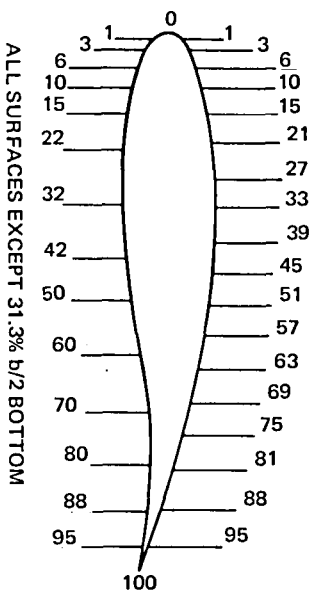
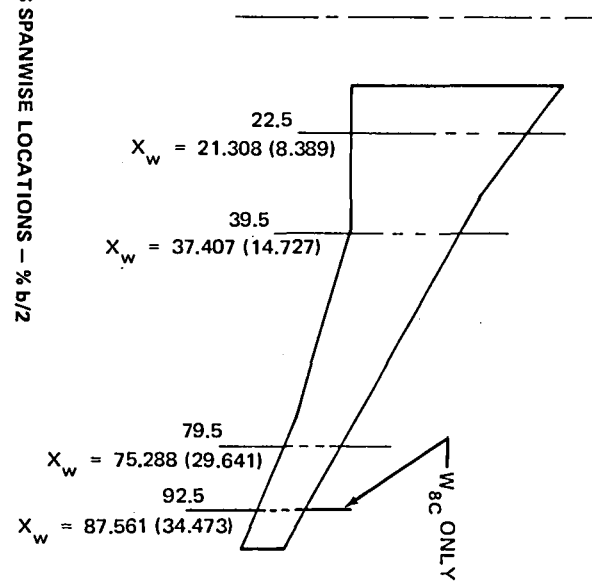
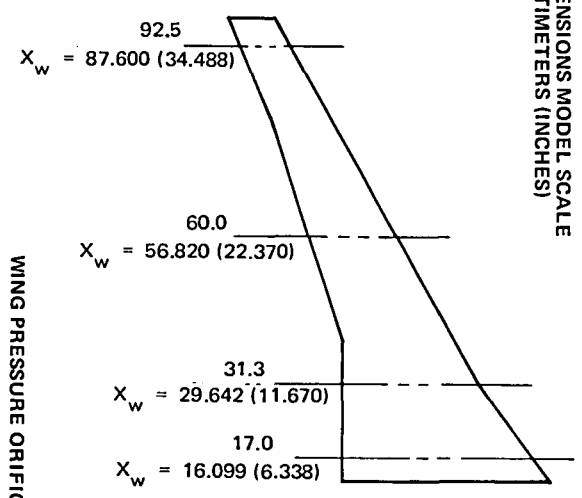


FIGURE 25. COMPARISON OF TESTED WING GEOMETRIES

The Douglas traversing wake rake used in the fourth test consists of an array of 21 pressure tubes mounted on a traversing arm which is attached to the model supporting sting. The rake assembly is shown in Figures 30 through 32. The rake measured total and static pressures in the wing wake. It was remotely controlled by a dedicated computer, the Douglas SEL system computer, which directed it through a vertical traverse (a short arc) at each of a programmed series of spanwise locations just behind the left wing. The computer also provided on-line printout of results during the testing.



DIMENSIONS MODEL SCALE
CENTIMETERS (INCHES)



WING PRESSURE ORIFICES SPANWISE LOCATIONS - % b/2
FIGURE 26. PRESSURE ORIFICE LOCATIONS

$S_W = 0.3402 \text{ m}^2 \text{ (3.662 SQ FT)}$

$b_W = 189 \text{ cm (6.201 FT)}$

$\bar{c}_W = 21.402 \text{ cm (8.426 IN.)}$

$AR = 10.5020$

$\lambda = 0.1407$

$\Lambda = 28.62^\circ$

ABOVE VALUES FOR TRAPEZOIDAL
IN-JIG WING PROJECTED ON FRP

ALL DIMENSIONS MODEL SCALE
CENTIMETERS (INCHES)

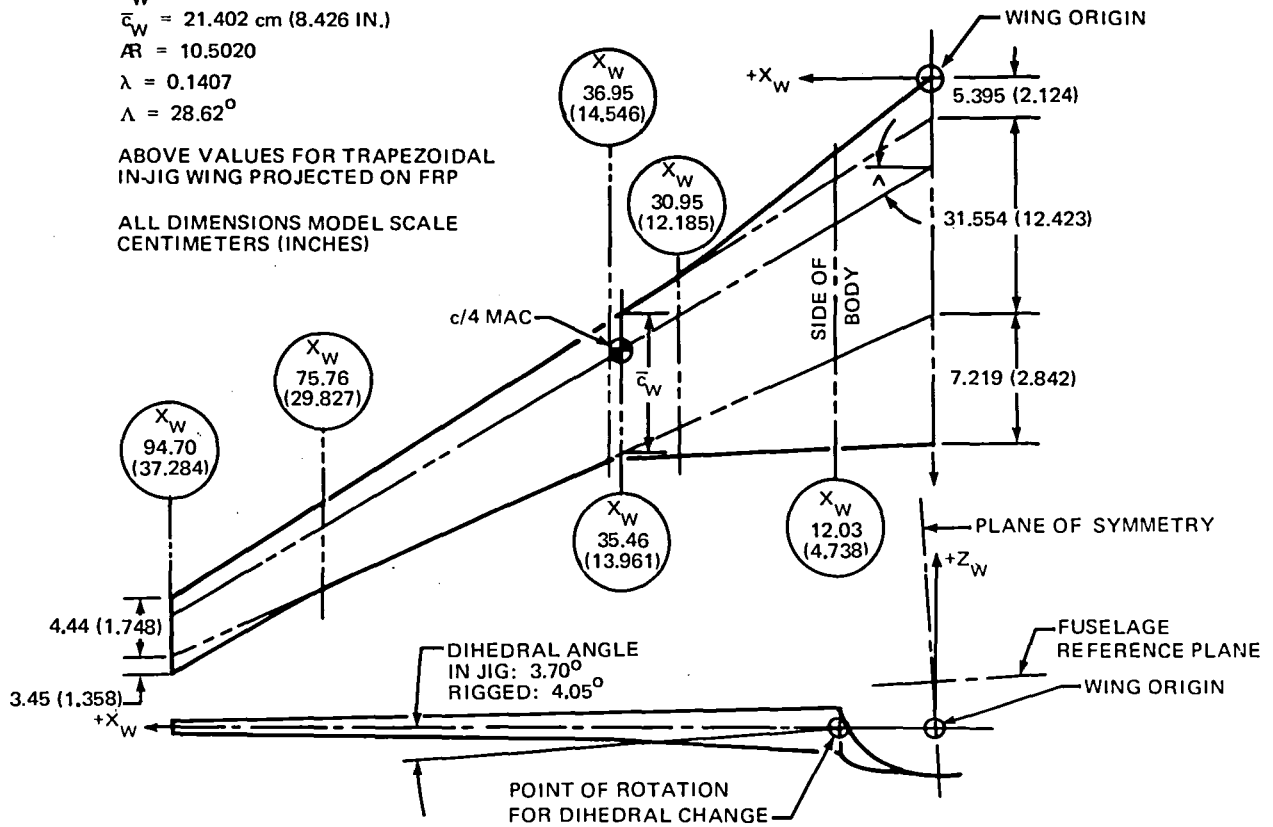


FIGURE 27. WING LINE DIAGRAM - W₃

$S_W = 0.3402 \text{ m}^2 \text{ (3.662 SQ FT)}$
 $b_W = 189 \text{ cm (6.201 FT)}$
 $\bar{c}_W = 20.627 \text{ cm (8.121 IN.)}$
 $AR = 10.5020$
 $\lambda = 0.2034$
 $\Lambda = 28.983^\circ$

ABOVE VALUES FOR TRAPEZOIDAL
 IN-JIG WING PROJECTED ON FRP

ALL DIMENSIONS MODEL SCALE
 CENTIMETERS (INCHES)

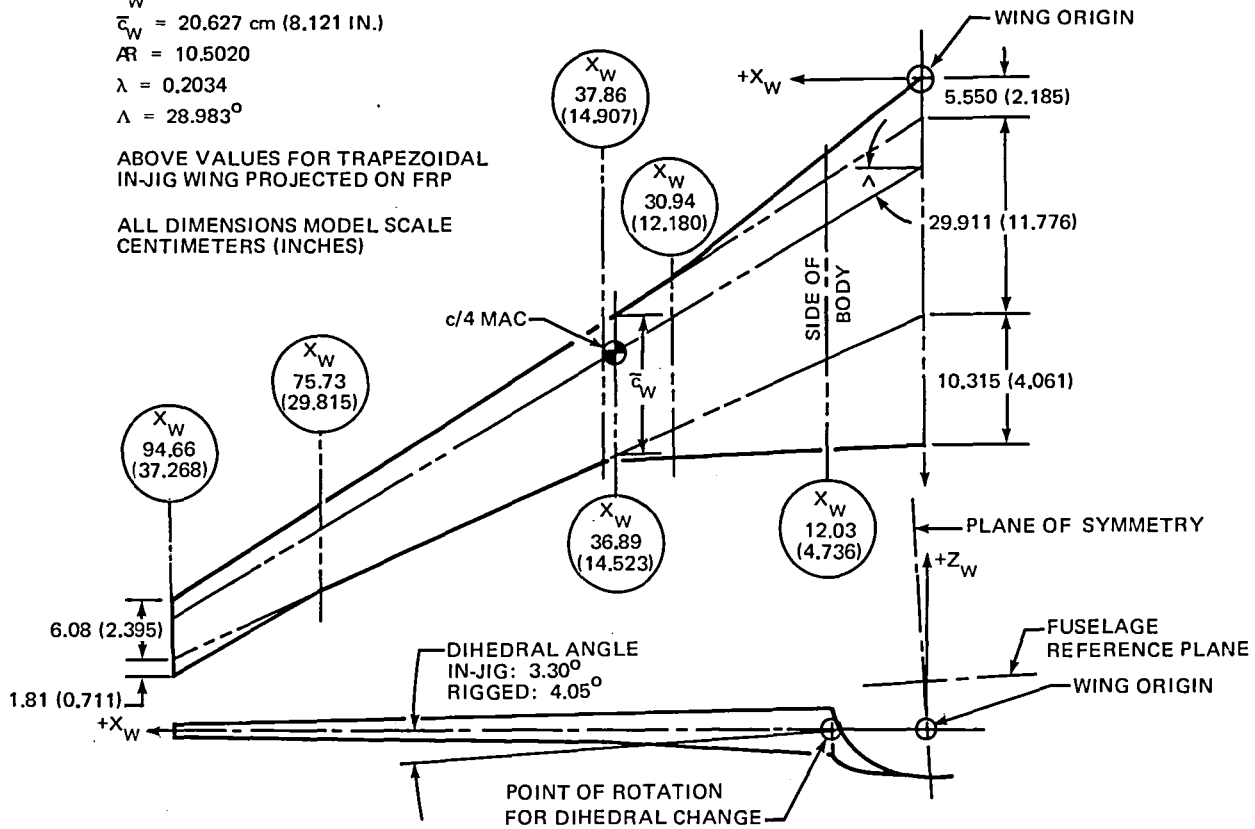


FIGURE 28. WING LINE DIAGRAM - W_4, W_5, W_7, W_8

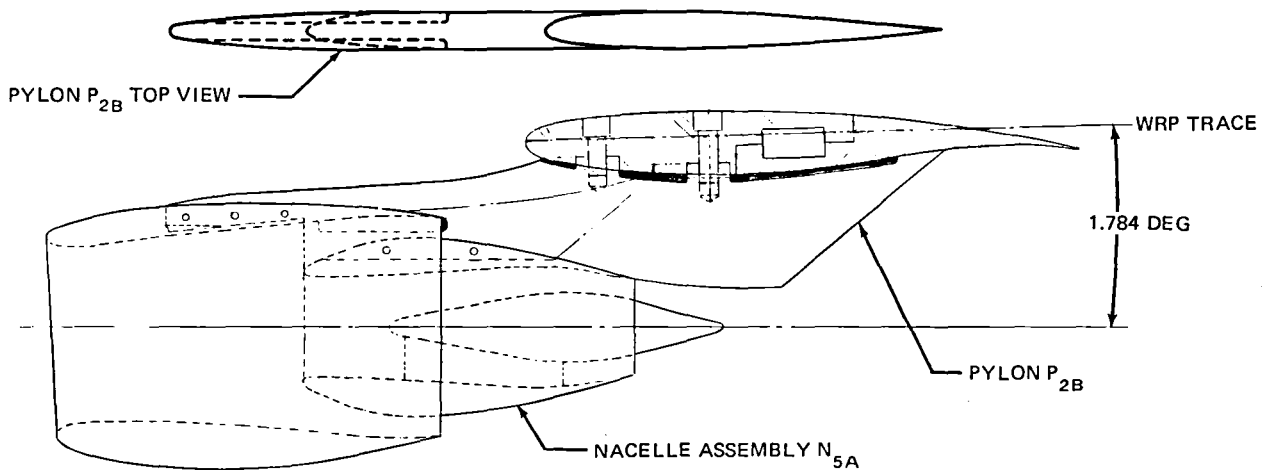


FIGURE 29. NACELLE/PYLON ASSEMBLY

TABLE 2
DIMENSIONAL DATA

Component	Unit	Model Scale Dimension		
Fuselage (B3A)				
Length	m (ft)	1.692 (5.550)		
Diameter-constant section	cm (in.)	24.08 (9.480)		
Wing - all dimensions projected on FRP				
		W3A	W4A	W5A
Area	m ² (ft ²)	0.3402 (3.662)	0.3402 (3.662)	0.3402 (3.662)
Span	m (ft)	1.890 (6.201)	1.890 (6.201)	1.890 (6.201)
Root chord trapezoidal wing	cm (in.)	31.554 (12.423)	29.911 (11.776)	29.911 (11.776)
Total root chord	cm (in.)	44.166 (17.388)	45.776 (18.022)	45.776 (18.022)
Tip chord - trapezoidal wing	cm (in.)	4.440 (1.748)	6.083 (2.395)	6.083 (2.395)
Total tip chord	cm (in.)	7.889 (3.106)	7.889 (3.106)	7.889 (3.106)
Mean aerodynamic chord (MAC)	cm (in.)	21.40 (8.426)	20.63 (8.121)	20.63 (8.121)
Spanwise station of MAC	cm (in.)	35.39 (13.932)	36.83 (14.499)	36.83 (14.499)
Aspect ratio	—	10.502	10.502	10.502
Taper ratio	—	0.1407	0.2034	0.2034
Sweepback of quarter-chord line	deg	28.62	28.983	28.983

TABLE 2

DIMENSIONAL DATA (Continued)

Component	Unit	Model Scale Dimension	
		Horizontal	Vertical
Stabilizer			
Area	m ² (ft ²)	0.0940 (1.012)	0.0713 (0.768)
Span	cm (in.)	59.776 (23.534)	33.787 (13.302)
Root Chord	cm (in.)	23.304 (9.175)	31.285 (12.317)
Tip Chord	cm (in.)	8.156 (3.211)	10.950 (4.311)
MAC	cm (in.)	16.947 (6.672)	22.751 (8.957)
Aspect Ratio		3.800	1.600
Taper Ratio		0.350	0.350
Sweepback of quarter-chord line (in surface reference plane)	deg	30.0	35.0
Dihedral angle (HRP)	deg	10.0	—
Tail length		29.176	27.576
Incidence point of rotation Fuselage station	cm (in.)	211.05 (83.090)	—
Distance above FRP	cm (in.)	3.86 (1.520)	—
<hr/>			
Nacelles (N _{5A}) - Pylon (P _{2B})			
Spanwise location-intersection of pylon plane of symmetry and wing W _{4A} leading edge	cm (in.)	30.864 (12.151)	
Pylon-wing intersection			
Leading edge	%C _w	3.250	
Trailing edge	%C _w	75.600	
Nacelle centerline incidence	deg	1.784	
Nacelle centerline toe-in	deg	1.800	

TABLE 2
DIMENSIONAL DATA (Concluded)

Component	Unit	Model Scale Dimension
Flap Mechanism Fairings (b _{F3A}) (Numbered inboard to outboard) Spanwise location of centerline at wing T.E.		
No. 1	%b/2	26.90
No. 2	%b/2	42.49
No. 3	%b/2	54.28
No. 4	%b/2	66.07
No. 5	%b/2	77.87
Cant angle (nose inboard is positive)		
No. 1	deg	0
No. 2	deg	-3.00
No. 3	deg	0.67
No. 4	deg	4.33
No. 5	deg	8.00

DIMENSIONS MODEL SCALE
CENTIMETERS (INCHES)

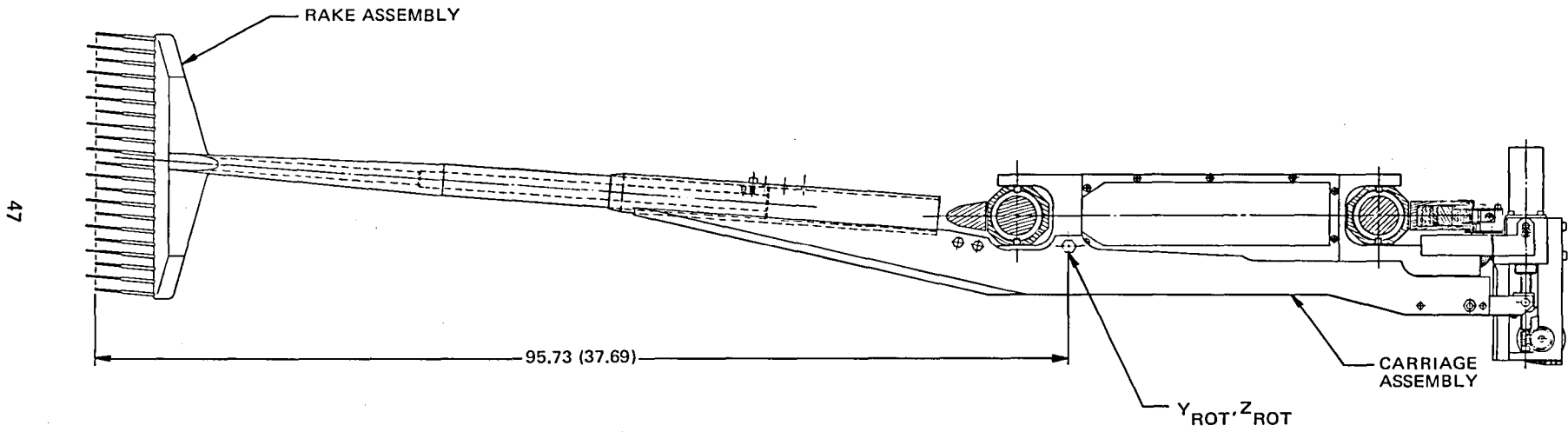


FIGURE 30. VERTICAL TRAVERSE ARM – WAKE RAKE

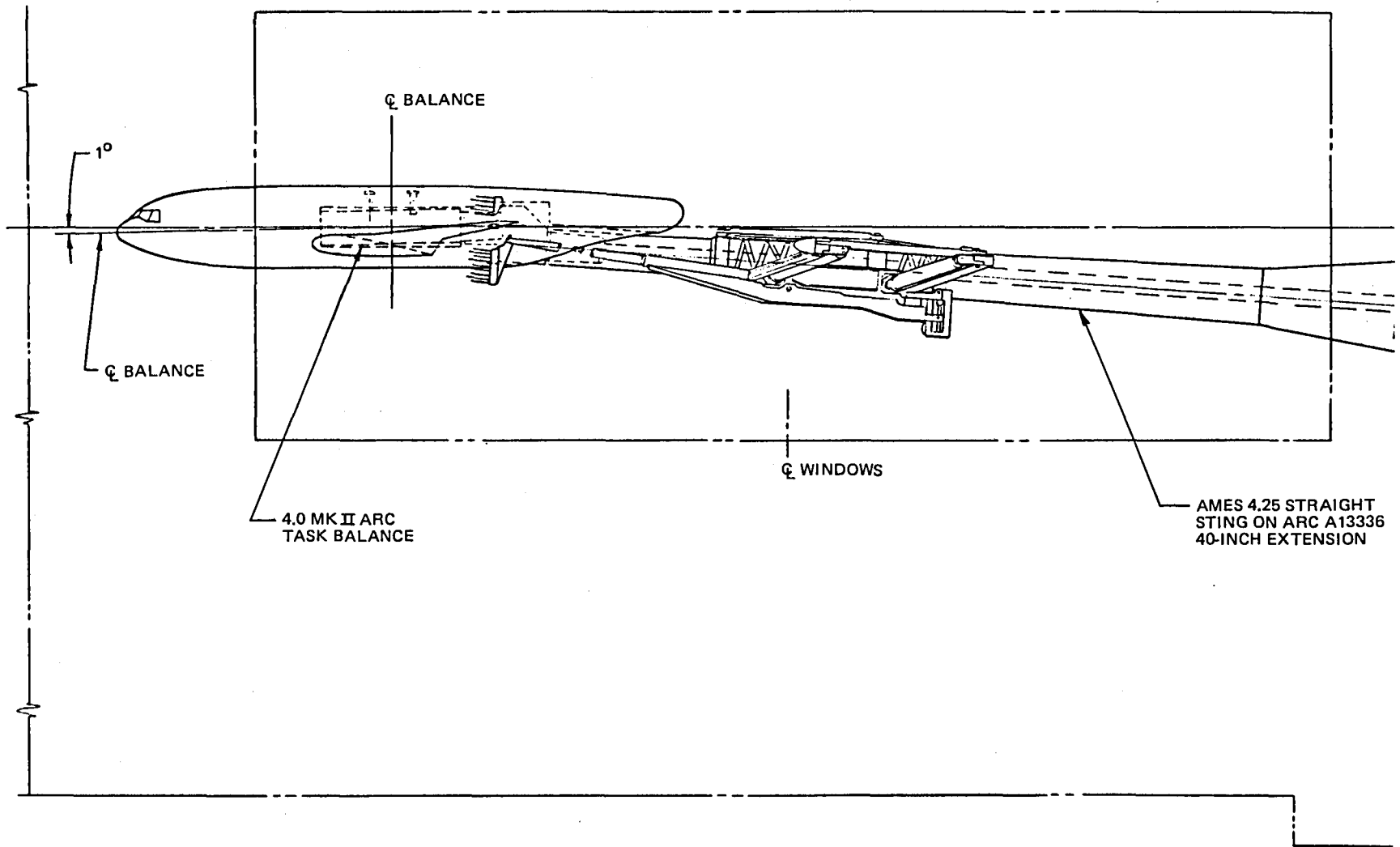


FIGURE 31. MODEL AND RAKE INSTALLATION IN ARC 11-FT TRANSONIC WIND TUNNEL – SIDE VIEW

DIMENSIONS MODEL SCALE
CENTIMETERS (INCHES)

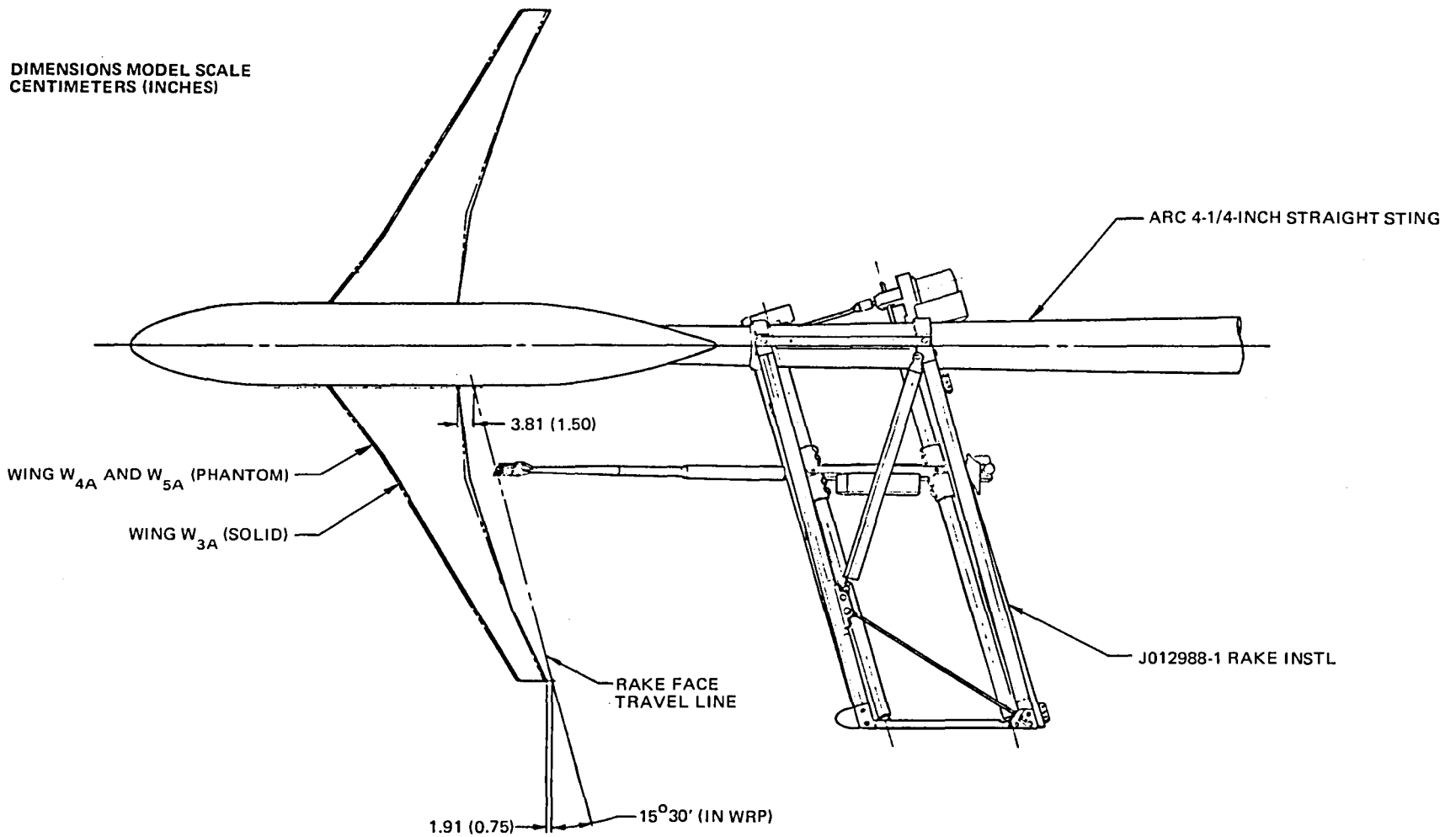


FIGURE 32. MODEL AND RAKE INSTALLATION IN ARC 11-FT TRANSONIC WIND TUNNEL – TOP VIEW

This Page Intentionally Left Blank

ANALYSIS

The wind tunnel data were analyzed to determine the effects of the design variables on the aerodynamic characteristics and to assess the validity of the design methods in predicting the basic and incremental characteristics. In the sections that follow, each of the significant aerodynamic characteristics is discussed in terms of the design variables studied and the test results.

Basic Data

Basic force data for the configurations tested are presented in the figures in the Appendix. Drag polars, lift curves, and pitching moment curves are shown for each configuration over a range of Mach numbers. Both transition-fixed and transition-free data are shown where appropriate. Transition-free data are used to evaluate buffet boundary and stability characteristics, since Douglas experience has shown that for characteristics at lift coefficients above cruise, transition-free data correlate better with flight test results. Transition-fixed data are used for drag-rise estimation. In some cases, both forward and aft transition locations are used to assess the drag rise. Table 3 summarizes the configurations tested and the figures in which the corresponding force and moment data are presented.

Drag-Rise Characteristics

In Figure 33, the drag-rise characteristics for the five wings tested are shown at lift coefficients bracketing the cruise regime. These curves are taken directly from the test data and contain no corrections for Reynolds number, for transition location, or for differences in the low-speed level due to induced drag. The tests were run at the maximum Reynolds number available, which was constant above $M = 0.70$ but decreased at the lower Mach numbers.

Transition, for the cruise drag determination, was fixed at an aft location on the chord to minimize the boundary-layer thickness in the regions of adverse pressure gradients near the trailing edge. Sublimation studies run

TABLE 3

SUMMARY OF PLOTTED FORCE AND MOMENT DATA

CONFIGURATION	WING TRANSITION	REMARKS	FIGURES
B _{3A} W _{3A} X _{2A} + T ₃	fixed		A-1 to A-3
B _{3A} W _{3A} X _{2A} + T ₁	free		A-4 to A-7
B _{3A} W _{3A} X _{2A} + T ₅	fixed		A-8 to 8-11
B _{3A} W _{4A} X _{3A} + T _{3, T₅}	fixed		A-12 to A-17
B _{3A} W _{4A} X _{3A} H _{1A} V _{1A} + T ₄	free	vary i _H	A-18 to A-20
B _{3A} W _{4A} X _{3A} N _{5A} P _{2B} + T ₅	fixed		A-21 to A-24
B _{3A} W _{4A} X _{3A} ^b F _{3A} + T ₅	↓		A-25 to A-26
B _{3A} W _{4A} X _{3A} N _{5A} P _{2B} ^b F _{3A} + T ₅			A-27 to A-30
B _{3A} W _{4A} X _{3A} N _{5A} P _{2B} ^b F _{3A} H _{1A} V _{1A} + T ₅		vary i _H	A-31 to A-38
B _{3A} W _{5A} X _{3A} + T ₁	free		A-39 to A-42
B _{3A} W _{5A} X _{3A} + T ₅	fixed	vary Re	A-43 to A-47 A-47
B _{3A} + T ₁			A-48 to A-49
B _{3A} W _{7A} X _{3A} + T ₅	fixed		A-50 to A-53
B _{3A} W _{7A} X _{3A} + T ₁	free		A-54 to A-57
B _{3A} W _{8A} X _{3A} + T ₅	fixed		A-58 to A-61
B _{3A} W _{8A} X _{3A} + T ₁	free		A-62 to A-65
B _{3A} W _{8C} X _{3A} + T ₁	free	vary δ _a vary Re	A-66 to A-76 A-76

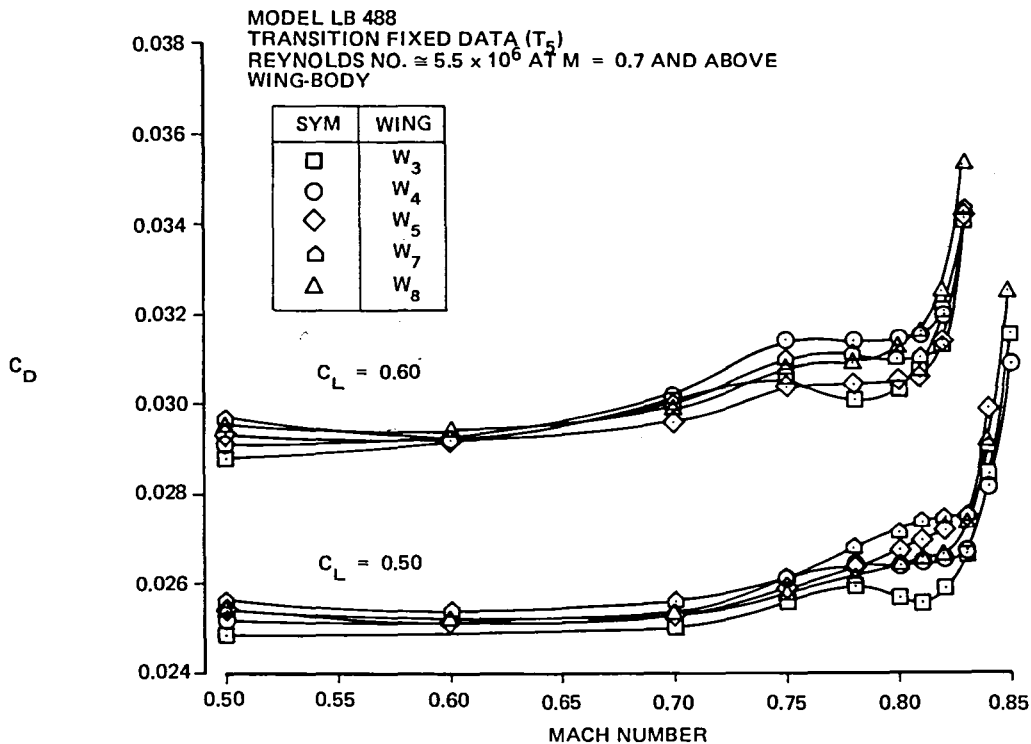


FIGURE 33. DRAG-RISE CHARACTERISTICS IN THE CRUISE REGIME FOR EET WINGS TESTED IN ARC 11-FT WIND TUNNEL

over a range of Mach numbers showed that, at the lower Mach numbers, natural transition occurred near the leading edge on the upper surface. These studies were used to select a transition location as far aft as possible, consistent with the assurance that the shock would be in turbulent flow. For this reason, the data do not reflect a constant transition location although the trip was not changed throughout the runs. Differences in the drag levels at low speeds can be partially attributed to the differences in the induced drag between wing W_3 and the other wings. Wing W_3 had less washout than the other wings, resulting in a loading which was closer to elliptical. The other four wings had identical span-loadings and therefore any low-speed differences between these would have to be attributed to viscous effects (due to differences in leading- and trailing-edge pressure distributions) or to tunnel repeatability. The differences in the spanwise distributions of lift for wing W_3 and for the other wings are shown in Figure 34.

In Figure 35, the data, at an average cruise lift coefficient, have been corrected for Reynolds number and for transition location using the

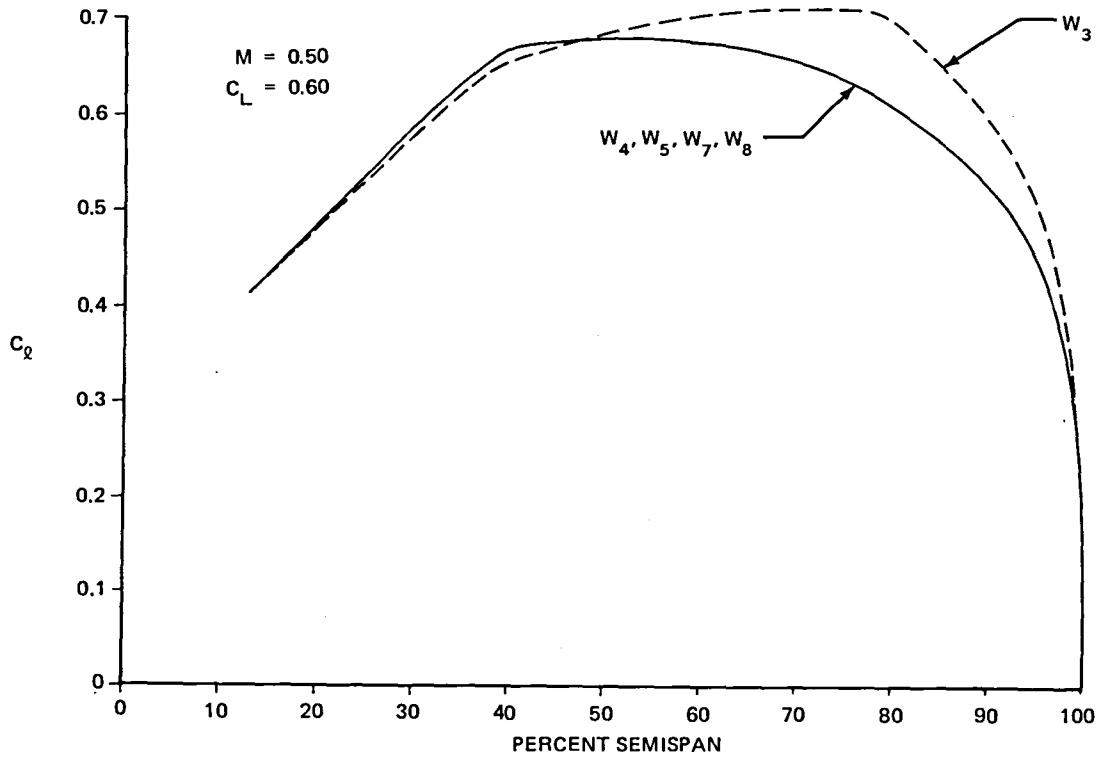


FIGURE 34. COMPARISON BETWEEN THEORETICAL SPANWISE VARIATIONS OF SECTIONAL LIFT

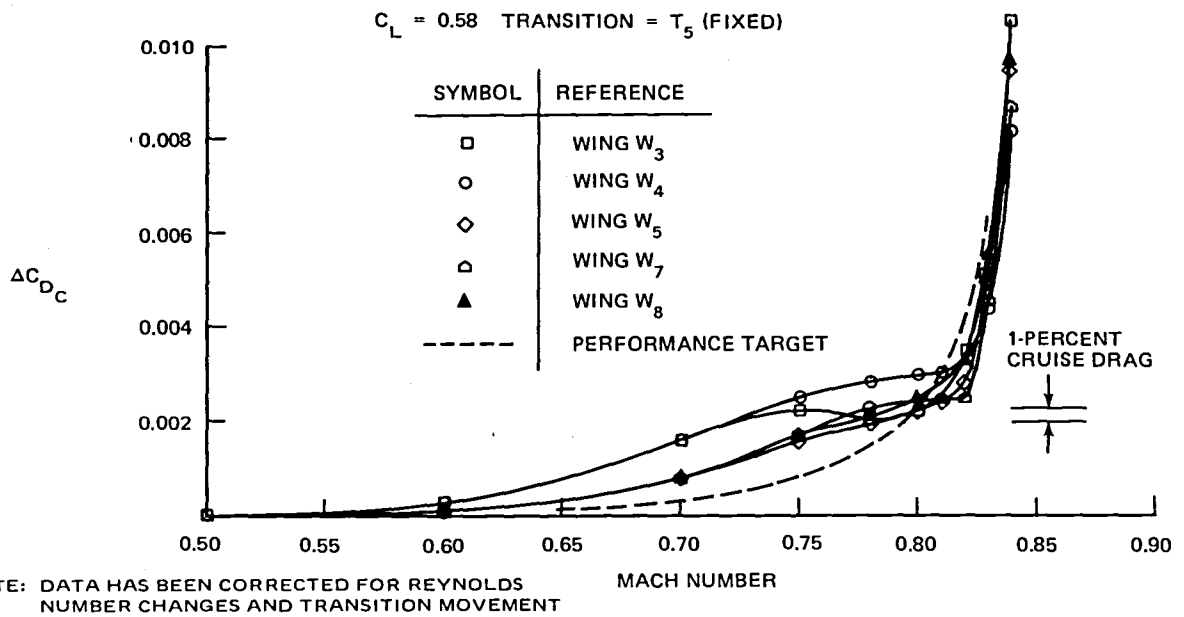


FIGURE 35. COMPARISON BETWEEN MEASURED AND PERFORMANCE TARGET DRAG-RISE CHARACTERISTICS

sublimation photos. No attempt was made to reconcile the levels at $M = 0.5$, and the drag-rise characteristics are shown relative to these values.

In the Mach number regime between $M = 0.6$ and 0.78 , the drag creep is the greatest for the wings with the largest nose radii and the lowest cambers, W_3 and W_4 . This phenomenon is due to shocks forming near the leading edge in regions of high peak suction. These peaks can be relieved by a reduction in leading-edge radius or an increase in camber. Although this characteristic is noted in two-dimensional supercritical airfoil data, it can be attributed to any portion of the wing where the local negative pressures near the leading edge are excessive. Increasing the camber reduces the creep as evidenced by W_5 and W_7 , but almost equally as effective is a reduction in the nose radius in combination with the lower camber, W_8 . The amount that the nose radius could be reduced was somewhat limited by the wind tunnel model constraint of fairing into the basic wing forward of 40-percent chord. Indications are that a further reduction in nose radius would be beneficial. However, since the nose geometry is critical to the development of the supercritical region and since larger radii also benefit the low-speed performance, the amount of reduction which is practical is limited.

The drag divergence Mach number, based on $dC_D/dM = 0.05$, is approximately the same for all of the wings tested; only the levels of drag at Mach divergence differ. This Mach divergence of 0.815 to 0.82 is approximately 0.07 to 0.08 higher than that which would be attainable with a conventional wing having the same sweep and thickness; this assumes a lift coefficient of 0.58 and a C_{DC} of 0.0018 for the conventional wing at Mach divergence. The compressibility drags at Mach divergence for the wings tested (0.0025 to 0.0035) are higher than those of the conventional wing because of the drag creep. This drag level could be reduced by a reduction in thickness, but tradeoff studies have shown that the weight penalty of the thinner wing has a much larger negative effect on the total airplane than the increased drag level.

In the following figures, the isolated effects of the various design changes are shown at Mach numbers bracketing the cruise conditions. These

data are not corrected for Reynolds number or transition location, since only the incremental changes are of interest, and the sublimation studies for each configuration were limited to the one condition shown in Figure 35.

In Figure 36, the effects of span loading on the drag-rise characteristics are shown (W_3 vs W_4). The wing with the higher local lift coefficients on the outboard panel has the better drag-rise characteristics. Analysis of the pressure data indicates that the stronger shocks on the outboard wing panel of this configuration are more than compensated for by the weaker shocks on the inboard wing where the effective area is significantly larger. The experimental spanwise distributions of lift for the two wings are shown in Figure 37. The spanwise distributions of local normal Mach number at cruise are shown in Figure 38.

The effects of leading-edge radius on the drag-rise characteristics for 2.1-percent and 2.5-percent aft camber are shown in Figures 39 and 40. In both cases, the reduction in radius results in an improvement in the drag creep in the regions approaching Mach divergence.

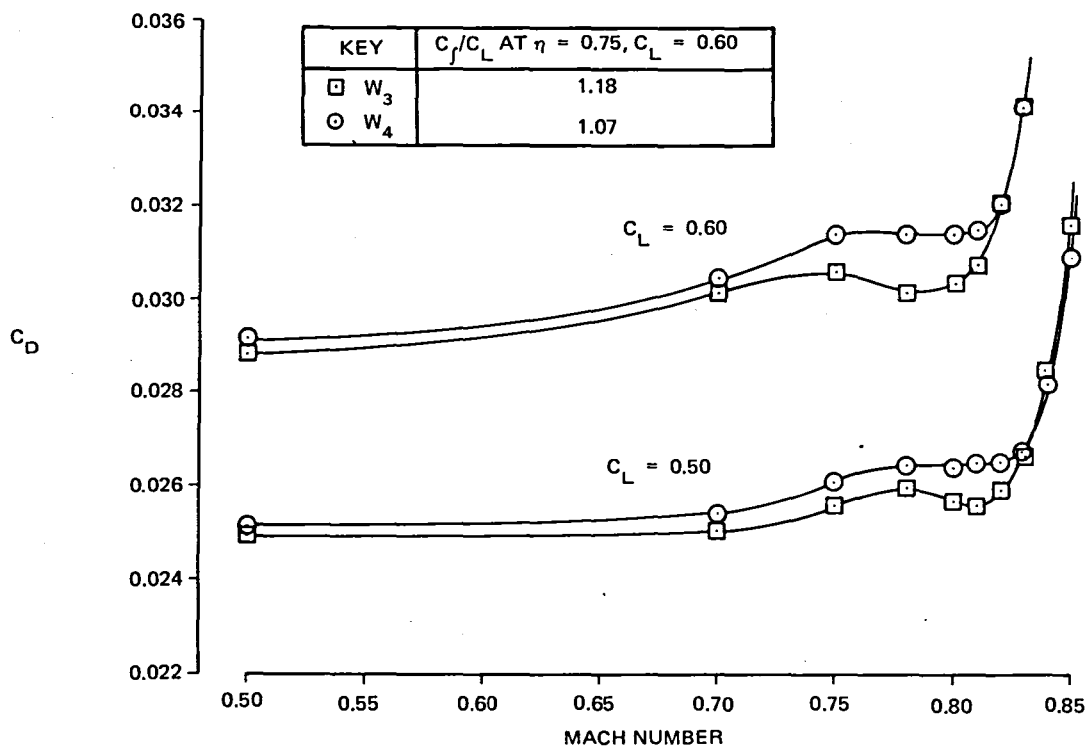


FIGURE 36. EFFECT OF SPANWISE LIFT DISTRIBUTION ON DRAG-RISE CHARACTERISTICS

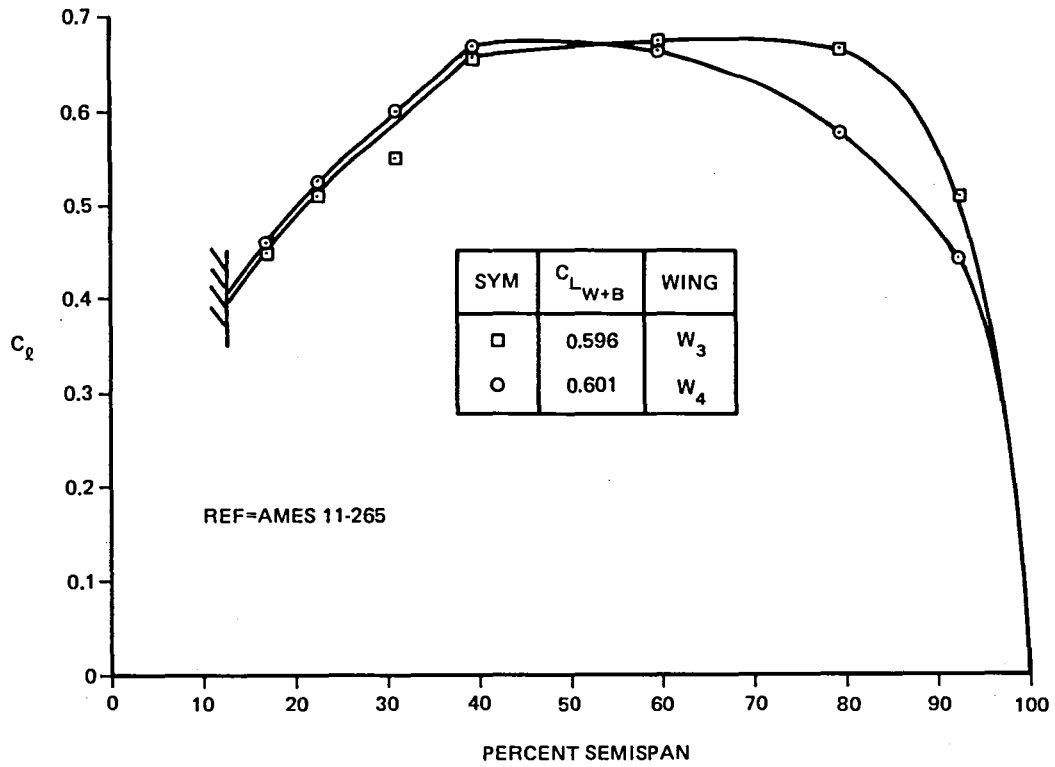


FIGURE 37. COMPARISON BETWEEN W_3 AND W_4 EXPERIMENTAL VARIATION IN SECTIONAL LIFT COEFFICIENT, $M=.50$.

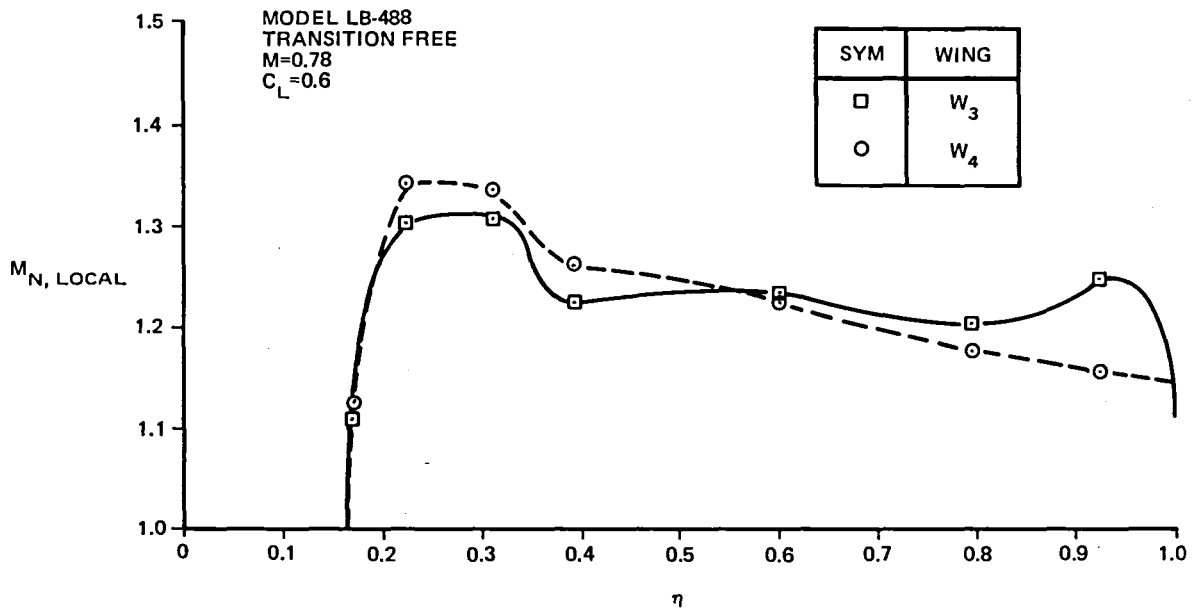


FIGURE 38. SPANWISE DISTRIBUTION OF LOCAL NORMAL MACH NUMBER INTO THE SHOCK

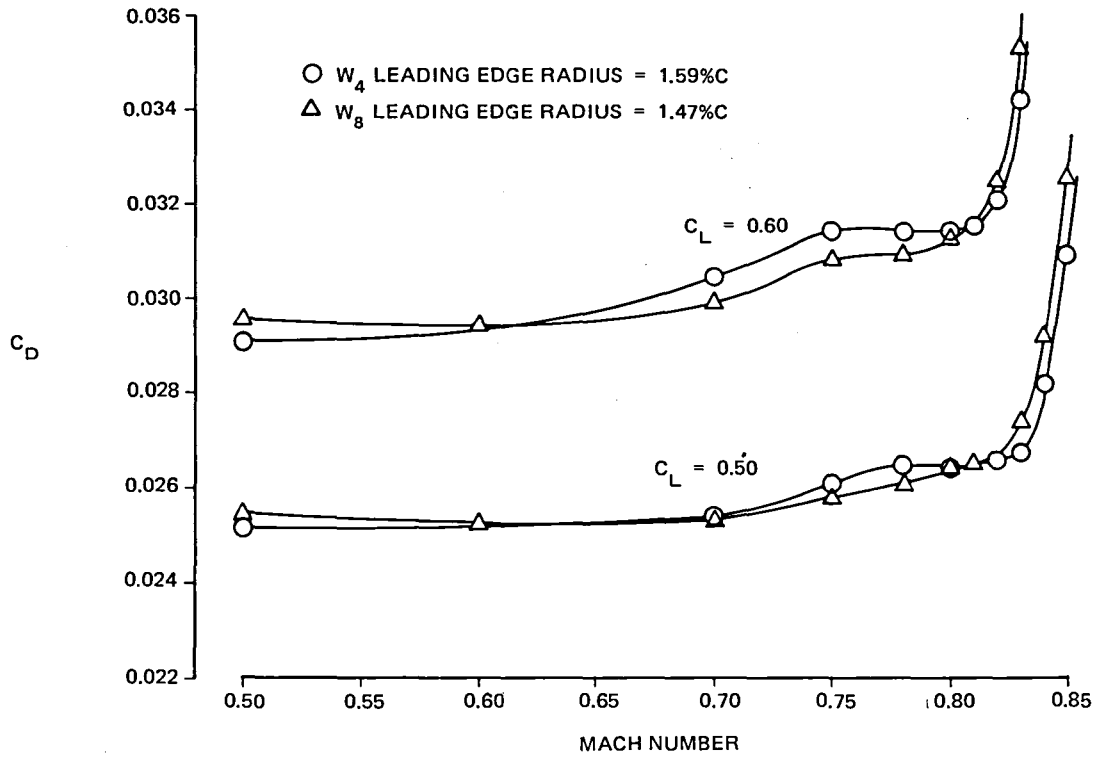


FIGURE 39. EFFECT OF LEADING EDGE RADIUS ON DRAG-RISE CHARACTERISTICS
MAX CAMBER = 2.1%

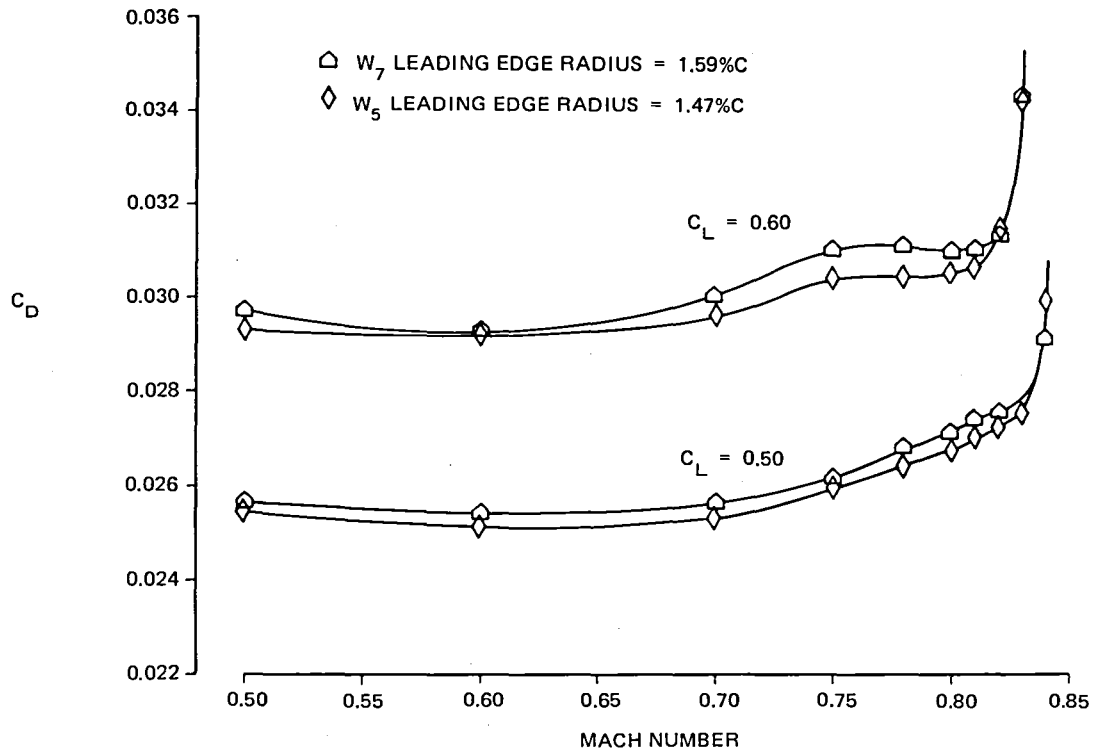


FIGURE 40. EFFECT OF LEADING EDGE RADIUS ON DRAG-RISE CHARACTERISTICS
MAX CAMBER = 2.5%

Characteristics at drag divergence Mach number and above are approximately the same for all five wings. Although some of the curves cross over at high Mach numbers, this is eliminated if the $M = 0.5$ points are superimposed, so no significance is attached to these differences.

In Figure 41, the effects of an increase in aft camber are compared. The baseline value of aft camber of 2.1 percent was originally chosen after analyzing a significant amount of test data and performing some two-dimensional analytical studies with various amounts of camber. However, since the prediction of three-dimensional boundary-layer characteristics, particularly near the trailing edge of a swept wing, is something of a black art, it was decided to push the camber further in order to obtain additional test data. Figure 41 shows that while a reduction in drag over most of the Mach number range was achieved by the more highly cambered wing at $C_L = 0.6$, it suffered a significant penalty at the lower lift coefficient. For this comparison, the discrepancy in the drag levels at $M = 0.5$ can be partially justified due to the increased

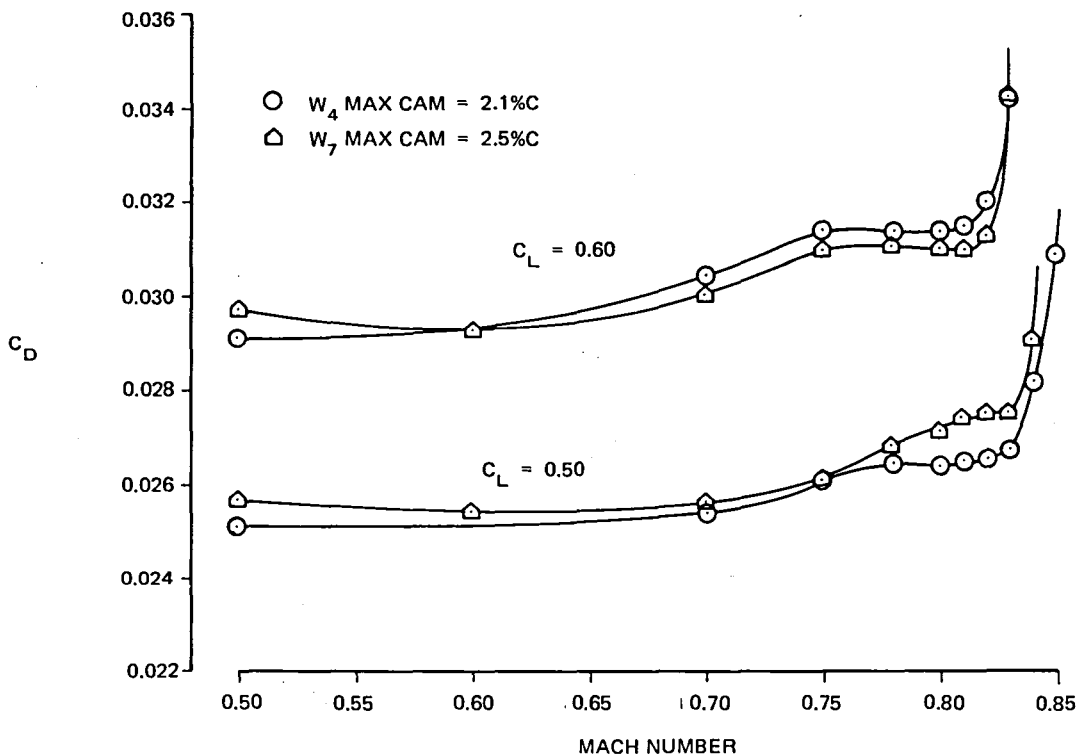


FIGURE 41. EFFECT OF AFT CAMBER ON DRAG-RISE CHARACTERISTICS
LEADING EDGE RADIUS = 1.59% C

viscous drag associated with the higher camber. Analysis of the pressure data, confirmed by flow visualization pictures, shows a small region of separation, just outboard of the wing planform break, which is associated with the aft shock of a forked shock system. This is cleared up at higher lift coefficients when a single shock system develops. The trailing-edge pressures in the region of the separated flow are shown in Figure 42. As shown, the pressures at the lower lift coefficients are less positive than those at the higher lift coefficients approaching buffet onset.

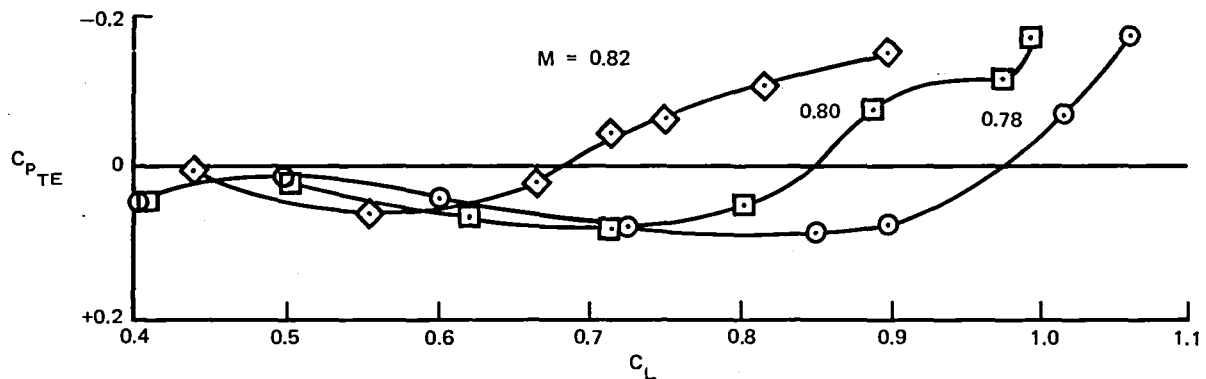


FIGURE 42. TRAILING-EDGE PRESSURES FOR WING W_5 AT 60-PERCENT SEMISPAN

The combined effects of an increase in camber with a reduction in leading-edge radius are shown in Figure 43 where wing W_5 is compared with wing W_4 . For this case, the reduction in the peak leading-edge negative pressures was enough to rectify the trailing-edge separation problem, and a significant reduction in drag is shown for this configuration at $C_L = 0.60$.

Buffet Boundary

The buffet boundary is one of the most influential aerodynamic characteristics in determining the final wing design. In many cases, it becomes the limiting factor for cruise lift coefficient, initial cruise altitude, and eventually the growth of the airplane. Douglas defines buffet for a transport aircraft as a ± 0.1 -g excursion in normal load factor (measured), with a 1.3-g margin in lift coefficient above that for cruise. In the case of the high-aspect-ratio wing, the lift coefficient for optimum lift-to-drag ratio is considerably higher than in existing transports. Achieving good cruise drag characteristics at these high-lift coefficients

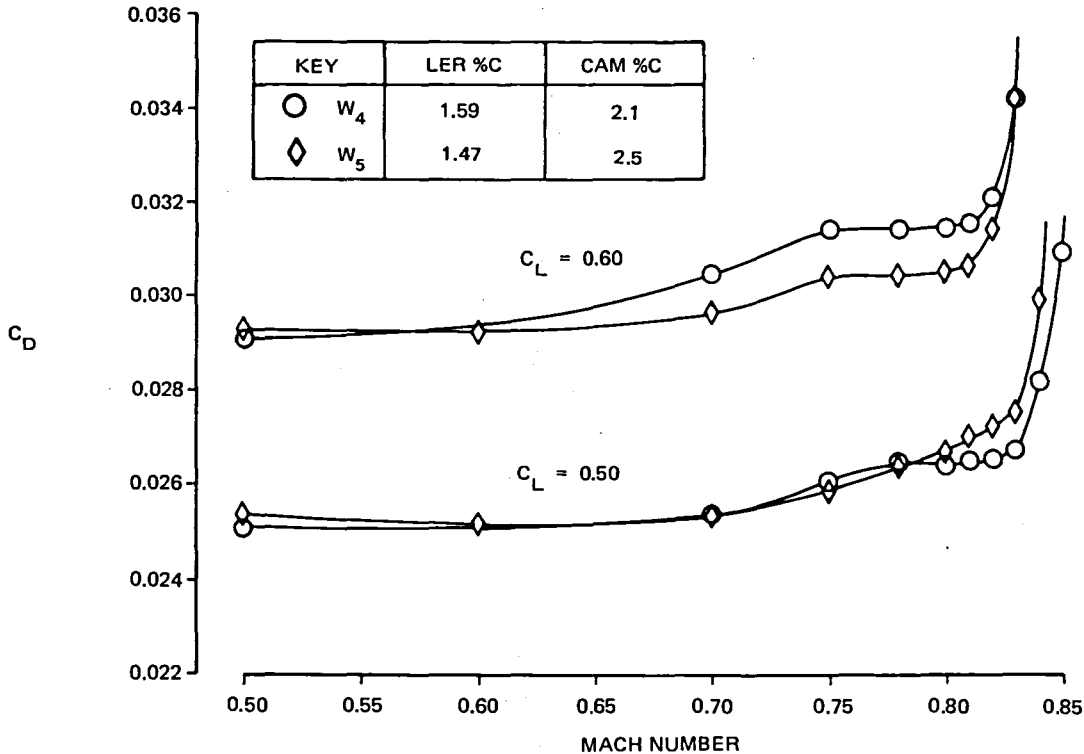


FIGURE 43. COMBINED EFFECT OF CAMBER AND LEADING EDGE RADIUS ON DRAG-RISE CHARACTERISTICS

is not nearly as difficult as achieving a buffet boundary consistent with the high cruise C_L . In this section, the buffet boundaries and the various methods of assessing them from wind tunnel data are presented.

Douglas' experience with correlations of flight data and the data obtained in the NASA Ames 11-foot wind tunnel has shown that transition-free data correlate well, while transition-fixed data are conservative. For this reason, both types of data are obtained in each test, with the transition-fixed data used for drag determination, and transition-free data used for buffet boundaries and stability characteristics. For airplanes like the DC-10, where transition is fixed fairly far forward, the trip tends to spoil the flow near the trailing edge at high angles of attack; this results in a premature lift break. For supercritical wings, where transition is fixed further aft to minimize the thickness of the boundary layer going into the steep aft pressure gradients, this effect is not as pronounced; however, since YC-15 (supercritical wing) transition-free wind tunnel data agreed well with flight, transition-free data are being used in this study for buffet prediction.

Several different criteria are used to determine buffet boundary, some of which are the lift curve break, pitching moment break, break in the curve of C_L versus M at constant angle of attack, and trailing-edge pressure divergence. In an ideal world, all of these might agree, but normally they do not and the final determination becomes somewhat subjective. Douglas' experience has shown that where the lift curve break is clearly defined, as it usually is for a wing which has undergone considerable development, this criterion works very well as long as the Reynolds number of the test is relatively high. In cases where small local separations cause slight breaks in the curve, as is the case with some of the wings tested in this program, an examination of the trailing-edge pressures is usually required. The trailing-edge pressures also offer more insight into the spanwise breakdown of the flow.

One concern with the tests conducted during this program was that, while the wind tunnel Reynolds number per foot was high, the small, high-aspect-ratio wing's local chords were significantly smaller than those of a DC-10 when both models were sized for the same tunnel. These lower local Reynolds numbers, particularly near the tip, combined with the steep aft pressure gradients, gave rise to the concern that the data might not be representative of that which would be obtained in flight. However, examinations of the pressure data, with and without transition, and comparisons with theory, indicate that the Reynolds numbers were sufficiently high to obtain representative data. This will be discussed further in the section on Methodology.

In Figures 44 through 48, the buffet boundaries, as estimated by four different criteria, are shown for wings W_3 , W_4 , W_5 , and W_8 . Wing W_7 is not shown since its data are almost identical to that of wing W_5 .

In Figure 44, wing W_3 , while all the criteria tend to agree near the cruise Mach number of 0.8, they differ significantly at the lower and higher Mach numbers. The agreement is better for wing W_4 , shown in Figure 45. In Figure 46, the same criteria are used to analyze the more highly cambered wing, W_5 . In this case, while three of the methods tend to agree, the trailing-edge pressure criterion is more optimistic. A comparison of the

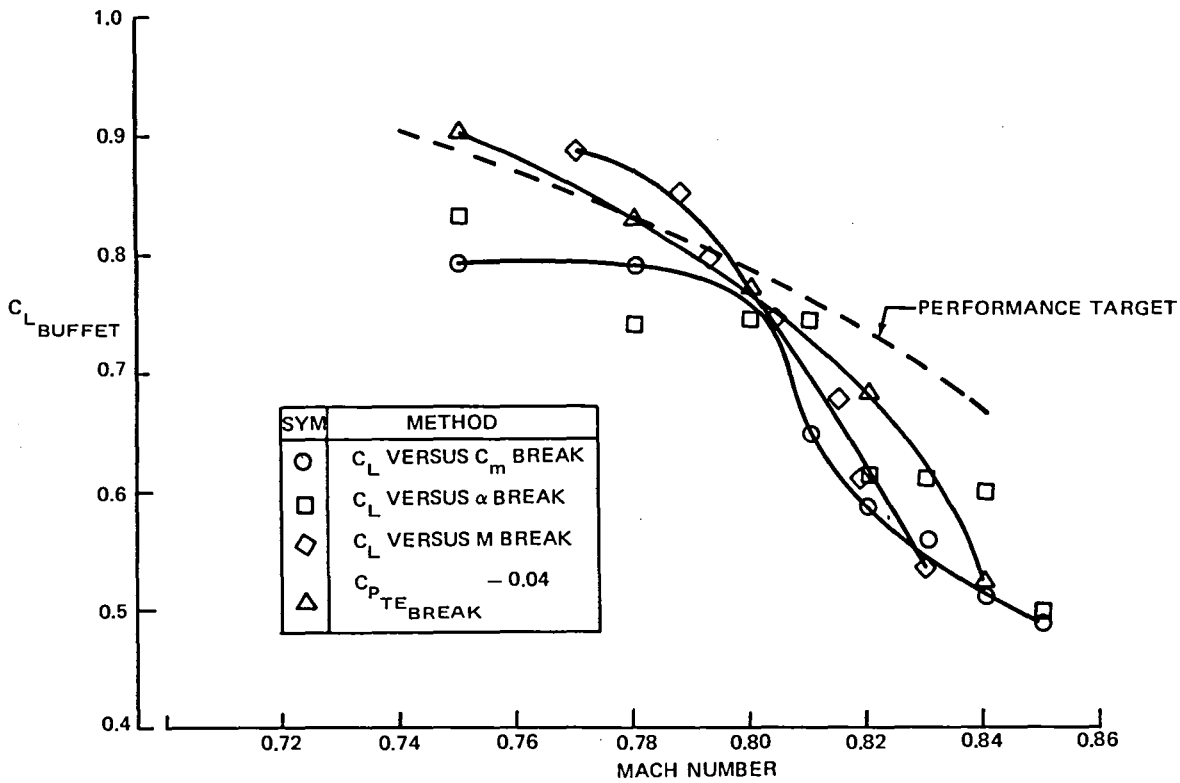


FIGURE 44. BUFFET BOUNDARY BY VARIOUS CRITERIA - WING W_3

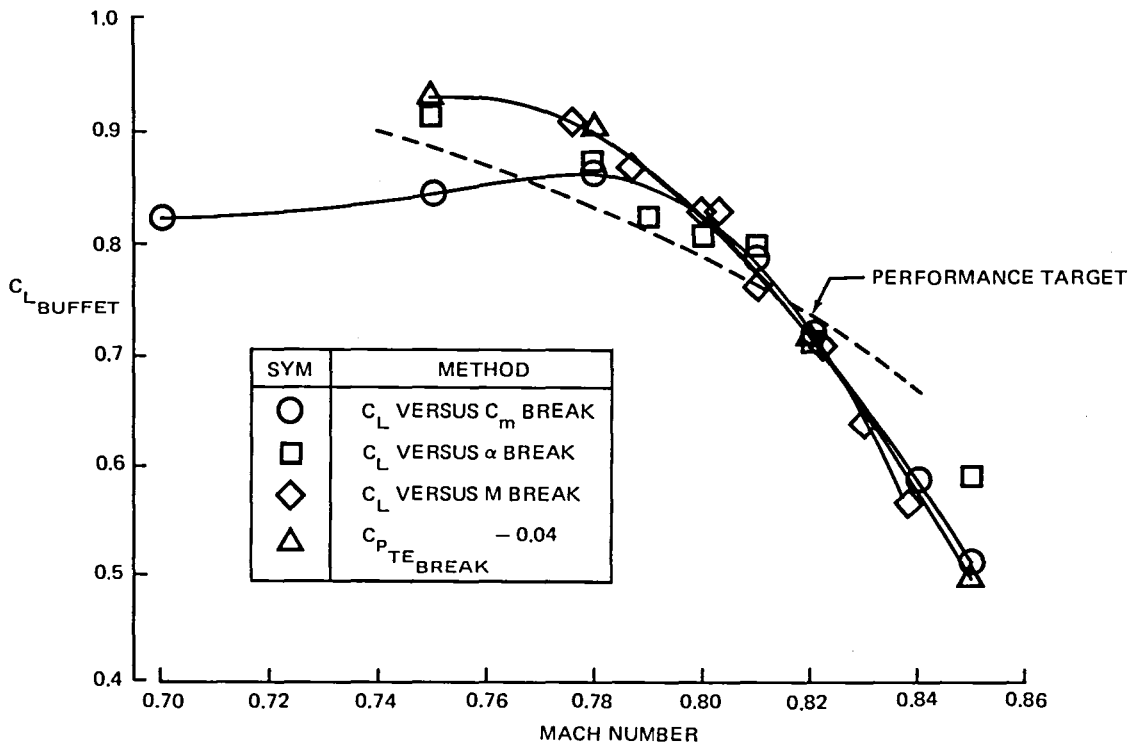


FIGURE 45. BUFFET BOUNDARY BY VARIOUS CRITERIA - WING W_4

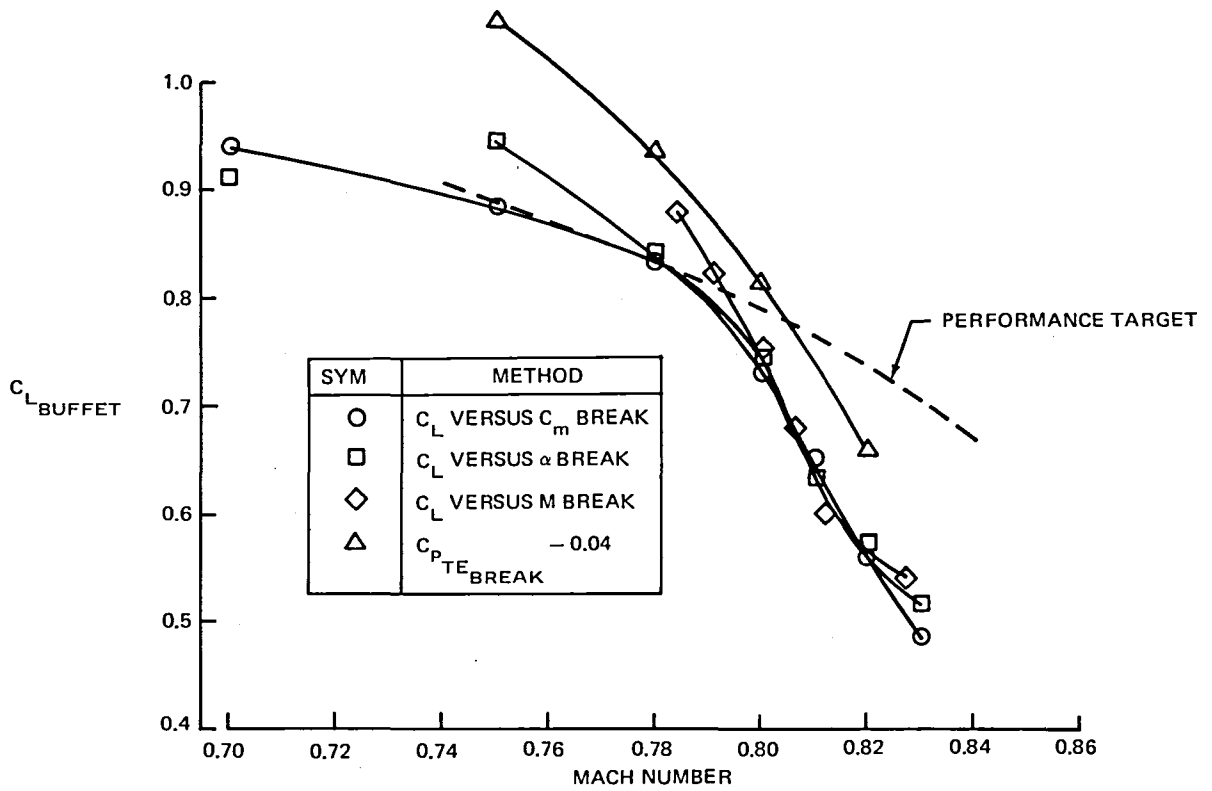


FIGURE 46. BUFFET BOUNDARY BY VARIOUS CRITERIA - WING W_5

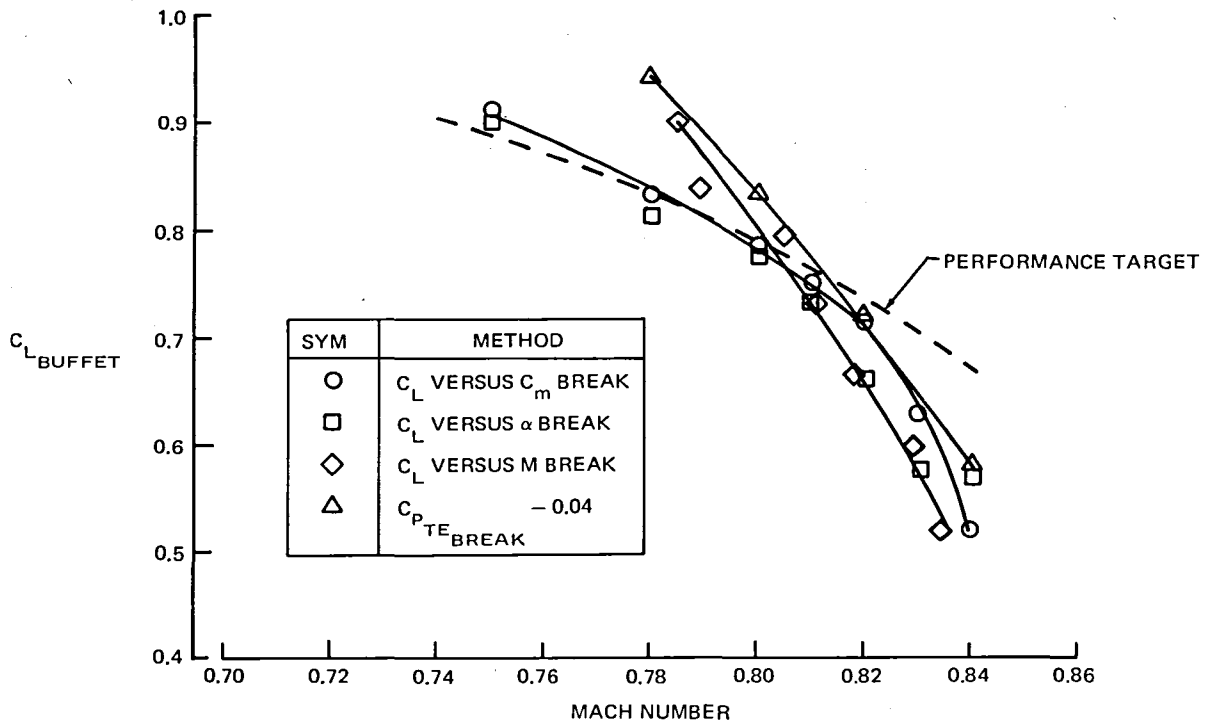


FIGURE 47. BUFFET BOUNDARY BY VARIOUS CRITERIA - WING W_8

M = 0.80

SYM	WING
○	W _{3A}
◇	W _{4A}
△	W _{5A}
□	W _{8A}

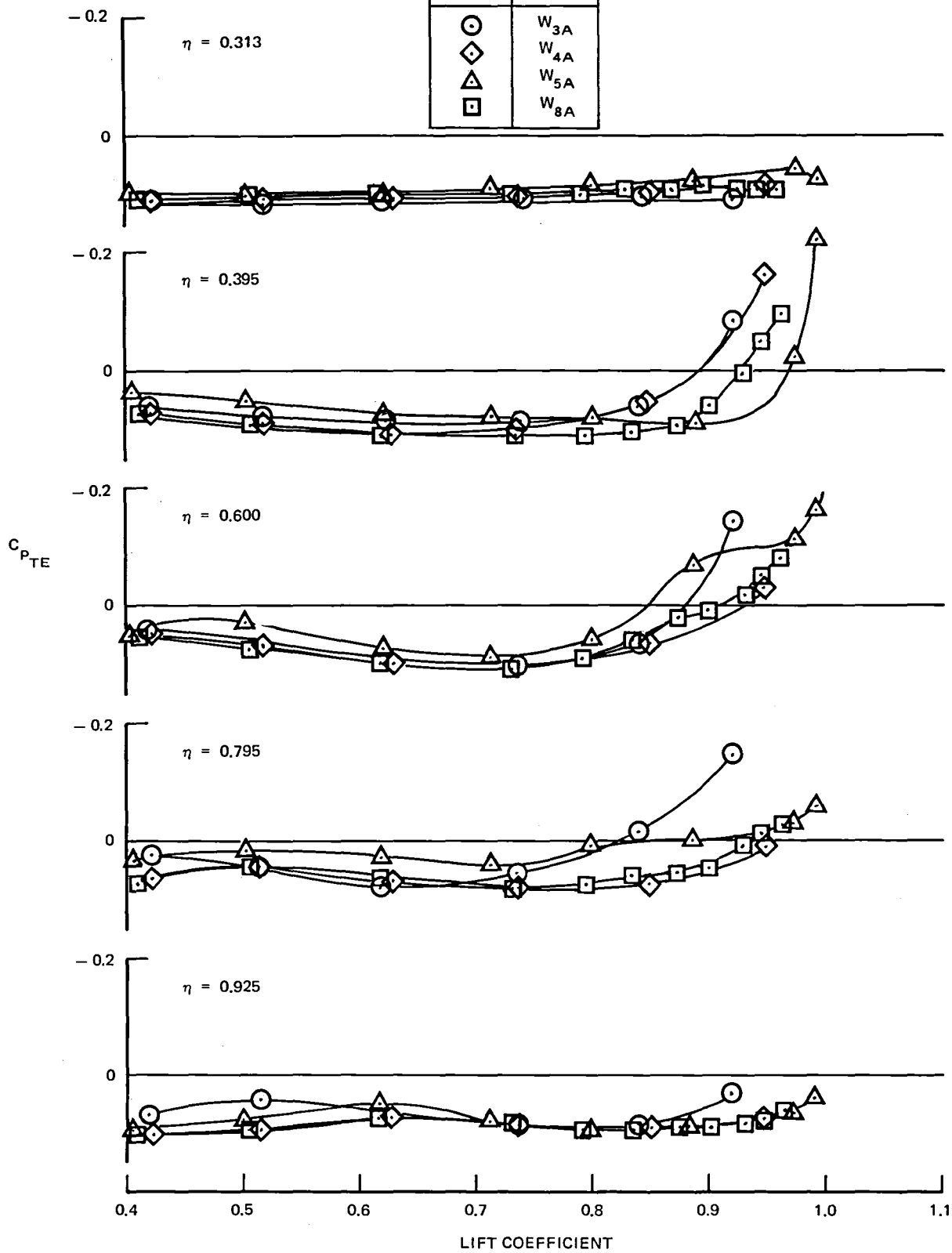


FIGURE 48. TRAILING EDGE PRESSURE CHARACTERISTICS

trailing-edge pressures for this wing, and for the others (Figure 48), shows that the pressure recovery on the outboard panel is poorer at lift coefficients near 0.5, with this situation improving with increasing angle. Therefore, the less optimistic correlation of the other three methods is considered to be more representative. For wing W_8 , shown in Figure 47, the trailing-edge pressure criterion is again optimistic, with the other three criteria being close at $M = 0.8$. In this case, the trailing-edge pressures, like those of wing W_4 , show a very gradual loss in pressure recovery with increasing lift on the outboard wing panel, making it difficult to define a point of divergence.

A composite curve for all of the wings tested is shown in Figure 49. It is based primarily on the break in the pitching moment curve, with the lift curve and trailing-edge pressures also used to interpret the data where necessary. The conclusions drawn from the study are:

- (1) It is possible to achieve a buffet boundary consistent with the high-cruise-lift coefficient of the high-aspect-ratio supercritical wing. The data obtained bracket the performance target for the wing except

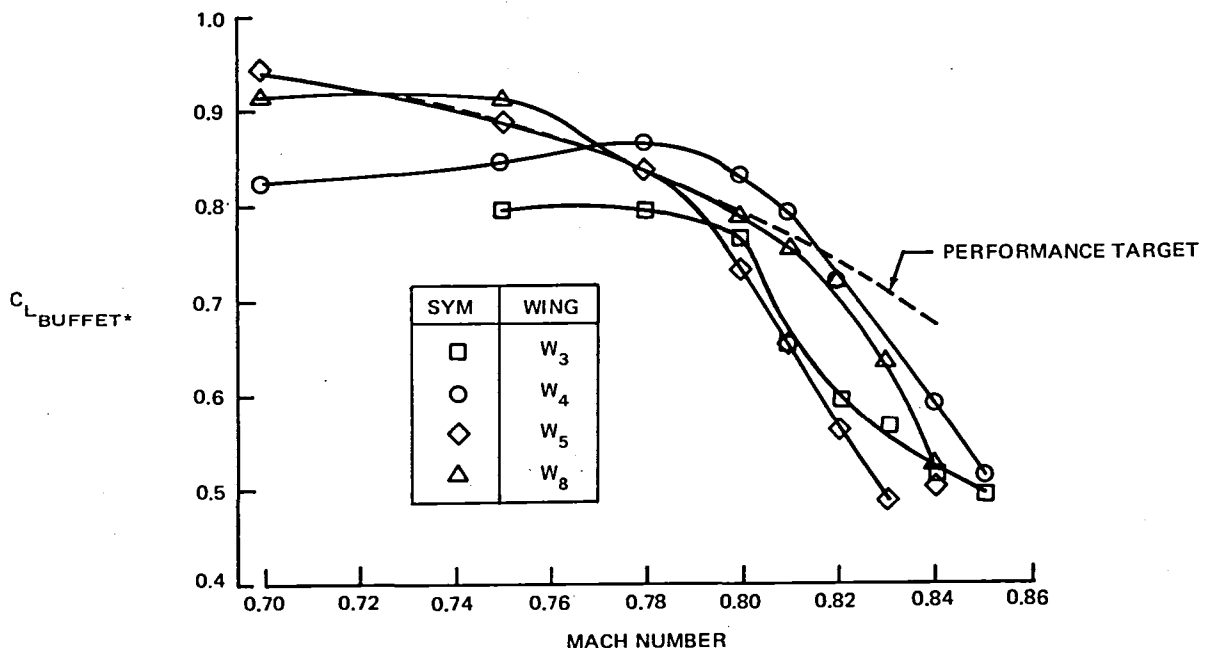


FIGURE 49. COMPARISON OF BUFFET BOUNDARIES FOR TESTED WINGS

at very high Mach numbers where requirements had not yet been established.

- (2) The addition of aft camber does not necessarily contribute to a higher buffet boundary.
- (3) While larger nose radii, wing W_4 , are desirable for a higher buffet boundary at the cruise Mach number where the separation is shock-induced, they contribute to poorer characteristics at lower Mach numbers where the separation is a function of the steep adverse pressure gradients. This is consistent with the effect on cruise drag where the larger nose radii are best at cruise Mach number but contribute significantly to drag creep at lower Mach numbers.
- (4) More elliptical span loadings, wing W_3 , while contributing to a reduction in induced drag, are not necessarily desirable from the standpoint of buffet boundary for a swept wing having the type of spanwise thickness distribution considered in this study. In all cases, the initial separation starts on the outboard wing panel as shown by the trailing-edge pressures, and the higher local lift coefficients of the more elliptically loaded wing in this region only aggravate this problem. It should be pointed out that all of the wings tested have approximately the same thickness-to-chord ratio, so this is not a variable in this study.
- (5) Although a requirement at Mach numbers above cruise had not been established, the drop-off in the characteristics of all of the wings gave rise to concern about the characteristics at dive conditions. For this reason, the high-speed aileron test, described in a later section, was conducted.
- (6) Wing W_6 was chosen as the candidate for further work since it meets the buffet boundary target at the cruise conditions and at lower Mach numbers, and this is consistent with good overall drag characteristics.

Interference Effects

Most of the wind tunnel testing of the five wings (W_3 , W_4 , W_5 , W_7 , and W_8) produced wing-body test data with no wing appendages or empennage. This configuration is adequate for comparing the wings but not sufficient to define characteristics for the complete cruise configuration. In order to assess the interference effects of the wing lower surface appendages and the empennage, one wing was selected for testing in the complete configuration. Wing W_4 was tested with a set of flap linkage fairings and with a pair of nacelles and uncambered pylons. These appendages were tested both individually on the wing and together to determine the interference effects between them. The effects on wing W_4 are assumed to be representative of what would be seen on the other four wings.

The effects of nacelles and pylons alone on the wing-body lift curve are shown in Figure 50. The primary effect is a loss in lift coefficient at a constant angle of attack of approximately 0.04.

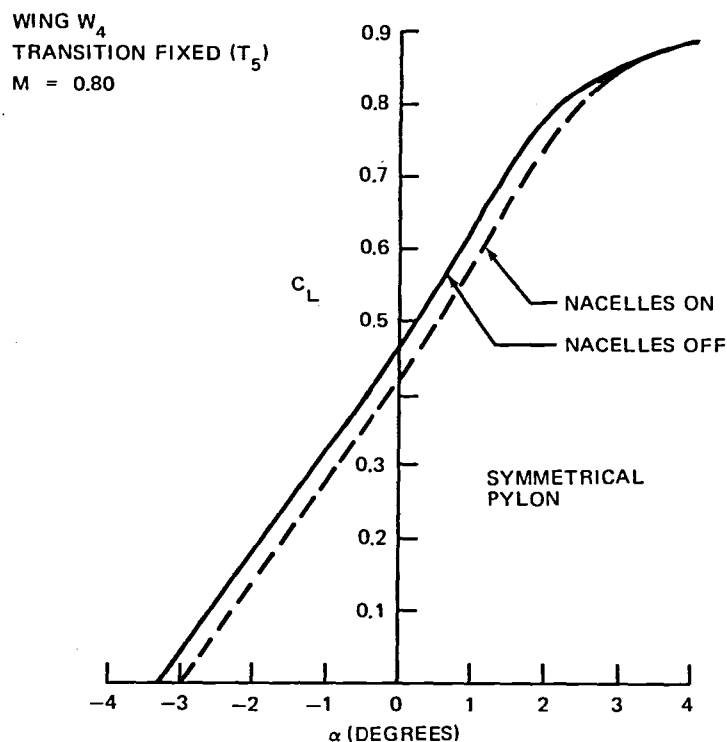


FIGURE 50. EFFECT OF NACELLES AND PYLONS ON WING-BODY LIFT CURVE

The spanwise distribution of lift was altered by the presence of the nacelles and pylons, as shown in Figure 51 for the cruise condition.

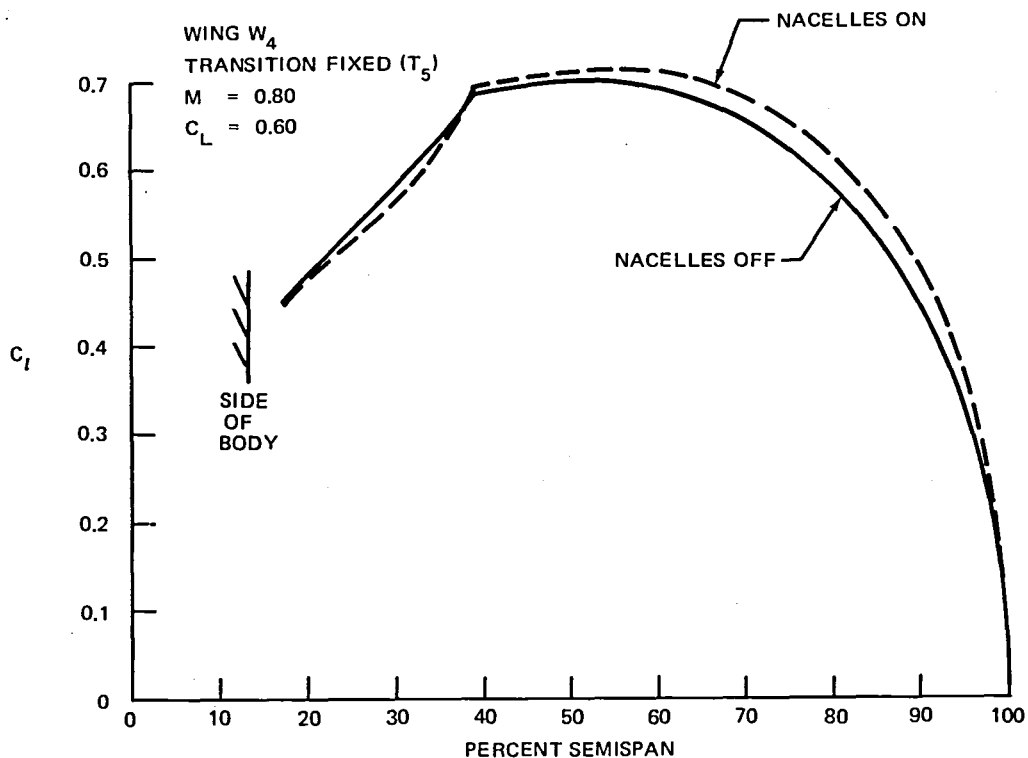
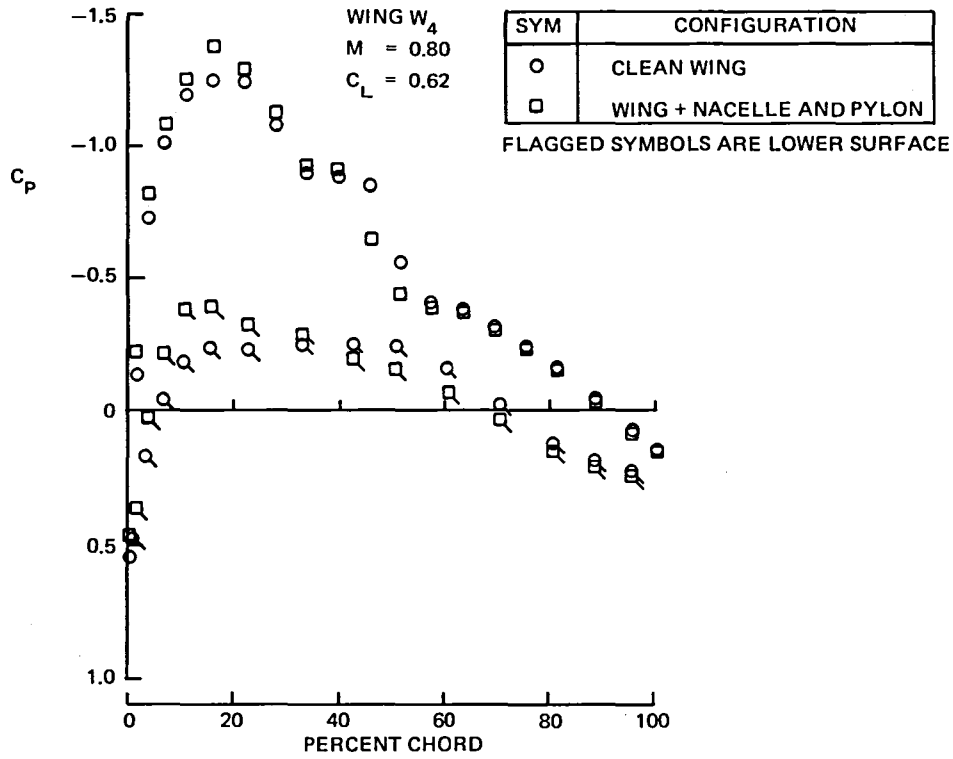
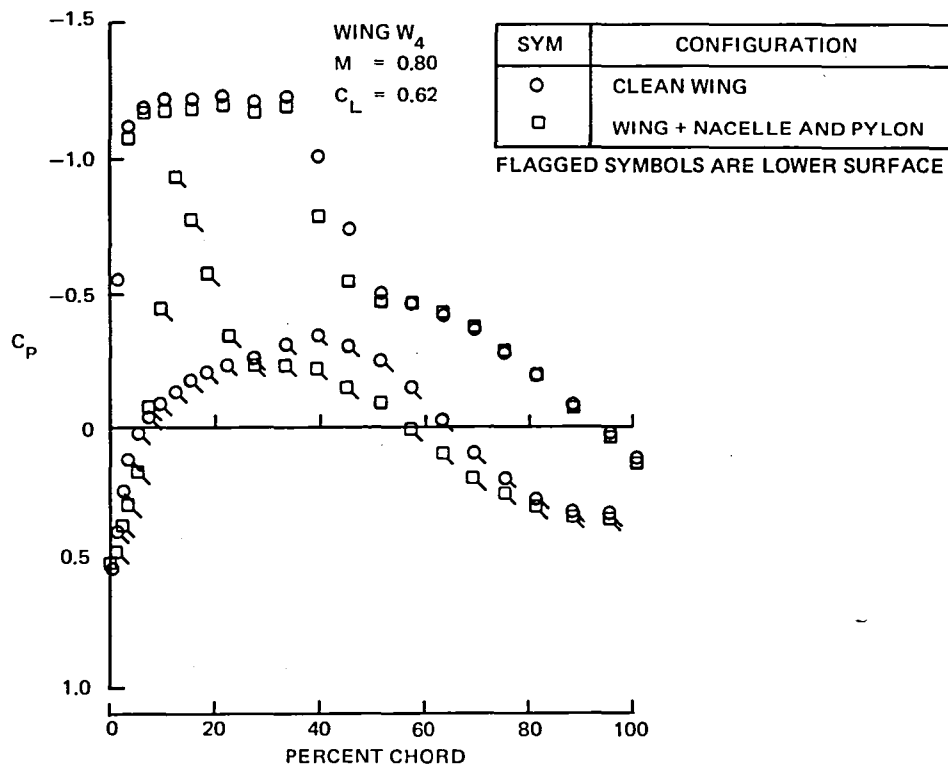


FIGURE 51. EFFECT OF NACELLES AND PYLONS ON SPANWISE LIFT DISTRIBUTION

For a constant total lift coefficient, the lift inboard, in the vicinity of the nacelles and pylons, was decreased and the outboard wing became more heavily loaded to compensate. This loss of lift inboard is responsible for the shift in the wing lift curve. Figure 52 shows the corresponding sectional pressures near the cruise condition from the four pressure orifice rows located from 22.5-percent to 60-percent semispan, including the row next to the inboard side of the pylon at $\eta = 0.313$. The shock on the pylon is clearly visible in the lower surface pressures. The effect washes out on either side of that station, becoming nearly indiscernible at $\eta = 0.60$. In Figure 53, a comparison of wing pressures on the inboard side of the pylon station with and without the nacelle and pylon for a constant angle off attack is shown. A greater impact is seen on the pressures when the angle of attack is not changed to maintain the total wing lift coefficient. Most of the lift loss occurs on the upper surface, through lowering of the peak pressures and forward movement of the shock.

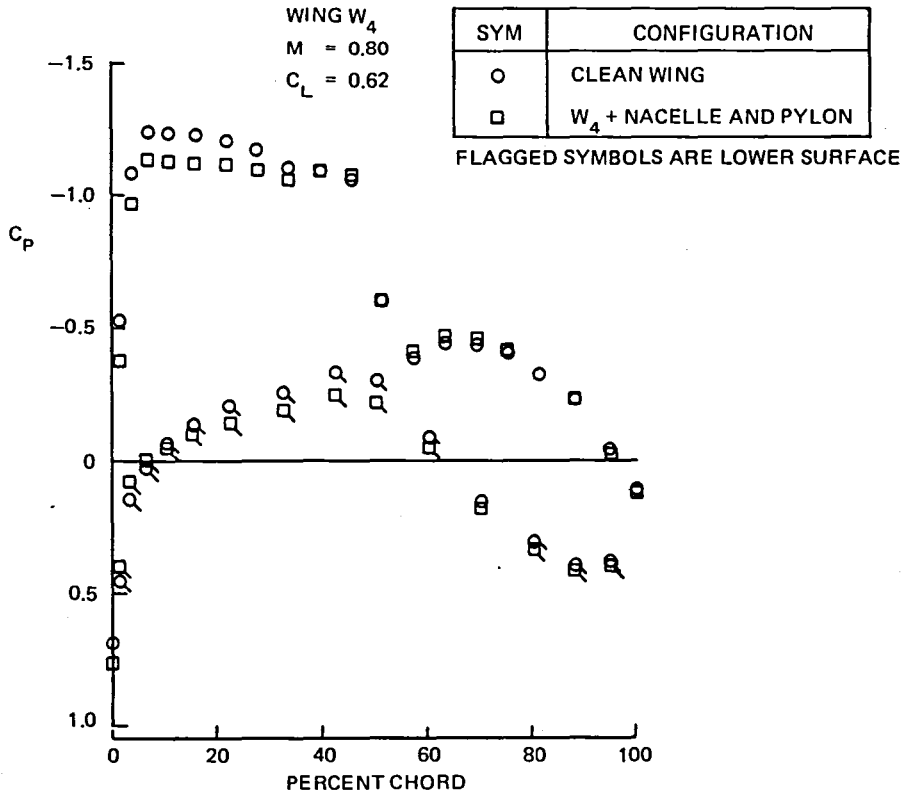


a. 22.5-PERCENT SEMISPAN

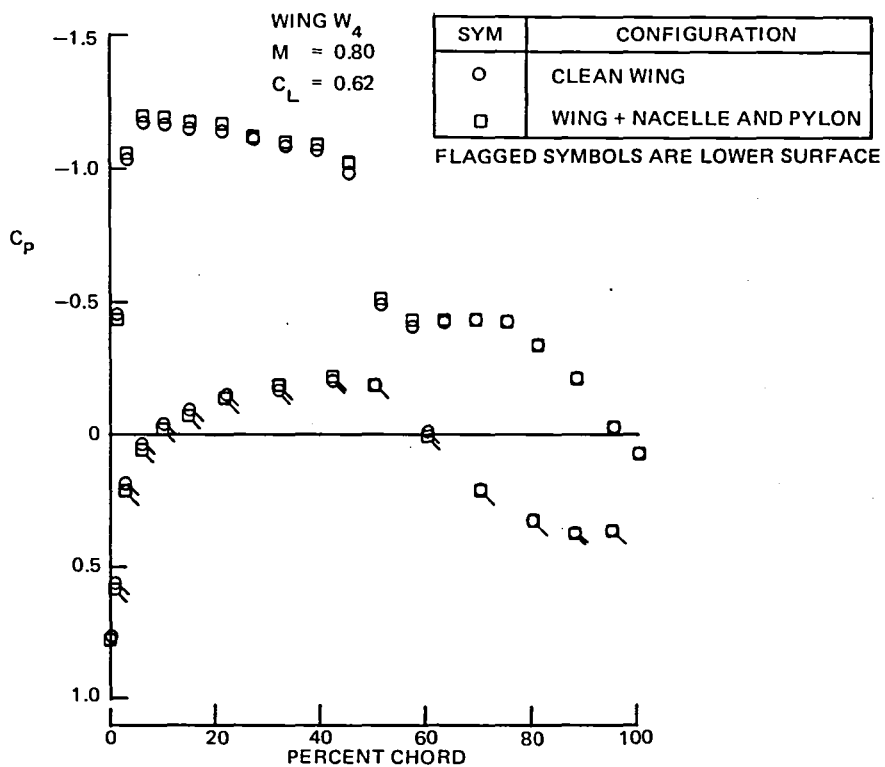


b. 31.3-PERCENT SEMISPAN

FIGURE 52. EFFECT OF NACELLES AND PLYONS ON WING PRESSURES



c. 39.5-PERCENT SEMISPAN



d. 60-PERCENT SEMISPAN

FIGURE 52. EFFECT OF NACELLES AND PYLONS ON WING PRESSURES (CONTINUED)

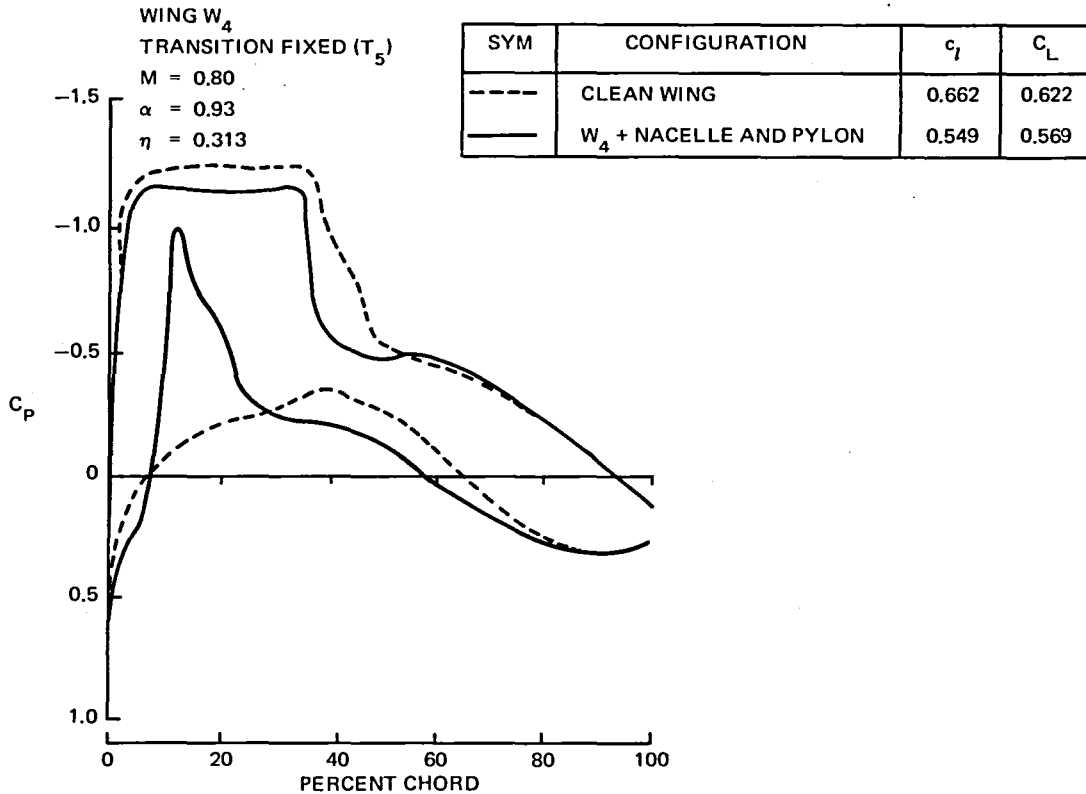


FIGURE 53. EFFECT OF NACELLES AND PYLONS ON WING PRESSURES NEAR PYLON AT CONSTANT ANGLE OF ATTACK (INTERPOLATED DATA)

An analysis was performed using the Douglas Friedman-Neumann program⁵ (a 3-D panel method) at zero Mach number to assess the individual contributions of nacelles and pylons on lift. Figure 54 shows the span loading of the wing alone, wing with nacelle in position, and wing with nacelle and pylon, all at a constant angle of attack. These results show that the pylon has little effect on the lift at subsonic conditions; the lift loss is almost entirely due to the effect of the nacelle. Therefore, any refinements to the pylon geometry such as cambering would not be expected to improve the lift loss.

The effect of nacelles and pylons on compressibility drag is displayed in Figure 55 for a wide range of lift coefficients. The nacelle/pylon drag increments relative to the basic wing-body configuration drag at subsonic and cruise Mach numbers are shown, the difference between them being the compressibility drag increment. Over the normal cruise lift coefficient range (0.5-0.6), the compressibility drag increment is seen to decrease

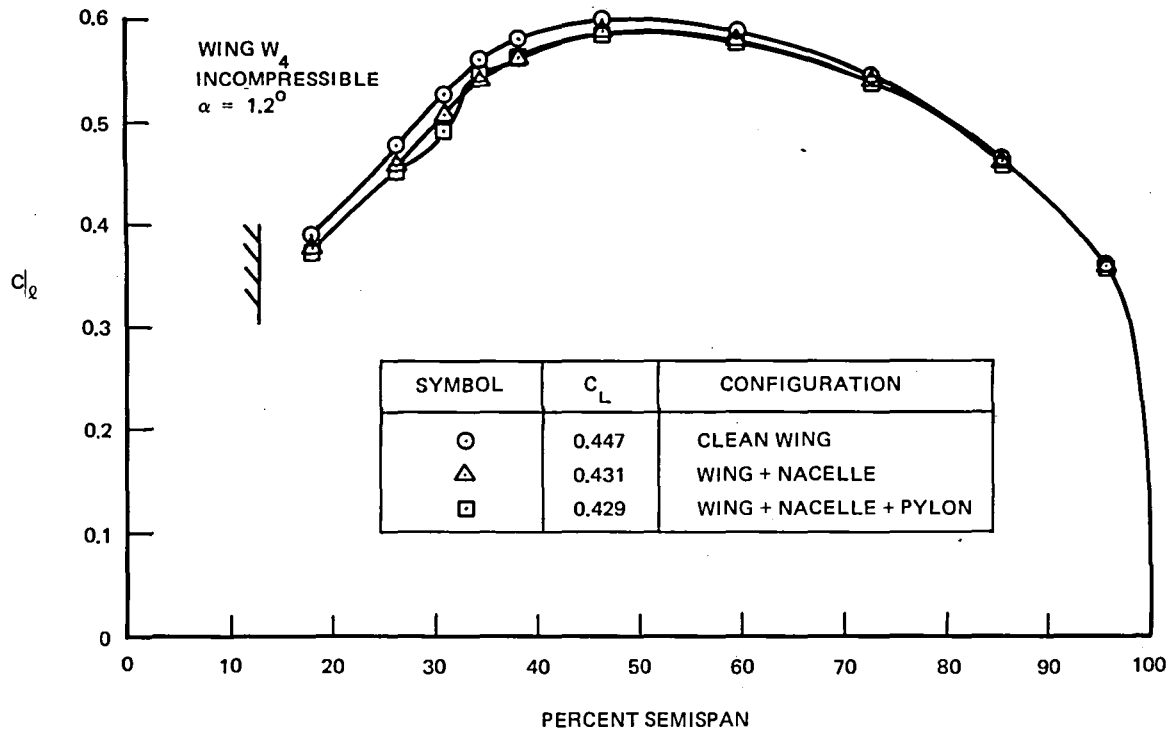


FIGURE 54. CALCULATED EFFECTS OF NACELLES AND PYLONS ON SPANWISE DISTRIBUTION OF LIFT

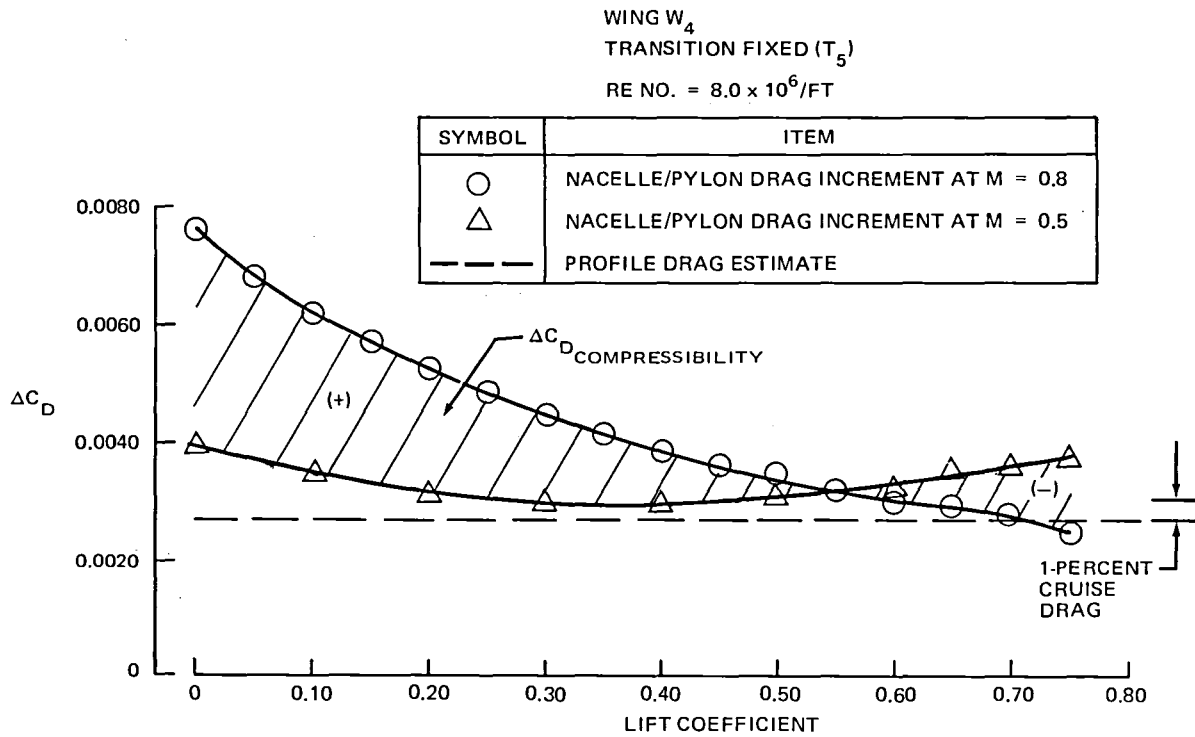


FIGURE 55. NACELLE/PYLON INSTALLED DRAG INCREMENT WITHOUT FLAP LINKAGE FAIRINGS

to zero and then become negative as the compressibility drag of the nacelle/pylon decreases and the interference effect with the wing becomes more favorable. The average compressibility increment over this range is zero. The compressibility drag due to the shock on the lower surface of the wing near the pylon shown in Figures 52a and 53 is counteracted by the effect of the nacelle/pylon on the wing compressibility drag, which is reduced due to the shift in span loading and wing upper surface pressures. The compressibility interference is such that the compressibility drag increment due to nacelles and pylons is negative at the higher lift coefficients despite the shock on the pylon.

At the lower lift coefficients the higher velocities on the wing lower surface are responsible for a stronger shock on the pylon and a larger drag increment, but the region is not in the normal operating range of the aircraft. Further development of the nacelle/pylon in Phase II of the program is likely to involve cambering the pylon to suppress the peak causing the shock. This would be expected to improve the compressibility drag across the entire range of lift coefficients.

Figure 56 shows corresponding data for nacelles and pylons installed on the wing in the presence of the flap linkage fairings. An increase in the subsonic drag increment due to the nacelles and pylons is apparent when compared to Figure 55. However, a decrease in the increment at $M = 0.8$ over the entire lift coefficient range, due to favorable interference effects between nacelle/pylon and flap linkage fairings, yields a smaller compressibility drag increment.

The effect on drag divergence Mach number due to the wing appendages is shown in Figure 57. The nacelles and pylons alone decrease M_{DIV} , but the addition of the flap linkage fairings introduces interference which regains some of the loss in M_{DIV} .

Figure 58 displays the effects of the nacelles and pylons on the wing-body pitching moment at subsonic and cruise Mach numbers. Their presence is destabilizing.

WING W_4
 TRANSITION FIXED (T_3)
 RE NO. = $8.0 \times 10^6/FT$

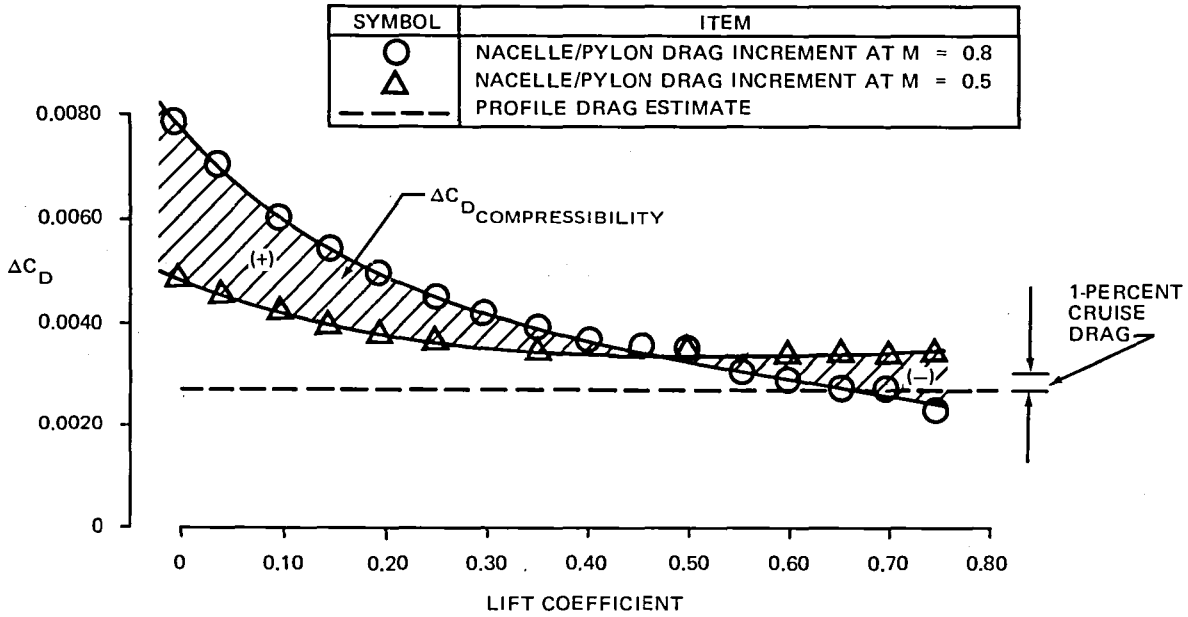


FIGURE 56. NACELLE/PYLON INSTALLED DRAG INCREMENT WITH FLAP LINKAGE FAIRINGS INSTALLED

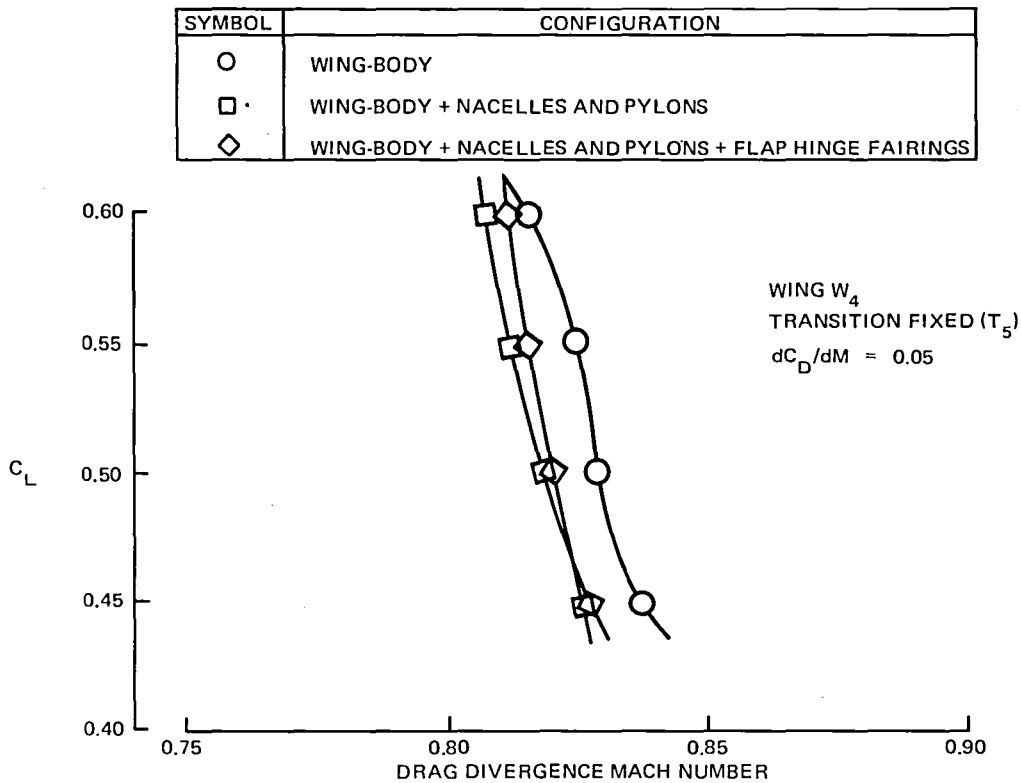


FIGURE 57. EFFECTS OF NACELLES, PYLONS, AND FLAP LINKAGE FAIRINGS ON DRAG DIVERGENCE MACH NUMBER

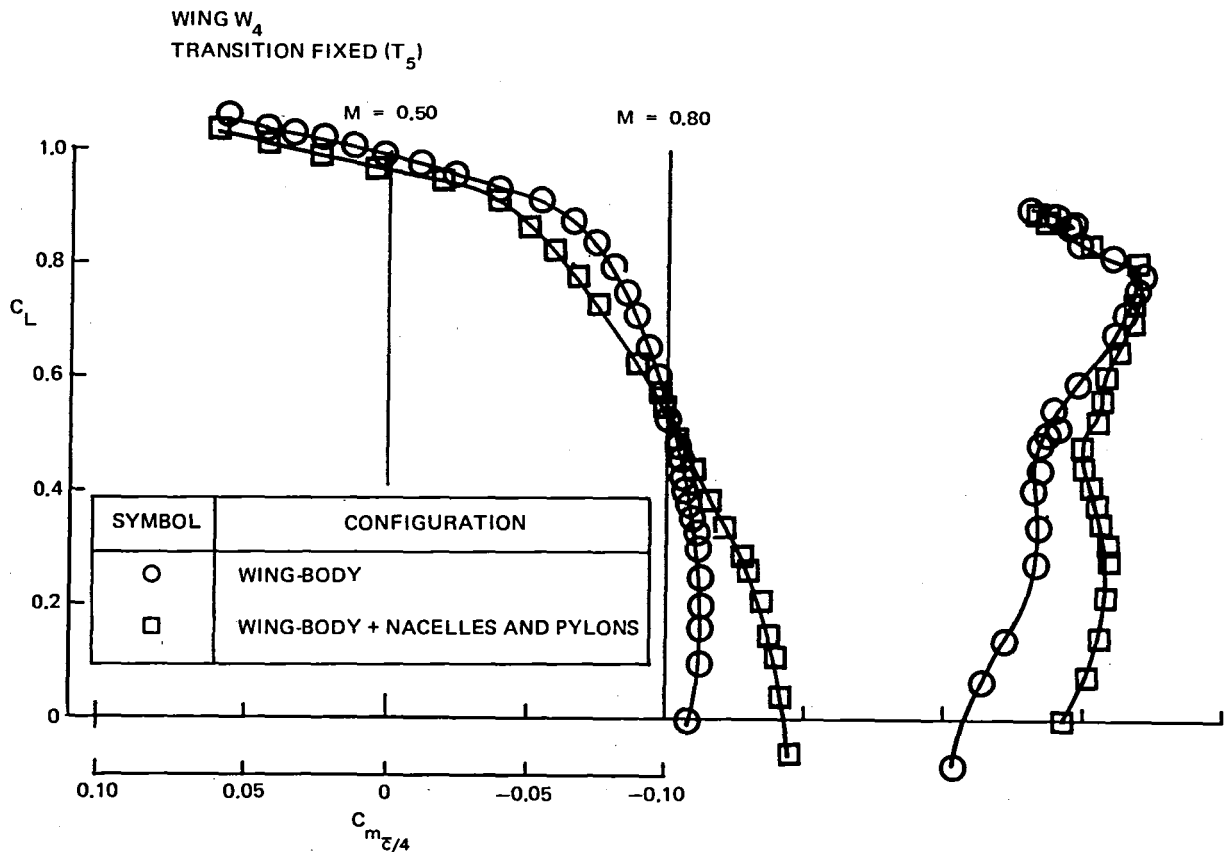


FIGURE 58. EFFECT OF NACELLES AND PYLONS ON THE TAIL-OFF PITCHING MOMENTS

In Figure 59, a breakdown of the contributions to the pitching moment shift at $M = 0.8$ near zero lift is shown. The three contributing effects shown are the change in span loading of the wing, the change in sectional C_m across the span, and the change in C_m due to the angle-of-attack change (fuselage effects) necessary to maintain wing lift coefficient. These three effects account for all of the measured change in moment coefficient. There is no lift on the nacelles at this condition; thus, the change in $C_{m_{ac}}$ due to the nacelles and pylons is not due to lift on the nacelles but rather to the changes in the flow over the wing induced by their presence.

Tail-on Characteristics

The tail-on pitching moment data for Wing W₄ (see Appendix Figures A-18 through A-20, and A-31 through A-38) show acceptable characteristics at high speed ($M = 0.80$ and above). A small region of neutral stability at stall is exhibited, but stability is recovered quickly. However, lower Mach number data display more severe pitch-up characteristics. This is due to wing characteristics, as the comparison with wing-body (tail-off) data

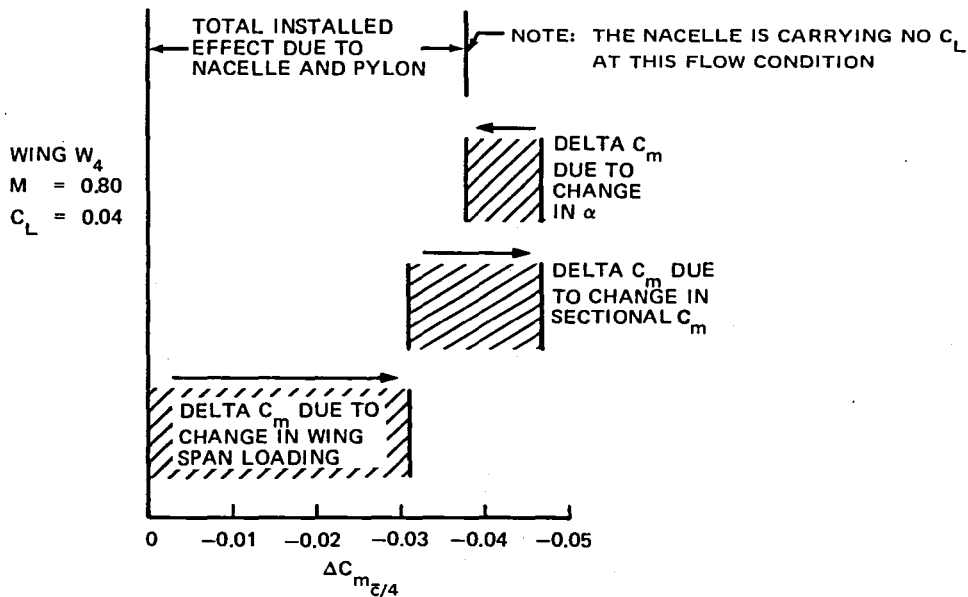


FIGURE 59. NACELLE AND PYLON INSTALLATION EFFECTS ON THE CONFIGURATION PITCHING MOMENT (TAIL-OFF)

indicates. The outboard portion of the wing, which carries relatively high section lift coefficients, stalls before the inboard portion which has large chords and low section lift coefficients. This loss of lift outboard creates a pitch-up moment which is aggravated by the high aspect ratio. This characteristic can be improved by tailoring the loading and the airfoil sections.

Trim Drag

Trim drag can be a more significant portion of the total cruise drag of a supercritical wing configuration than a conventional wing due to the higher pitching moment coefficients of the supercritical wing. This is aggravated by the short tail length of a wide-body fuselage like the DC-X-200, which requires large down loads from the tail surfaces to trim the aircraft. The wing must compensate for this download by maintaining a higher lift coefficient. The wing C_L for the cruise condition, when the aircraft is trimmed, becomes as much as 0.05 higher than that of the untrimmed lift coefficient. Not only is the drag increased by trimming, but the buffet boundary is effectively lowered due to the effect on wing C_L . Likewise, the drag divergence Mach number at the trimmed lift coefficient can be lower than that of the simple wing-body configuration.

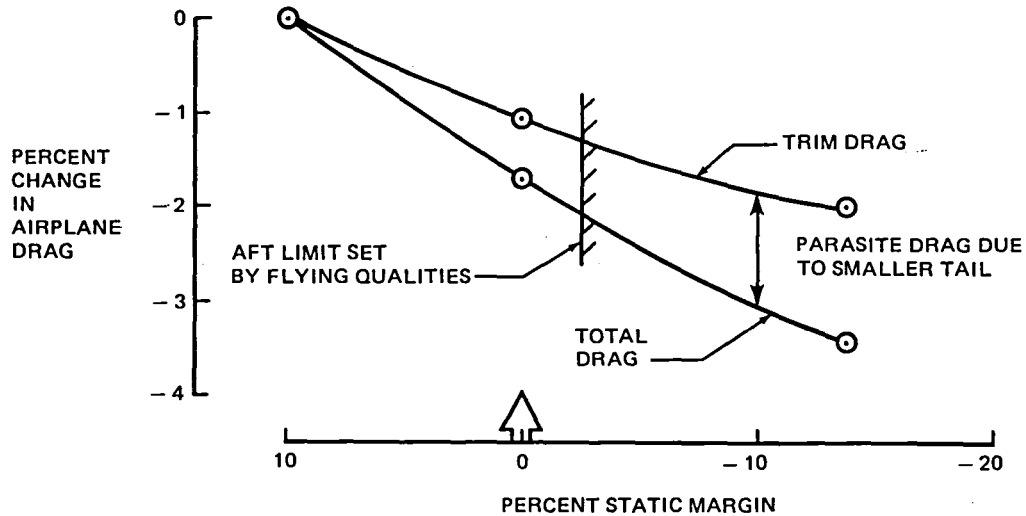


FIGURE 60. ESTIMATED EFFECT OF STATIC MARGIN ON DRAG

The DC-X-200 design incorporated relaxed static stability with a longitudinal stability augmentation system to reduce drag. The static margin of the configuration was reduced by approximately 10-percent MAC relative to the DC-10-10. This amount of relaxation placed the aft limit of the center-of-gravity range at the neutral point at the most critical flight condition, for a static margin of zero. The estimated effect on trim drag of reducing the static margin is shown in Figure 60. The effect on total aircraft drag is also shown. Flying qualities studies, using a flight simulator, established a lower limit for the static margin of -2.5 percent MAC. The static margin of the DC-X-200 was reduced by 80 percent of the allowable amount relative to the conventional DC-10-10. The result was a reduction in trim drag of 0.00036, and a reduction in total airplane drag, with the appropriately sized tail, of 1.7 percent.

Wing W_4 was selected for testing in the complete cruise configuration, i.e., with horizontal and vertical tail surfaces in addition to the wing lower surface appendages. The horizontal tail volume was 0.993 with a tail arm of 74.107 cm (29.176 in.) model scale. The test data from these runs were used to evaluate the trim drag of the model.

The analysis of the test data, when compared to pretest predictions, showed a difference in downwash of approximately 1 degree. This discrepancy was assumed to be an effect of the model support sting. The presence of the sting behind the model has a significant effect on the downwash field

behind the wing, which affects the tail incidence angle required for trim. That incidence angle shift affects trim drag through the rotation of the tail lift vector.

To verify the source of the discrepancy, an analysis of the effect of the sting on the downwash at the horizontal tail was performed using the three-dimensional Friedman-Neumann program⁵. A sting-on and a sting-off configuration (both tail-off) were analyzed at zero Mach number. These were panelled so that the sting was interchangeable with a "plug" which covered the sting entry opening in the aft fuselage, to change from one configuration to the other.

In order to obtain the flow angles in the region of the horizontal tail, off-body control points were placed spanwise along the leading edge, quarter-chord, and trailing edge of the horizontal tail location (the configurations were still tail-off). Using the velocity components computed at the off-body points, the local flow-field "pitch" angle was defined as

$$\phi = \tan^{-1} - \left(\frac{V_z}{V_x} \right)$$

The negative sign was included so that the sign convention for ϕ would be the same as for the downwash angle, ϵ .

The change in ϕ between the two configurations, equivalent to the change in downwash, proved to be very nearly independent of lift coefficient. The spanwise distribution of the downwash change along the tail quarter-chord is shown in Figure 61. The effect decreases along the span as distance from the sting increases. The average decrease in downwash was slightly less than the difference between test results and pretest estimates, but did verify the source of the discrepancy and showed the need for a revised estimate. The effect of the sting on the pitching moment of the model was also analyzed. For the zero Mach number condition, the effect of the sting on the flow field was very nearly cancelled by the effect of the sting

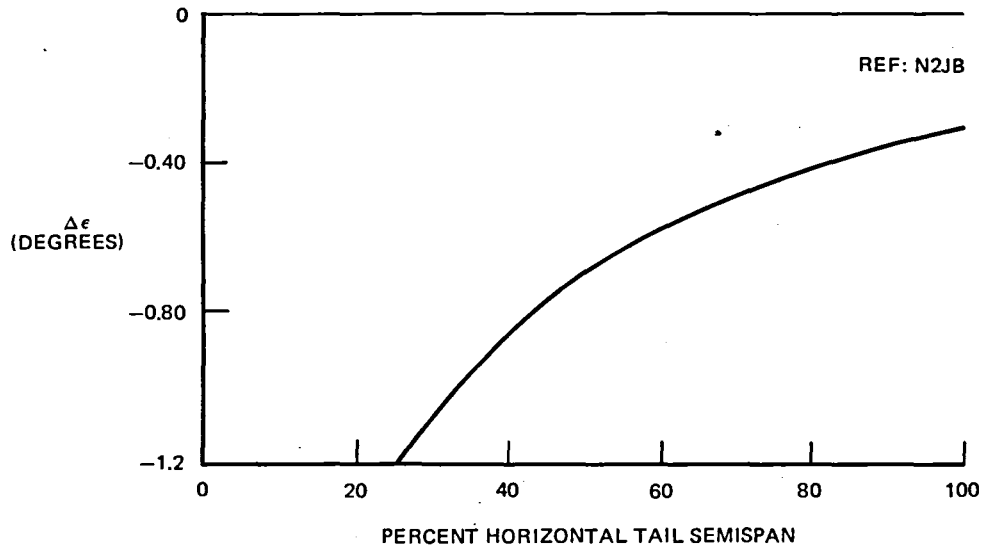


FIGURE 61. ESTIMATED CHANGE IN SPANWISE DISTRIBUTION OF DOWNWASH ON HORIZONTAL TAIL DUE TO STING

entry opening in the fuselage being nonmetric. Therefore, no pitching moment correction was necessary.

The compressibility drag increase with wing lift coefficient of the model proved to be less in the test data than in the pretest estimates. This resulted in an improvement in the trim drag. The downwash correction which was used in the final trim drag analysis was derived from wind tunnel determinations of the DC-10 fuselage, which is similar to the fuselage used in this test. The assumed effect of the sting at cruise conditions is a decrease in downwash of 1.35 degrees, which includes compressibility effects.

The variation of trim drag with trimmed lift coefficient at the cruise Mach number, derived from the test data, is shown in Figure 62. The tail-on and tail-off data, referenced to the quarter-chord of the MAC, together with a tail profile drag estimate, were used in the determination. The lower curve includes the correction for the sting's effect on the downwash.

Figure 63 summarizes the cruise trim drag analysis for the model. The trim drag for the sting-mounted model at cruise, measured directly from data with the CG at 25 percent of the MAC, is 21 counts or 6.5 percent of total cruise drag. The correction for the sting effect on downwash results in a

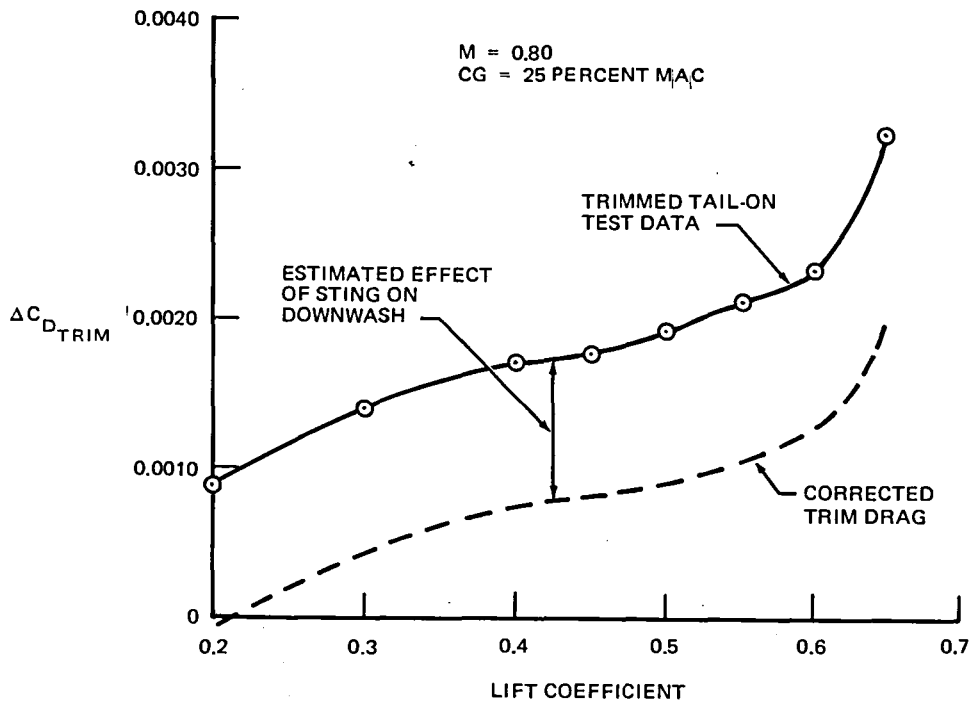


FIGURE 62. TRIM DRAG CHARACTERISTICS OF WING W₄

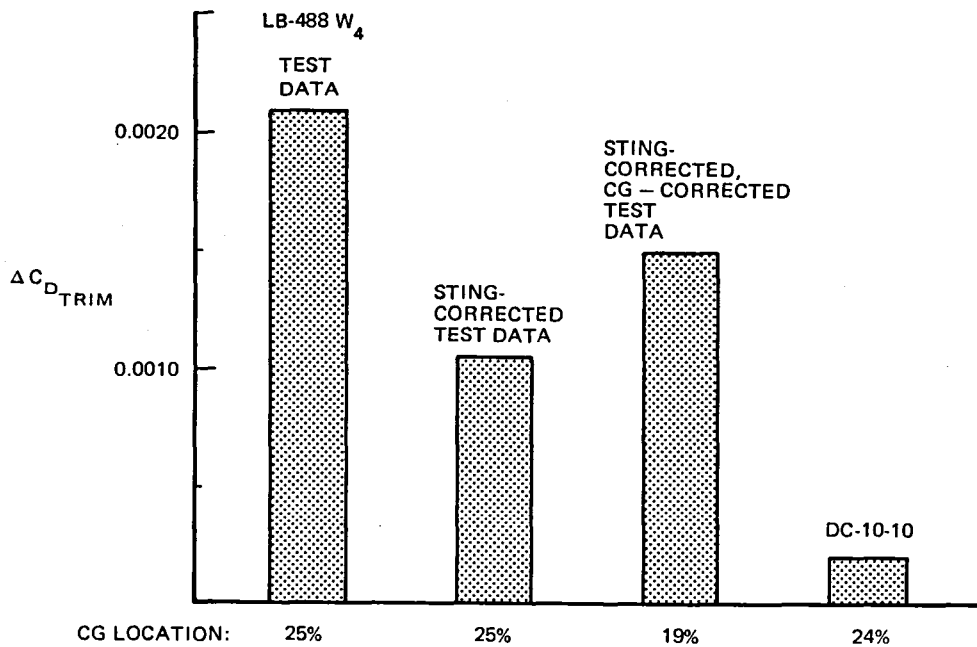


FIGURE 63. CRUISE TRIM DRAG

10-1/2 count reduction. Moving the center of gravity forward from the quarter-chord reference point to the midpoint of the configuration CG range at 19 percent MAC increases the trim drag by 5 counts for a total of 15-1/2 counts, or 4.8 percent of total cruise drag. The trim drag of the DC-10-10 is included for comparison. It is apparent that the trim drag of the wide-body, supercritical wing configuration is a significant portion of total cruise drag, an order of magnitude larger than that of the conventional-winged DC-10.

Wake Rake Results

The force and pressure measurements which are normally obtained during high-speed testing do not provide a quantitative measure of the spanwise distribution of wing profile drag. For this reason, wake measurements were obtained for wing configuration W₈ during the fourth wind tunnel test, LB-488D. The measurements were made using the Douglas traversing wake rake, shown in Figures 30 through 32 and 64. The rake assembly attaches to the model support sting and translates horizontally and vertically to measure both total and static pressure in the wake just behind the left wing trailing edge. The vertical movement of the rake is such that the pressures in the wake are accurately defined, while the horizontal movement allows for up to 24 predetermined spanwise locations at each angle of attack. The rake is controlled remotely by a dedicated computer which also provides on-line printout during testing.

Wake traces, such as the data presented in Figure 65, are the primary measurements obtained during wake rake testing. The wake profiles shown in Figure 65 were measured behind wing W₈ at 0.8 M and 0.6 C_L. At this condition a well-developed shock wave was present on the wing upper surface. Losses generated by the shock are largest at the 40-, 50-, and 60-percent semispan stations.

The measured wake profiles have been integrated to obtain section profile drag. Figure 66 presents the spanwise distribution of section profile drag for Mach numbers of 0.5, 0.75, 0.8, and 0.82 at approximately 0.55 C_L. The data shown at M = 0.5 is for a fully subcritical condition and the shock drag can be evaluated by considering the difference between this curve and

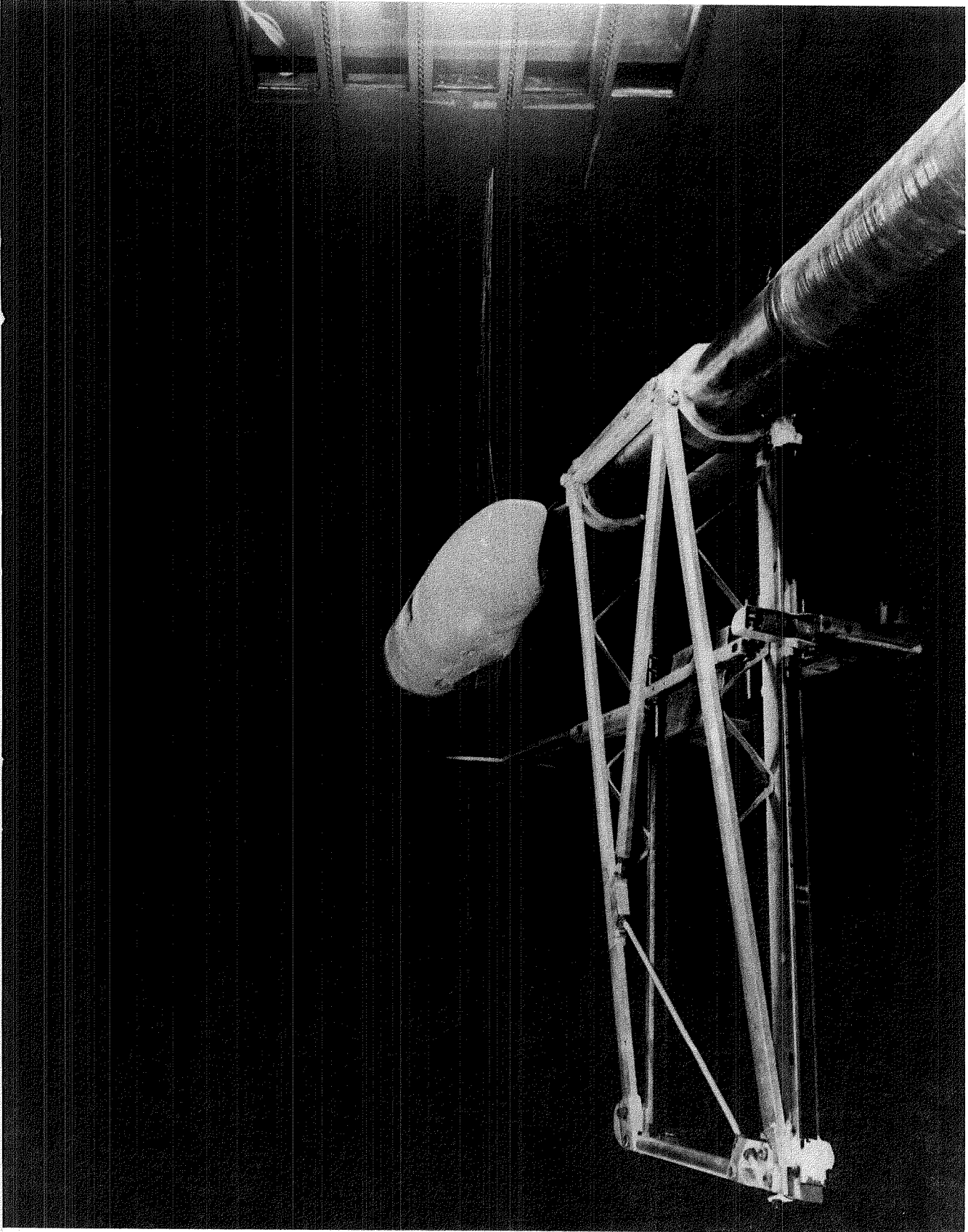


FIGURE 64. LB-488 W₈ WITH WAKE RAKE INSTALLED IN WIND TUNNEL

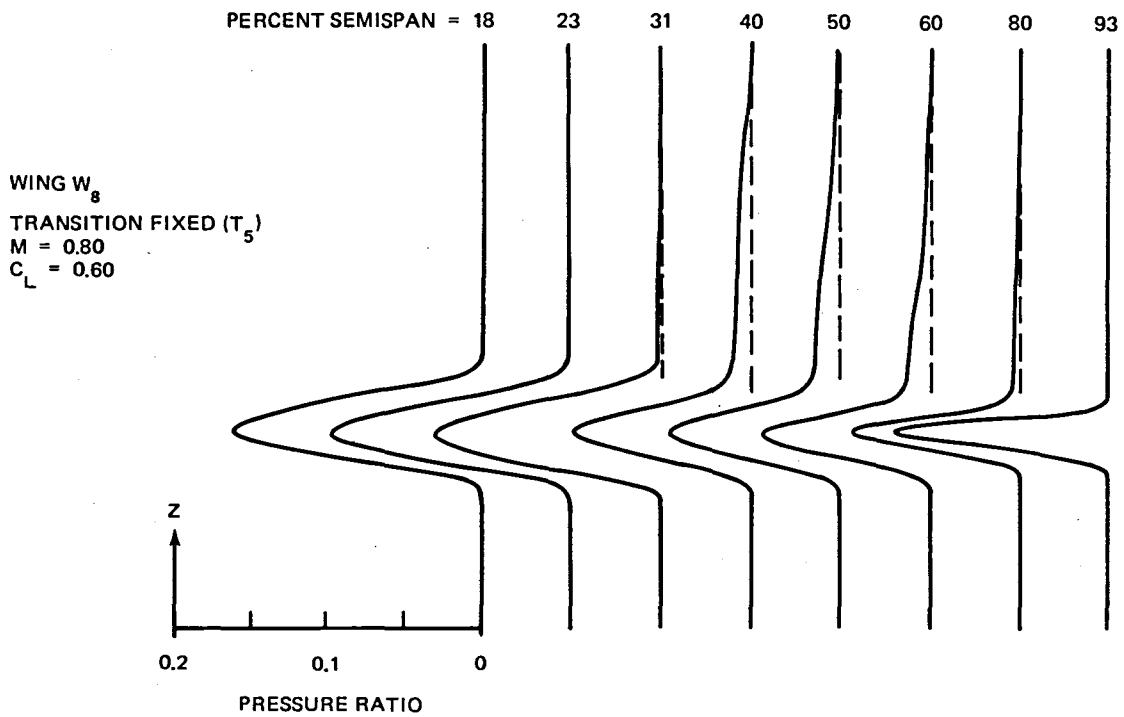


FIGURE 65. TYPICAL WING WAKE PRESSURE PROFILES

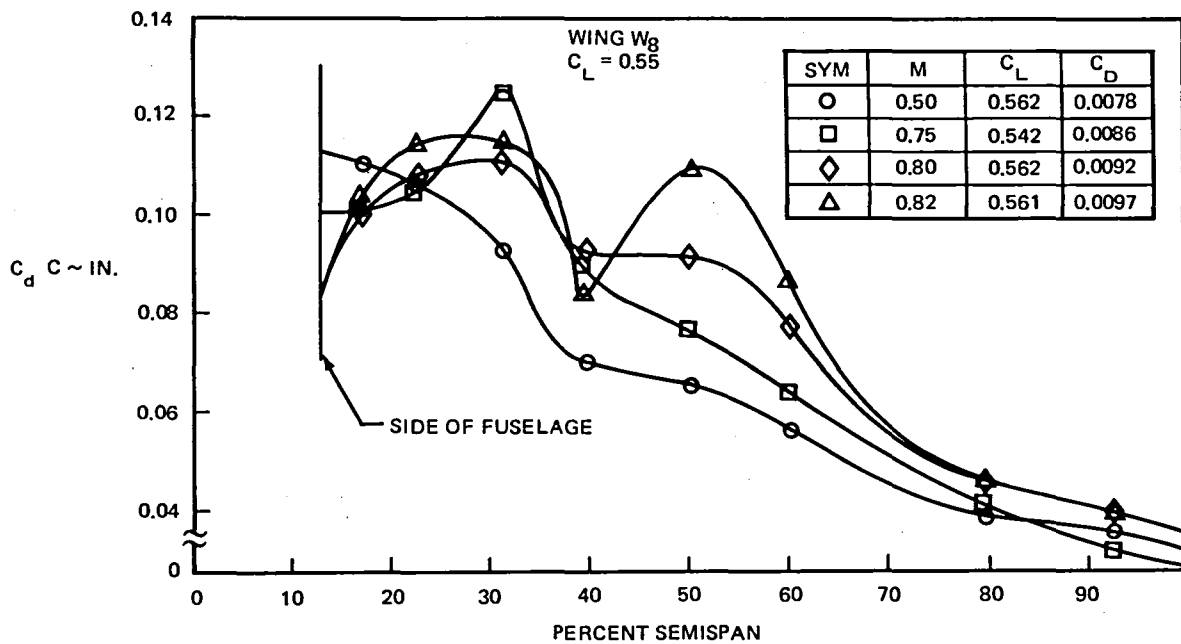


FIGURE 66. SPANWISE VARIATION OF PROFILE DRAG

those at high Mach numbers. At $M = 0.75$, a region of concern because of drag creep, the inboard wing near 30-percent semispan can be seen to contribute the most to the creep, with a lesser amount being contributed over the entire span. By the time the drag divergence Mach number, 0.82, is reached, strong shocks have developed on both the inboard and outboard wing. The dip in the curve occurs at the wing trailing-edge break where the inboard forked shock system intersects the single outboard shock system.

The spanwise distributions of section profile drag have been integrated to obtain a total wing profile drag. Figure 67 illustrates the resulting profile drag polars for a Mach number range from 0.5 to 0.82 for the T_5 transition pattern (see Table 1). These results have been used to define compressibility drag characteristics. Figure 68 compares compressibility drag increments obtained from the wake rake measurements and those obtained

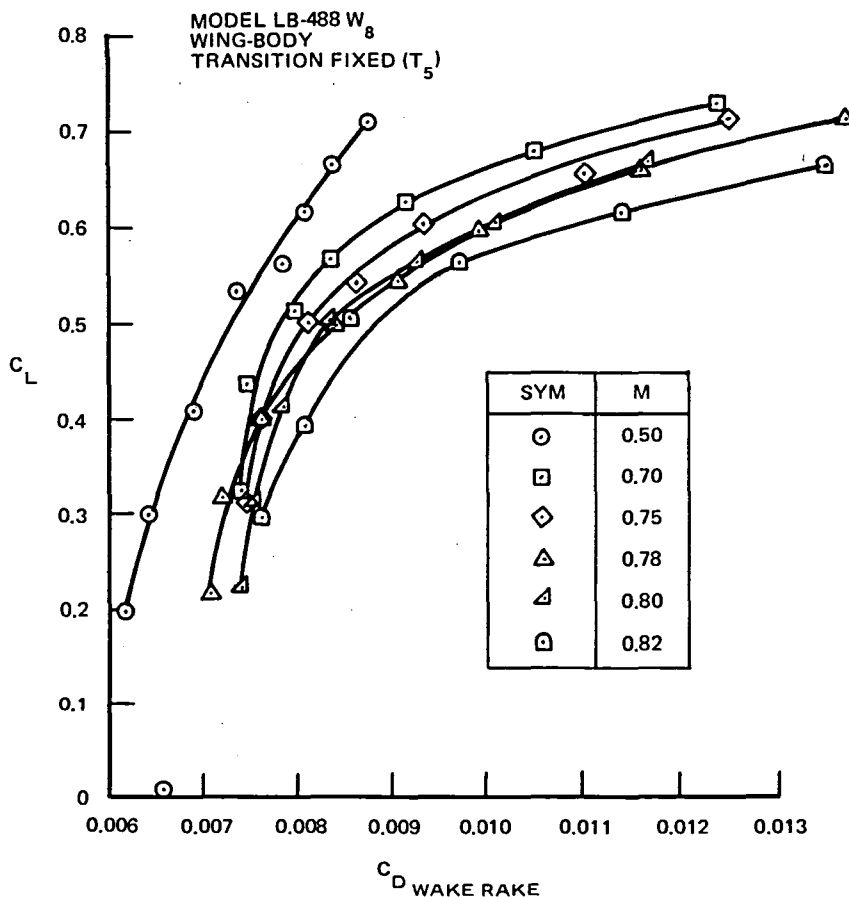


FIGURE 67. WAKE RAKE WING PROFILE DRAG POLARS

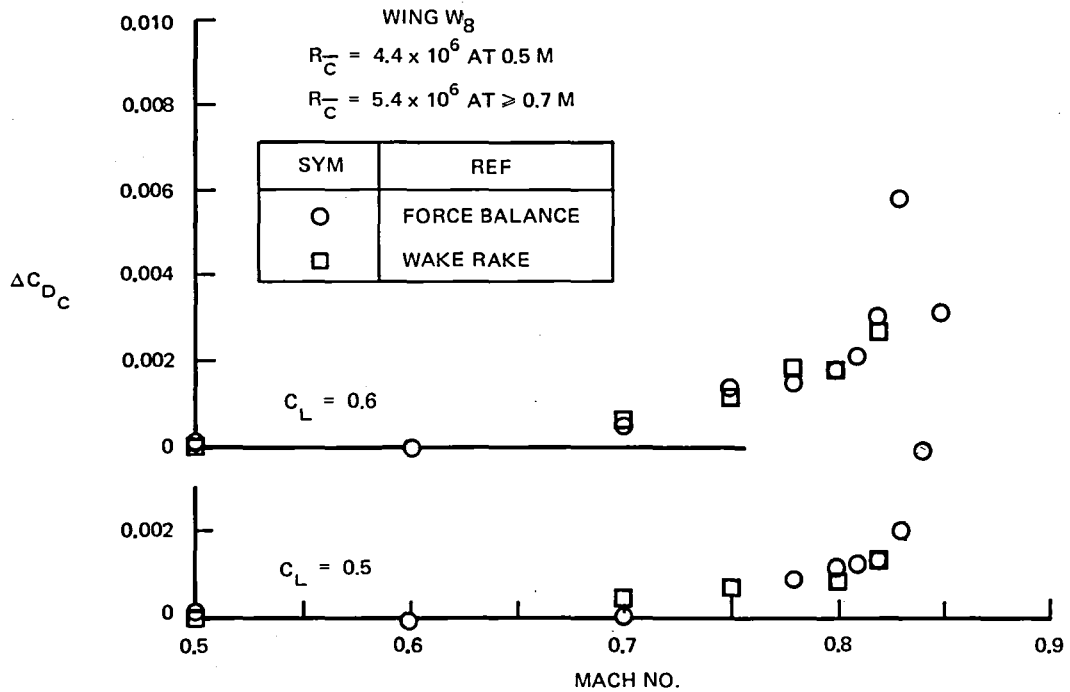


FIGURE 68. COMPARISON OF EXPERIMENTAL COMPRESSIBILITY DRAG INCREMENTS

from the force balance measurements. Data are presented for both 0.5 and 0.6 C_L . The agreement is very good.

In addition to the T_5 transition configuration, an alternate transition configuration near the leading edge, T_6 , was also tested at lower Mach numbers. The integrated profile drag at $M = 0.5$ is shown in Figure 69 for the two different transition locations. The steep curve for wing W_8 with transition forward (T_6) results from a lack of pressure recovery near the trailing edge at the lower lift coefficients. This was observed in the comparison of the pressure distributions obtained with the two different transition locations. For the curve obtained with the aft transition location (T_5), sublimation studies showed that natural transition was occurring forward of the upper surface trip at the higher lift coefficient, so this curve is not truly representative either. If higher Reynolds number flow could be properly simulated, the resulting profile drag polar would be somewhere between these two limits.

Aileron Effectiveness

The fourth test of the series, LB-488D, included testing of an outboard aileron at high Mach numbers. This aileron, installed in the right wing

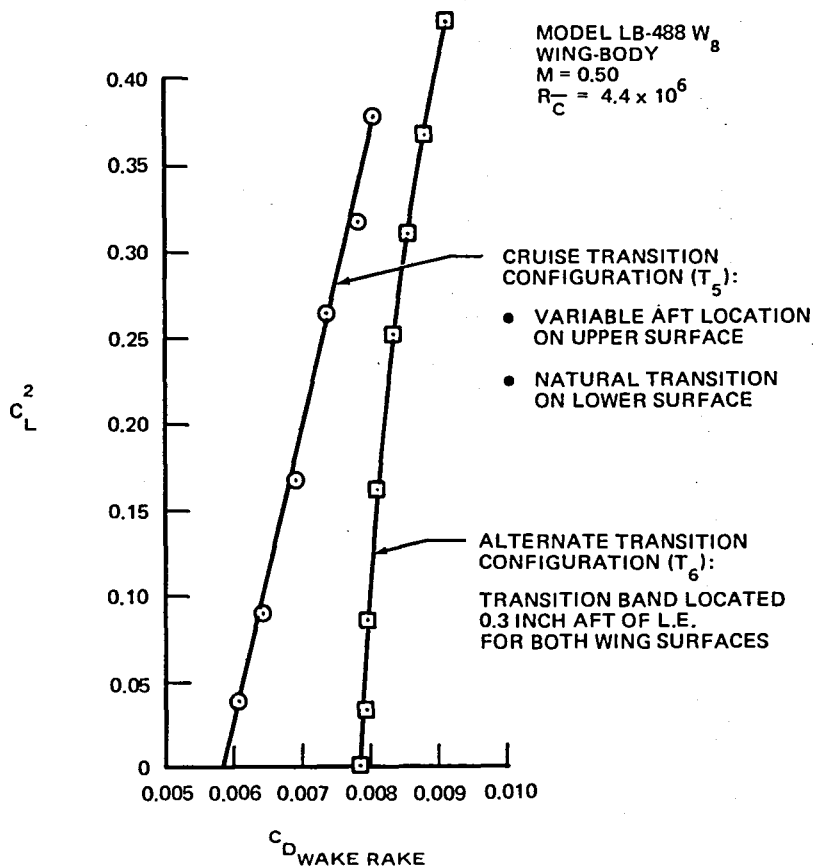


FIGURE 69. EFFECT OF TRANSITION CONFIGURATION ON WING PROFILE DRAG POLARS

only, had a chord which was 25 percent of wing chord, from 80 percent to 98.4-percent semispan. Deflections of ± 10 and ± 20 degrees were tested at Mach numbers from 0.5 to 0.925.

Rolling moment data showed relatively linear behavior throughout the low Mach number ranges to 0.9 Mach, where slight nonlinearity developed in both positive and negative directions. The rolling moment characteristics at $M = 0.90$ and $M = 0.925$ are shown in Figure 70.

At $M = 0.925$, a definite reversal of rolling moment with aileron deflection occurs. It is exhibited primarily in the trailing-edge up (negative) direction, over a range of 10 or 15 degrees of deflection. Outside of this deflection range, behavior is nonlinear but conventional. Since aileron reversal is exhibited only past the wing dive Mach number of 0.90, this characteristic is considered acceptable. In Figure 71, the aileron effectiveness from the test is compared with that of other Douglas aircraft.

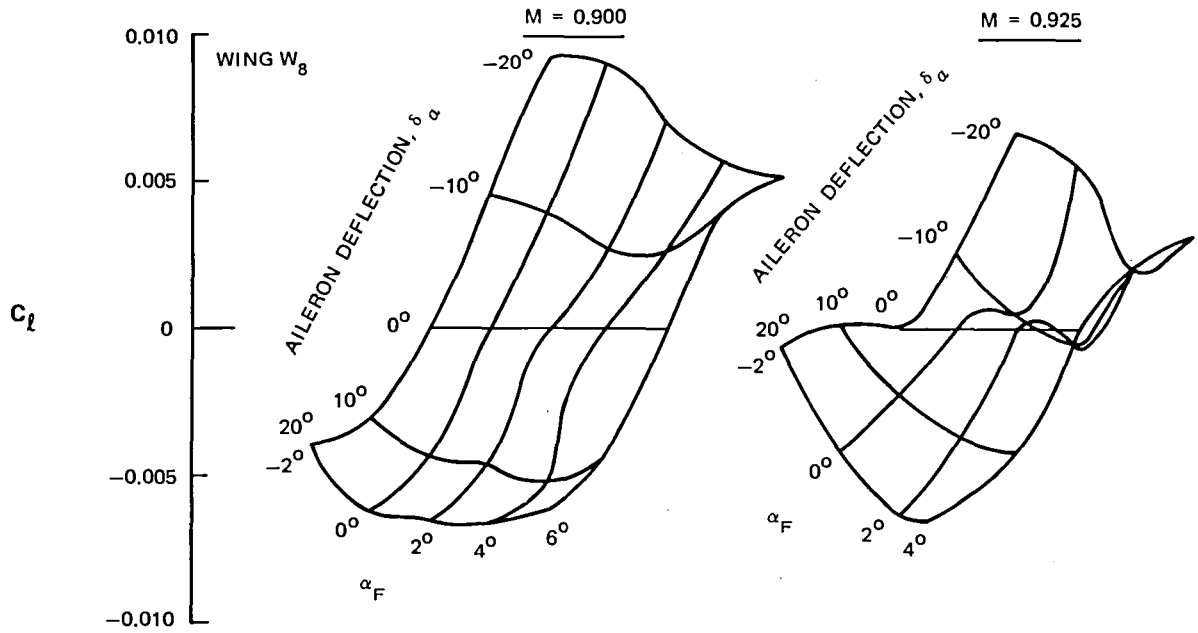


FIGURE 70. AILERON EFFECTIVENESS AT HIGH MACH NUMBER

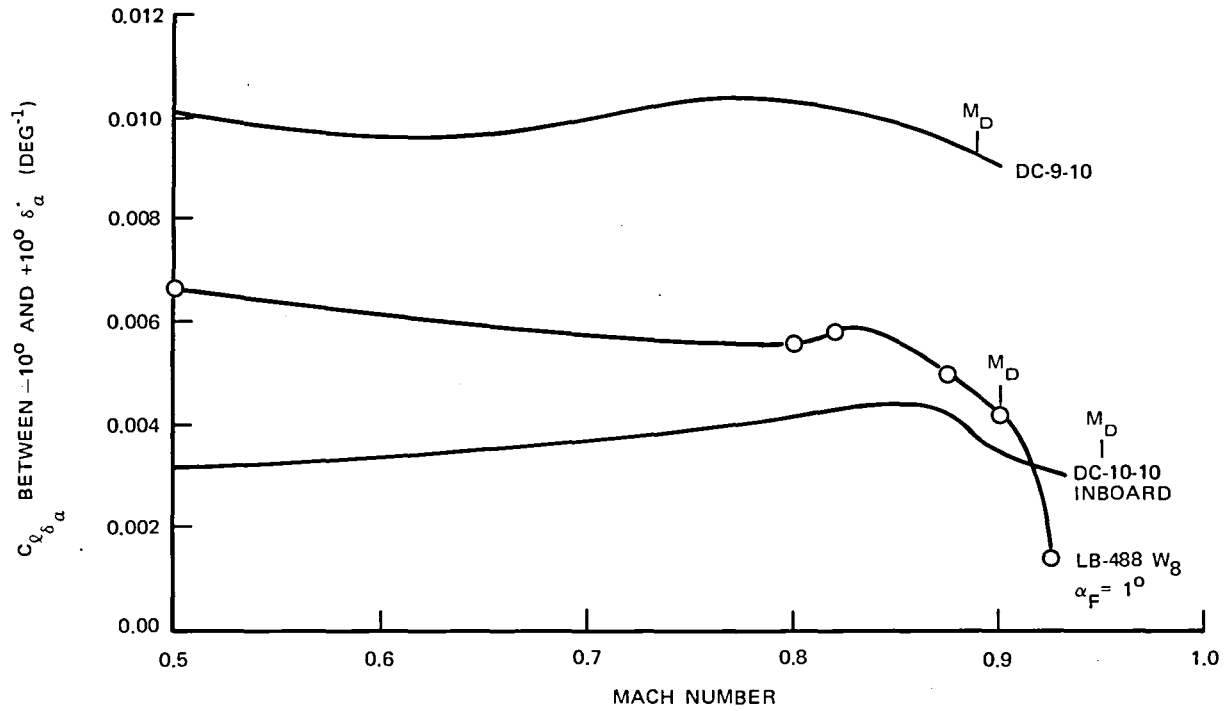


FIGURE 71. AILERON EFFECTIVENESS VERSUS MACH NUMBER

COMPARISON OF DATA WITH ESTIMATION METHODS

Comparisons of theoretical and experimental results have been made for wing W8. The theoretical results were calculated using the Douglas version of the Jameson-Caughey (FLO22) three-dimensional transonic flow program.⁴ This computational method includes approximate fuselage simulation, an accelerated iteration step, and an iterated two-dimensional strip boundary-layer solution. Comparisons have been made for surface pressure distributions and for lift and drag characteristics. These comparisons further validate the basic method and identify the accuracy and limitations associated with it.

Flow solutions were computed at numerous flow conditions. Calculated and experimental pressure distributions are presented in Figures 72 through 74 for Mach numbers of 0.5, 0.75, and 0.8, respectively. The transonic flow character and development are reasonably well calculated. The comparison of the calculated and experimental results is particularly good on the outboard wing panel. Inboard, at the higher Mach numbers, the calculated shock strength is weaker than the measured result. This difference is related to the low-fineness-ratio fuselage ($L/D \approx 7.0$) used for the testing. This fuselage produces a significantly nonuniform onset Mach number across the span, as illustrated in Figure 75. This effect was not simulated in the calculation; rather, an average onset Mach number was used to perform the calculations. The higher inboard local Mach numbers associated with this short fuselage lead to the stronger measured shock wave.

A comparison of the calculated and measured lift curves for $M = 0.8$ is presented in Figure 76. The calculated lift curves were developed by correcting the exposed wing lift for the fuselage lift carryover. This correction was derived using lifting surface theory. The calculations were performed both at wind tunnel Reynolds number and at a higher Reynolds number simulating full-scale flight conditions. At wind tunnel Reynolds number, the boundary-layer transition was specified to simulate the T_5 experimental transition as it varied with C_L . The lower Reynolds number calculation and the experimental data are in good agreement, including the

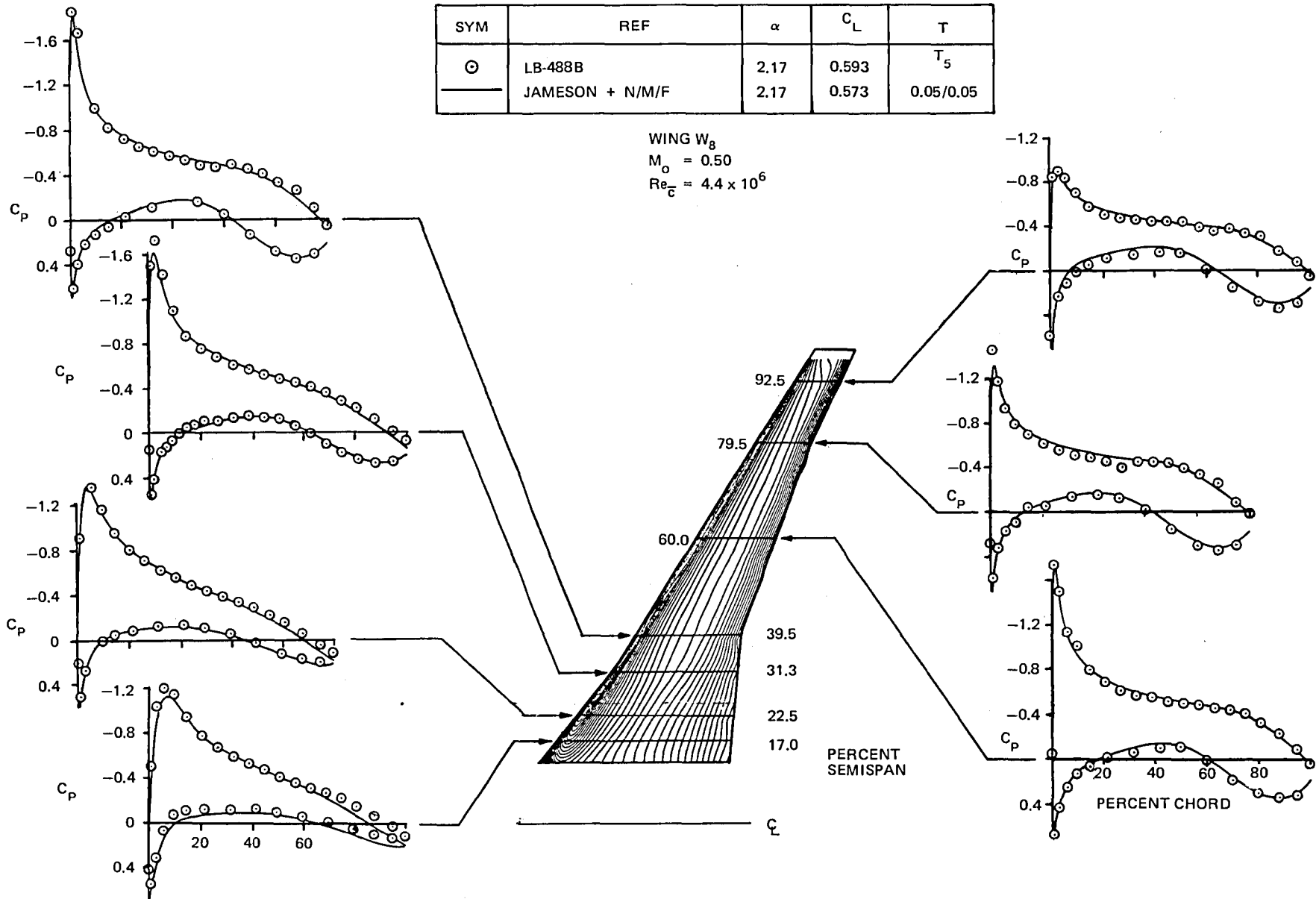


FIGURE 72. COMPARISON OF CALCULATED AND EXPERIMENTAL CHORDWISE PRESSURE DISTRIBUTIONS, $M = 0.50$

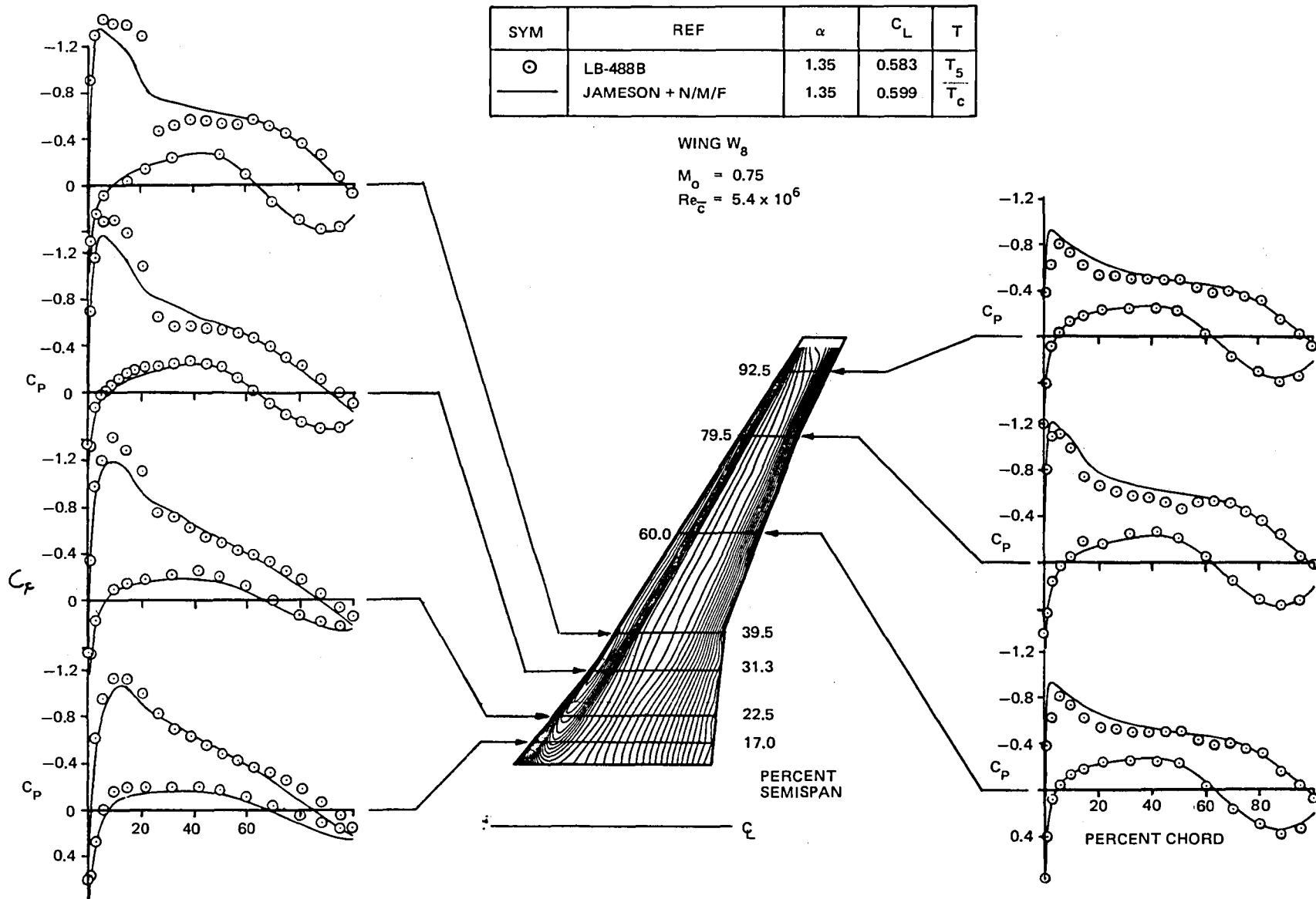


FIGURE 73. COMPARISON OF CALCULATED AND EXPERIMENTAL CHORDWISE PRESSURE DISTRIBUTIONS, $M = 0.75$

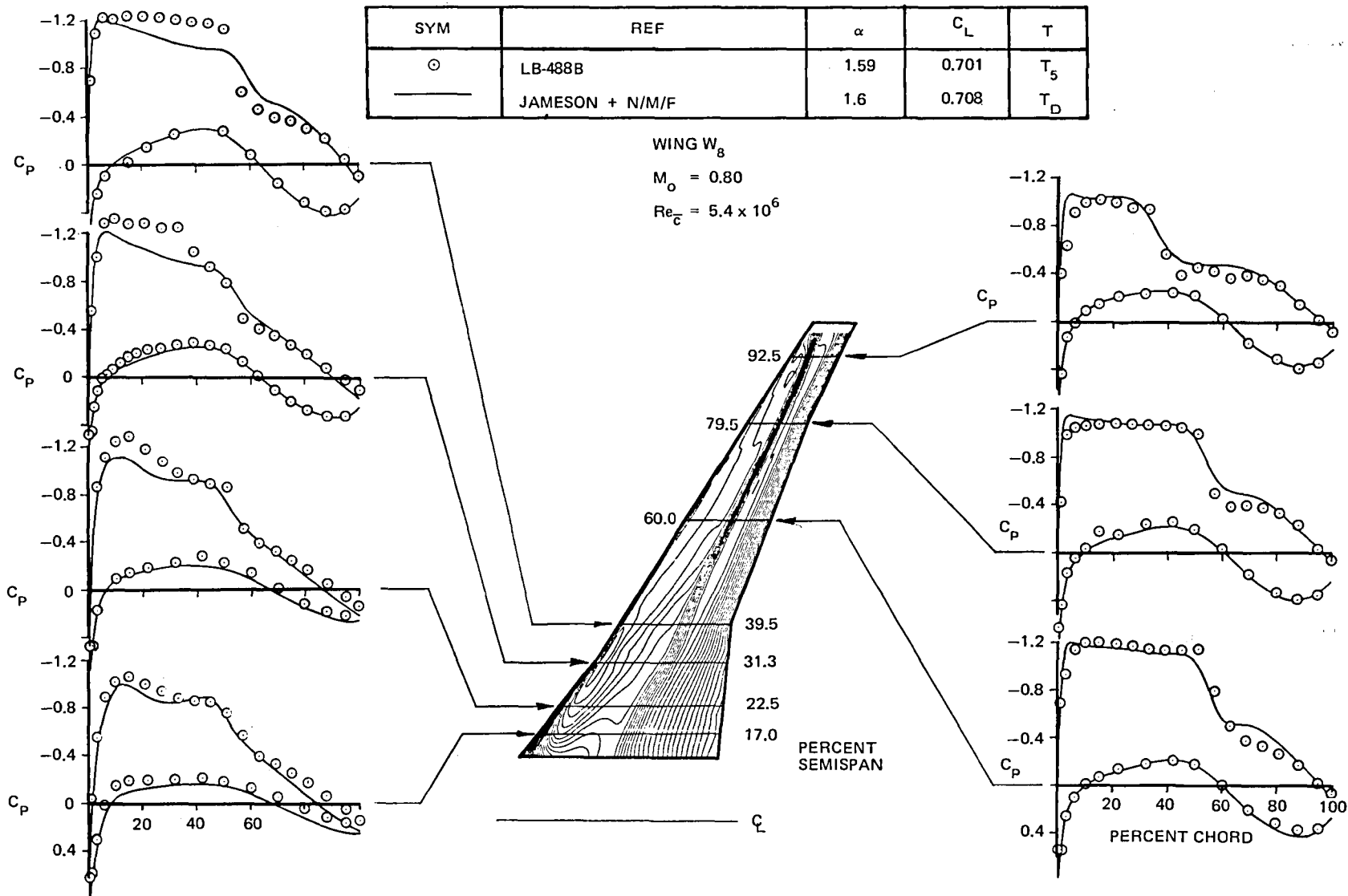


FIGURE 74. COMPARISON OF CALCULATED AND EXPERIMENTAL CHORDWISE PRESSURE DISTRIBUTIONS, $M = 0.80$

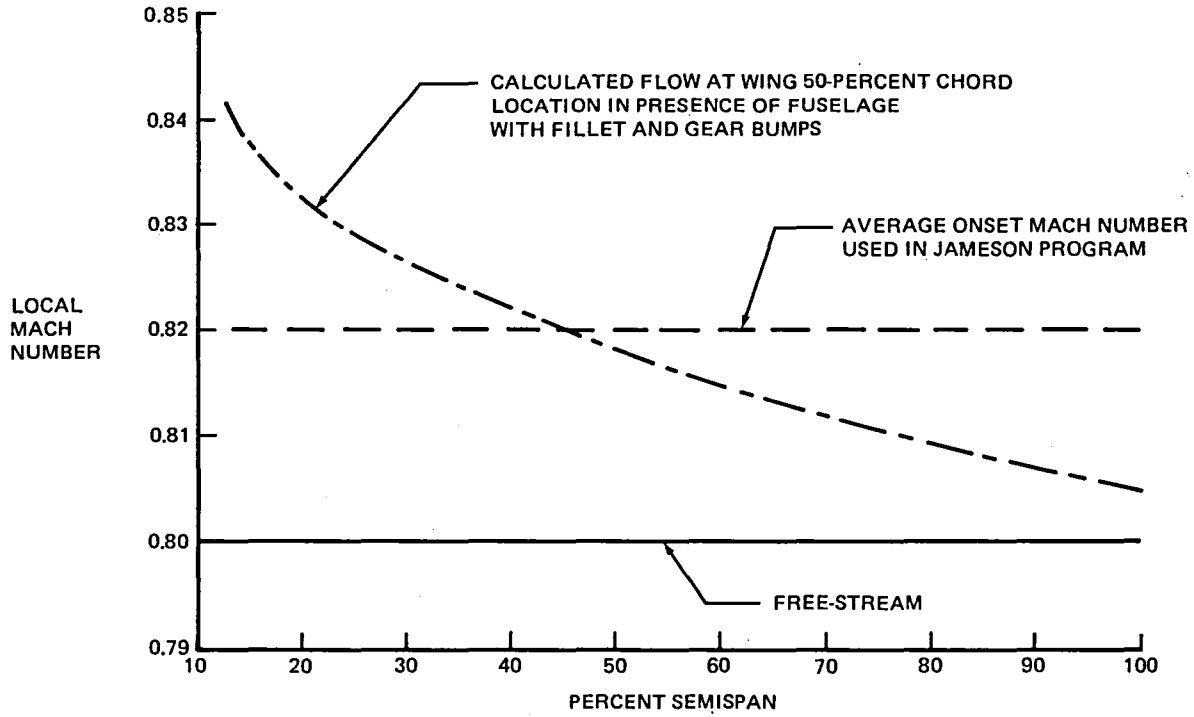


FIGURE 75. EFFECT OF FUSELAGE ON SPANWISE VARIATION OF MACH NUMBER

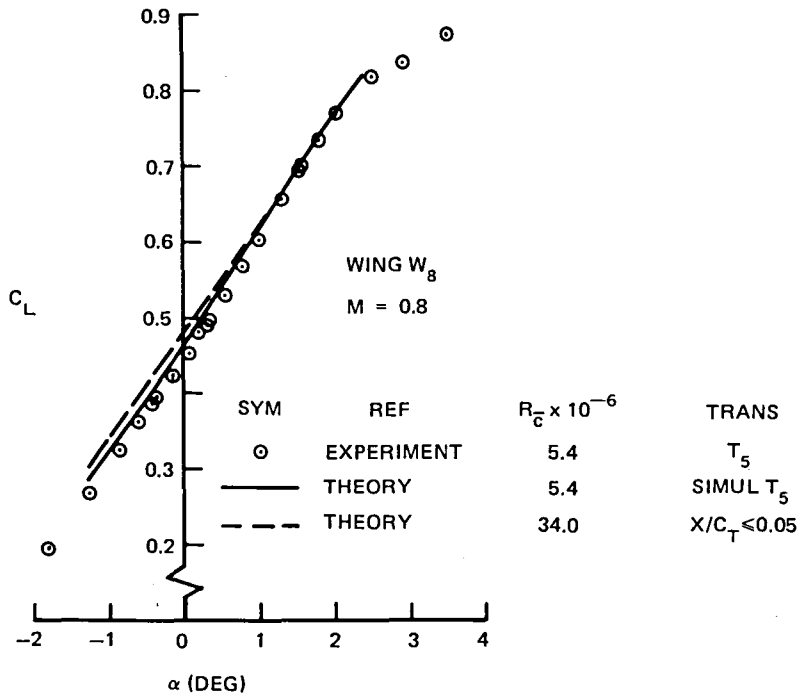


FIGURE 76. COMPARISON OF CALCULATED AND EXPERIMENTAL LIFT CURVES

nonlinearity. For the higher Reynolds number calculation, the transition location was specified at no further aft than 5 percent chord, which is representative of flight conditions. This calculation does not exhibit the nonlinearity of the lower Reynolds number case. The movement of upper-surface transition with C_L for the lower Reynolds number case seems to be the cause of the lift curve nonlinearity. At the lower lift coefficients of approximately 0.4, a leading-edge suction peak and forward shock cause boundary-layer transition to occur well ahead of the upper surface trip. The resulting long run of turbulent flow leads to a thick trailing-edge boundary layer and a corresponding large lift loss due to the decambering effect of the boundary layer. At higher lift coefficients such as 0.6 to 0.7, the pressure distributions develop into a supersonic plateau terminated by a shock downstream of the boundary-layer trip. Boundary-layer transition is delayed until the trip, and the amount of turbulent run is significantly less. Consequently, the trailing-edge boundary-layer thickness is reduced and more lift is obtained. This increase in lift causes the nonlinearity in the lift curve.

Calculated and measured drag rise characteristics are compared for 0.5 and 0.6 C_L in Figure 77. The results are presented in terms of a compressibility drag coefficient increment with $M = 0.5$ as the reference. Both balance measurements and wake rake measurements are included in the comparison. The calculated compressibility drag increment is slightly higher than the two measurements although the drag divergence Mach number agrees quite well.

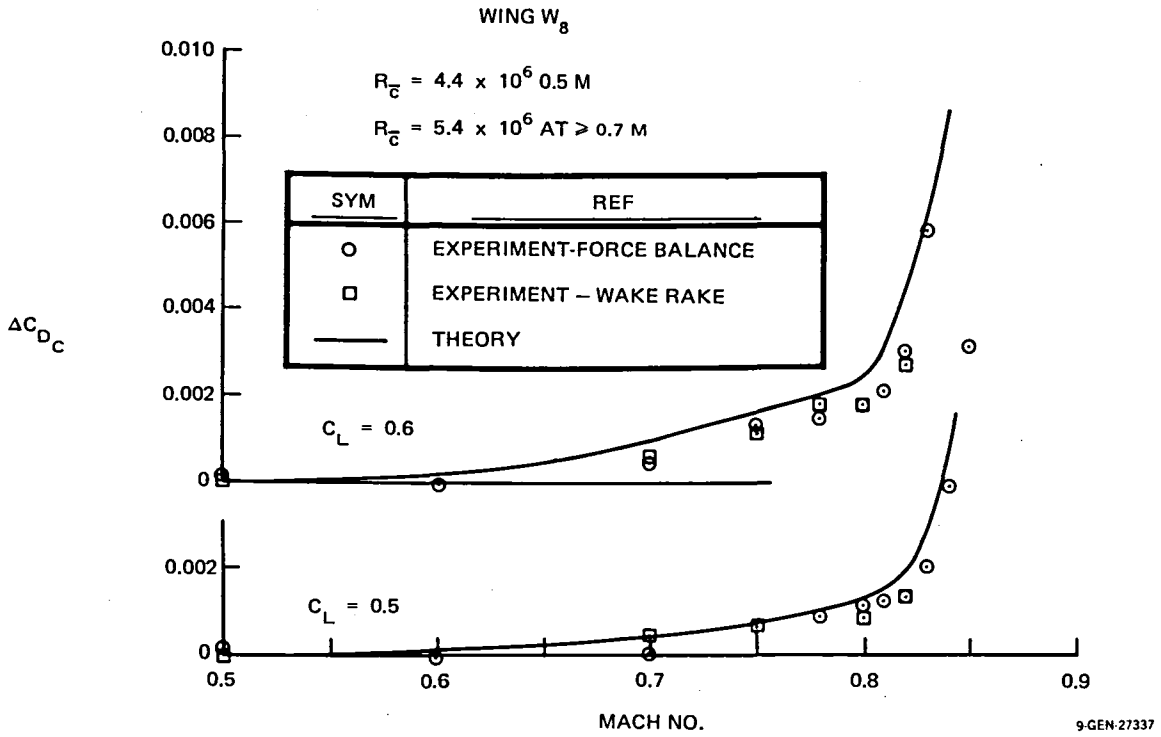


FIGURE 77. COMPARISON OF CALCULATED AND EXPERIMENTAL COMPRESSIBILITY DRAG INCREMENTS AT TEST REYNOLDS NUMBER AND TRANSITION CONDITIONS

This Page Intentionally Left Blank

CONCLUSIONS AND RECOMMENDATIONS

Design studies and wind tunnel tests of high-aspect-ratio supercritical wings suitable for a fuel-efficient, medium-range, wide-body transport have been completed. Five candidate wings were selected to be tested after the completion of total system studies and analytical aerodynamic studies which considered a large matrix of design variables. The following conclusions are drawn from the results of the system studies and the analysis of the test data:

- (1) A high-aspect-ratio supercritical wing can be designed to increase the energy efficiency of transport aircraft and reduce the direct operating costs when the supercritical technology is applied primarily to parameters which reduce weight (e.g., airfoil thickness or reduced sweep). This weight saving is then used to compensate for what would normally be the higher weight of the high-aspect-ratio wing. The supercritical airfoil is uniquely suited to the high-aspect-ratio wing since its inherent aft camber significantly improves its characteristics over those of conventional sections at high lift coefficients, where the high-aspect-ratio wing achieves its best L/D_s .
- (2) The differences in the cruise and buffet characteristics between the five wings tested show that although the variables studied did not produce significant changes in the drag divergence Mach number, they did produce large variations in the drag level at Mach divergence and in the drag levels at lower Mach numbers. They also produced large changes in the buffet boundaries of the five wings. Although only the aerodynamic effects in the cruise regime are shown for the five wings, the variable parameters tested, in all cases, affect the wing weight, or the low-speed performance, or both. Some of these effects, which must be weighed against the high-speed aerodynamics are,
 - a. Span-loading - The more elliptic loading favors induced drag, and also produced relatively good drag-rise characteristics in wing W_3 . On the negative side, it produces a heavier wing with poorer clean-wing buffet characteristics at cruise, and possibly poorer

stall characteristics in both the clean and high-lift configurations at low speeds.

- b. Aft-camber - Increasing aft camber can improve both the drag-rise characteristics and the buffet boundary, and can also improve the low-speed characteristics in terms of maximum lift capability. However, undesirably, it increases the negative pitching moment, hence increasing the trim drag, and increases the weight of the control surfaces because of the higher aft loading. The latter effect can also result in larger actuators which need external wing fairings, which also contribute to drag and weight. It should be pointed out that the two more highly cambered wings tested, W₅ and W₇, did not perform as well as they might have if the data now available were in hand at the time they were designed. However, any improvements which might be made in light of this data will have to be weighed carefully against the negative aspects of increasing the aft camber from the levels of W₃, W₄, and W₈.

- c. Leading-Edge Radius - Reducing the leading-edge radius by relatively small amounts (W₅ and W₈) produced improved drag characteristics in the Mach number regime approaching cruise. Although not significantly affecting the drag level at cruise, the shape of the drag-rise curve is important in regard to the ability of the aircraft to slow down in order to conserve fuel. The plateau in the drag-rise curve just ahead of Mach divergence, exhibited by some of the wings tested, is undesirable in this respect.

In the buffet regime, the smaller leading-edge radius produces better characteristics at Mach numbers approaching cruise, where the separation is gradient-induced, and poorer, although acceptable, characteristics at cruise and above where the separation is shock-induced. On the other hand, at low speeds in both the clean and high-lift configurations, the smaller leading-edge radius produces a reduction in C_{LMAX} . In the

high-lift configuration, this reduction may be a function of the type of leading-edge device.

- (3) Interference effects due to nacelles and pylons resulted in a sizable lift loss at a constant angle of attack. Although no significant drag penalty was shown at cruise lift coefficients, a significant penalty was shown at lower lift coefficients (which is only a transient condition). The lift loss has been shown theoretically to be due to the size of the nacelles relative to the wing. A shock on the lower surface of the wing due to the symmetrical pylon was somewhat counteracted by an improved upper-surface shock system in the presence of the nacelles and pylons. Flap support fairings alone showed an interference drag at all Mach numbers and lowered the drag divergence Mach number.
- (4) The test data did not uncover any problems at off-design conditions which were felt to be unsolvable. Aileron characteristics were obtained through the dive Mach number and were shown to be acceptable. No yaw data were obtained. Tail-on characteristics were also shown to be acceptable.

Recommendations

The results of the Phase I tests have shown that the high-aspect-ratio supercritical wing is a viable technology ready for incorporation into energy-efficient transports. These results have also shown that the effects of many different parameters and tradeoffs between aerodynamics and weights must be realistically assessed in order to achieve the most efficient system. Relatively small reductions in cruise drag result in significant fuel savings over the life of an aircraft, making attention to detail very important.

In reviewing the results obtained to date from the Douglas Phase I studies, as well as from those conducted by NASA-Langley, three areas stand out as deserving further work in order to achieve the maximum benefit from this technology. These are:

- (1) Drag Creep and Drag Level at Mach Divergence - In designing supercritical sections, an almost infinite number of combinations of

leading-edge radii and trailing-edge camber can be chosen for a given value of maximum thickness. In general, the more blunt, highly cambered sections have the highest drag divergence Mach numbers but also have significant drag creep and higher levels of drag at Mach divergence than those of conventional sections. The results of the tests have shown that relatively small changes in the airfoil design can achieve significant changes in the drag-rise characteristics. The three-dimensional tailoring across the span affords another means of improving these characteristics as does the selection of spanwise thickness and lift distributions. More work needs to be done in this area to achieve more optimum drag-rise characteristics at the high cruise lift coefficients associated with the high-aspect-ratio wing.

- (2) Trim Drag - Since a significant amount of aft camber is inherent to the success of the supercritical airfoil, and since this can result in relatively higher trim drags for this type of wing, despite the use of reduced static stability, more studies need to be made on the tradeoffs involved in minimizing these effects. Again, spanwise tailoring of the airfoil sections, as well as the choice of the spanwise lift distribution can significantly affect the pitching moments. Studies at NASA have also shown large effects due to nacelle positioning because of the nacelle effects on the loading. Since all of these parameters affect the wing weight, it is necessary to know both the aerodynamic and weight tradeoffs before the most efficient system can be selected. More work needs to be done.
- (3) Nacelle-Pylon Interference - This is believed to be more a function of the small (with advanced technology high lift systems), high-aspect-ratio wing than of the supercritical sections. The theoretical analysis shows the relationship of the large nacelle to the small wing chord to be the largest contributor to the lift loss shown when the nacelles and pylons are added to the wing. Although the supercritical sections have higher negative pressure peaks forward on the lower surface, this can be rectified by the pylon design; the nacelle lift loss, however, can only be counteracted by local changes in the clean-wing spanwise lift distribution. This has yet to be

attempted. Although the data obtained during the tests show little interference drag at cruise conditions, the analysis of the data shows that the interference penalty was counteracted by a more favorable upper-surface shock development due to a change in the spanwise lift distribution. This change, toward a higher outboard loading, would most likely have shown a penalty in the buffet boundary, had the data been obtained during the test. Unfortunately, transition-free data for the nacelles and pylons were not obtained. Much more work, including powered testing, needs to be done in this area.

This Page Intentionally Left Blank

REFERENCES

1. Mechtly, E.A.: The International System of Units - Physical Constants and Conversion Factors. NASA SP-7012, 1973.
2. Bauer, F.; Garabedian, P.R.; and Korn, D.G.: Supercritical Wing Sections. Springer-Verlag, New York, 1972.
3. Tranen, T.: A Rapid Computer Aided Transonic Airfoil Design Method. McDonnell Douglas Corporation, IRAD Report No. A2584, 1973.
4. Jameson, A.; and Caughey, D.A.: Numerical Calculation of the Transonic Flow Past a Swept Wing. New York University, ERDA Report C00 3077-140, 1977.
5. Friedman, D.M.: A Three Dimensional Lifting Potential Flow Program. McDonnell Douglas Corporation, IRAD Report No. J6182, 1974.

APPENDIX

PLOTTED FORCE AND MOMENT DATA

This Page Intentionally Left Blank

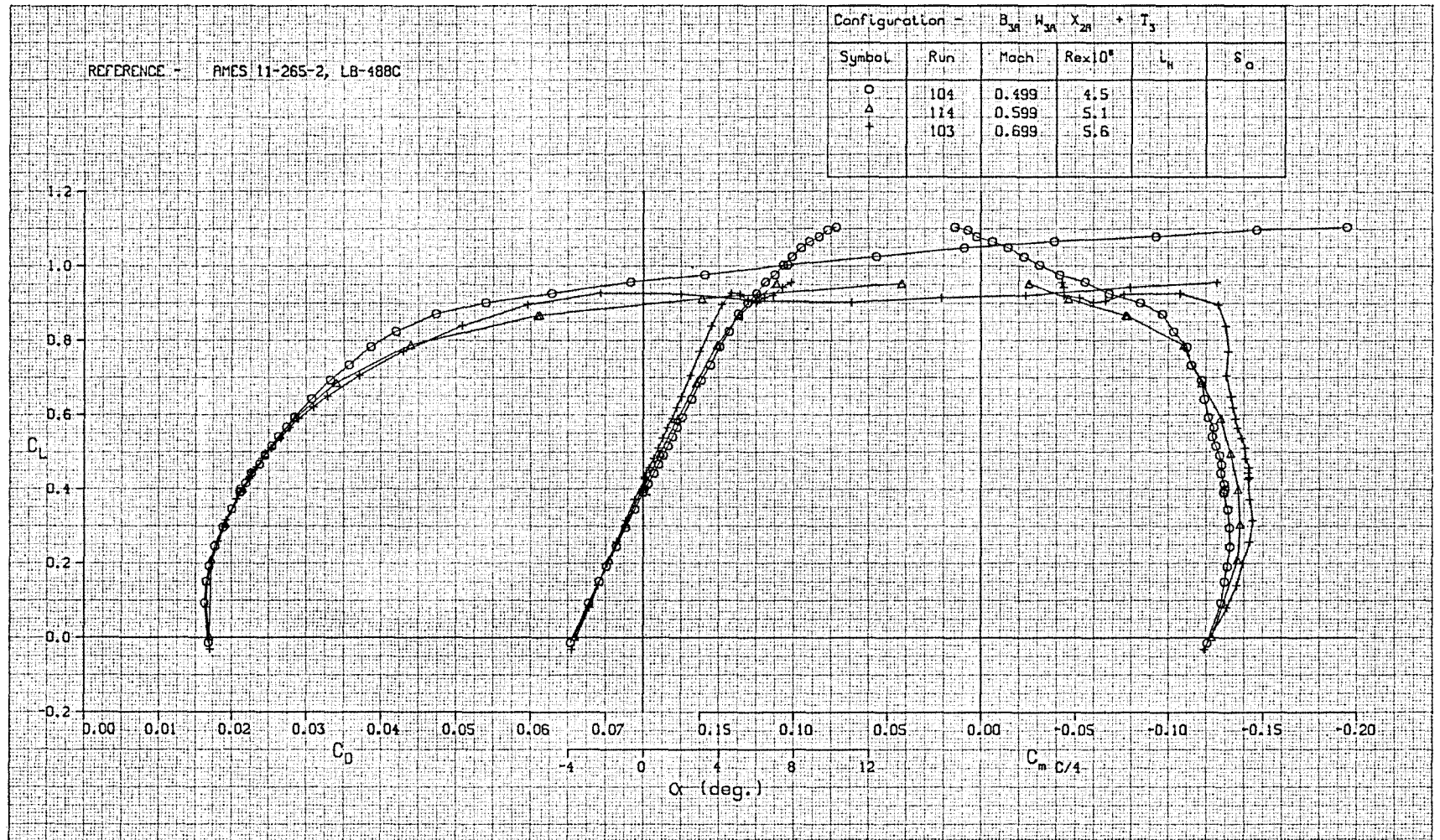


FIGURE A-1. LIFT, DRAG, AND PITCHING MOMENT CHARACTERISTICS OF WING W_{3A} , TRANSITION FIXED

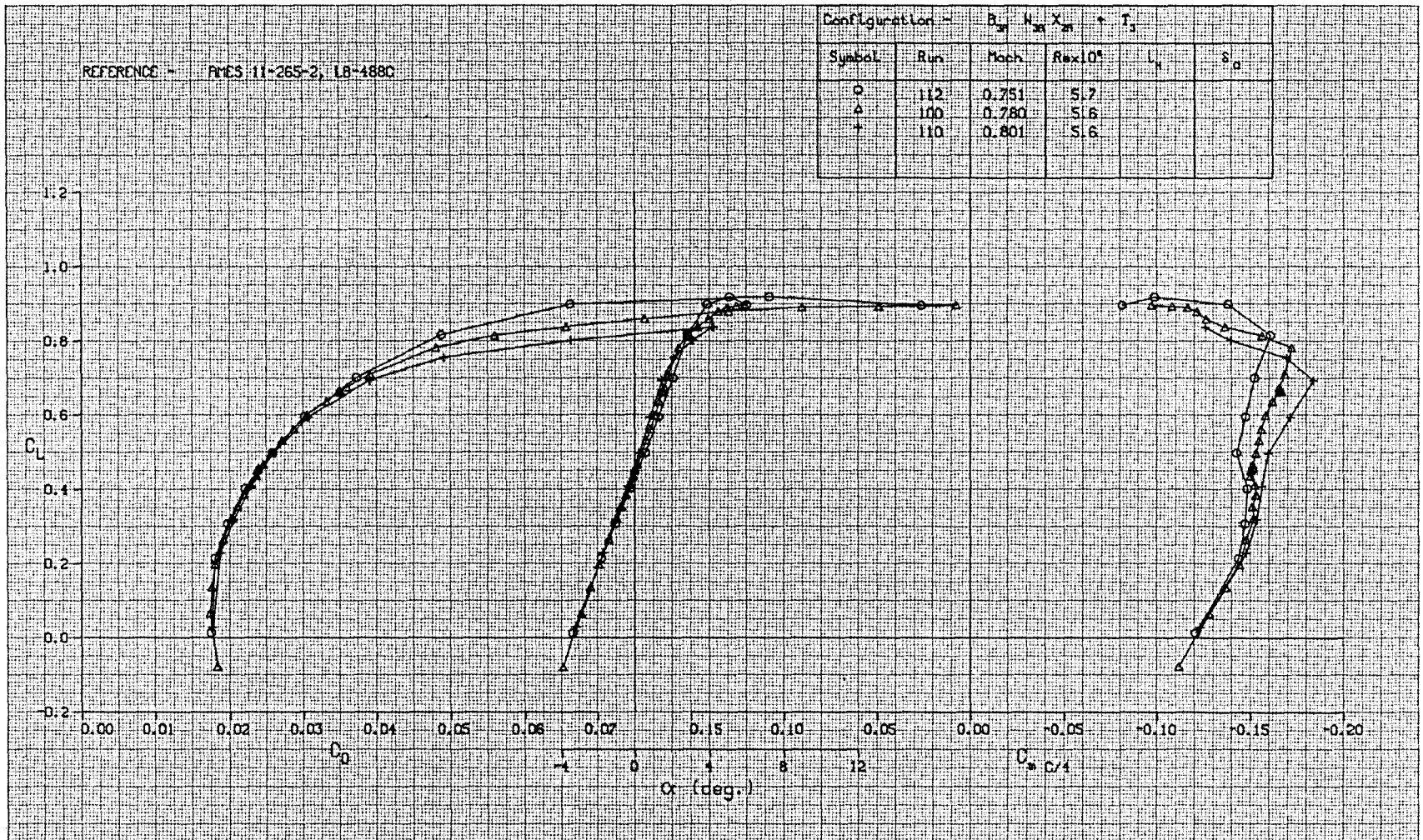


FIGURE A-2. LIFT, DRAG, AND PITCHING MOMENT CHARACTERISTICS OF WING W_{3A} , TRANSITION FIXED

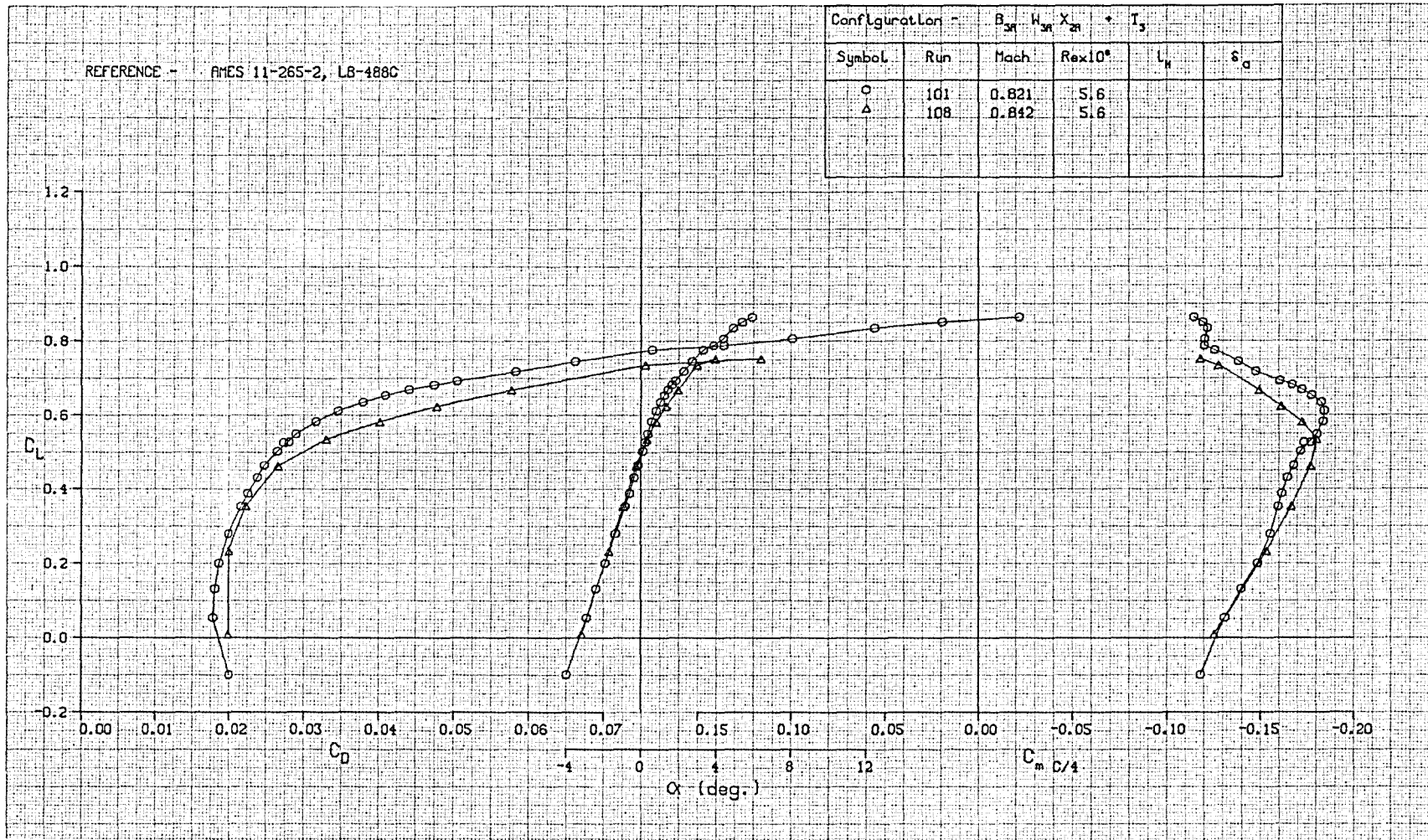


FIGURE A-3. LIFT, DRAG, AND PITCHING MOMENT CHARACTERISTICS OF WING W_{3A} , TRANSITION FIXED

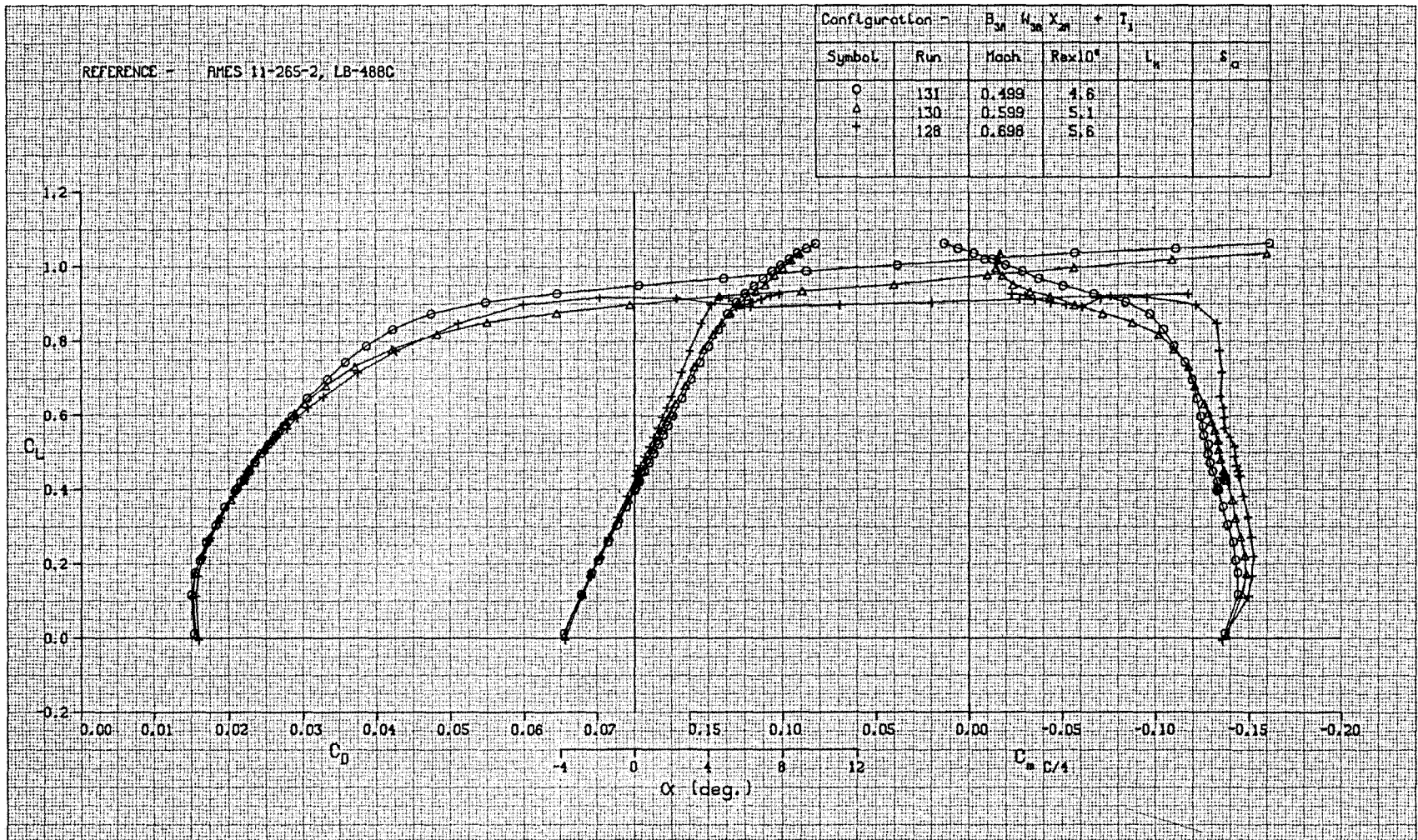


FIGURE A-4. LIFT, DRAG, AND PITCHING MOMENT CHARACTERISTICS OF WING W_{3A} , TRANSITION FREE

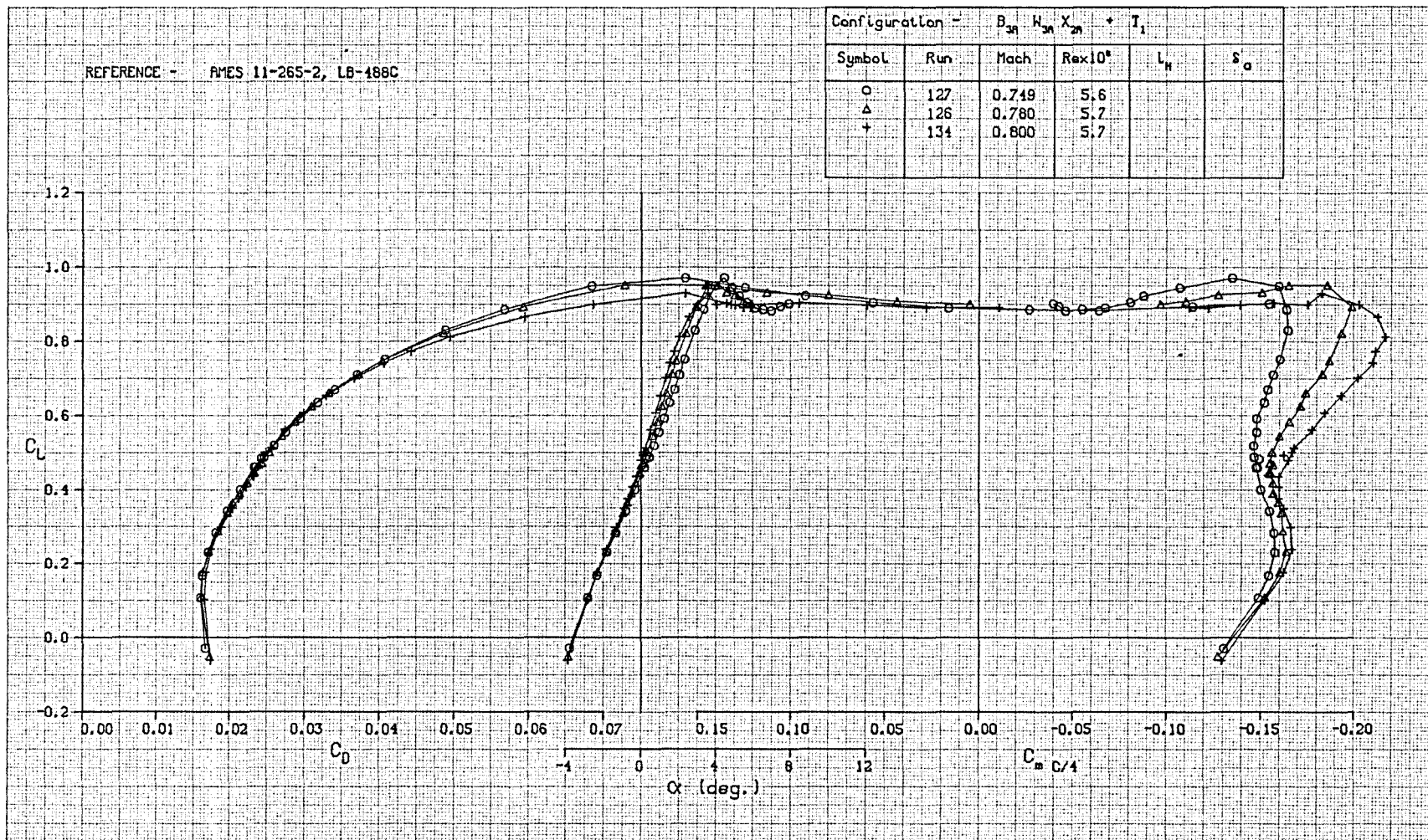


FIGURE A-5. LIFT, DRAG, AND PITCHING MOMENT CHARACTERISTICS OF WING W_{3A} , TRANSITION FREE

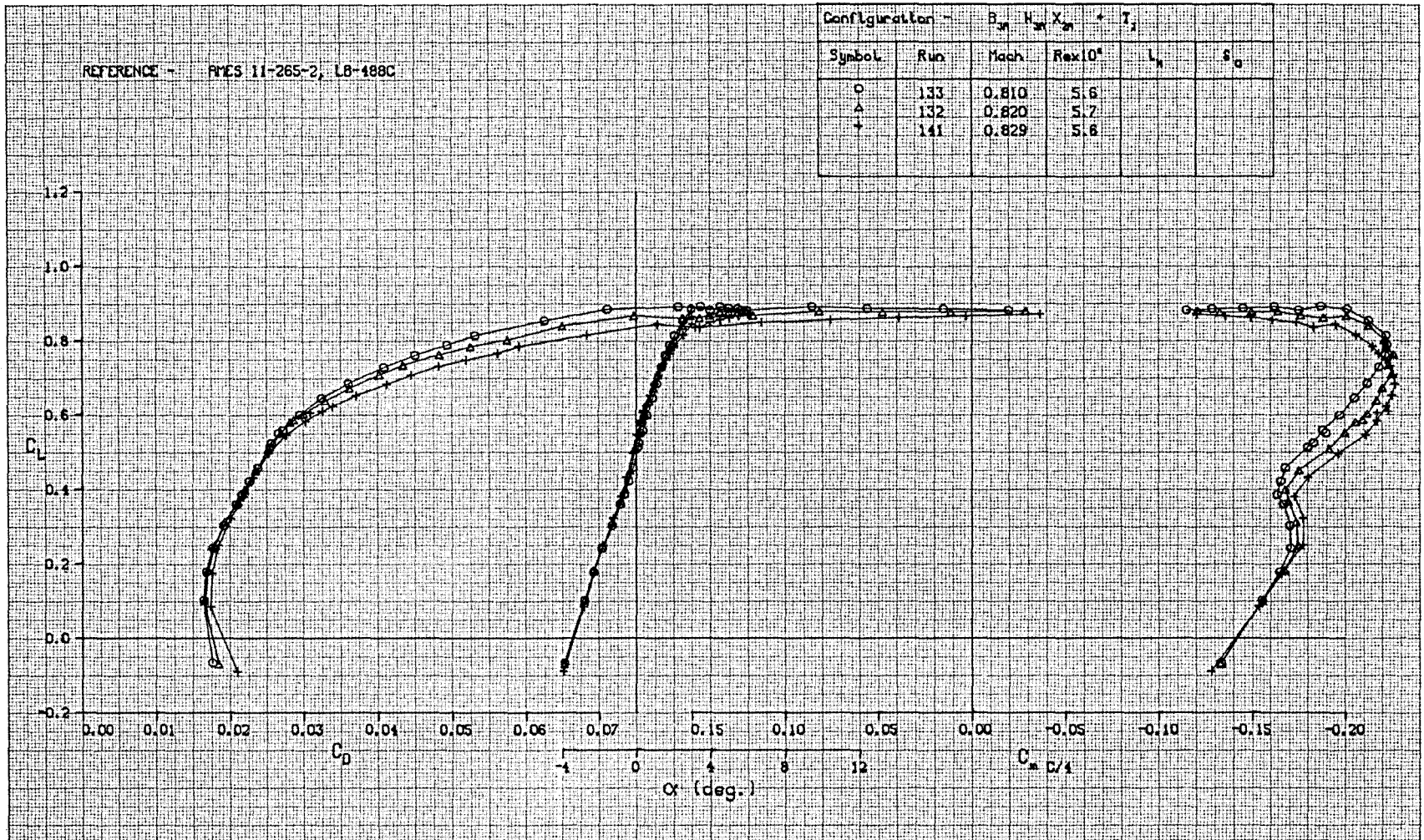


FIGURE A-6. LIFT, DRAG, AND PITCHING MOMENT CHARACTERISTICS OF WING W_{3A} , TRANSITION FREE

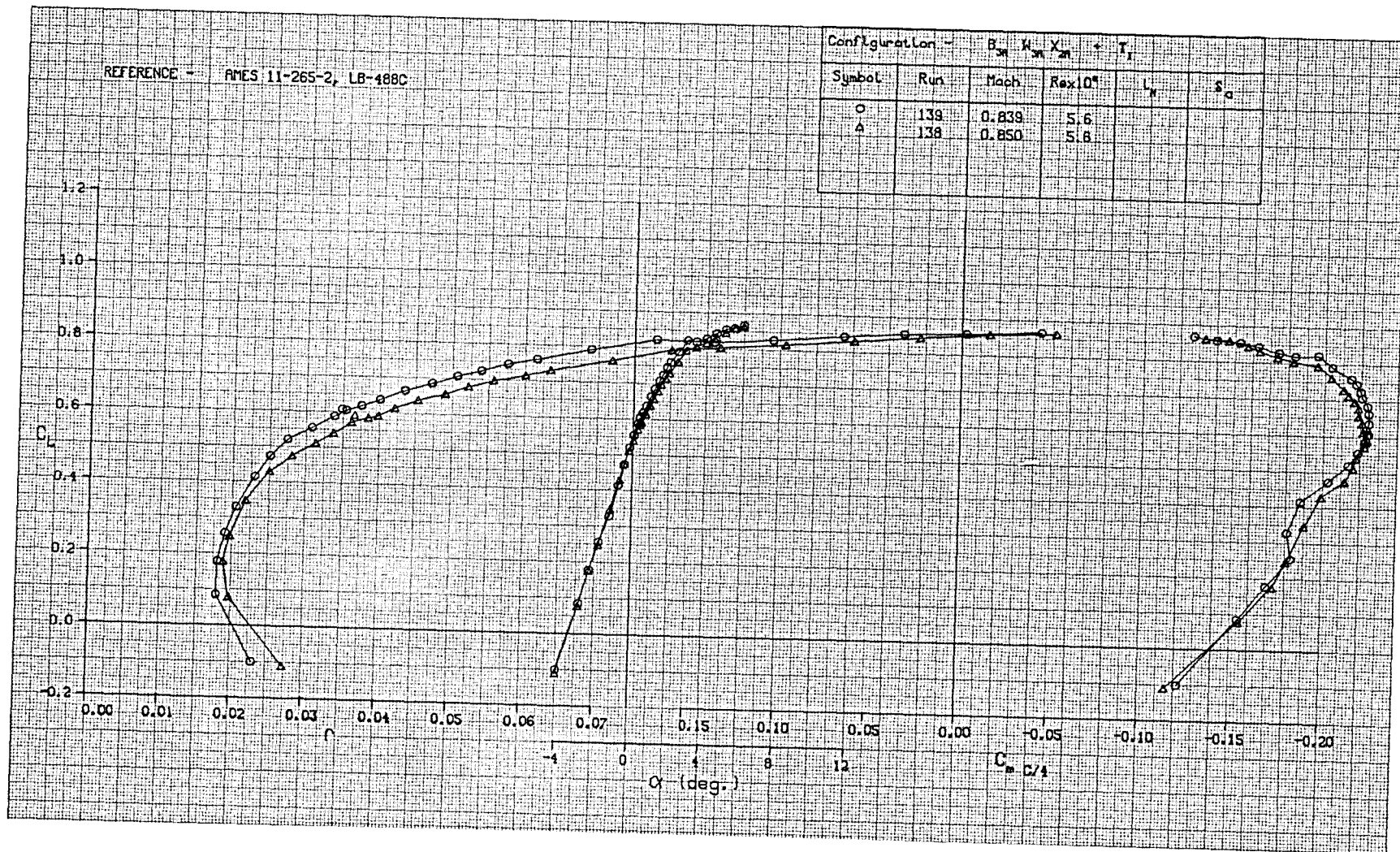


FIGURE A-7. LIFT, DRAG, AND PITCHING MOMENT CHARACTERISTICS OF WING W_{3A} , TRANSITION FREE

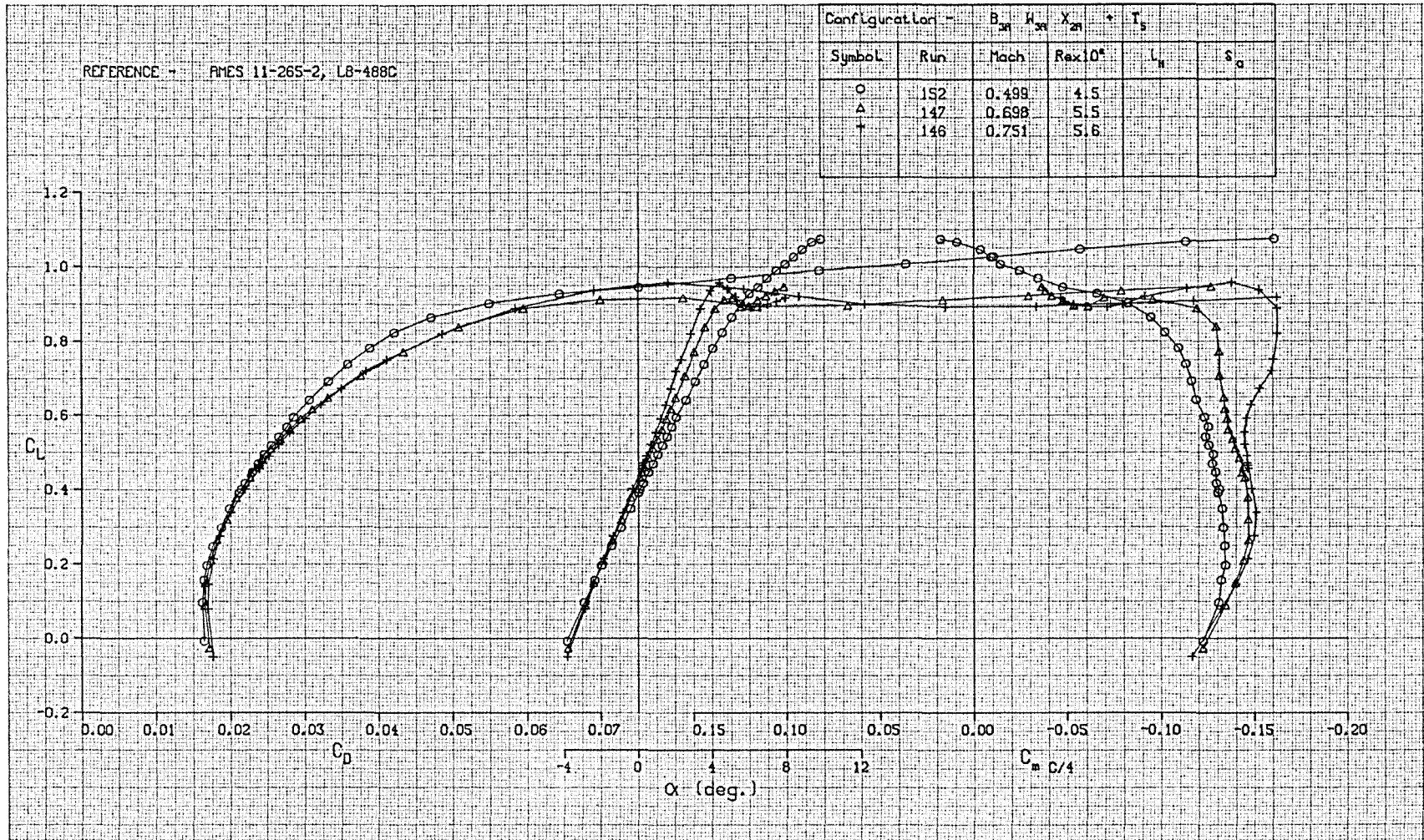


FIGURE A-8. LIFT, DRAG, AND PITCHING MOMENT CHARACTERISTICS OF WING W_{3A} , TRANSITION FIXED

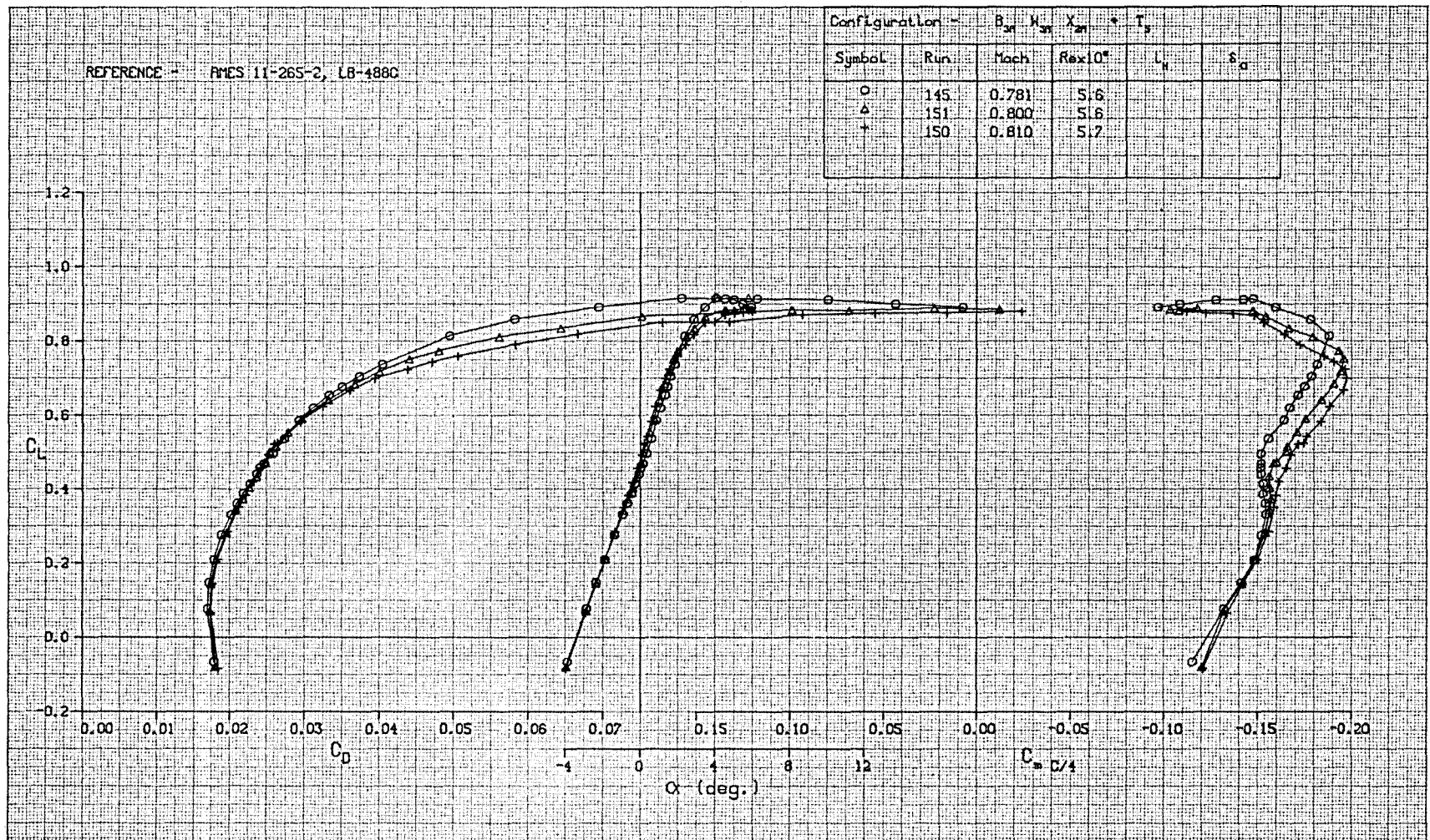


FIGURE A-9. LIFT, DRAG, AND PITCHING MOMENT CHARACTERISTICS OF WING W_{3A} , TRANSITION FIXED

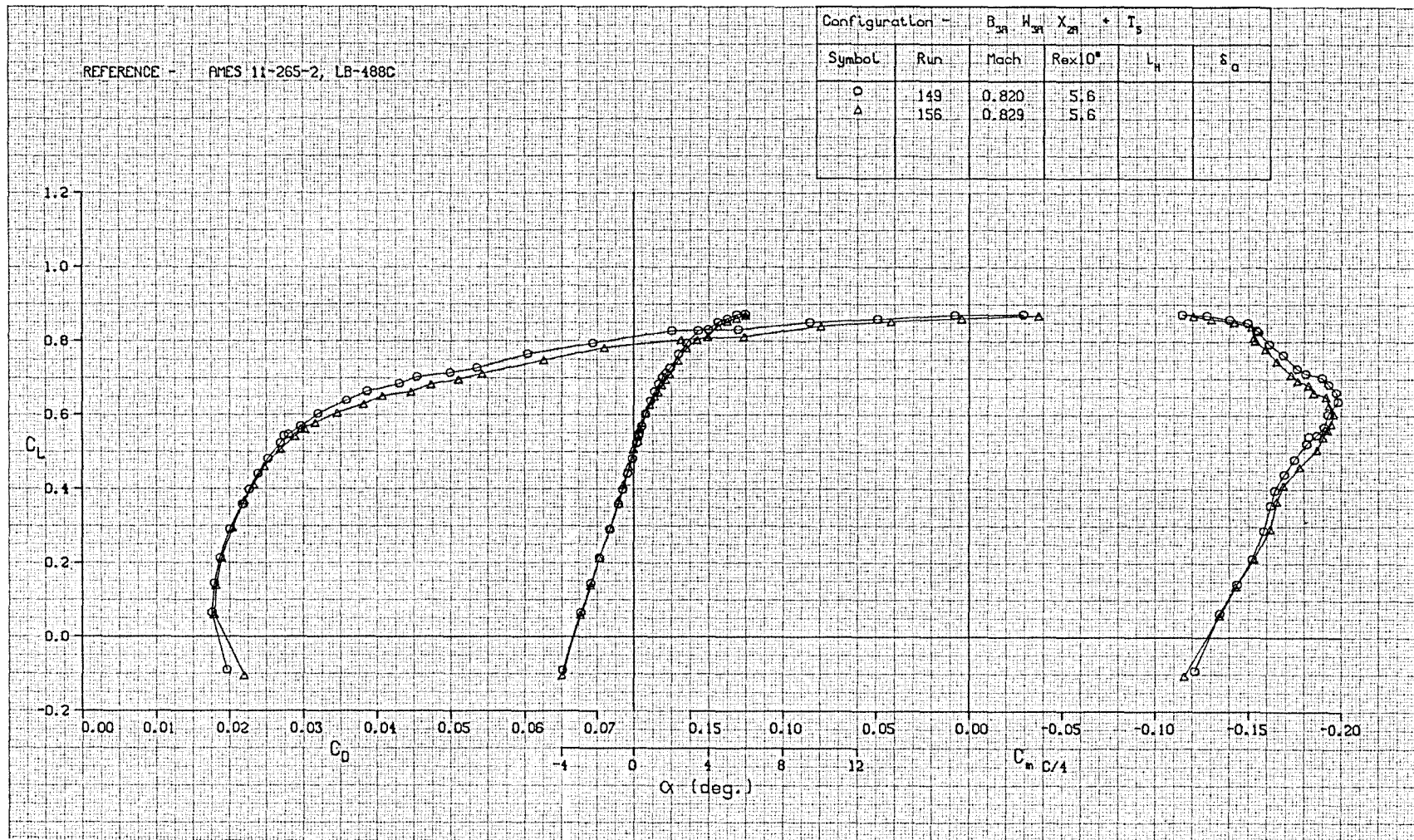


FIGURE A-10. LIFT, DRAG, AND PITCHING MOMENT CHARACTERISTICS OF WING W_{3A} , TRANSITION FIXED

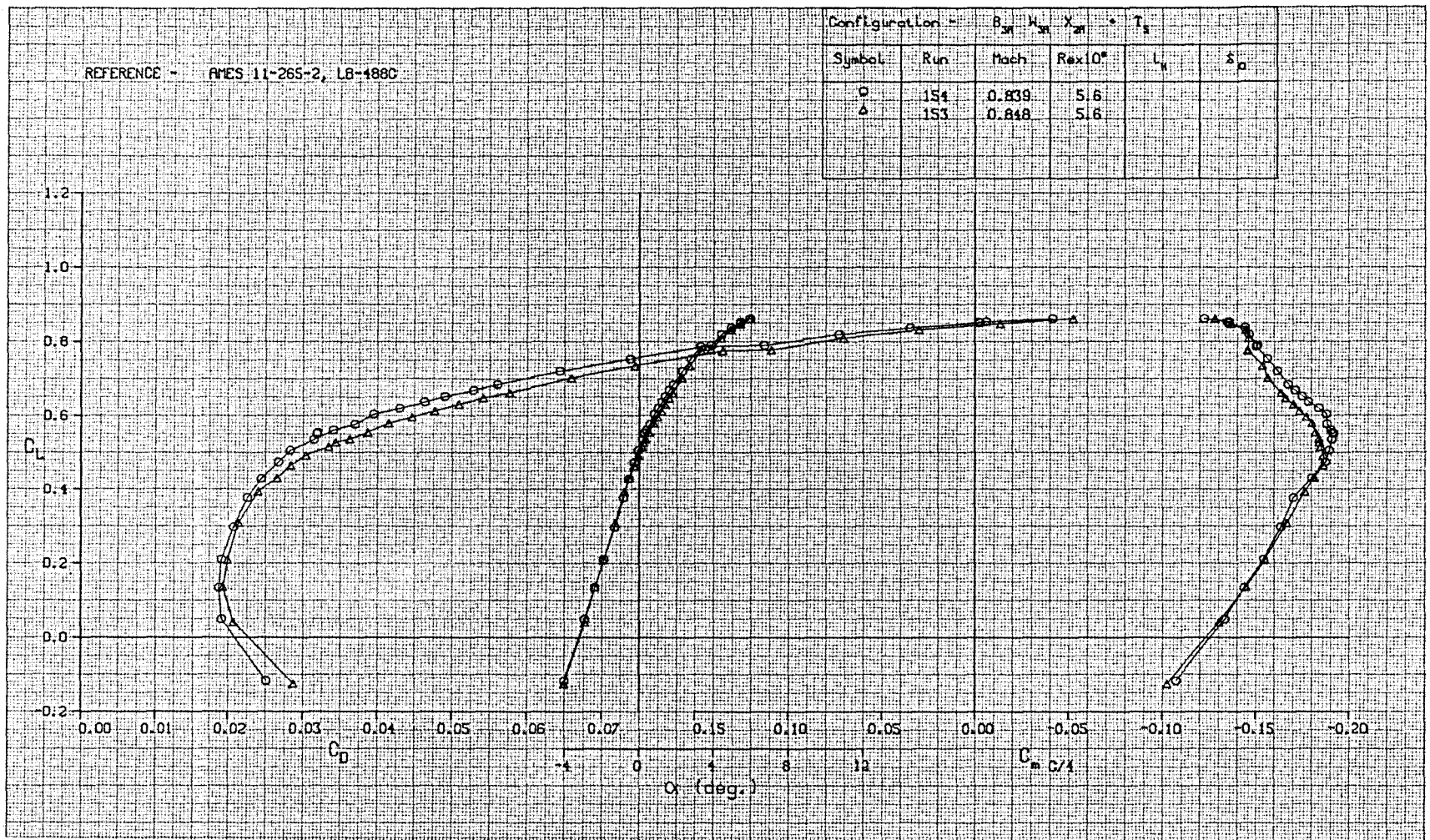


FIGURE A-11. LIFT, DRAG, AND PITCHING MOMENT CHARACTERISTICS OF WING W_{3A} , TRANSITION FIXED

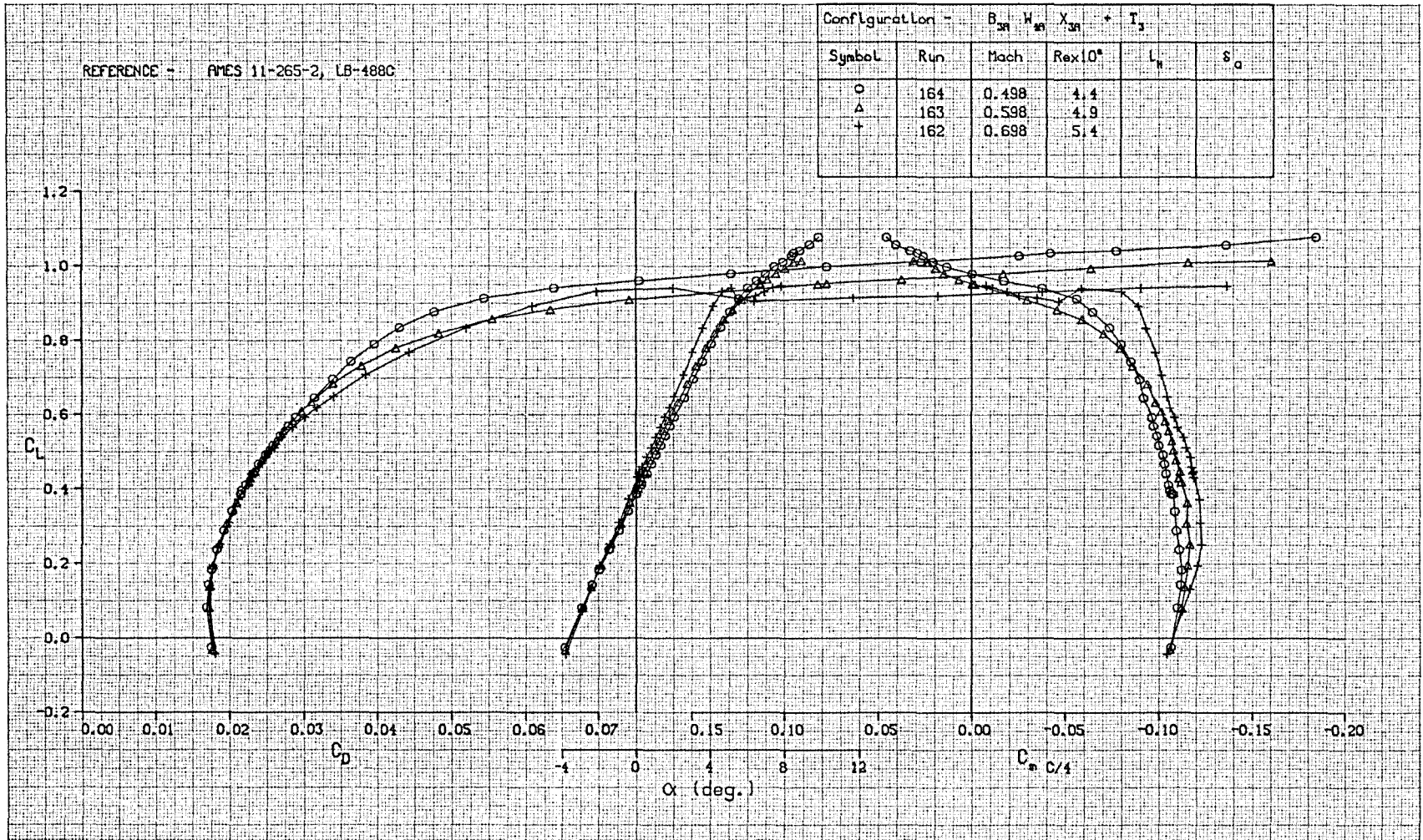


FIGURE A-12. LIFT, DRAG, AND PITCHING MOMENT CHARACTERISTICS OF WING W_{4A} , TRANSITION FIXED

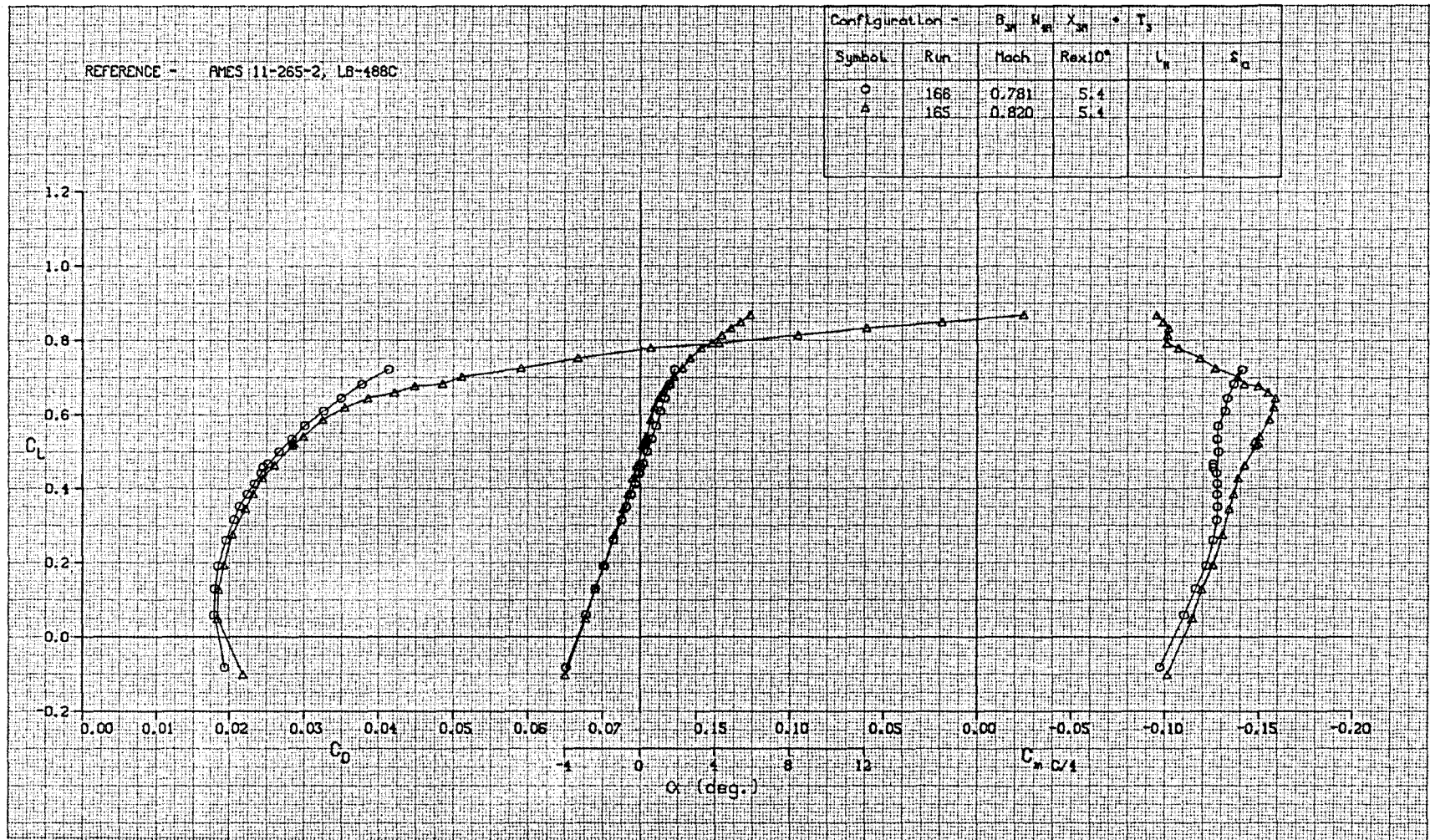


FIGURE A-13. LIFT, DRAG, AND PITCHING MOMENT CHARACTERISTICS OF WING W_{4A}, TRANSITION FIXED

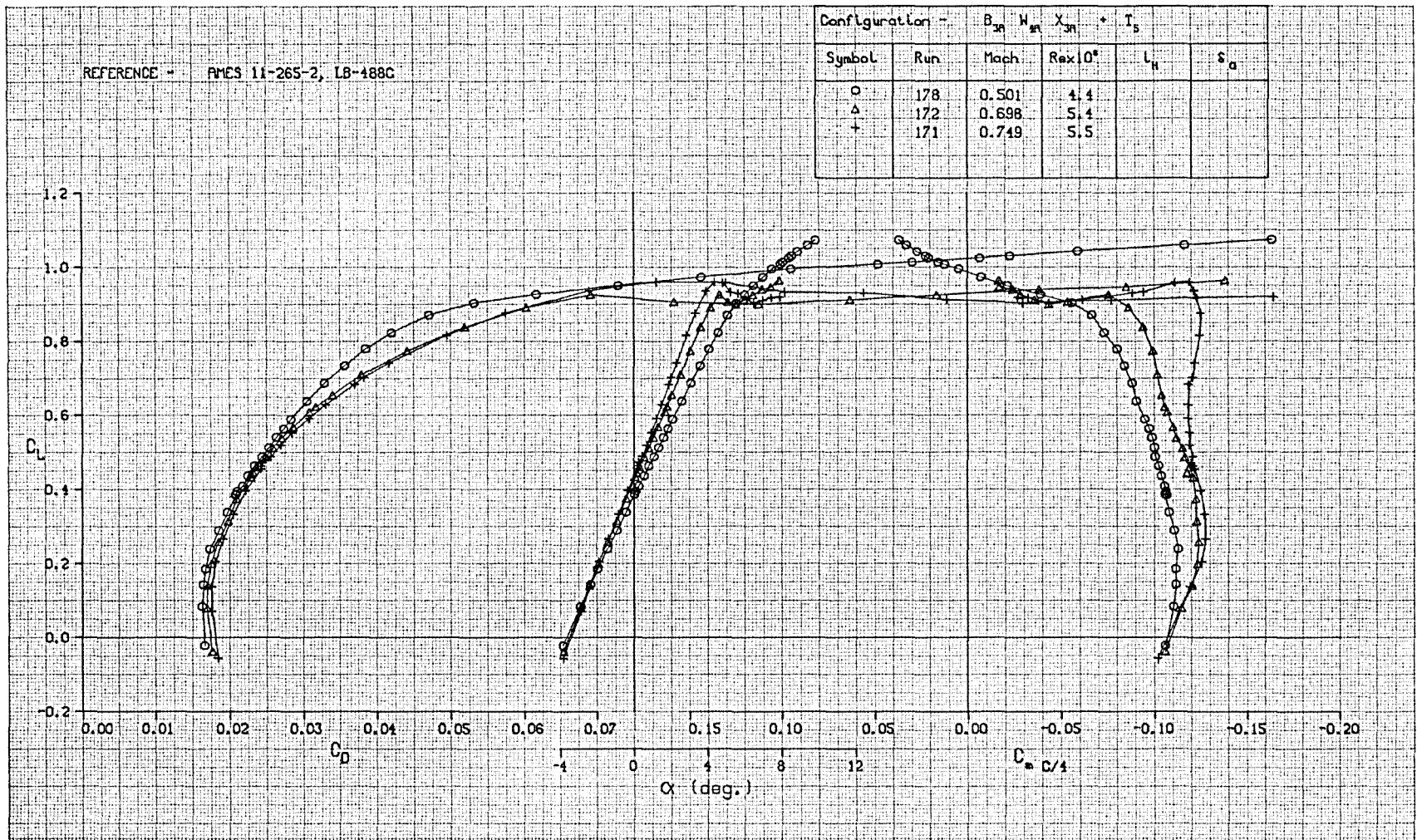


FIGURE A-14. LIFT, DRAG, AND PITCHING MOMENT CHARACTERISTICS OF WING W_{4A} , TRANSITION FIXED

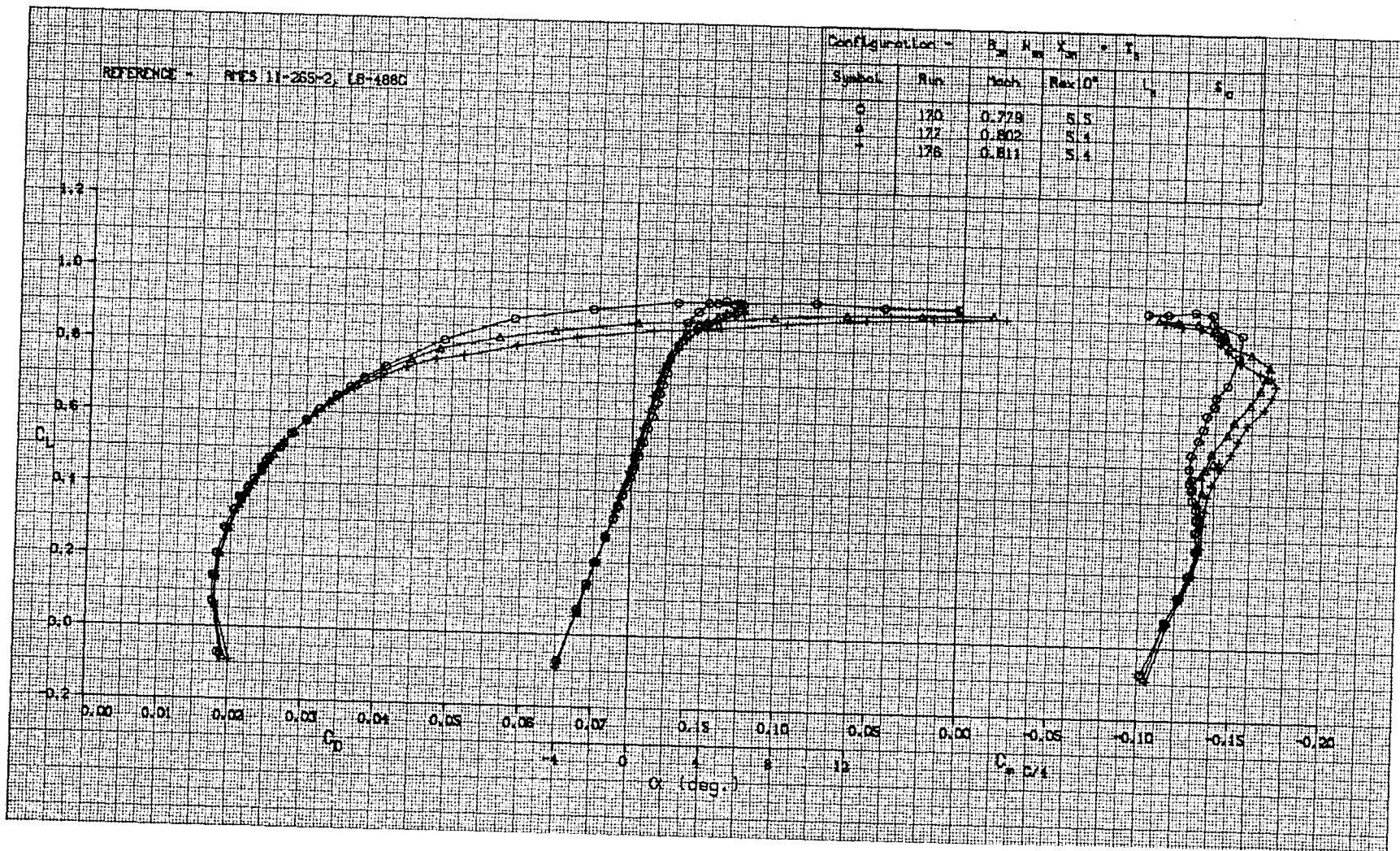


FIGURE A-15. LIFT, DRAG, AND PITCHING MOMENT CHARACTERISTICS OF WING W_{4A} , TRANSITION FIXED

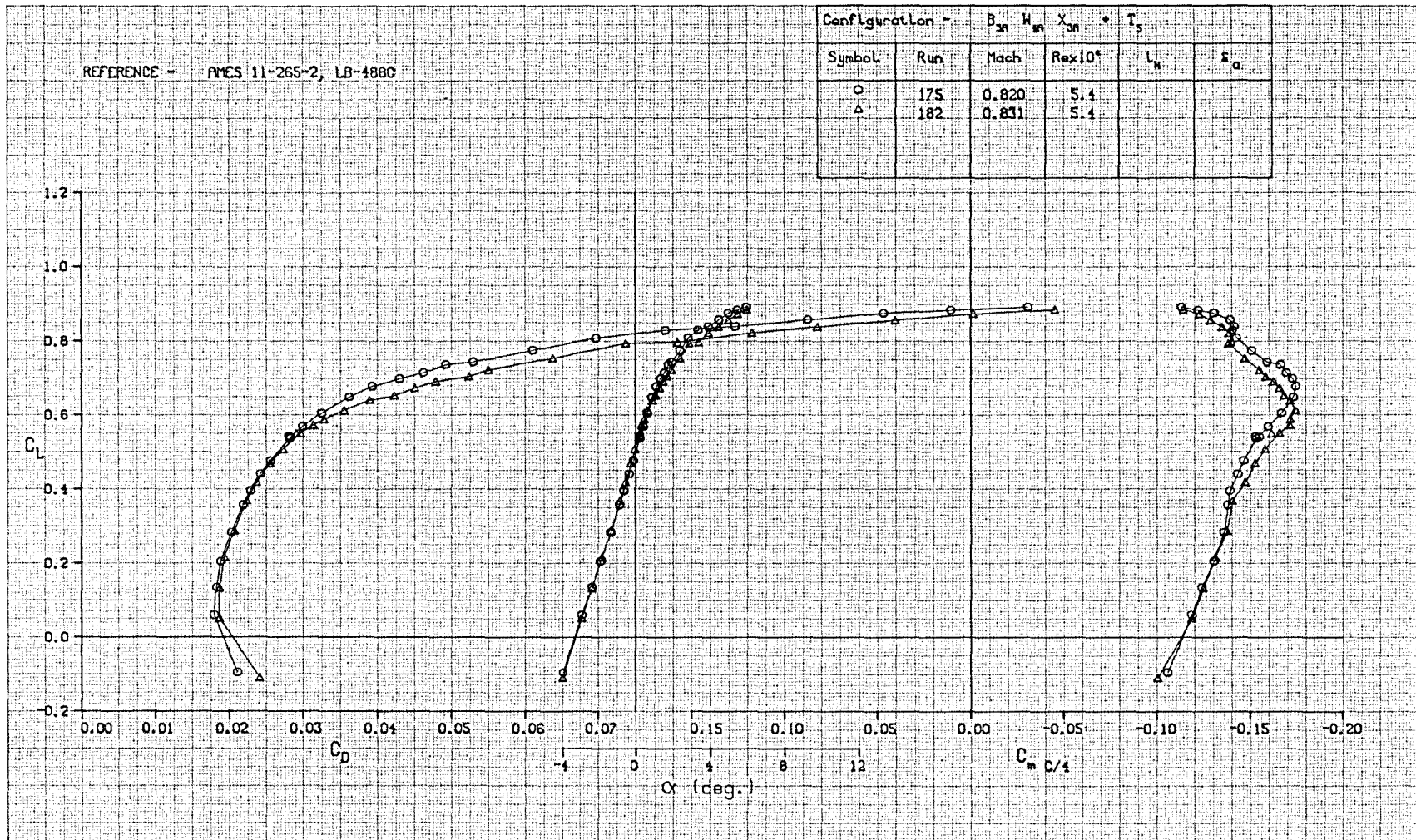


FIGURE A-16. LIFT, DRAG, AND PITCHING MOMENT CHARACTERISTICS OF WING W_{4A}, TRANSITION FIXED

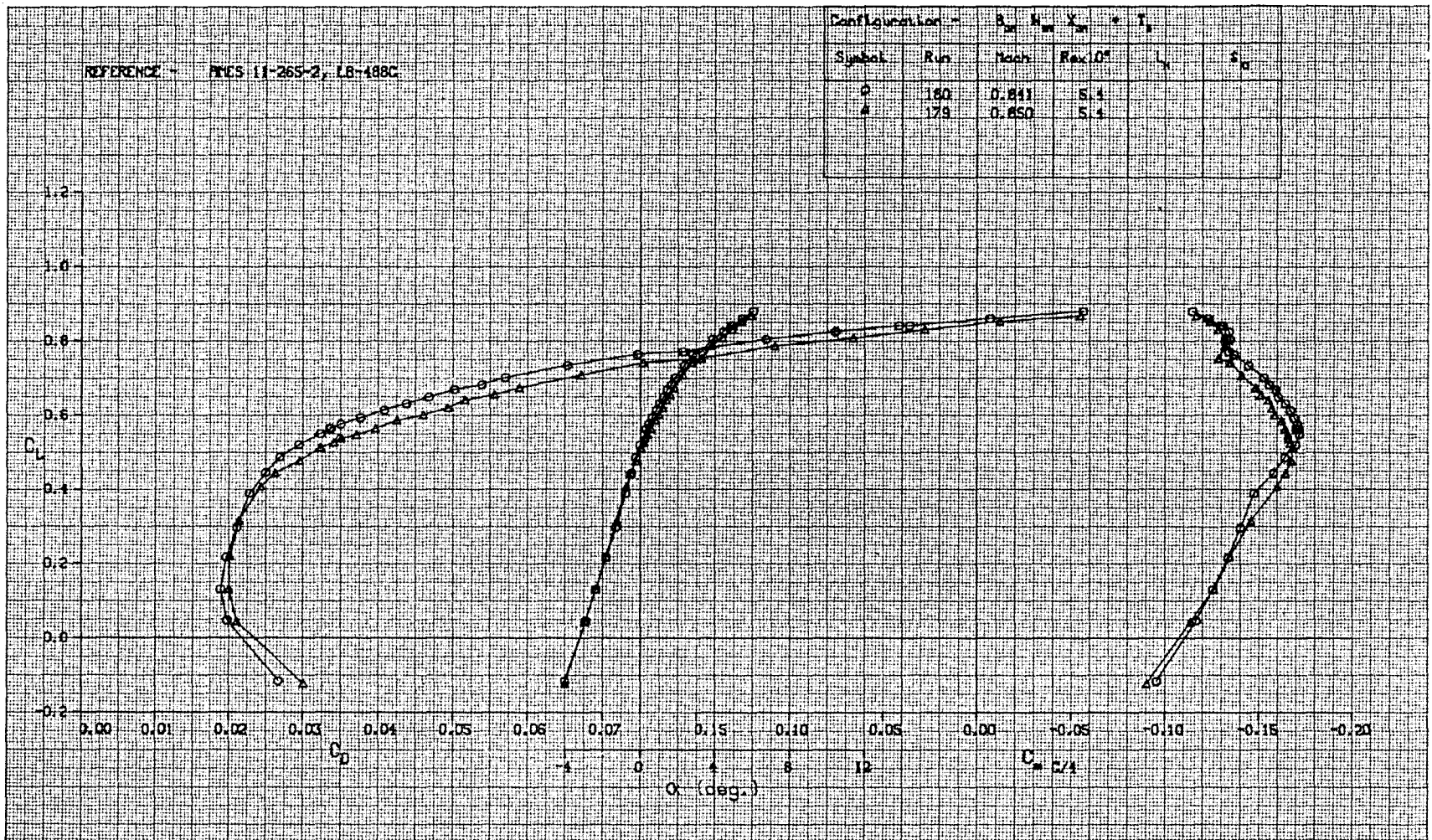


FIGURE A-17. LIFT, DRAG, AND PITCHING MOMENT CHARACTERISTICS OF WING W_{4A} , TRANSITION FIXED

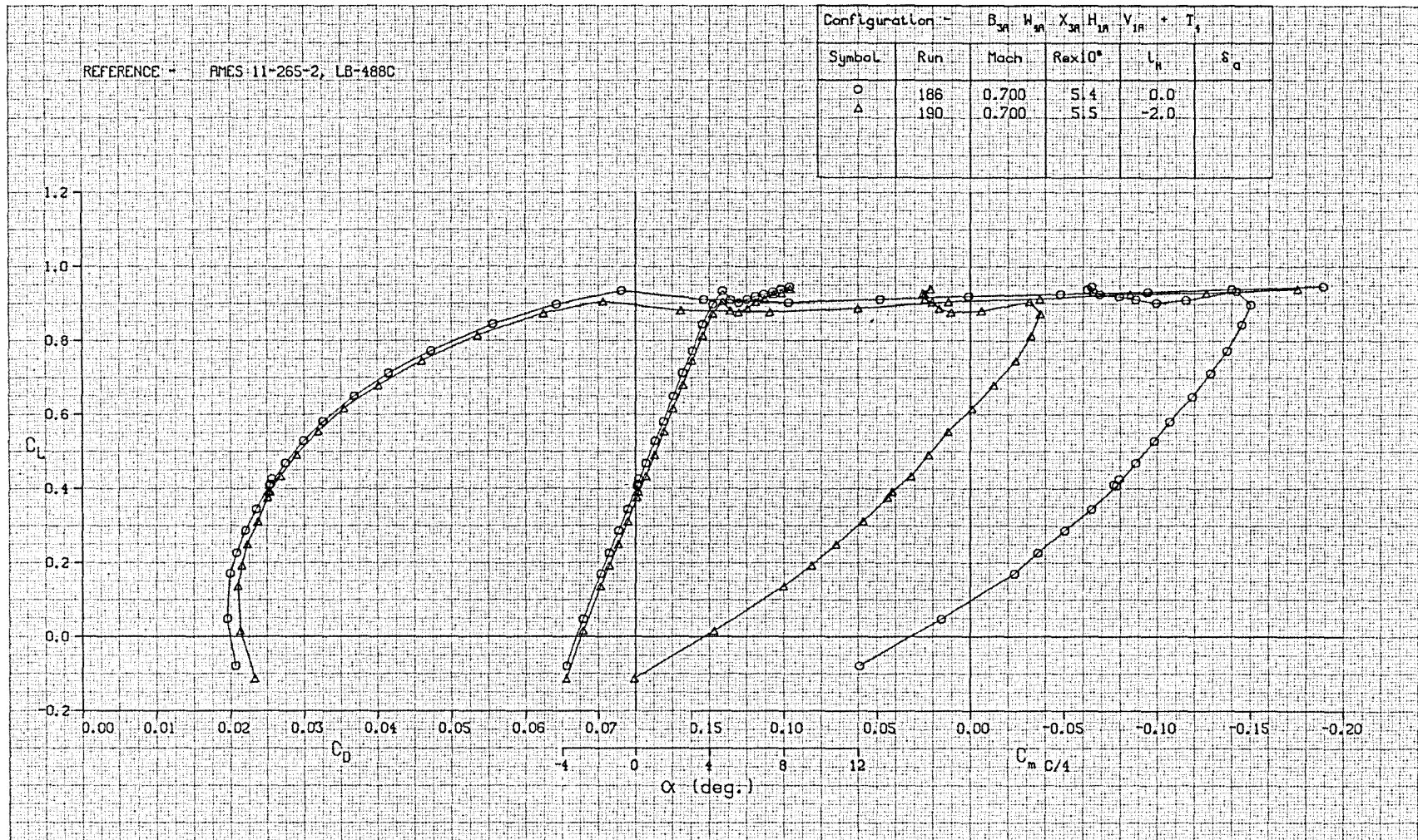


FIGURE A-18. LIFT, DRAG, AND PITCHING MOMENT CHARACTERISTICS OF WING W_{4A} AND TAIL, TRANSITION FREE

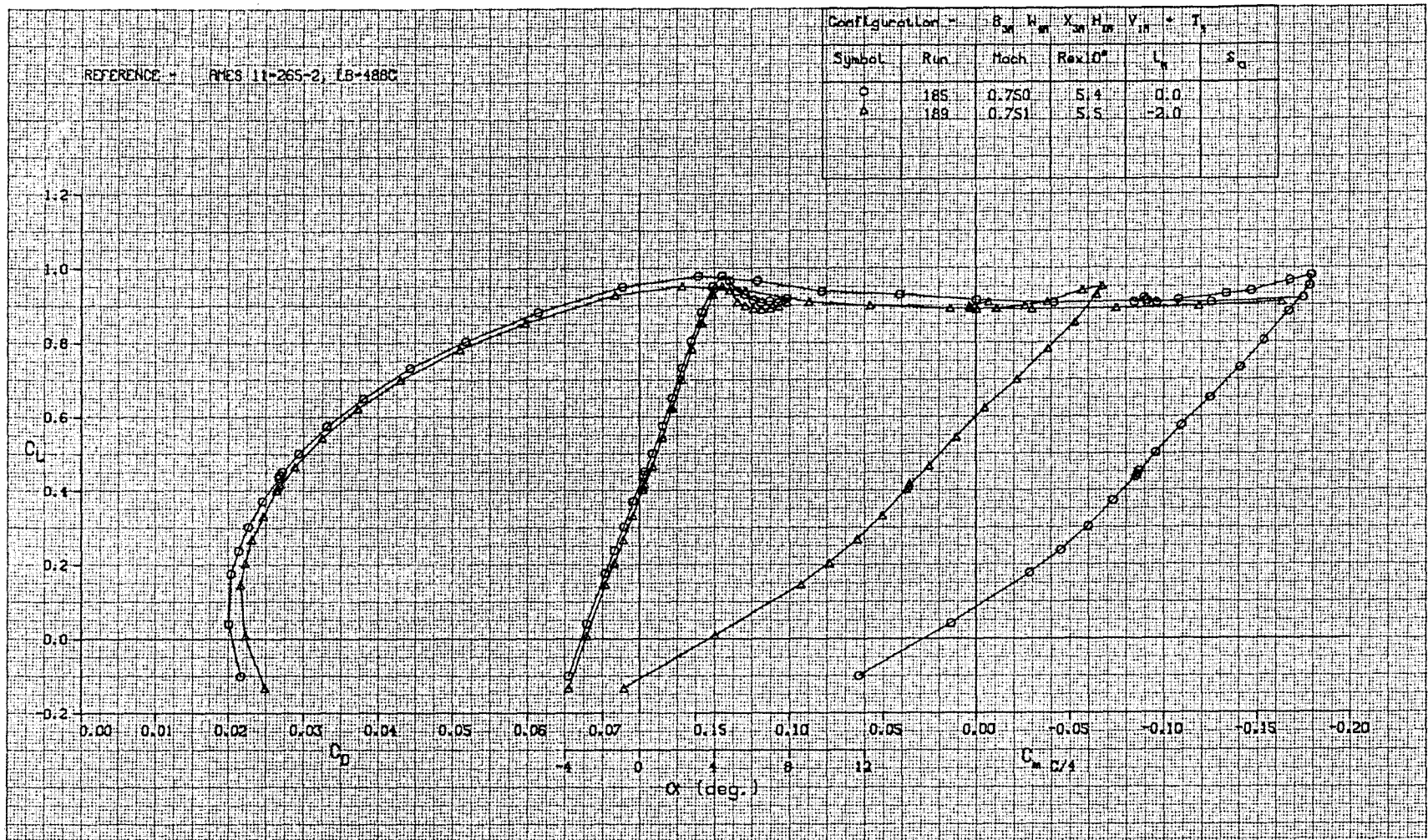


FIGURE A-19. LIFT, DRAG, AND PITCHING MOMENT CHARACTERISTICS OF WING W_{4A} AND TAIL, TRANSITION FREE

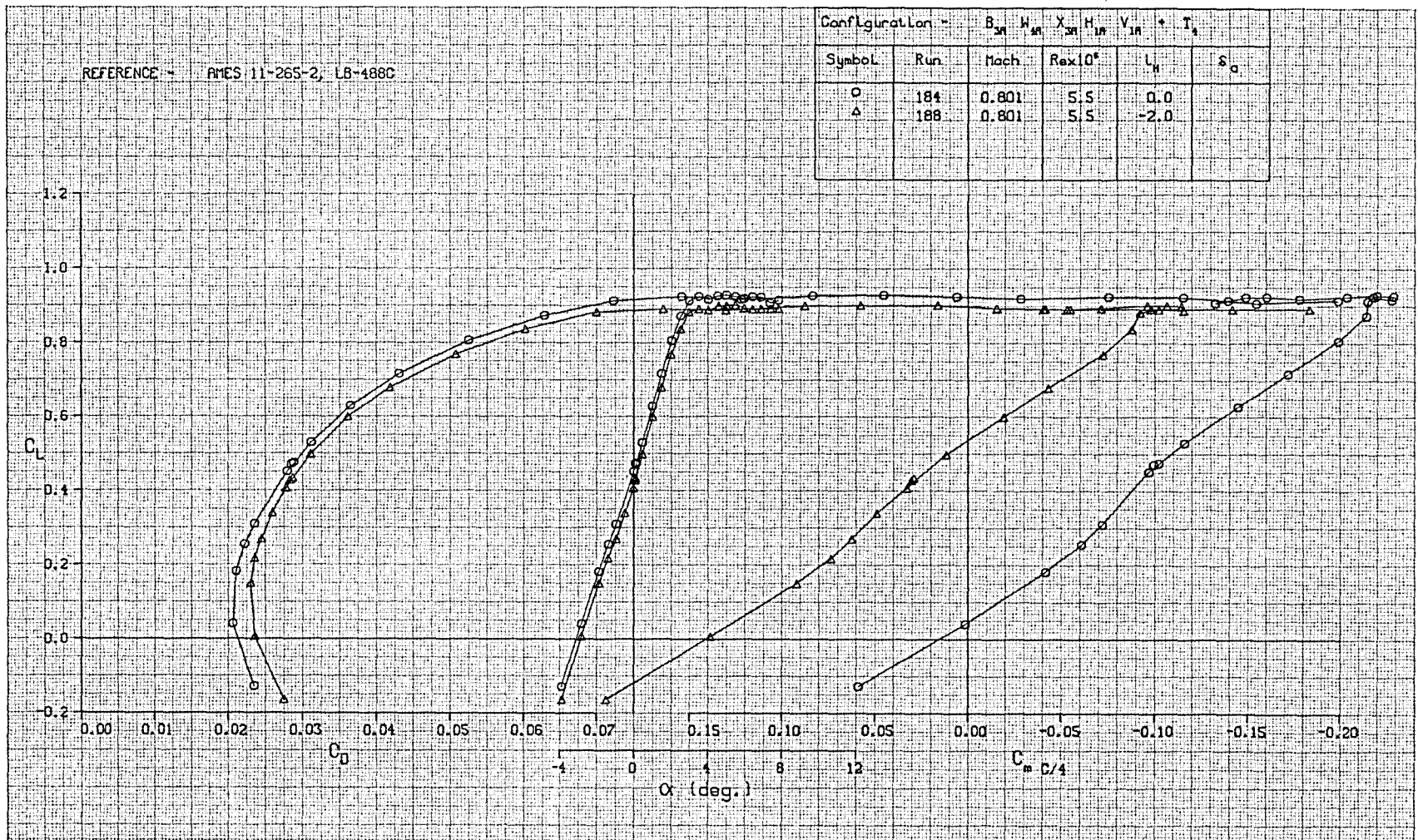


FIGURE A-20. LIFT, DRAG, AND PITCHING MOMENT CHARACTERISTICS OF WING W_{4A} AND TAIL, TRANSITION FREE

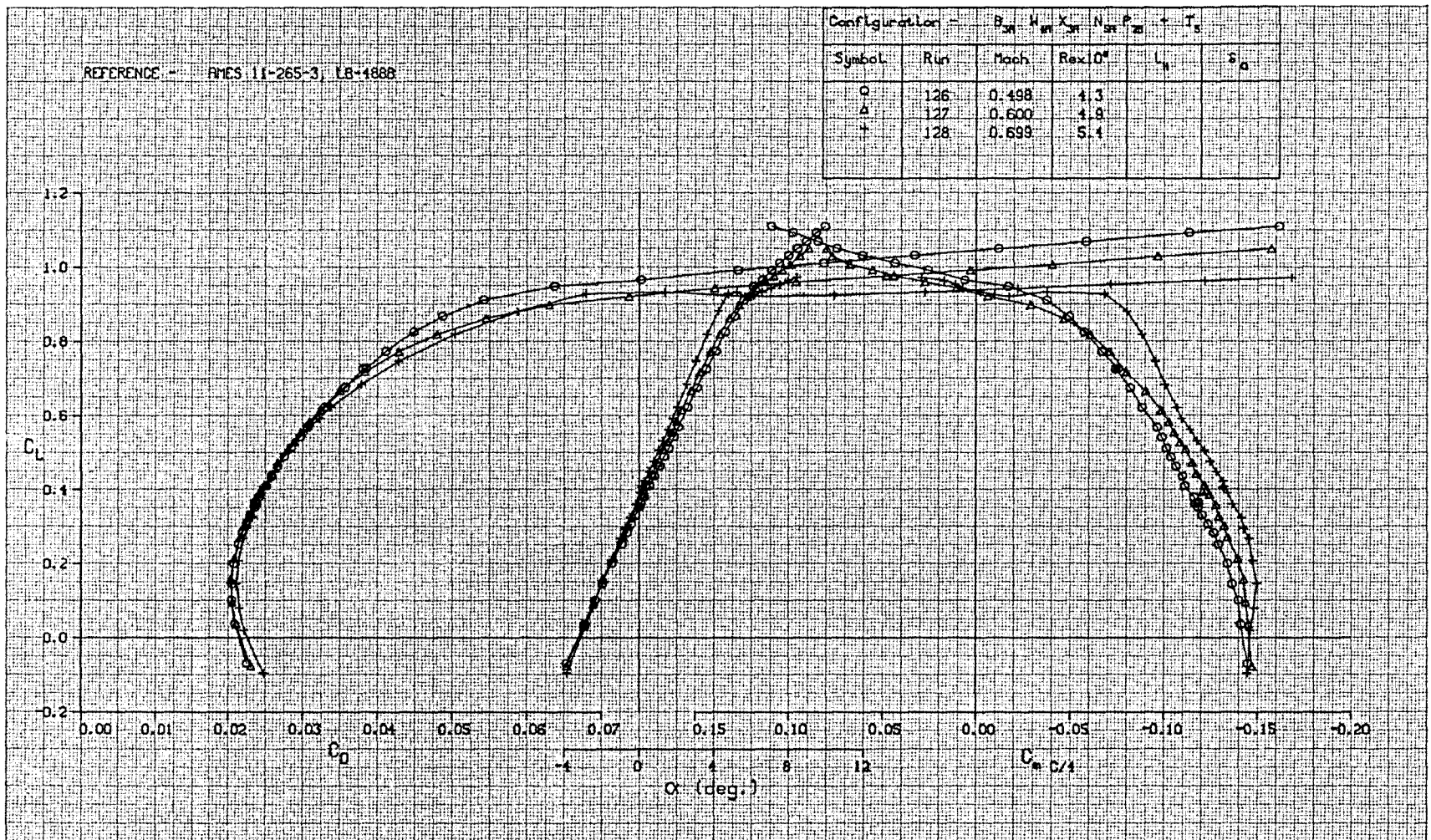


FIGURE A-21. LIFT, DRAG, AND PITCHING MOMENT CHARACTERISTICS OF WING W_{4A} WITH NACELLES AND PYLONS, TRANSITION FIXED

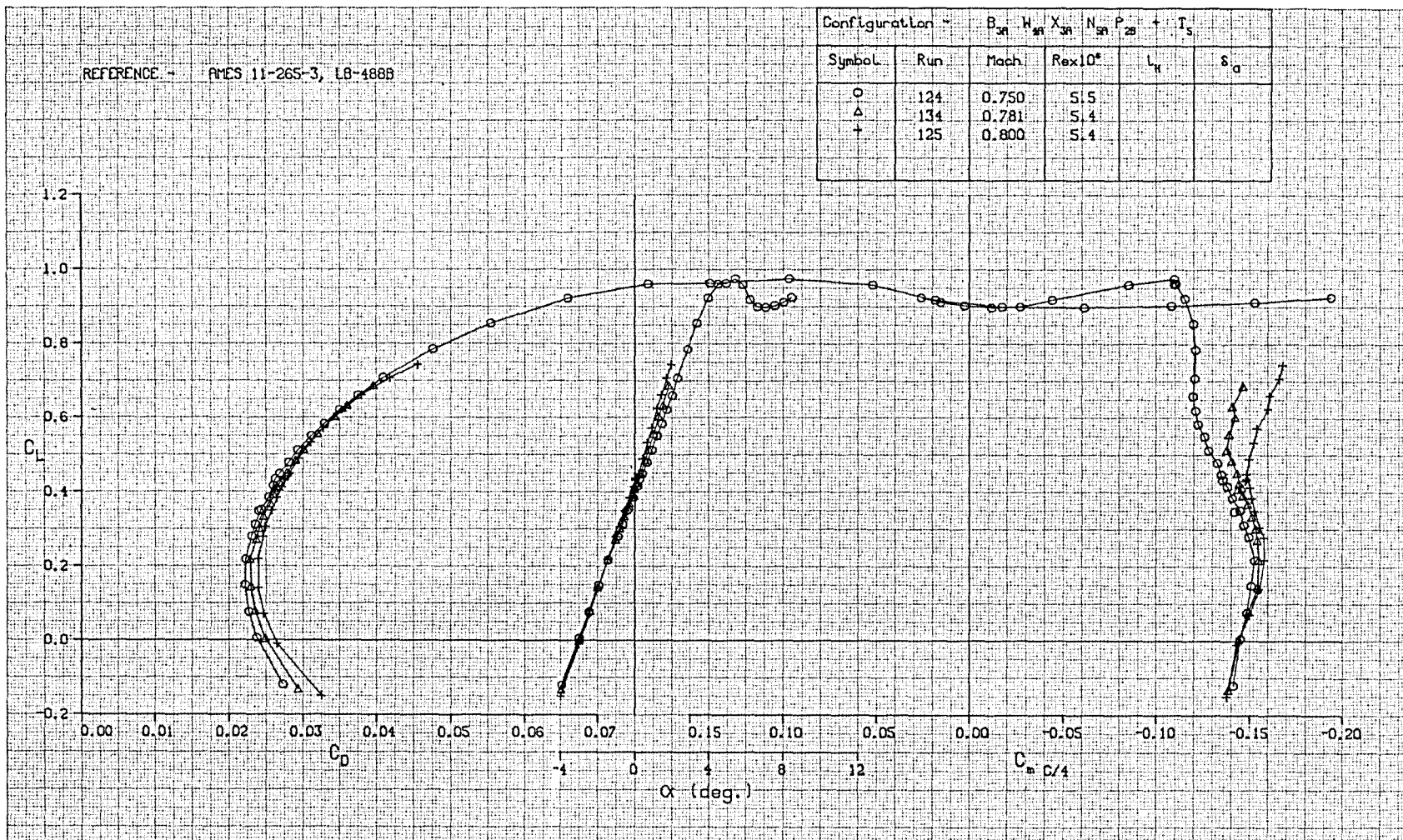


FIGURE A-22. LIFT, DRAG, AND PITCHING MOMENT CHARACTERISTICS OF WING W_{4A} WITH NACELLES AND PYLONS, TRANSITION FIXED

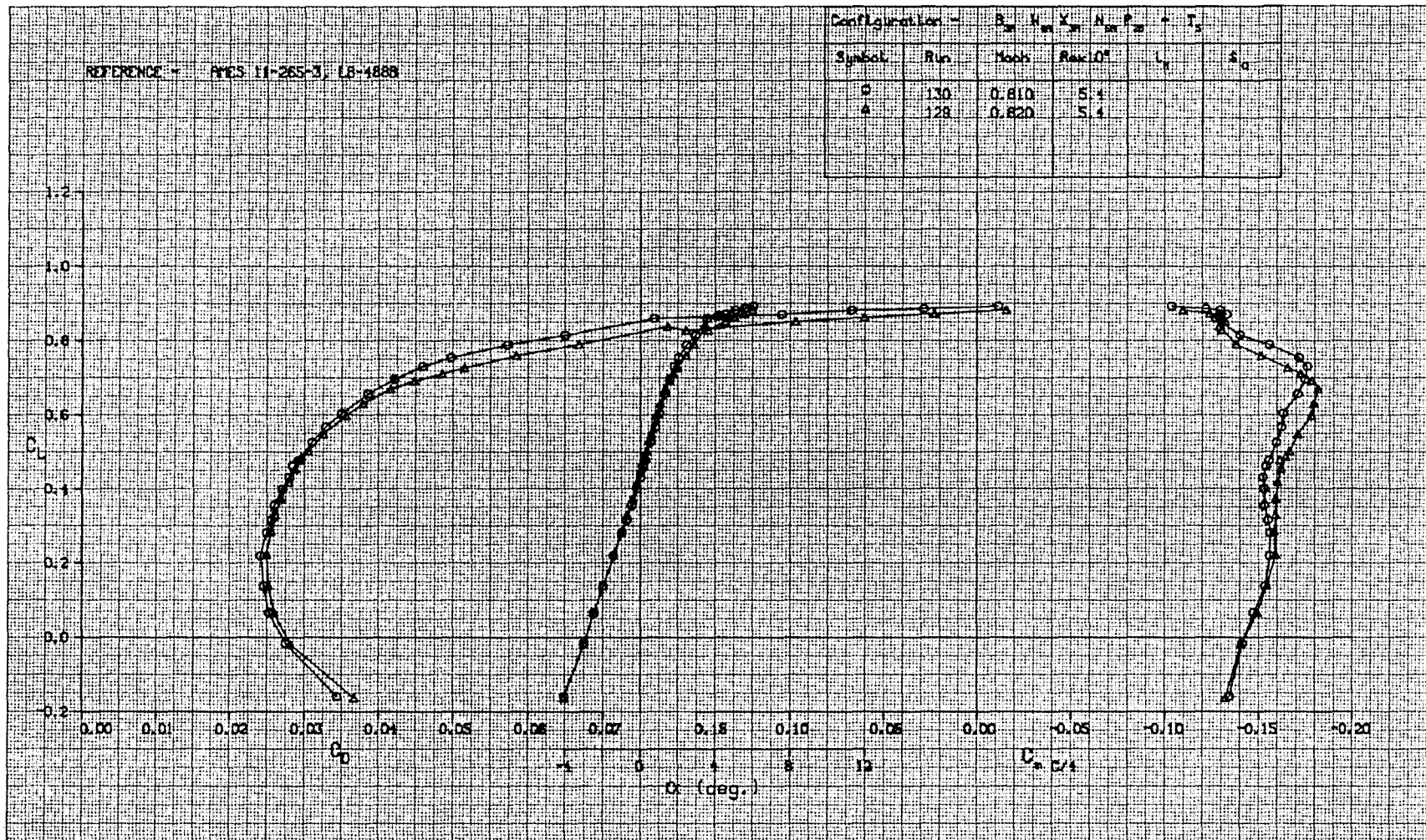


FIGURE A-23. LIFT, DRAG, AND PITCHING MOMENT CHARACTERISTICS OF WING W_{4A} WITH NACELLES AND PYLONS, TRANSITION FIXED

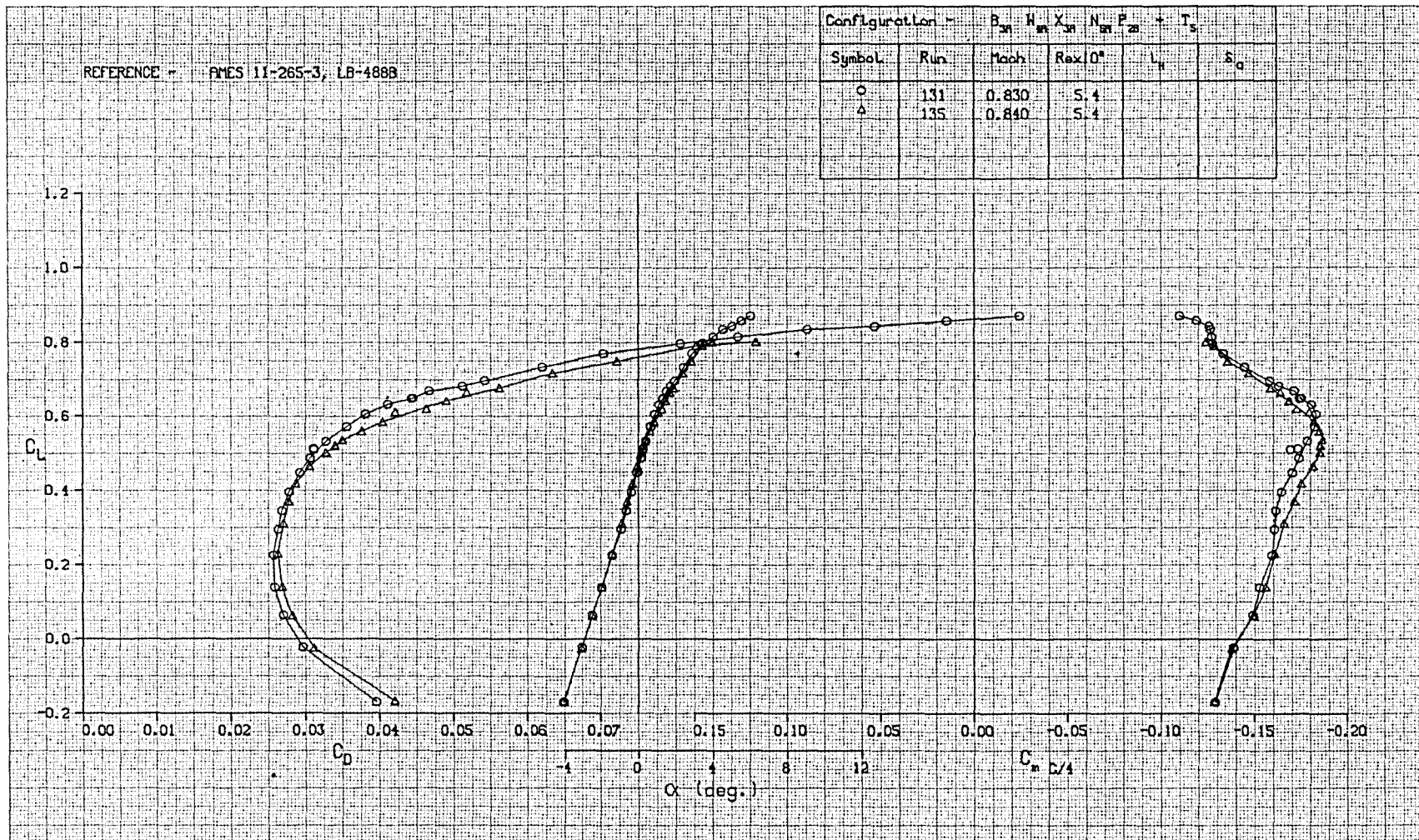


FIGURE A-24. LIFT, DRAG, AND PITCHING MOMENT CHARACTERISTICS OF WING W_{4A} WITH NACELLES AND PYLONS, TRANSITION FIXED

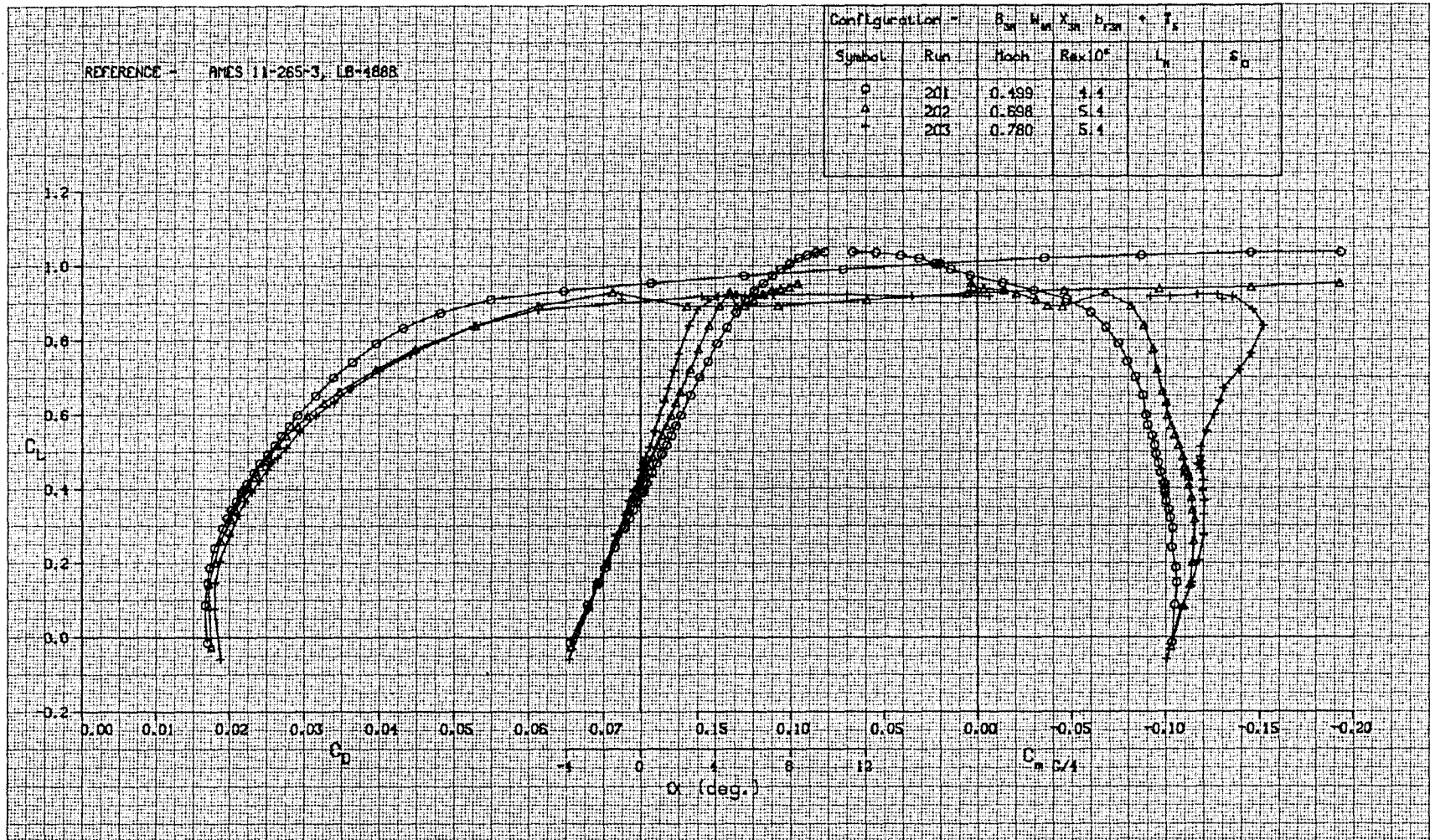


FIGURE A-25. LIFT, DRAG, AND PITCHING MOMENT CHARACTERISTICS OF WING W_{4A} WITH FLAP LINKAGE FAIRINGS, TRANSITION FIXED

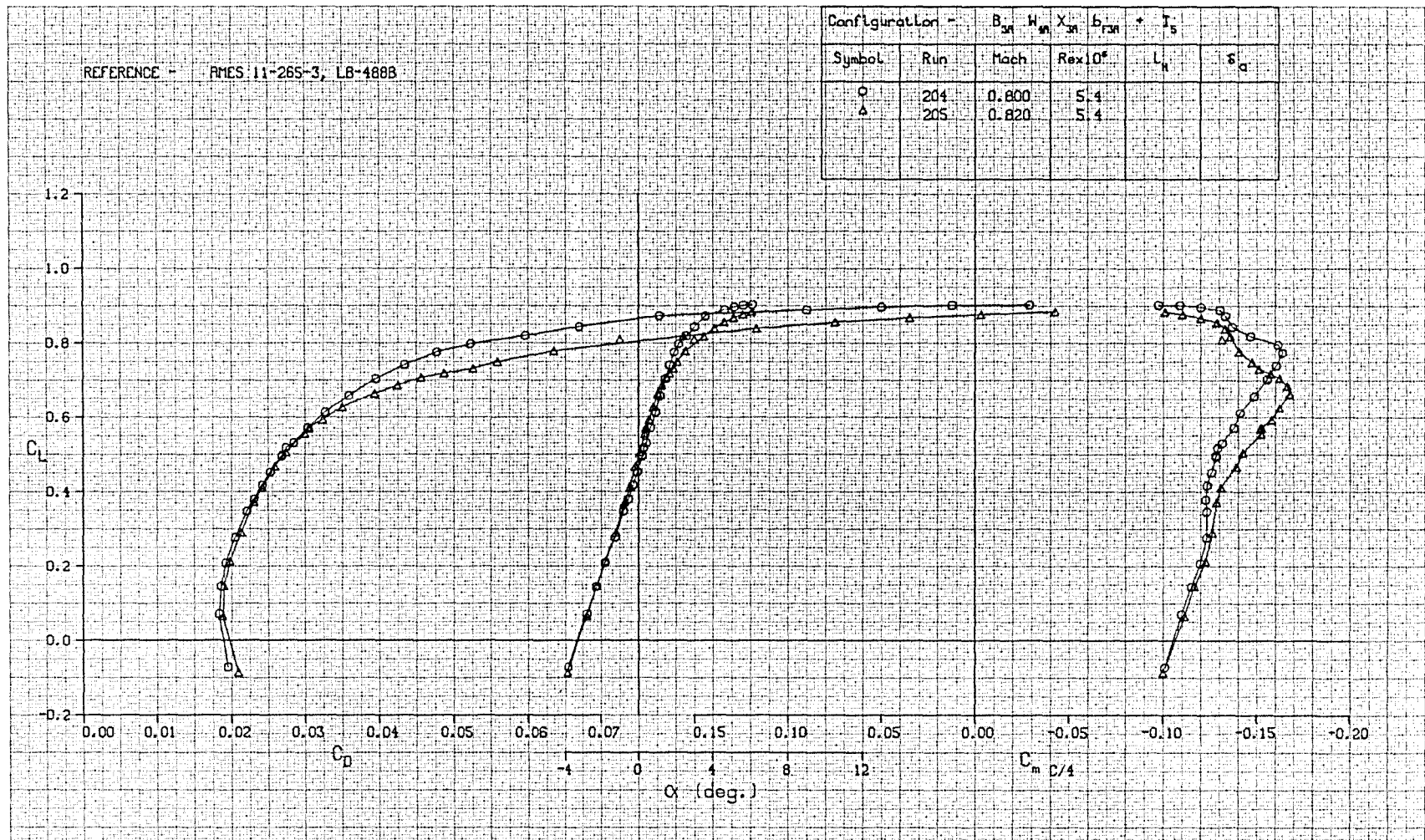


FIGURE A-26. LIFT, DRAG, AND PITCHING MOMENT CHARACTERISTICS OF WING W_{4A} WITH FLAP LINKAGE FAIRINGS, TRANSITION FIXED

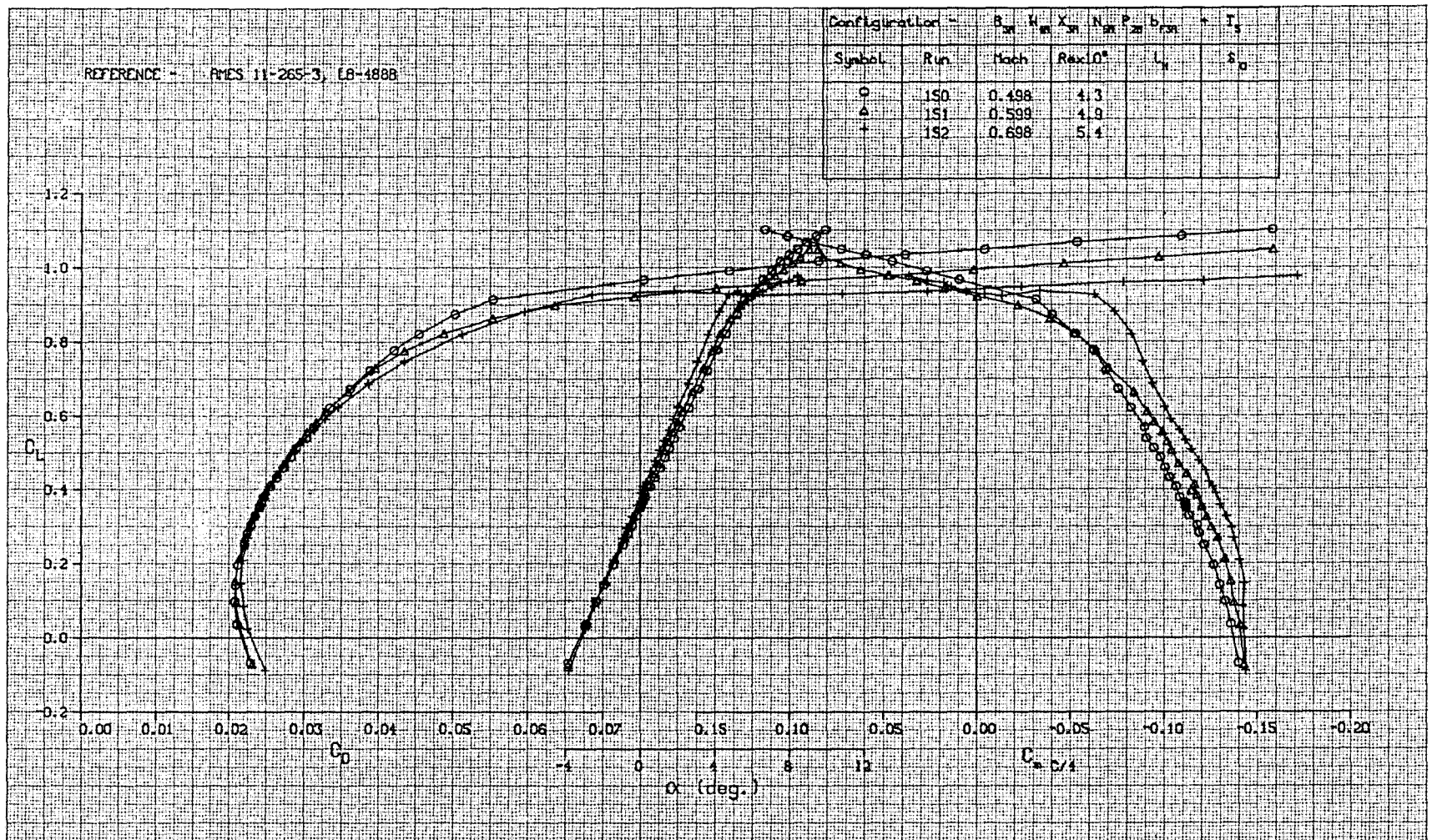


FIGURE A-27. LIFT, DRAG, AND PITCHING MOMENT CHARACTERISTICS OF WING W_{4A} WITH NACELLES, PYLONS, AND FLAP LINKAGE FAIRINGS, TRANSITION FIXED

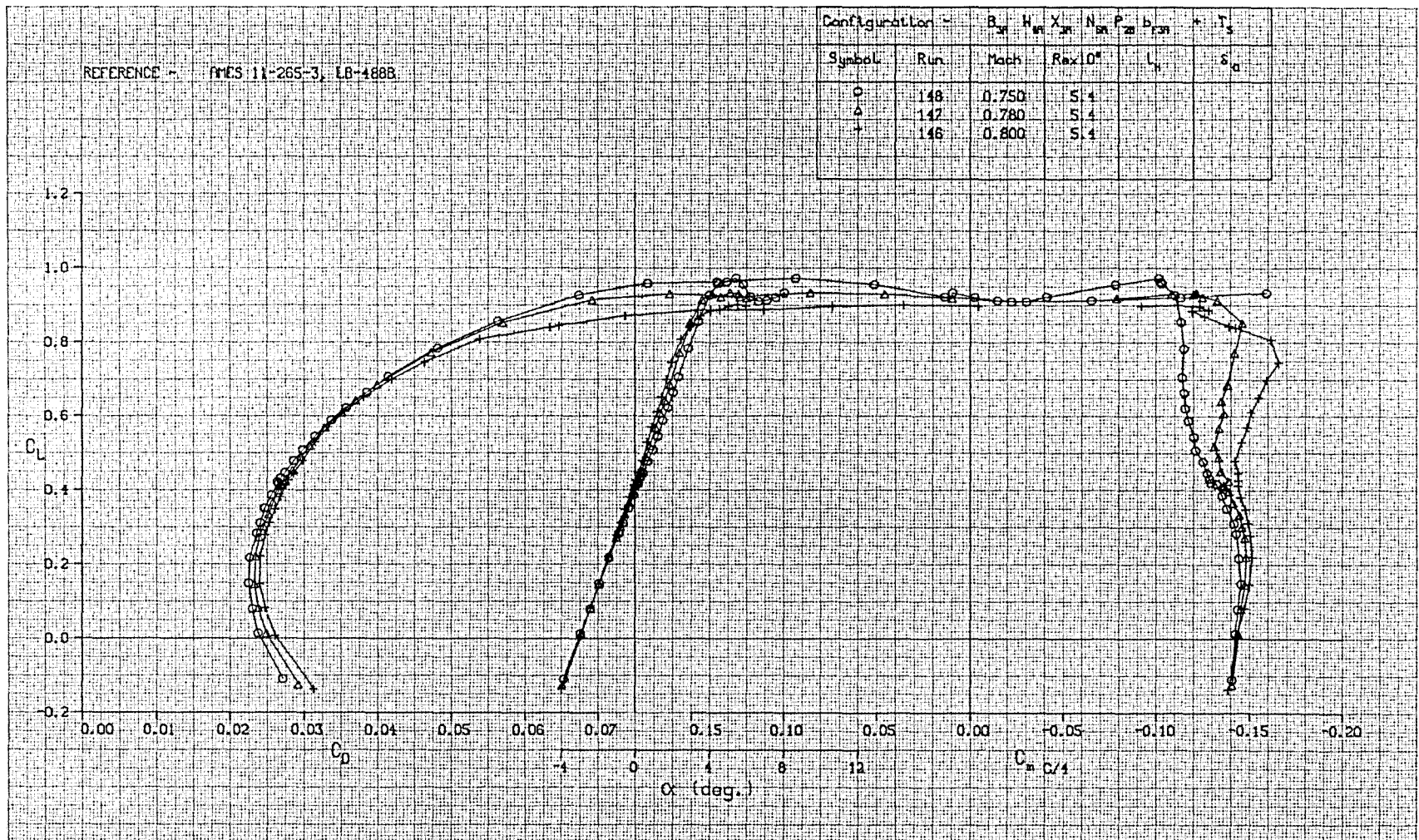


FIGURE A-28. LIFT, DRAG, AND PITCHING MOMENT CHARACTERISTICS OF WING W_{4A} WITH NACELLES, PYLONS, AND FLAP LINKAGE FAIRINGS, TRANSITION FIXED

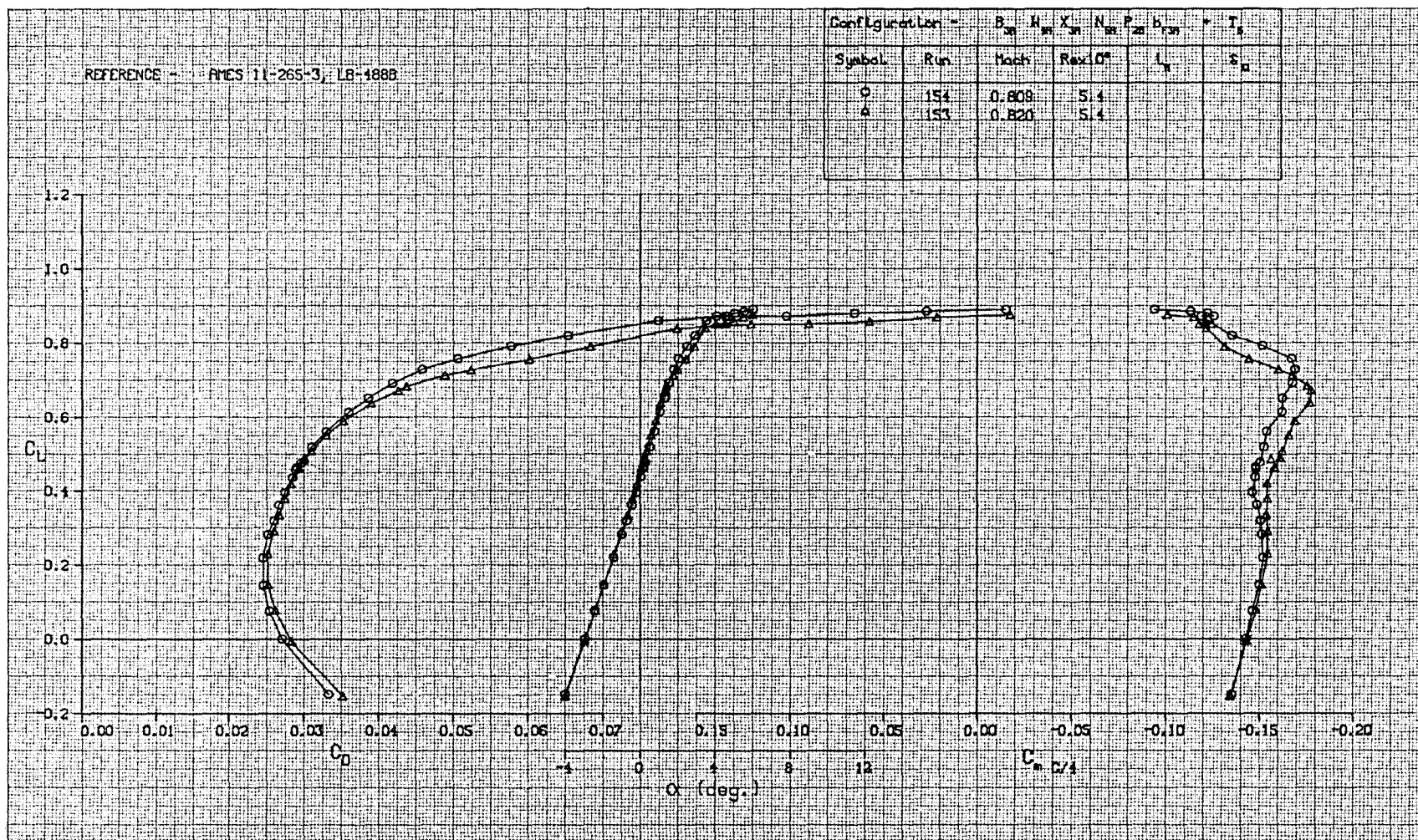


FIGURE A-29. LIFT, DRAG, AND PITCHING MOMENT CHARACTERISTICS OF WING W_{4A} WITH NACELLES, PYLONS, AND FLAP LINKAGE FAIRINGS, TRANSITION FIXED

REFERENCE - AMES 11-265-3, LB-488B

Configuration -		B_{21}	H_{21}	X_{21}	N_{21}	P_{22}	b_{22}	T_2
Symbol	Run	Mach	$Re \times 10^6$	L_{21}	δ_a			
○	155	0.829	5.4					
△	156	0.839	5.5					

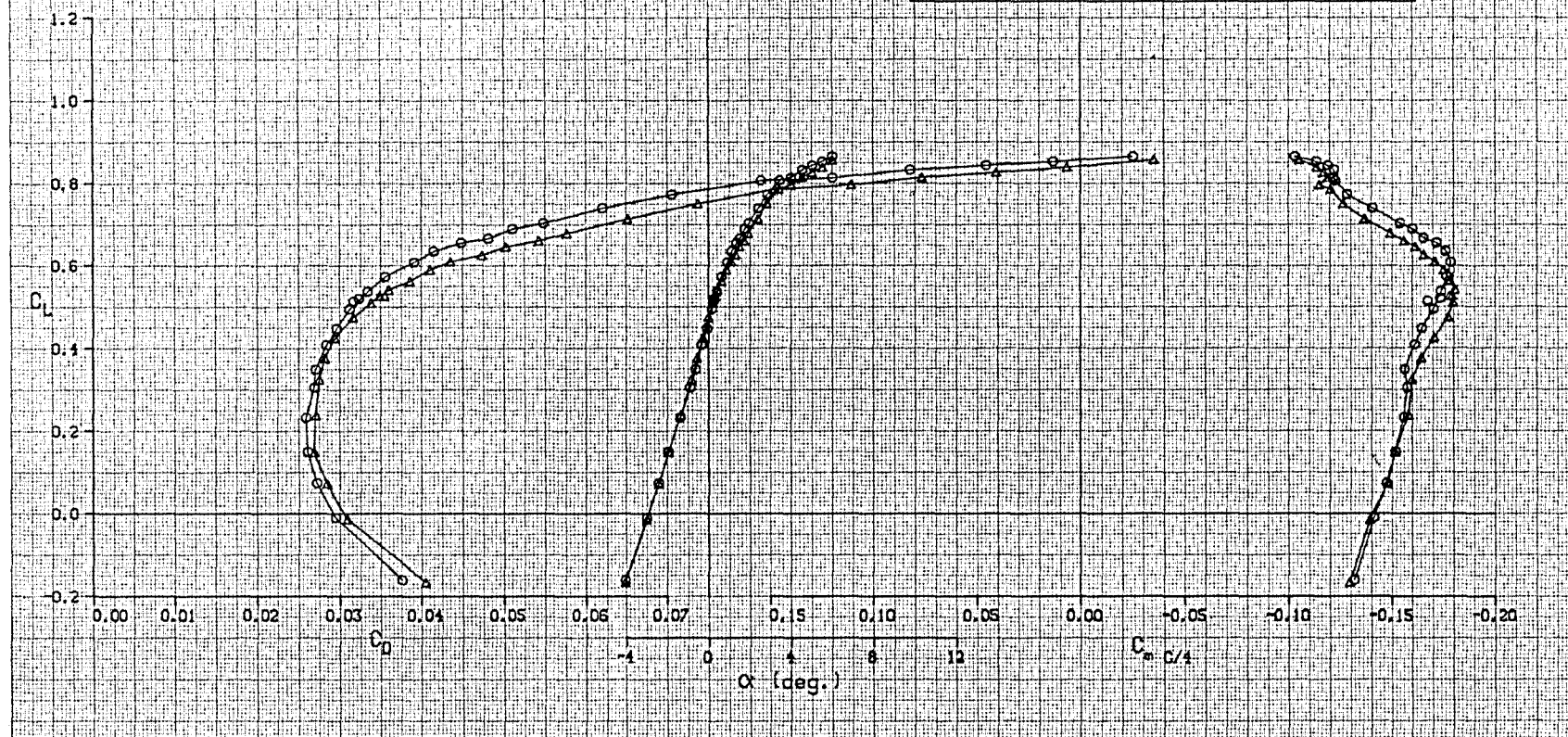


FIGURE A-30. LIFT, DRAG, AND PITCHING MOMENT CHARACTERISTICS OF WING W_{4A} WITH NACELLES, PYLONS, AND FLAP LINKAGE FAIRINGS, TRANSITION FIXED

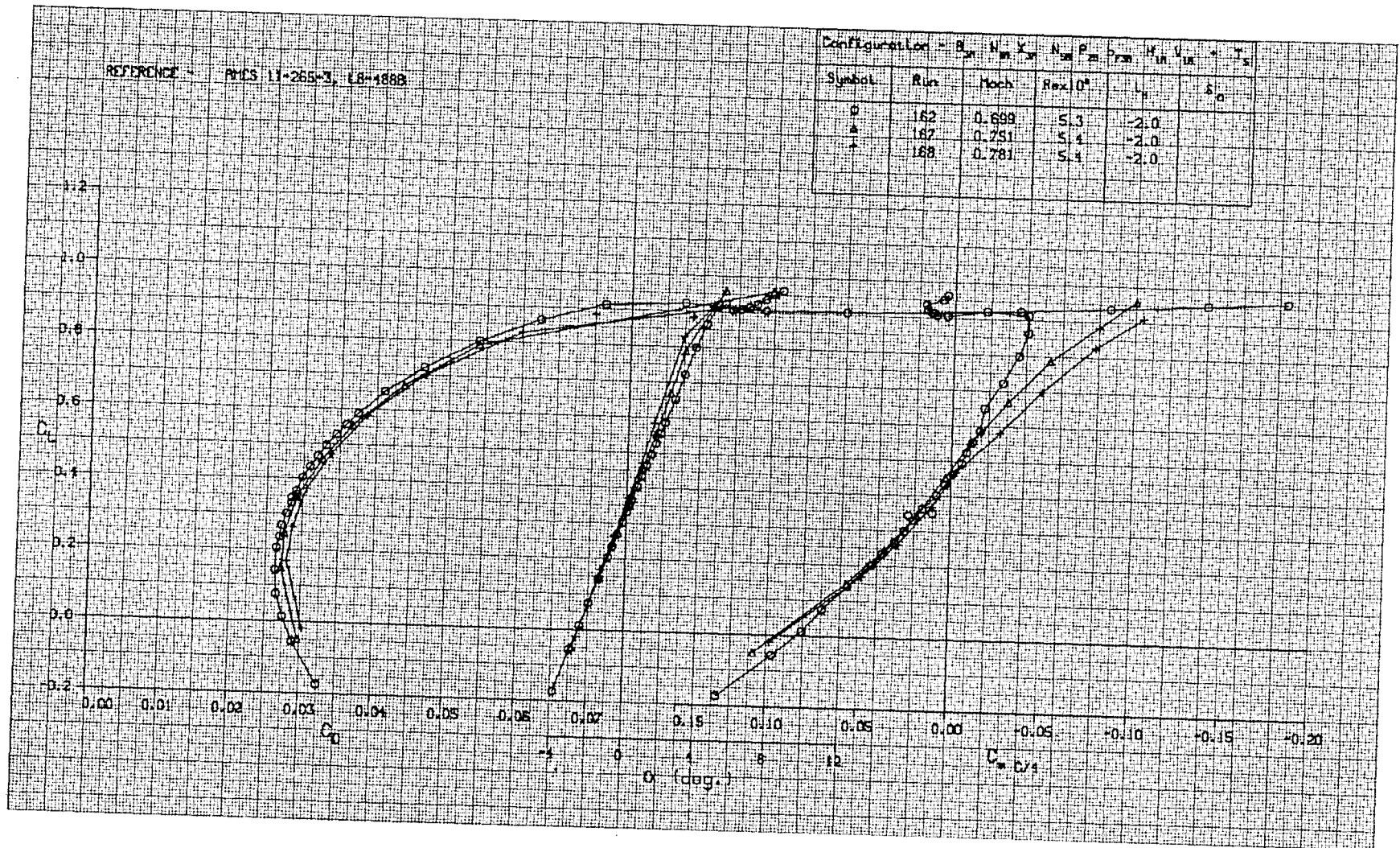
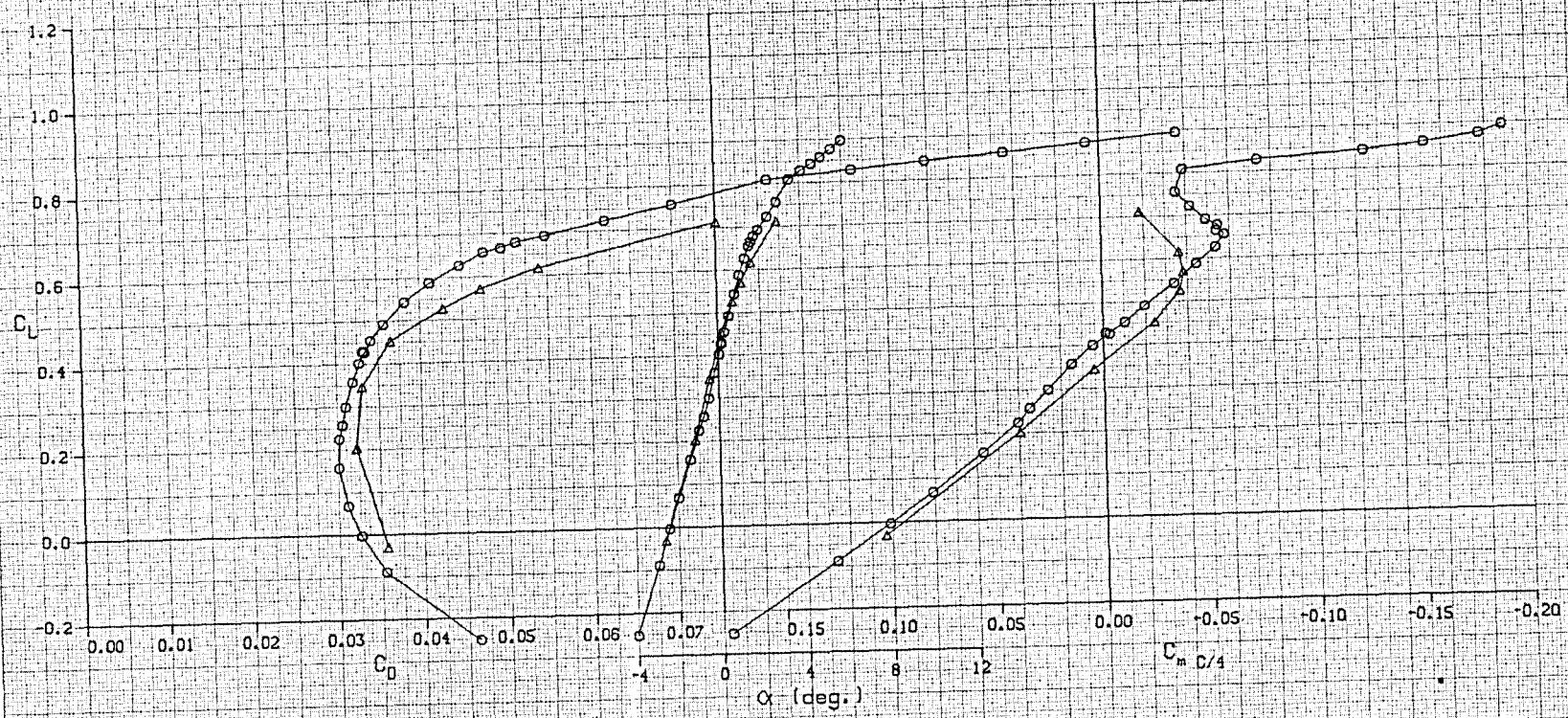


FIGURE A-31. LIFT, DRAG, AND PITCHING MOMENT CHARACTERISTICS OF WING W_{4A} WITH NACELLES, PYLONS, FLAP LINKAGE FAIRINGS, AND TAIL, TRANSITION FIXED

REFERENCE - AMES 11-265-3, LB-488B

Configuration -					
Symbol	Run	Mach	Re x 10 ⁶	τ_H	δ_a
○	161	0.820	5.4	-2.0	
△	172	0.840	5.4	-2.0	



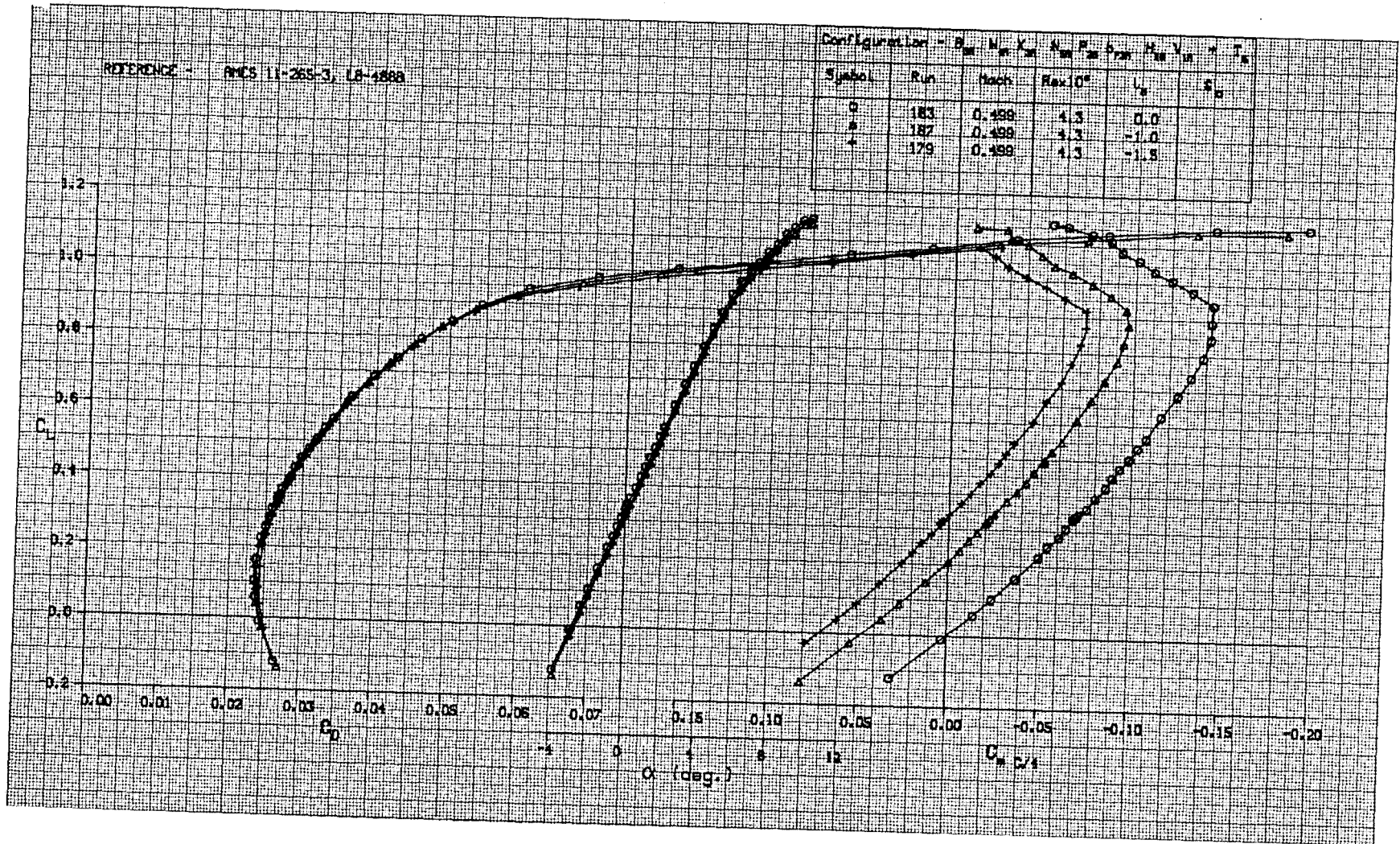


FIGURE A-33. LIFT, DRAG, AND PITCHING MOMENT CHARACTERISTICS OF WING W_{4A} WITH NACELLES, PYLONS, FLAP LINKAGE FAIRINGS, AND TAIL, TRANSITION FIXED

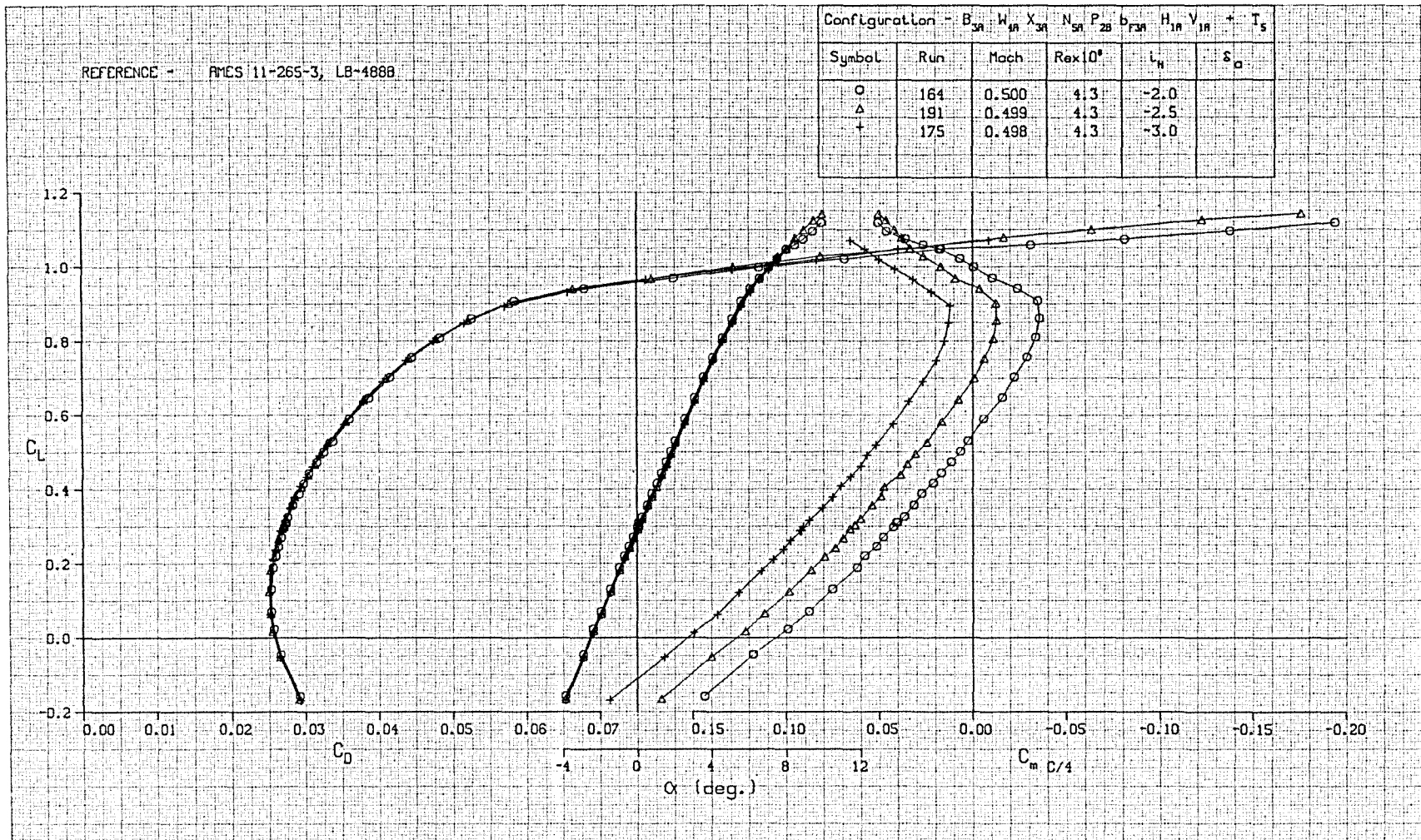


FIGURE A-34. LIFT, DRAG, AND PITCHING MOMENT CHARACTERISTICS OF WING W_{4A} WITH NACELLES, PYLONS, FLAP LINKAGE FAIRINGS, AND TAIL, TRANSITION FIXED

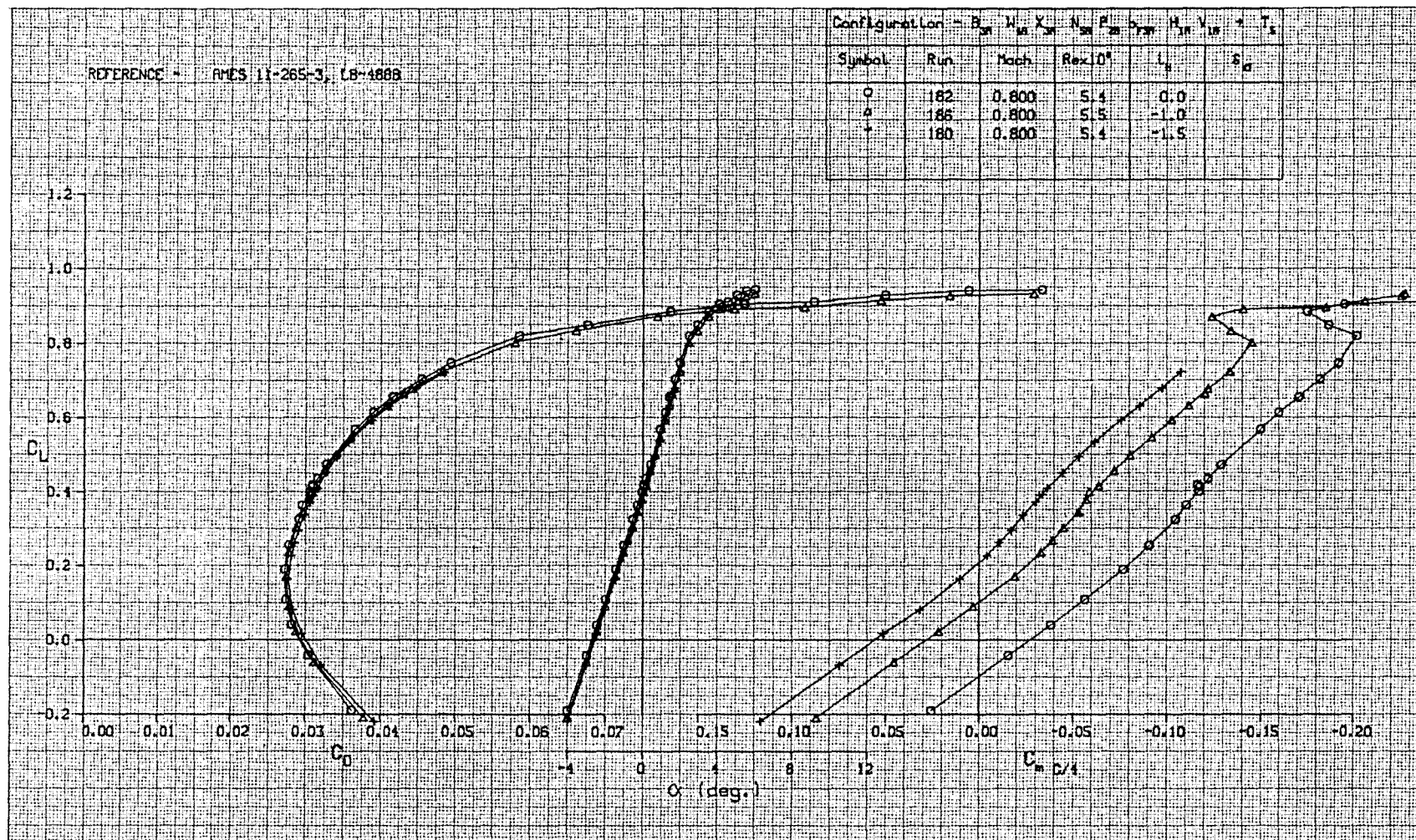


FIGURE A-35. LIFT, DRAG, AND PITCHING MOMENT CHARACTERISTICS OF WING W_{4A} WITH NACELLES, PYLONS, FLAP LINKAGE FAIRINGS, AND TAIL, TRANSITION FIXED

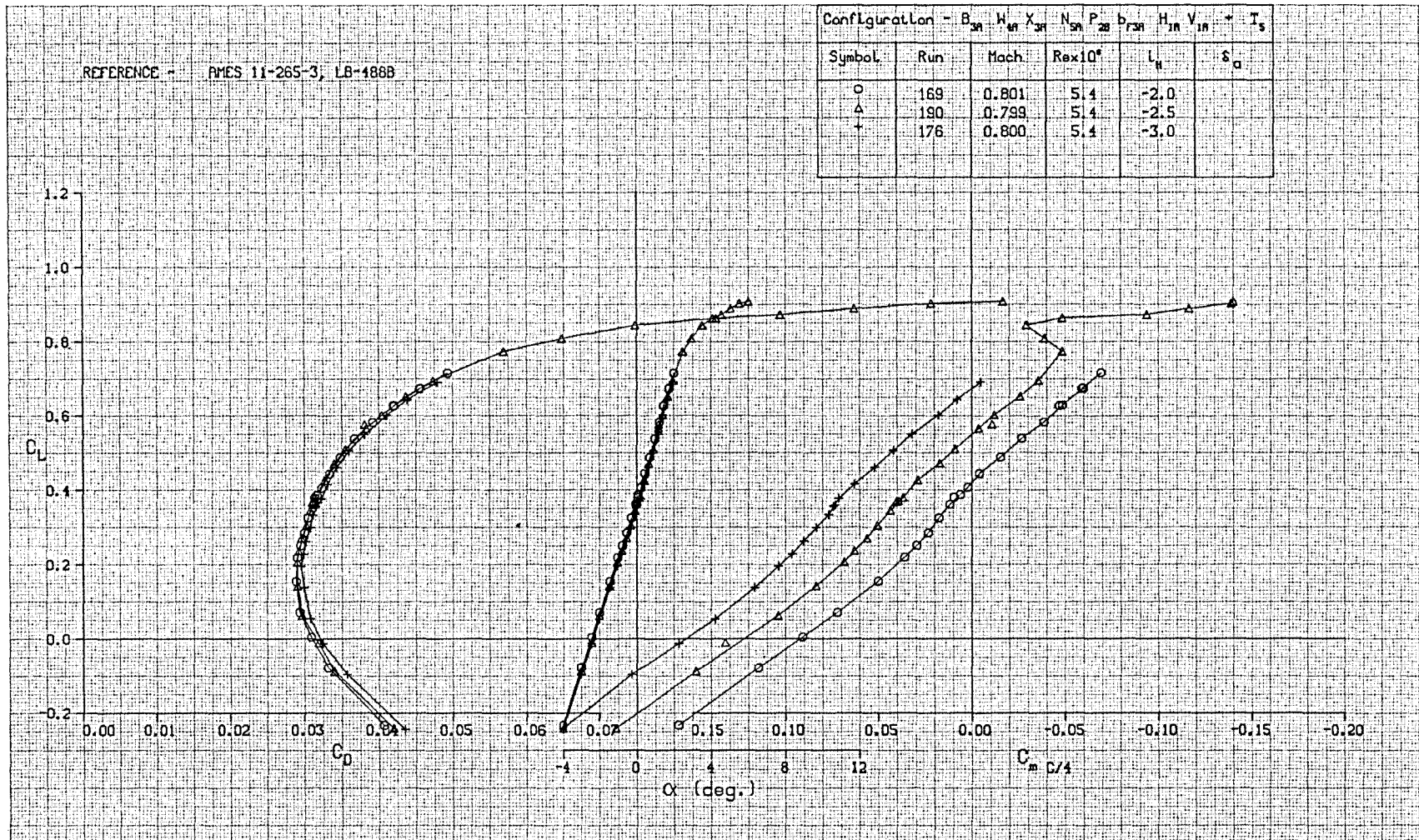


FIGURE A-36. LIFT, DRAG, AND PITCHING MOMENT CHARACTERISTICS OF WING W_{4A} WITH NACELLES, PYLONS, FLAP LINKAGE FAIRINGS, AND TAIL, TRANSITION FIXED

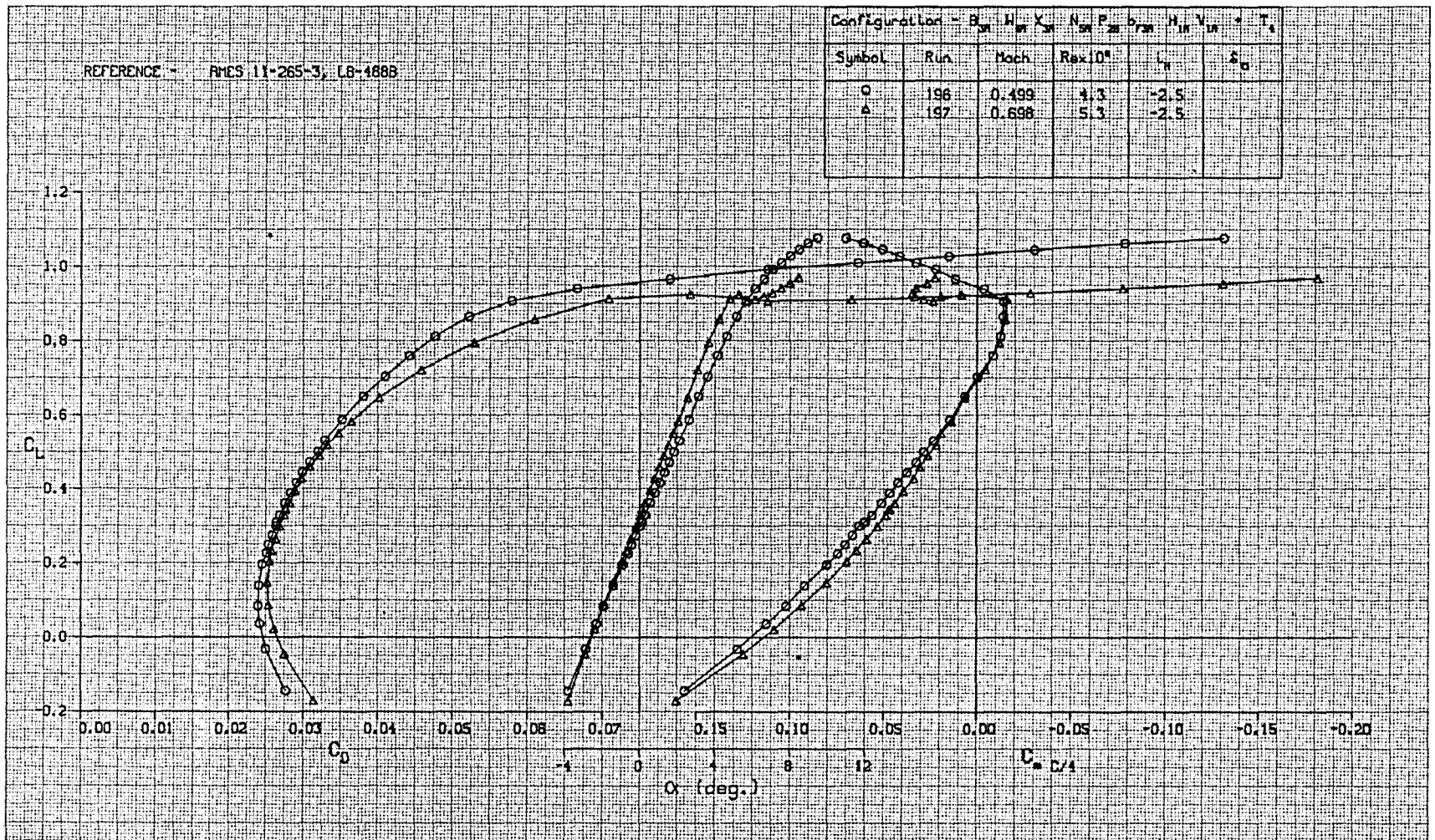


FIGURE A-37. LIFT, DRAG, AND PITCHING MOMENT CHARACTERISTICS OF WING W_{4A} WITH NACELLES, PYLONS, FLAP LINKAGE FAIRINGS, AND TAIL, TRANSITION FREE

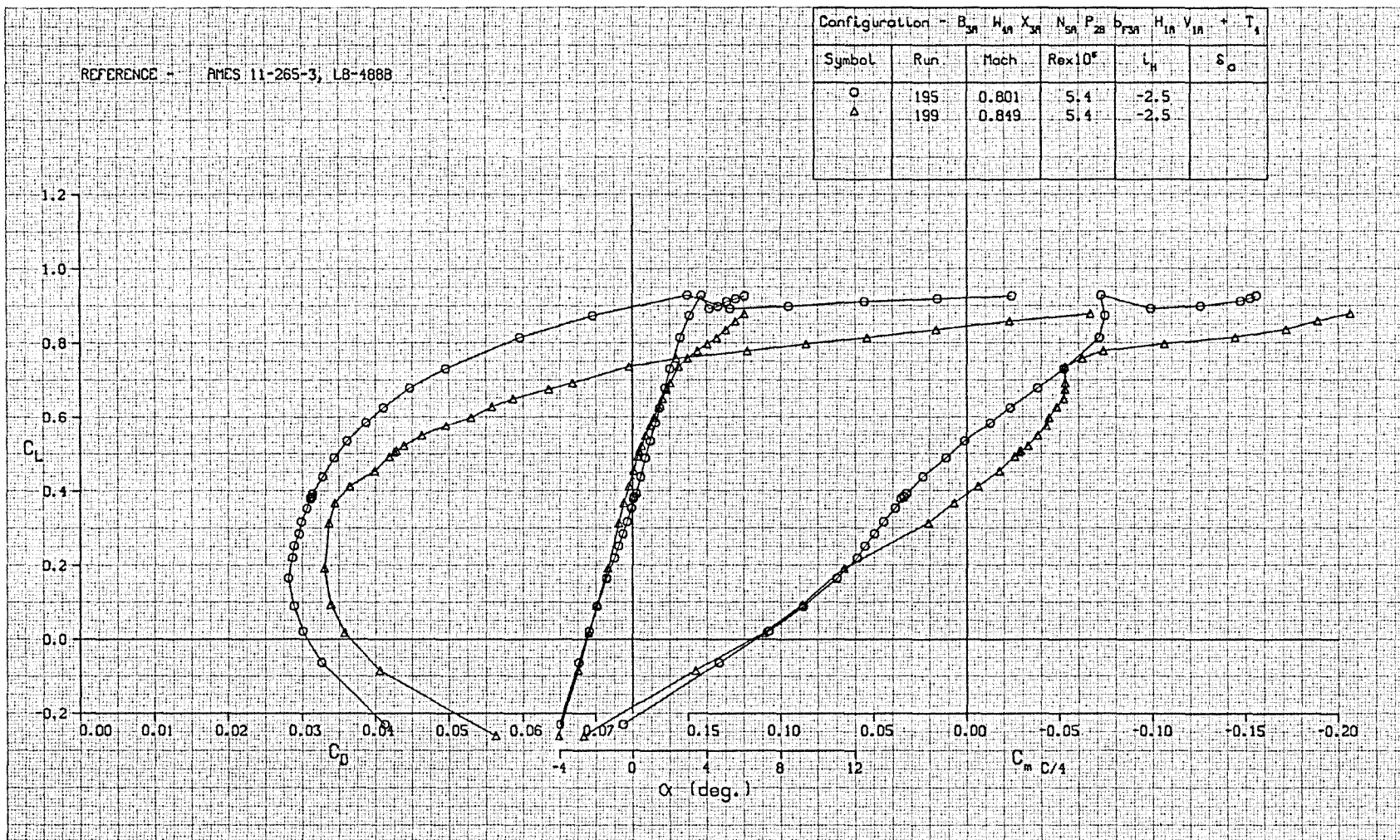


FIGURE A-38. LIFT, DRAG, AND PITCHING MOMENT CHARACTERISTICS OF WING W_{4A} WITH NACELLES, PYLONS, FLAP LINKAGE FAIRINGS, AND TAIL, TRANSITION FREE

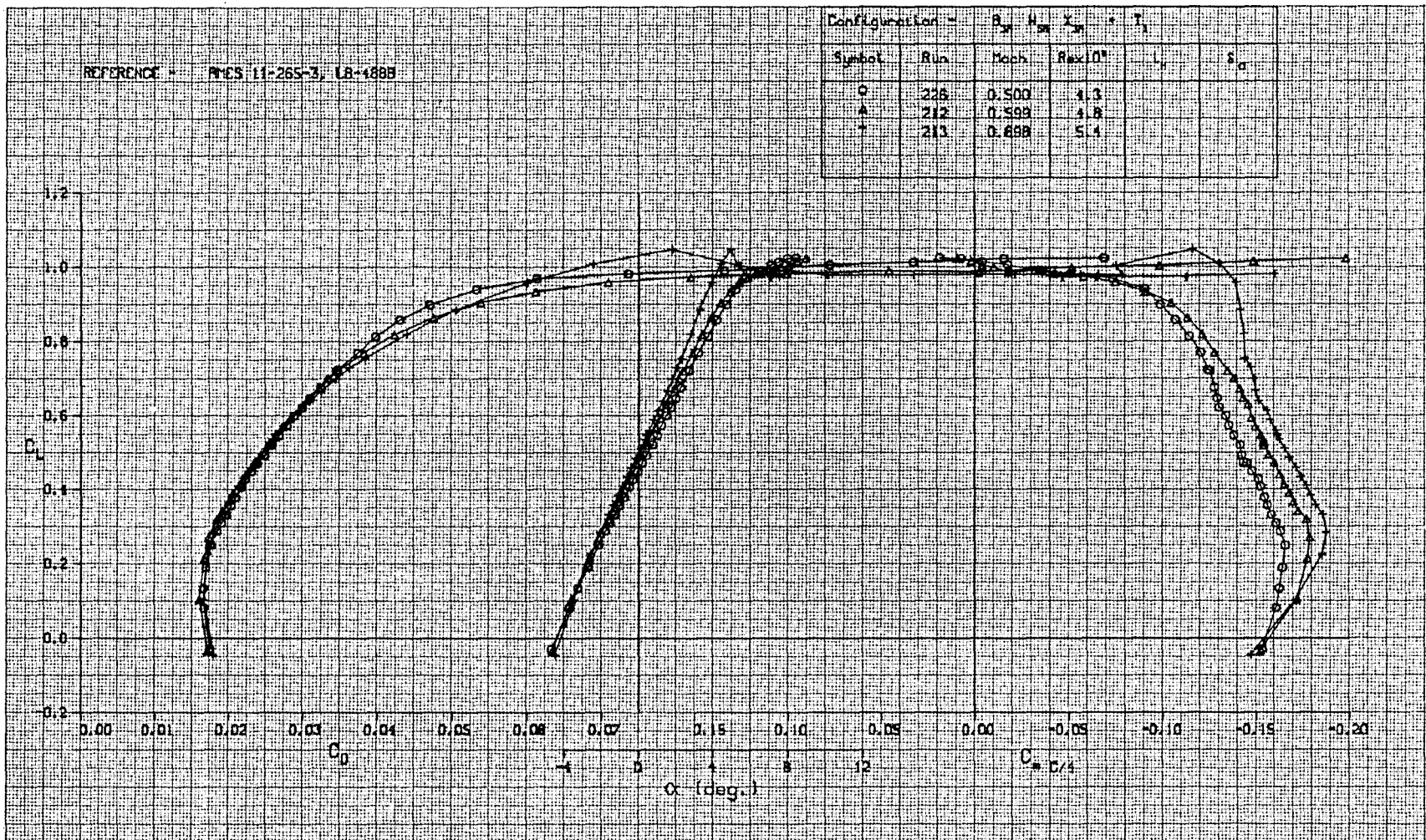


FIGURE A-39. LIFT, DRAG, AND PITCHING MOMENT CHARACTERISTICS OF WING W_{5A} , TRANSITION FREE



FIGURE A-40. LIFT, DRAG, AND PITCHING MOMENT CHARACTERISTICS OF WING W_{5A} , TRANSITION FREE

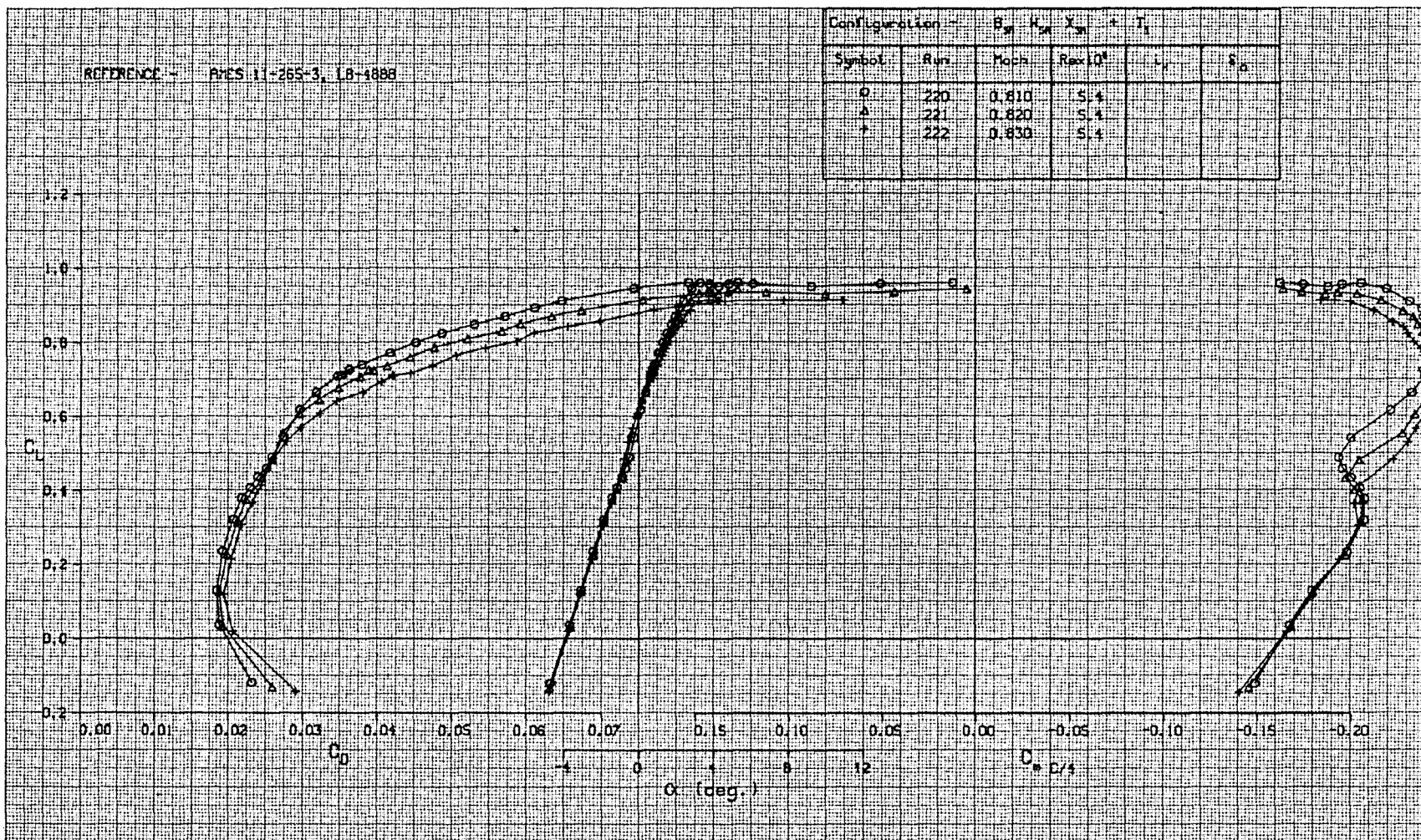


FIGURE A-41. LIFT, DRAG, AND PITCHING MOMENT CHARACTERISTICS OF WING W_{5A}, TRANSITION FREE

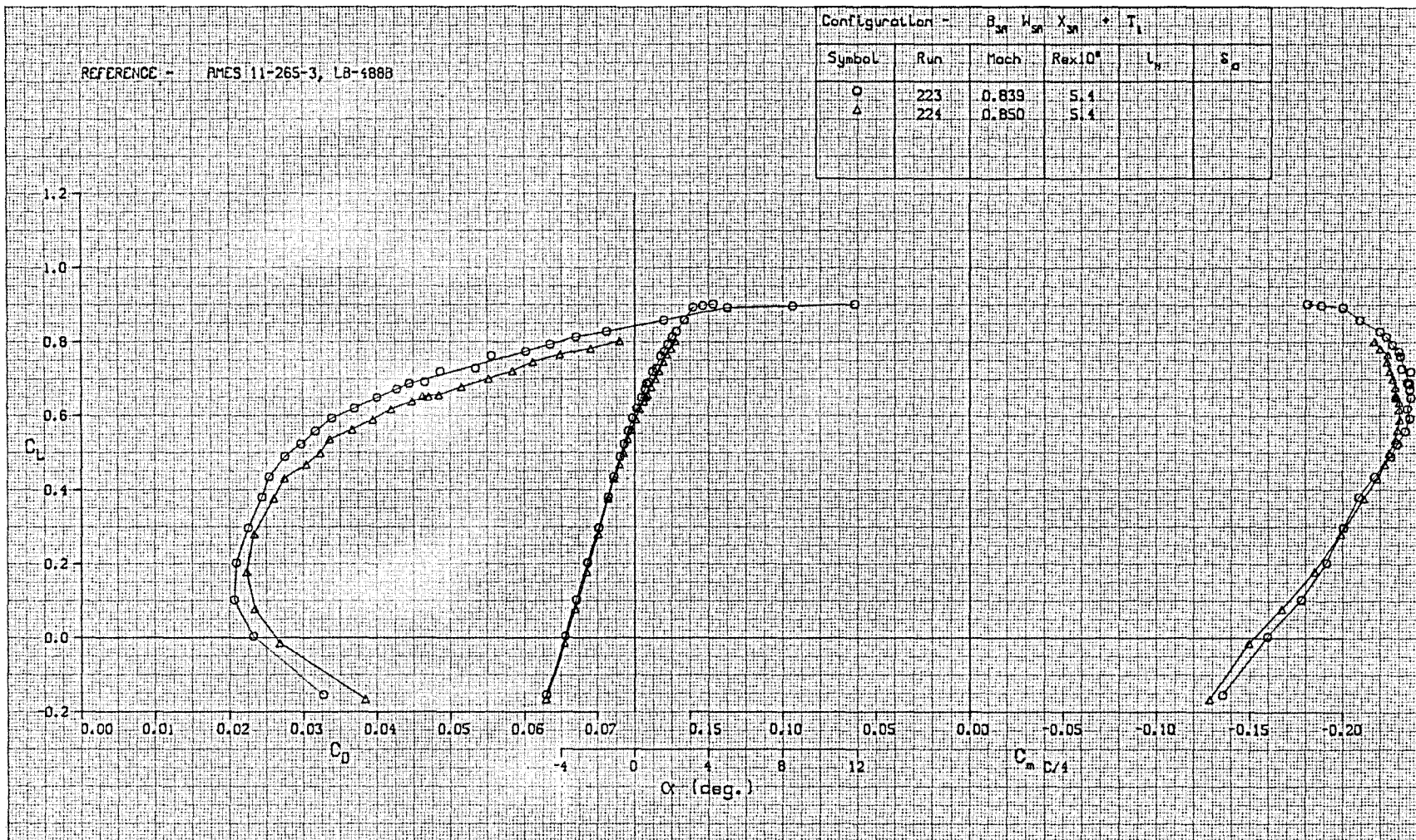


FIGURE A-42. LIFT, DRAG, AND PITCHING MOMENT CHARACTERISTICS OF WING W_{5A}, TRANSITION FREE

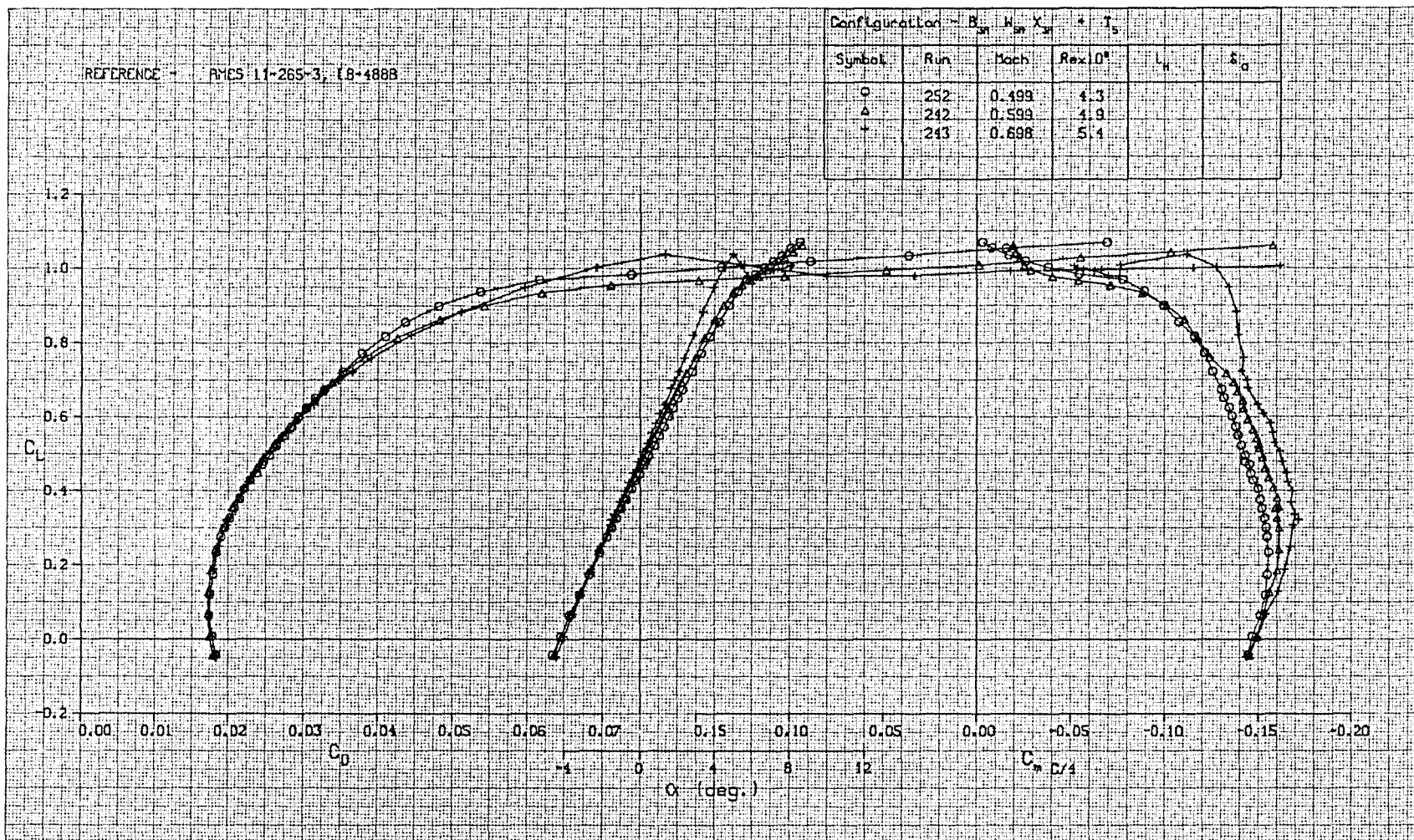


FIGURE A-43. LIFT, DRAG, AND PITCHING MOMENT CHARACTERISTICS OF WING W_{5A} , TRANSITION FIXED

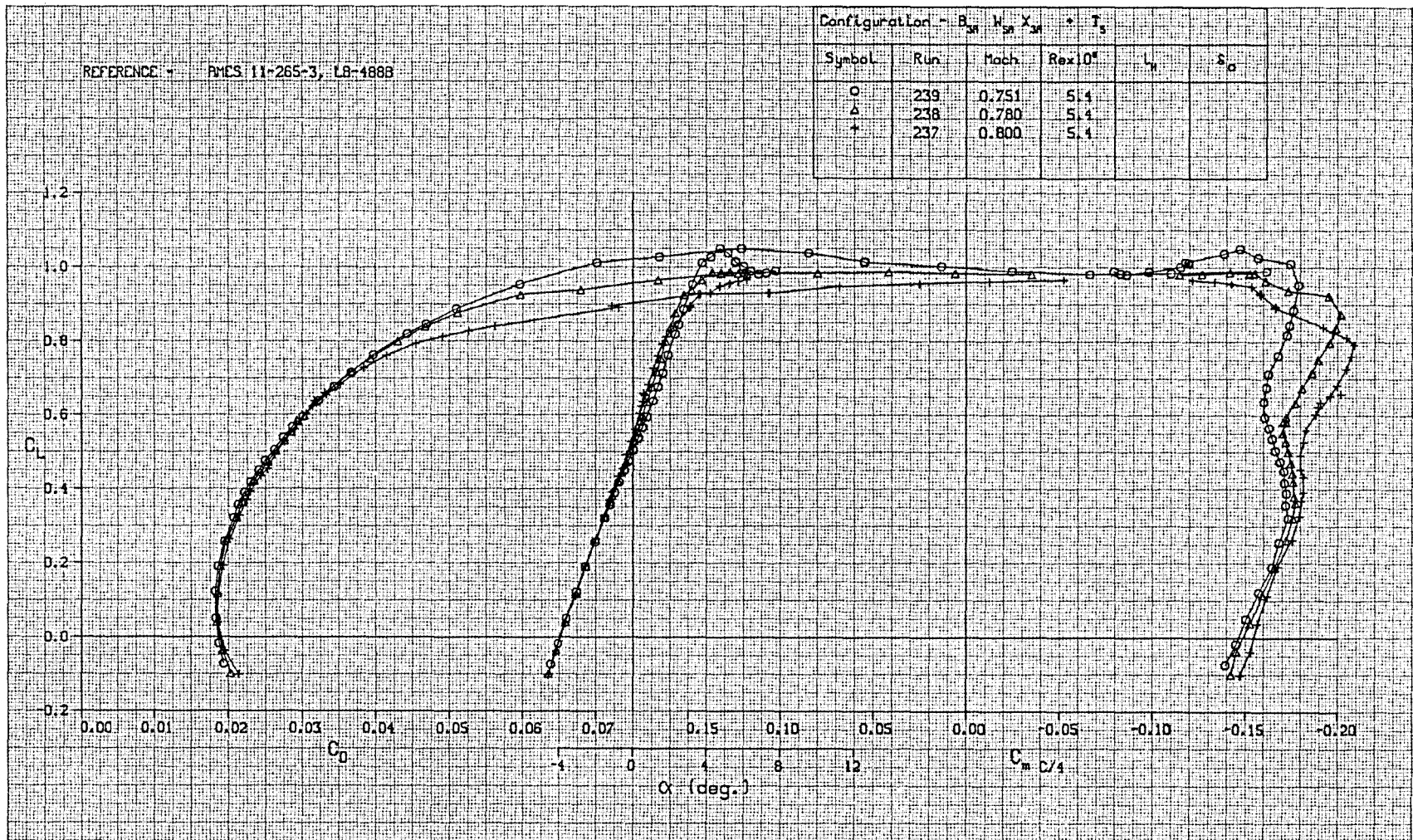


FIGURE A-44. LIFT, DRAG, AND PITCHING MOMENT CHARACTERISTICS OF WING W_{5A} , TRANSITION FIXED

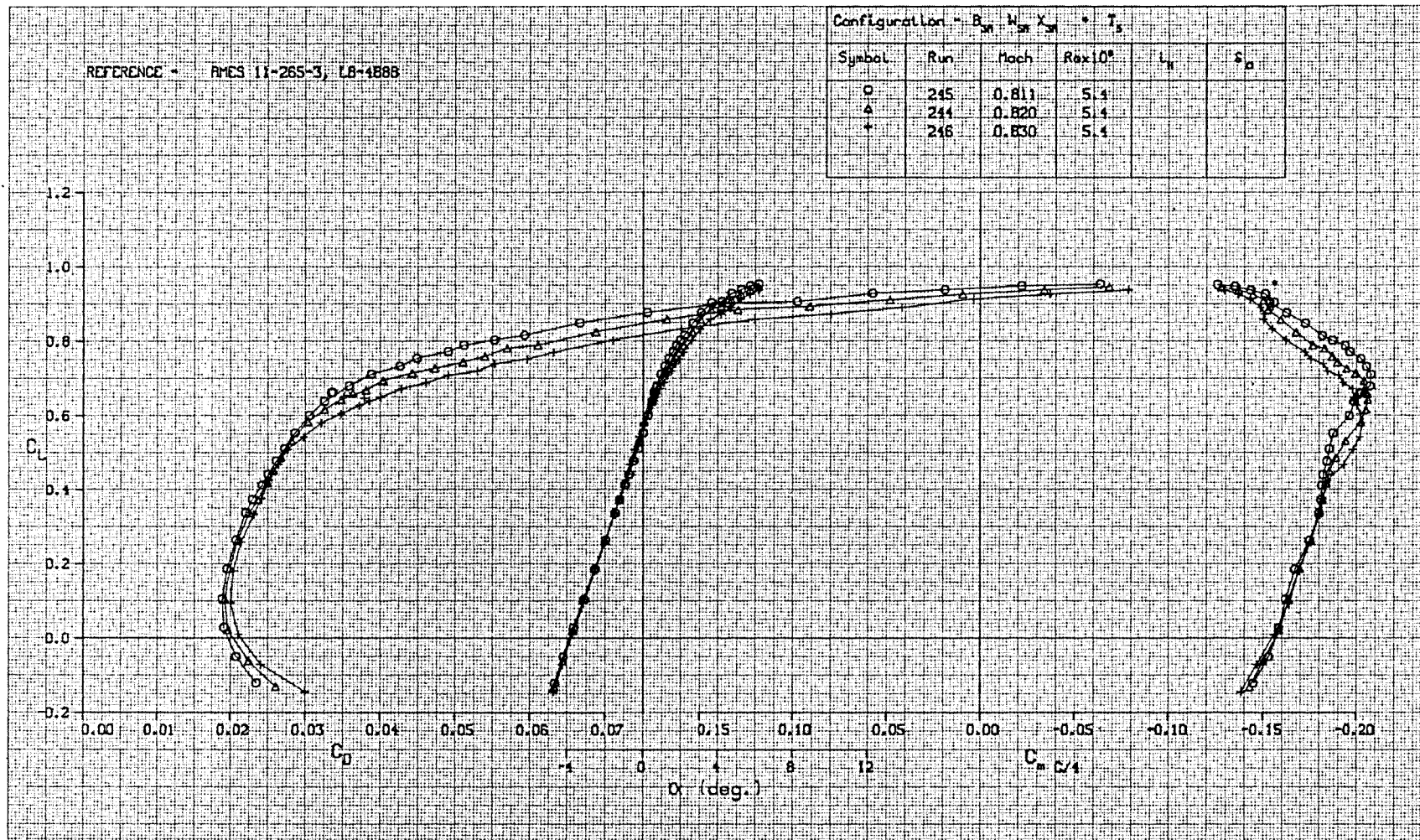


FIGURE A-45. LIFT, DRAG, AND PITCHING MOMENT CHARACTERISTICS OF WING W_{5A} , TRANSITION FIXED

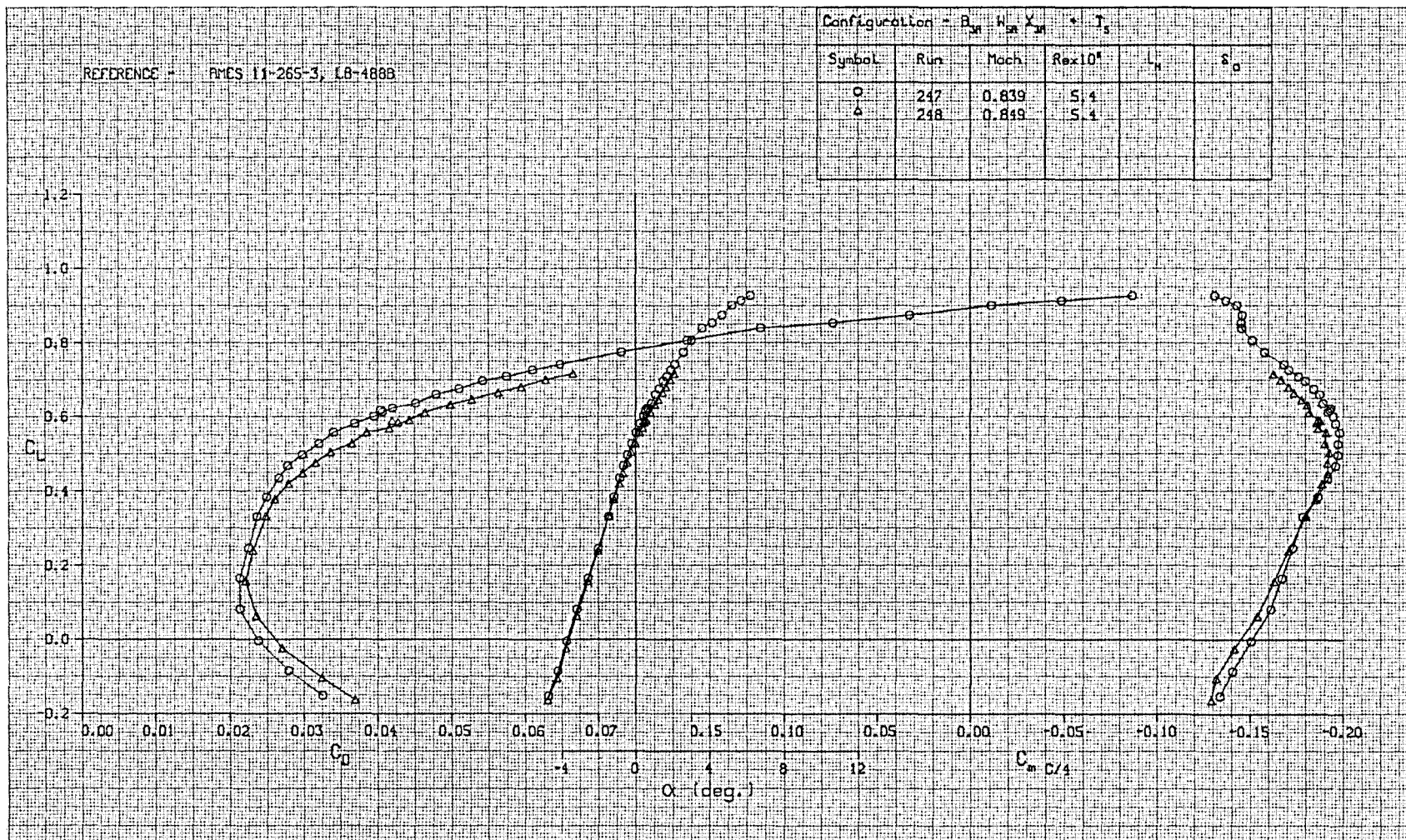


FIGURE A-46. LIFT, DRAG, AND PITCHING MOMENT CHARACTERISTICS OF WING W_{5A} , TRANSITION FIXED



FIGURE A-47. LIFT, DRAG, AND PITCHING MOMENT CHARACTERISTICS OF WING W_{5A} , TRANSITION FIXED - REYNOLDS NUMBER EFFECT

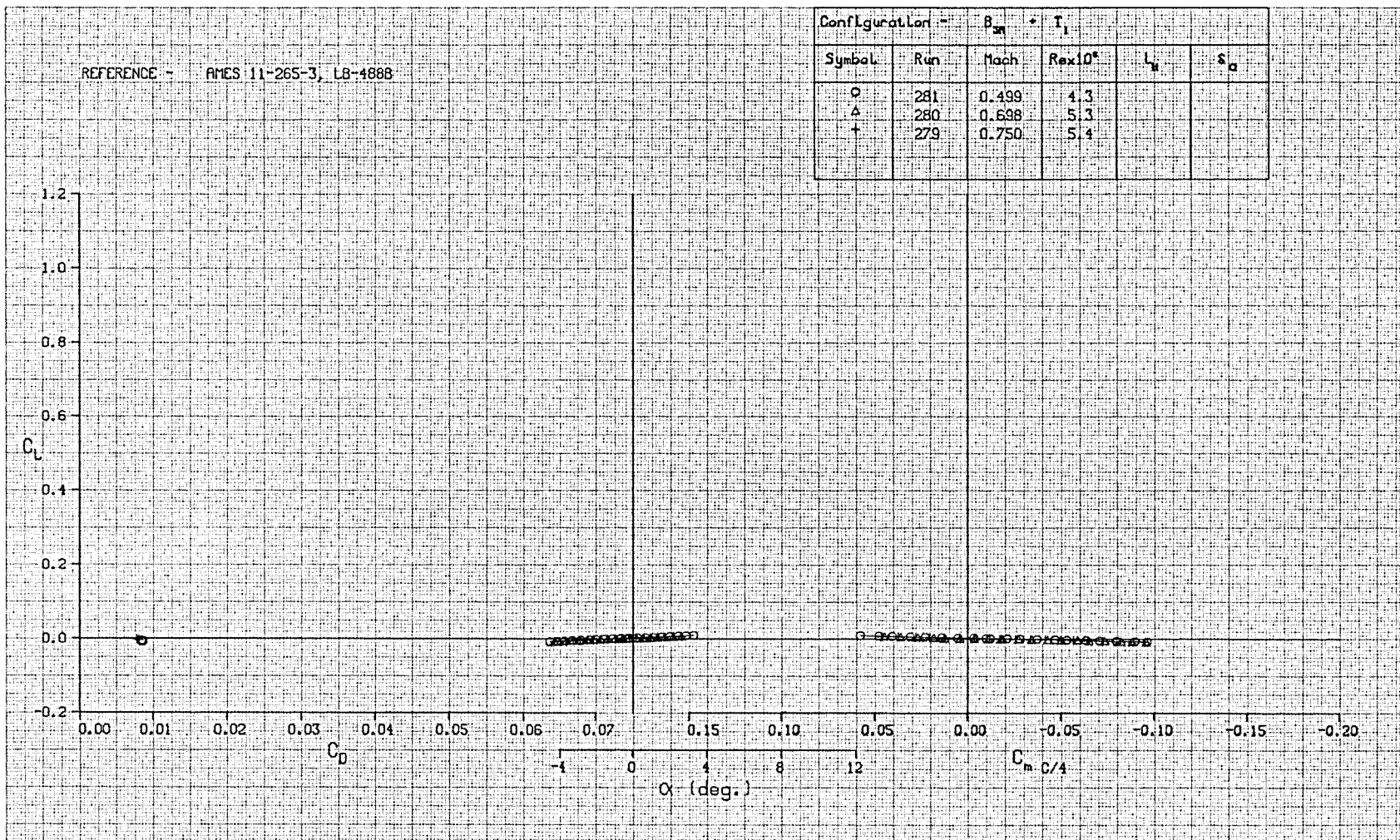


FIGURE A-48. LIFT, DRAG, AND PITCHING MOMENT CHARACTERISTICS OF BODY ALONE, TRANSITION FIXED

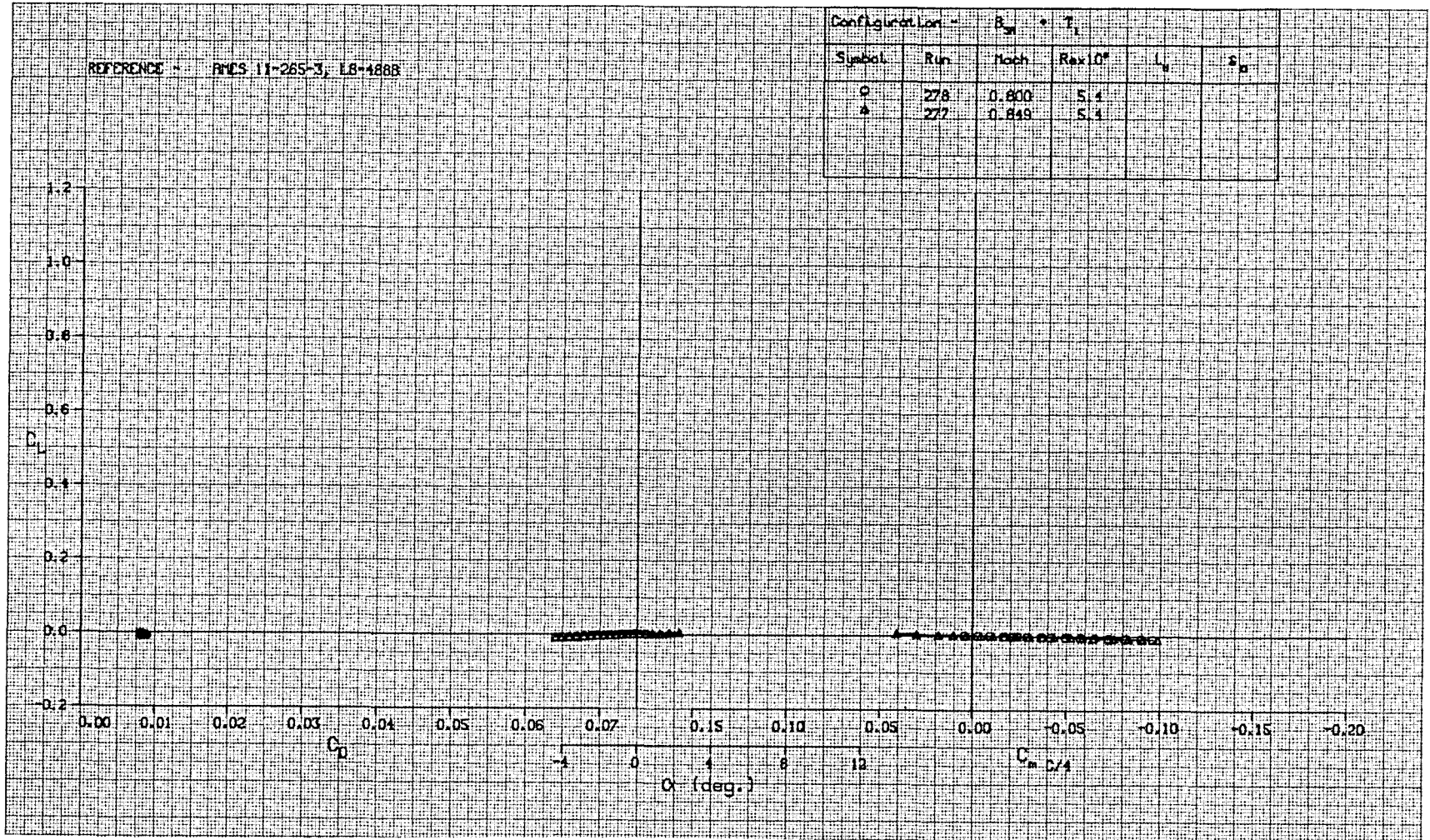


FIGURE A-49. LIFT, DRAG, AND PITCHING MOMENT CHARACTERISTICS OF BODY ALONE, TRANSITION FIXED

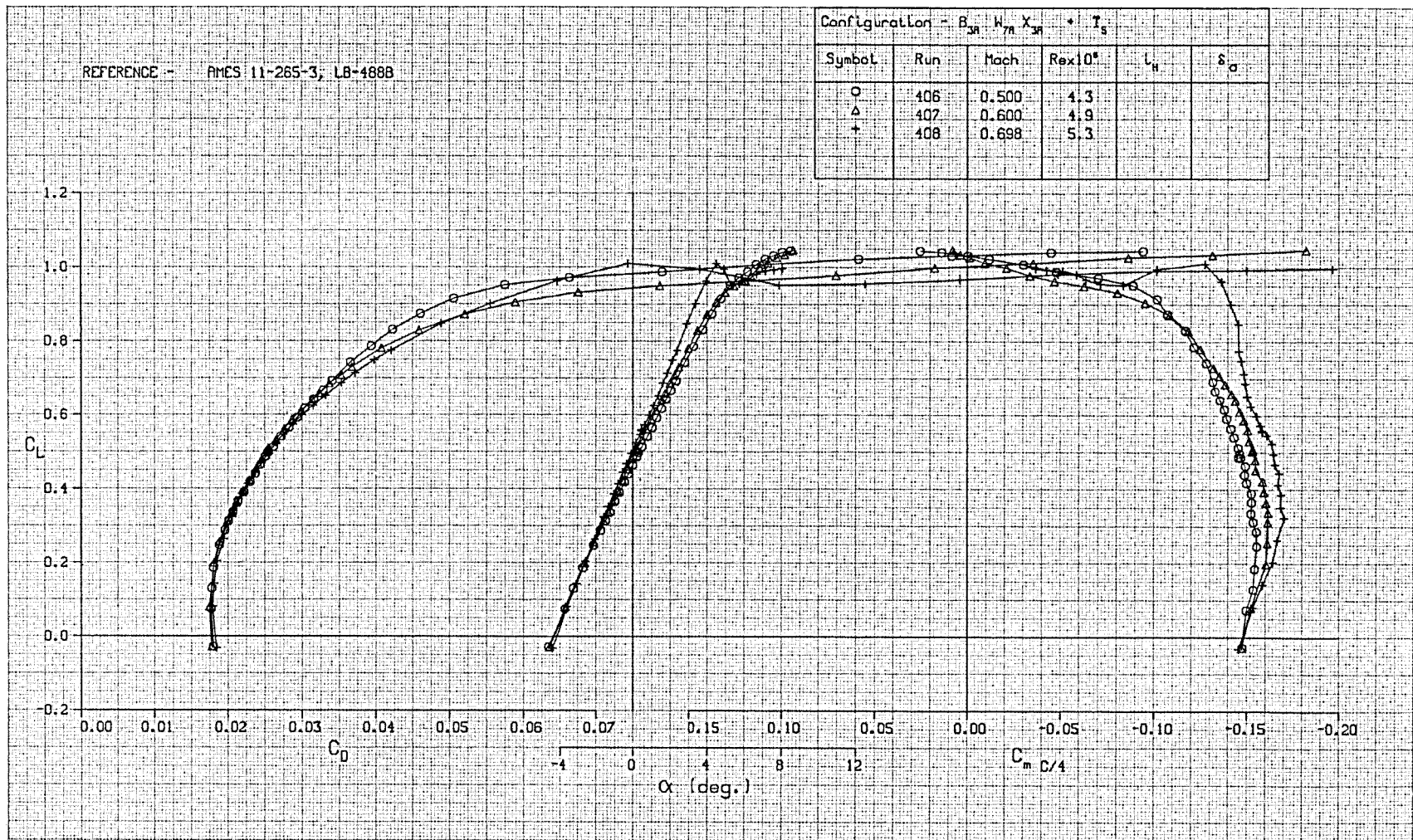


FIGURE A-50. LIFT, DRAG, AND PITCHING MOMENT CHARACTERISTICS OF WING W_{7A} , TRANSITION FIXED

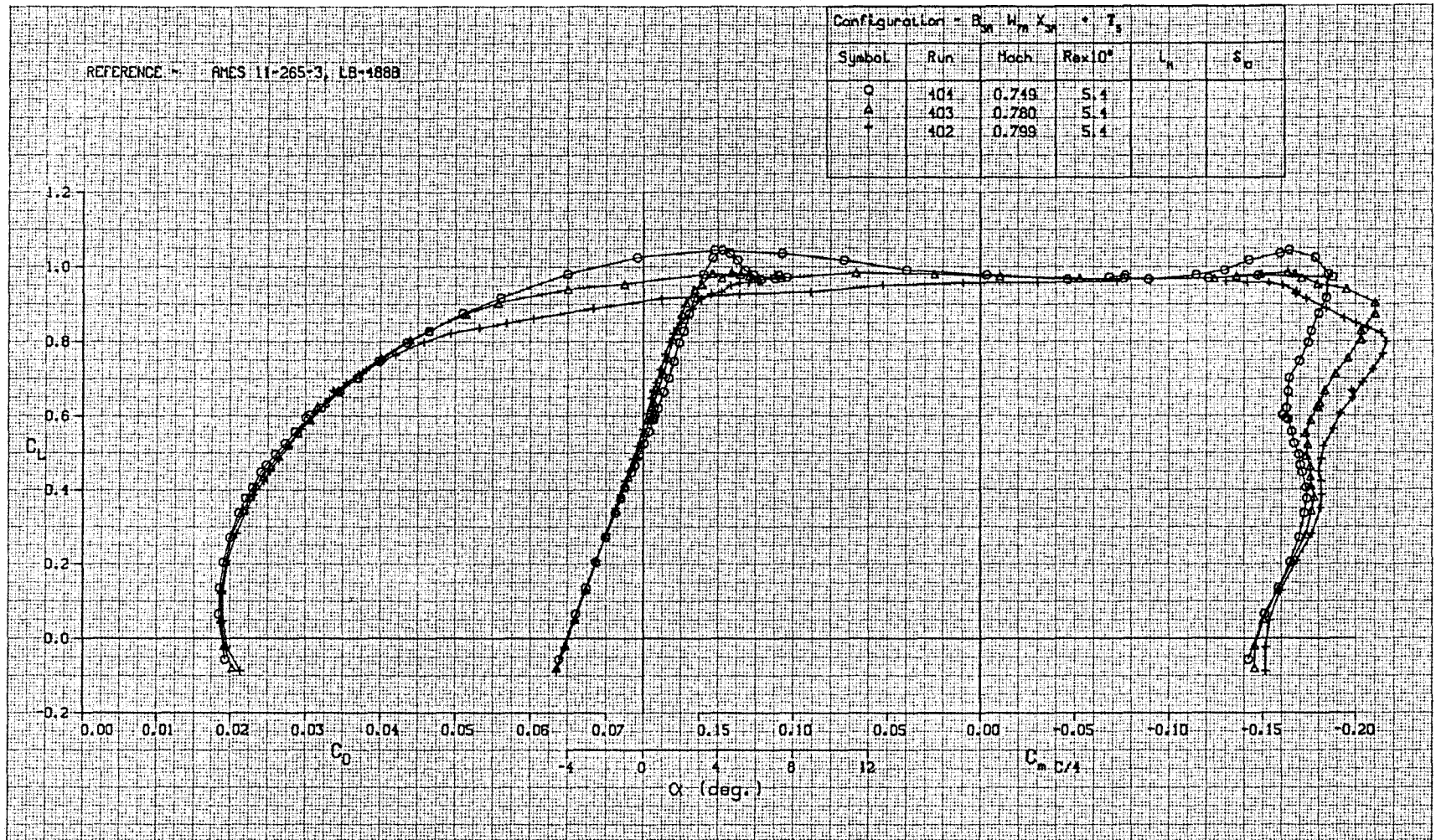


FIGURE A-51. LIFT, DRAG, AND PITCHING MOMENT CHARACTERISTICS OF WING W_{7A} , TRANSITION FIXED

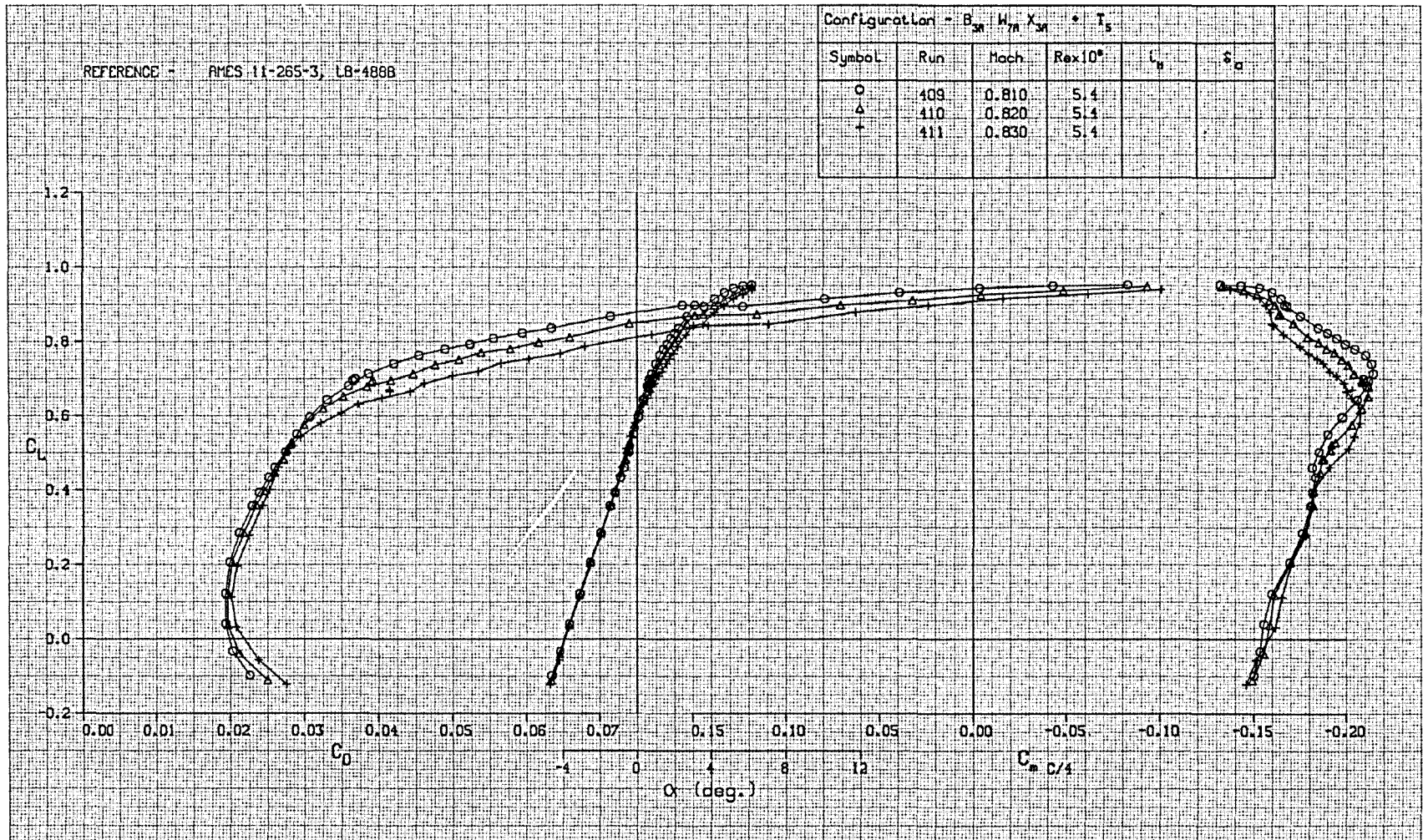


FIGURE A-52. LIFT, DRAG, AND PITCHING MOMENT CHARACTERISTICS OF WING W_{7A} , TRANSITION FIXED

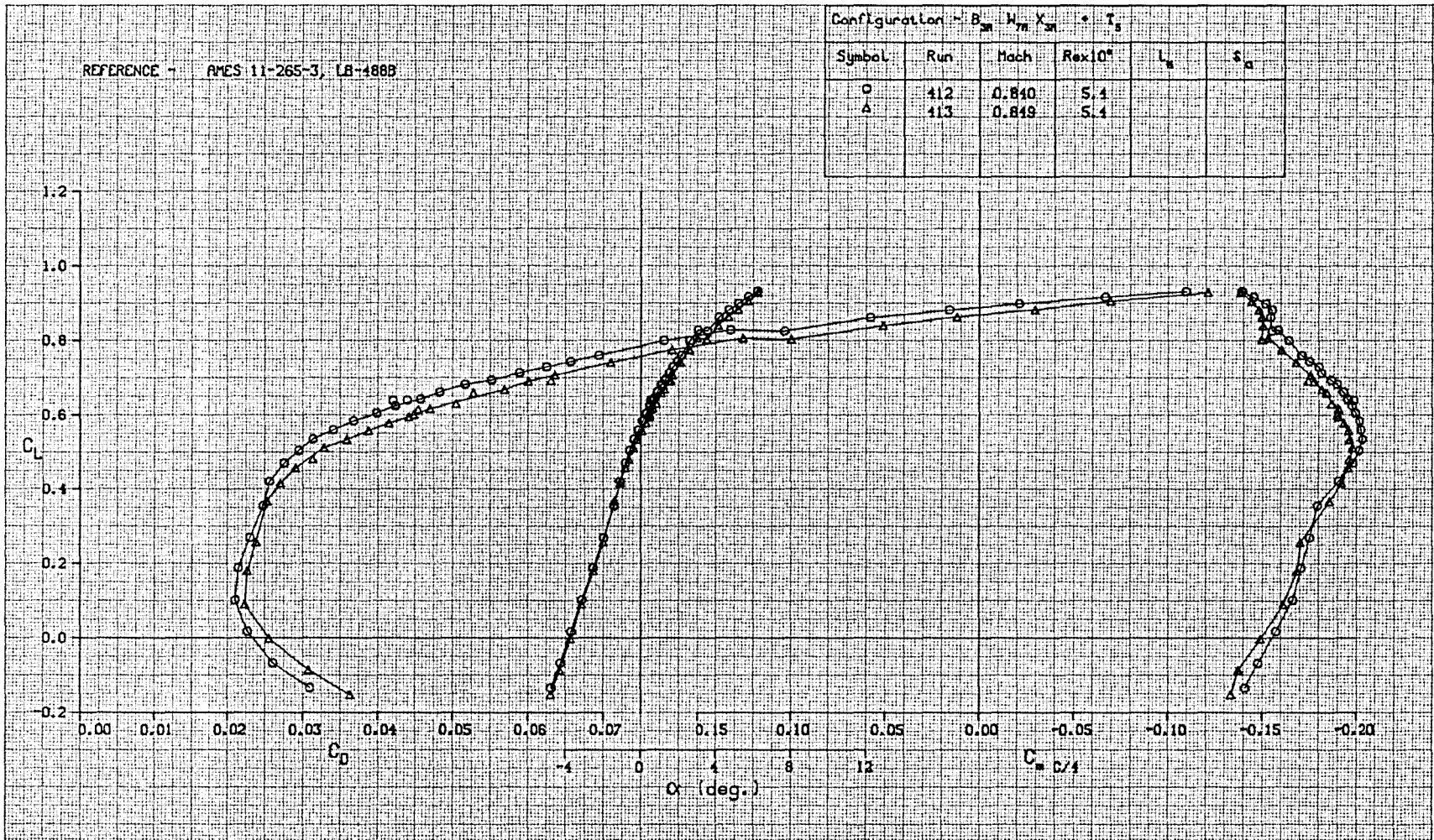


FIGURE A-53. LIFT, DRAG, AND PITCHING MOMENT CHARACTERISTICS OF WING W_{7A} , TRANSITION FIXED

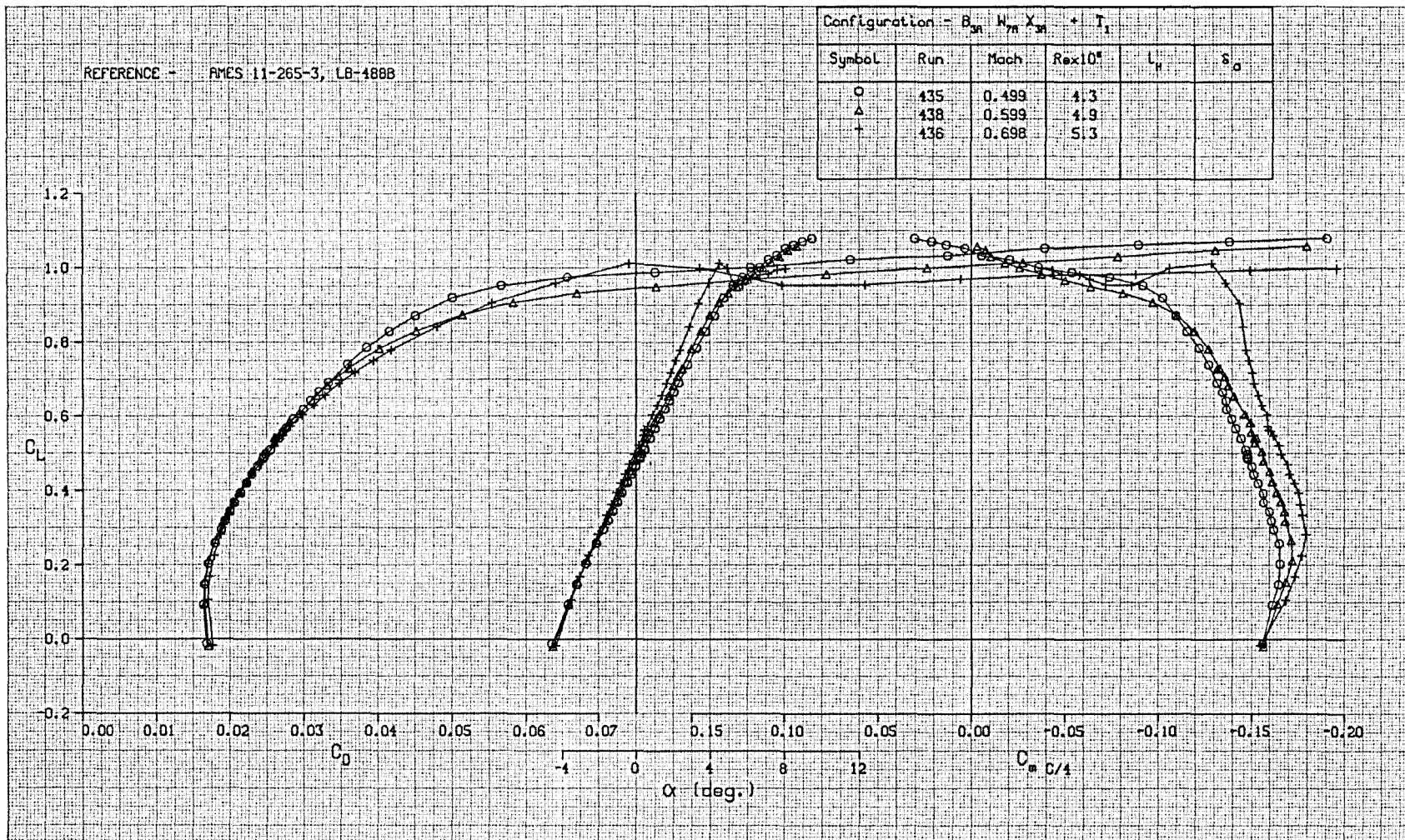


FIGURE A-54. LIFT, DRAG, AND PITCHING MOMENT CHARACTERISTICS OF WING W_{7A} , TRANSITION FREE

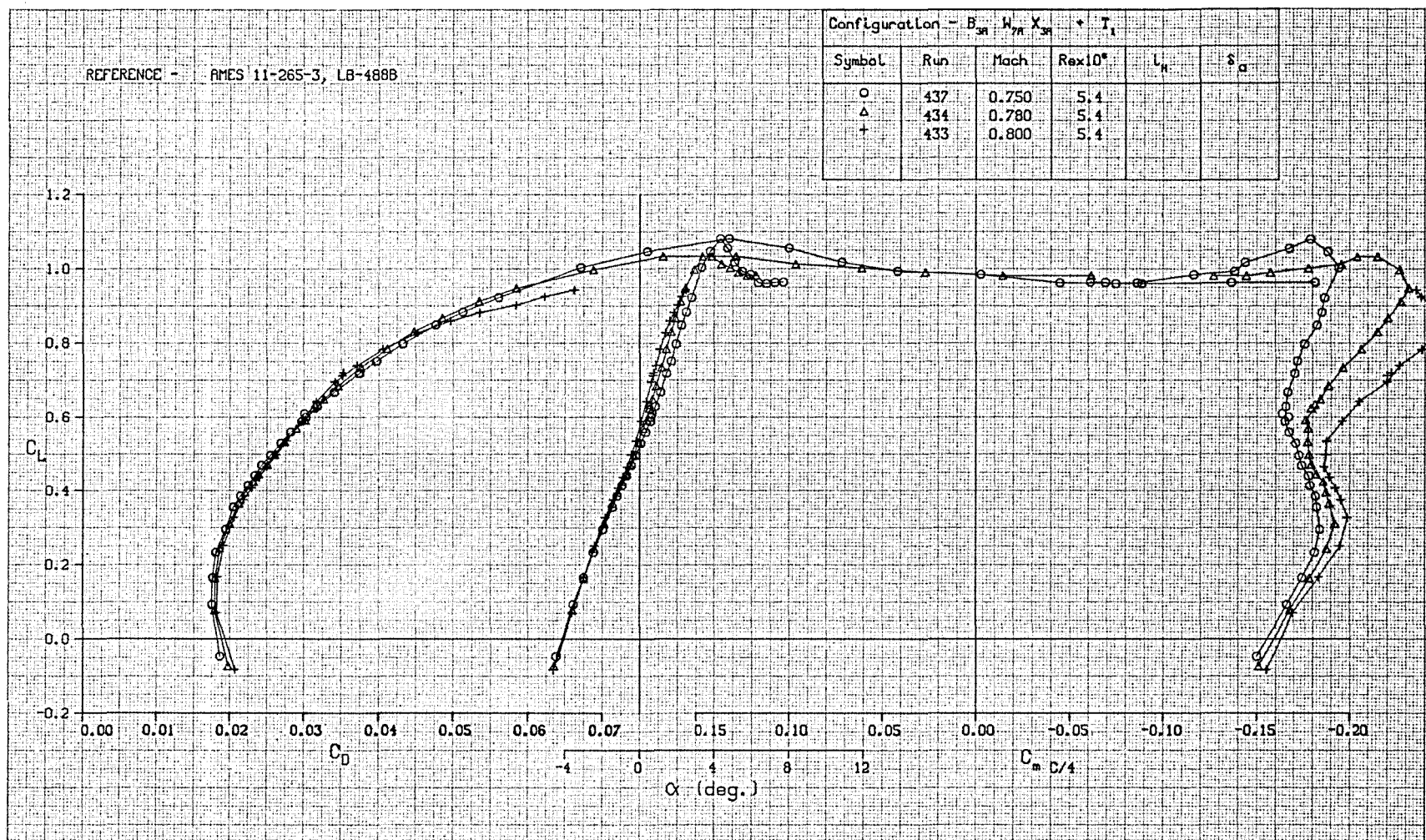


FIGURE A-55. LIFT, DRAG, AND PITCHING MOMENT CHARACTERISTICS OF WING W_{7A} , TRANSITION FREE

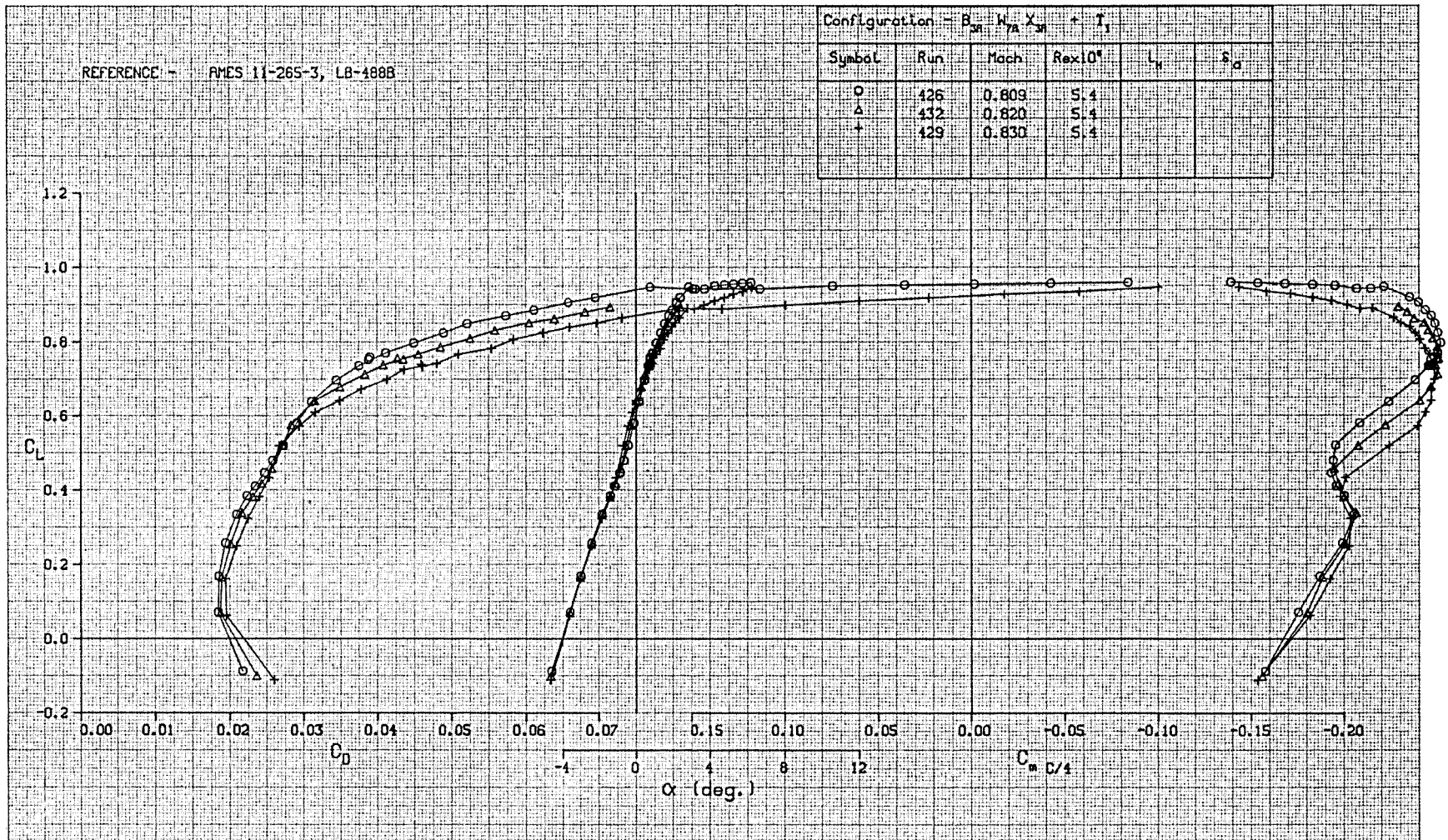


FIGURE A-56. LIFT, DRAG, AND PITCHING MOMENT CHARACTERISTICS OF WING W_{7A} , TRANSITION FREE

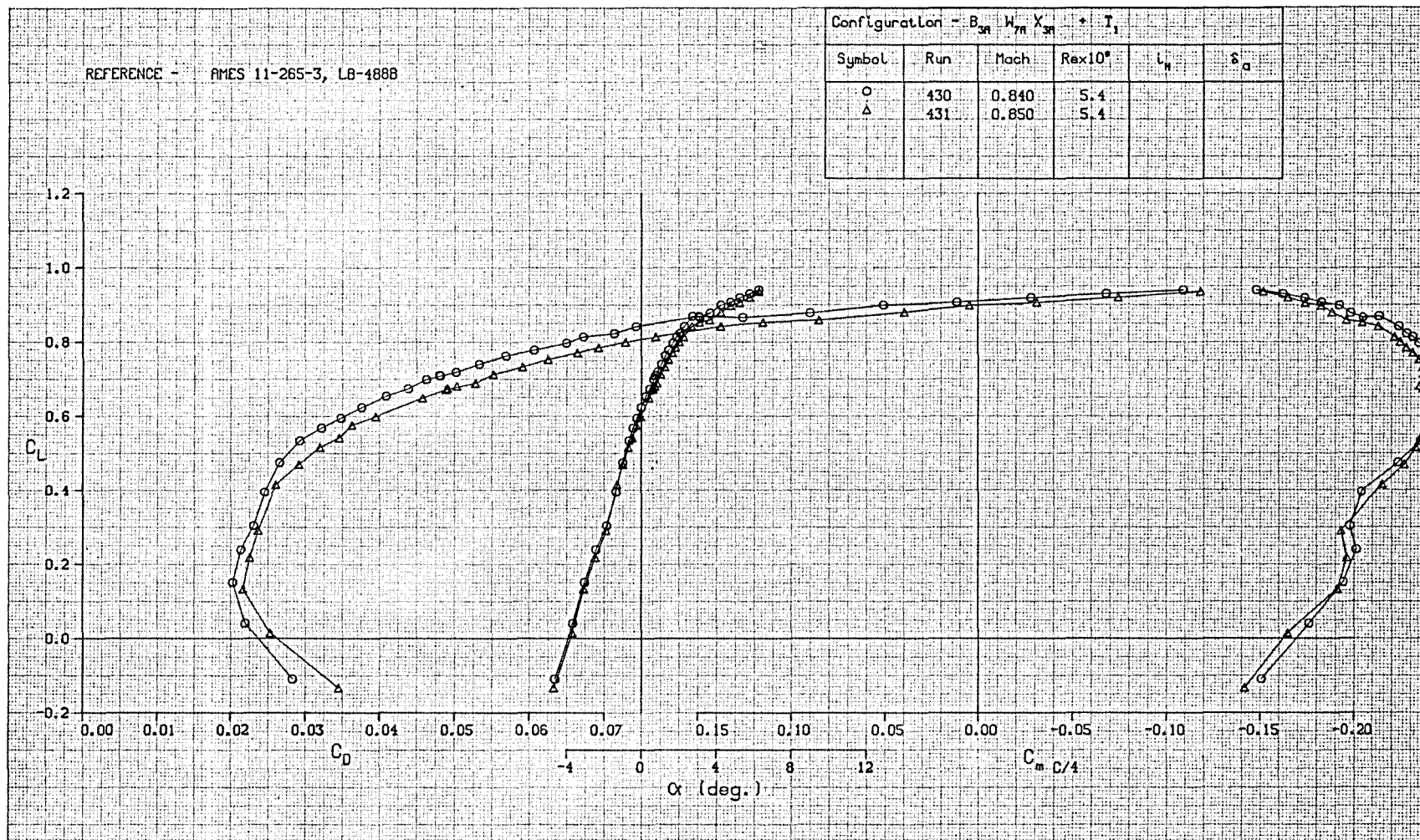


FIGURE A-57. LIFT, DRAG, AND PITCHING MOMENT CHARACTERISTICS OF WING W_{7A} , TRANSITION FREE

REFERENCE - AMES 11-265-3, LB-488B

Configuration -					
Symbol	Run	Mach	$Re \times 10^6$	L_H	δ_a
○	305	0.498	4.3		
△	306	0.598	4.9		
+	307	0.699	5.4		



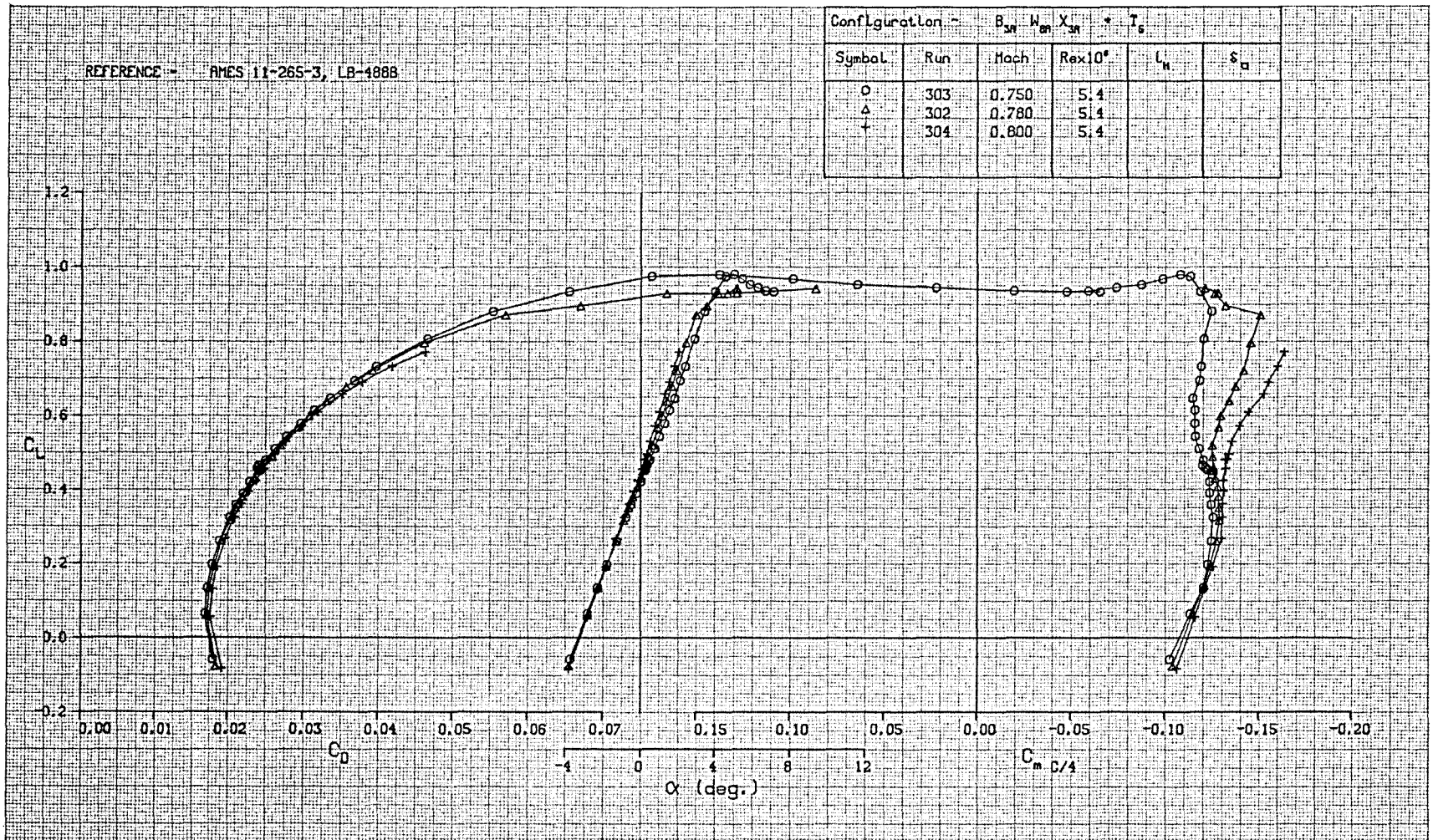


FIGURE A-59. LIFT, DRAG, AND PITCHING MOMENT CHARACTERISTICS OF WING W_{8A} , TRANSITION FIXED

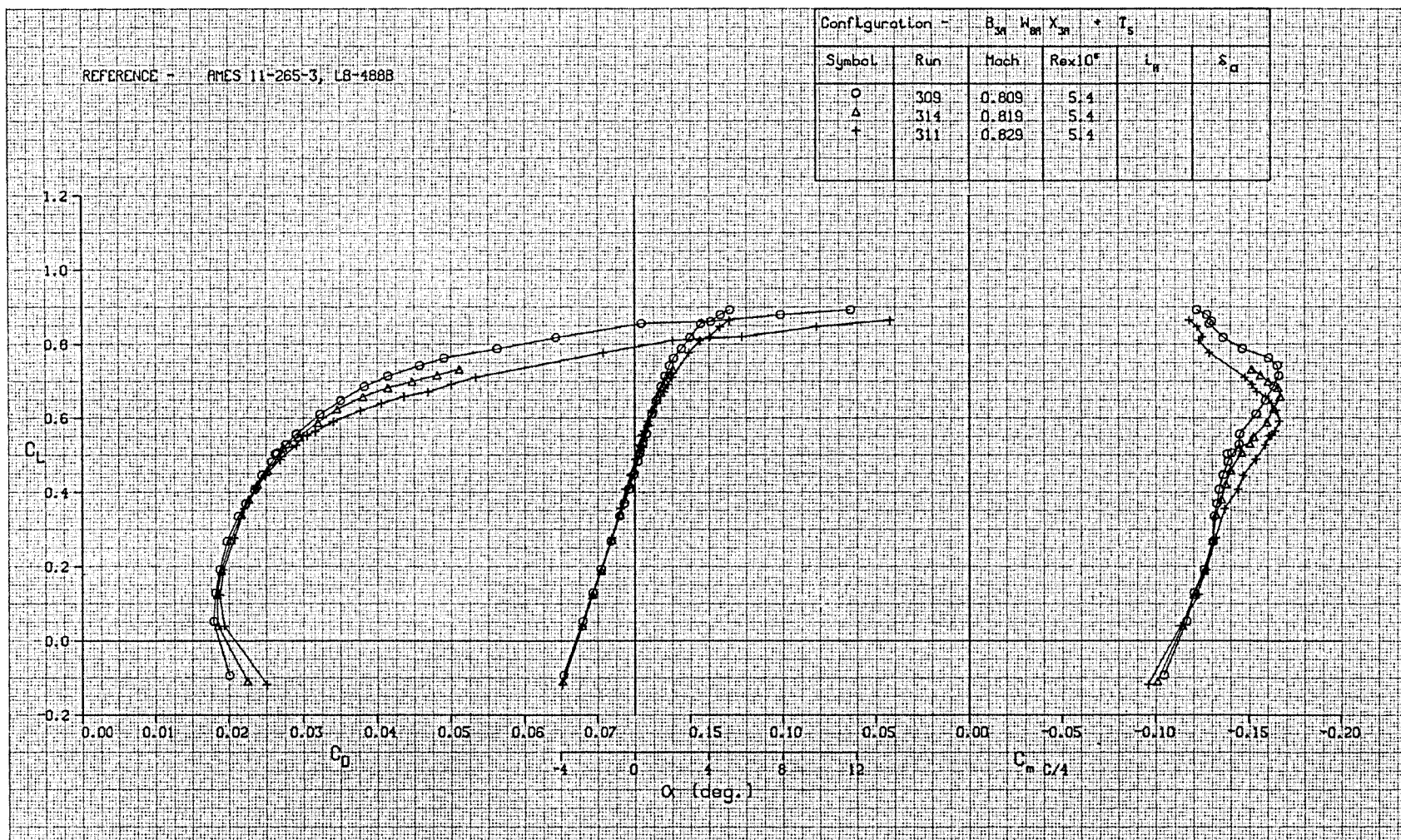


FIGURE A-60. LIFT, DRAG, AND PITCHING MOMENT CHARACTERISTICS OF WING W_{8A} , TRANSITION FIXED

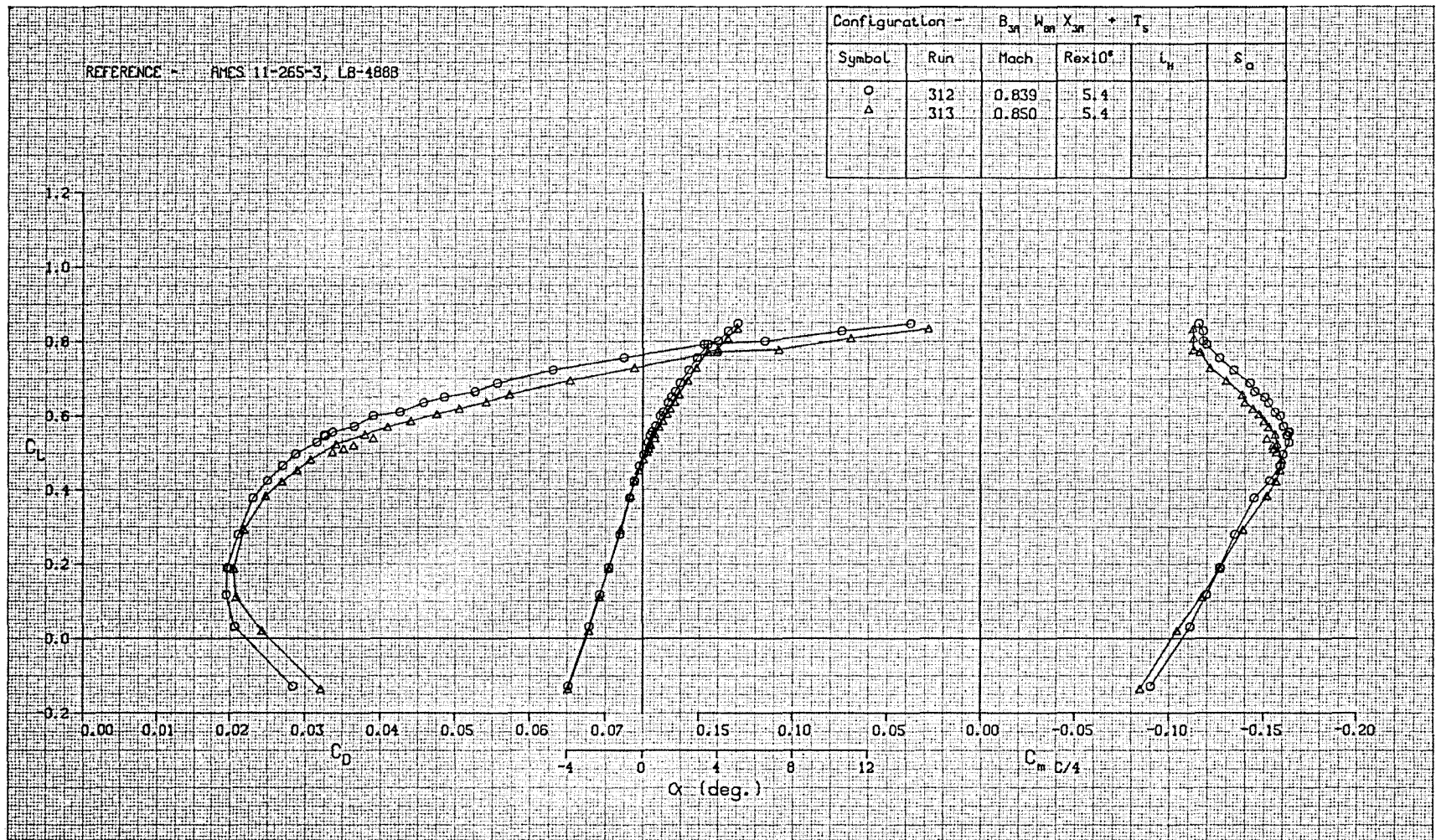


FIGURE A-61. LIFT, DRAG, AND PITCHING MOMENT CHARACTERISTICS OF WING W_{8A} , TRANSITION FIXED

REFERENCE - AMES 11-265-3, LB-4888

Configuration -					
Symbol	Run	Mach	Re x 10 ⁶	t_w	δ_a
○	332	0.499	4.3		
△	348	0.599	4.9		
+	333	0.698	5.3		

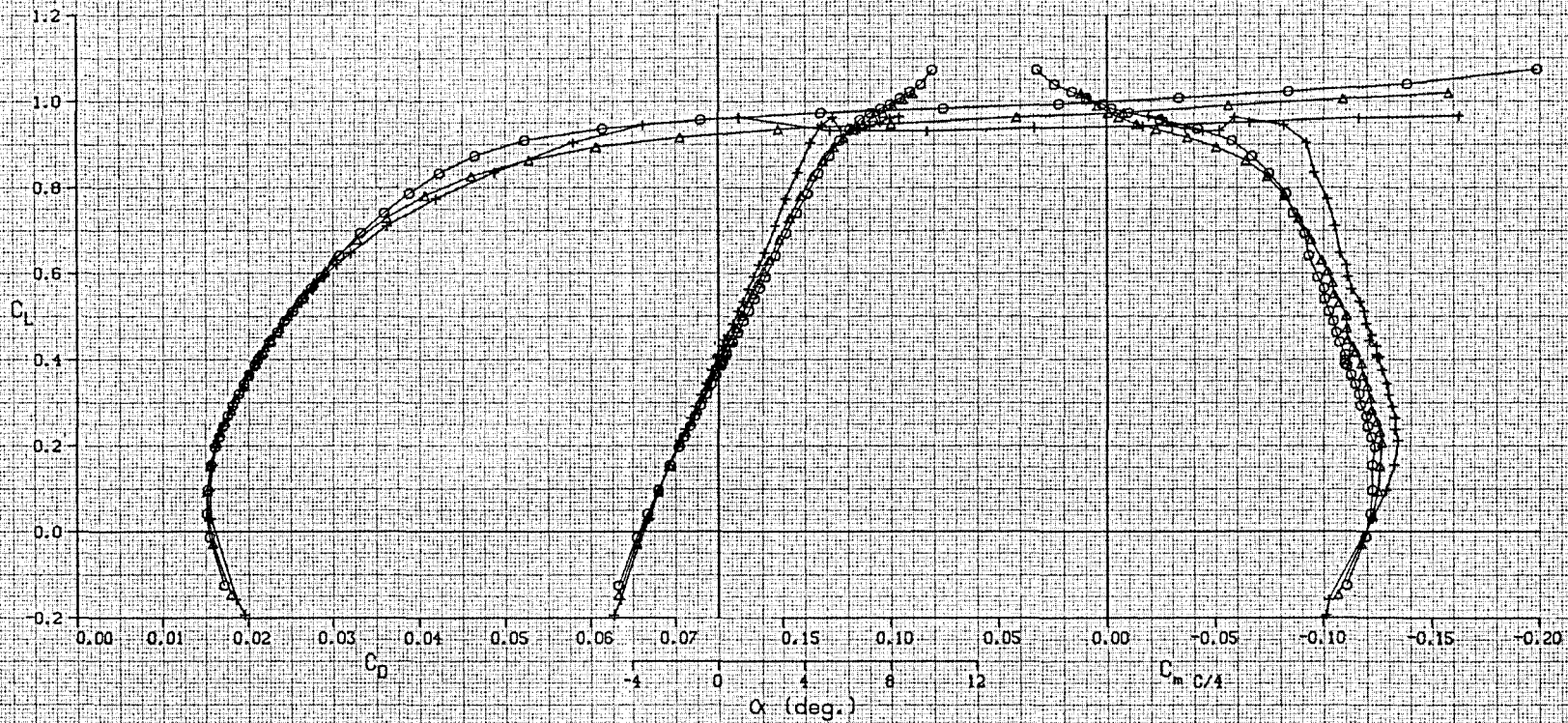


FIGURE A-62. LIFT, DRAG, AND PITCHING MOMENT CHARACTERISTICS OF WING W_{8A} , TRANSITION FREE

A-64

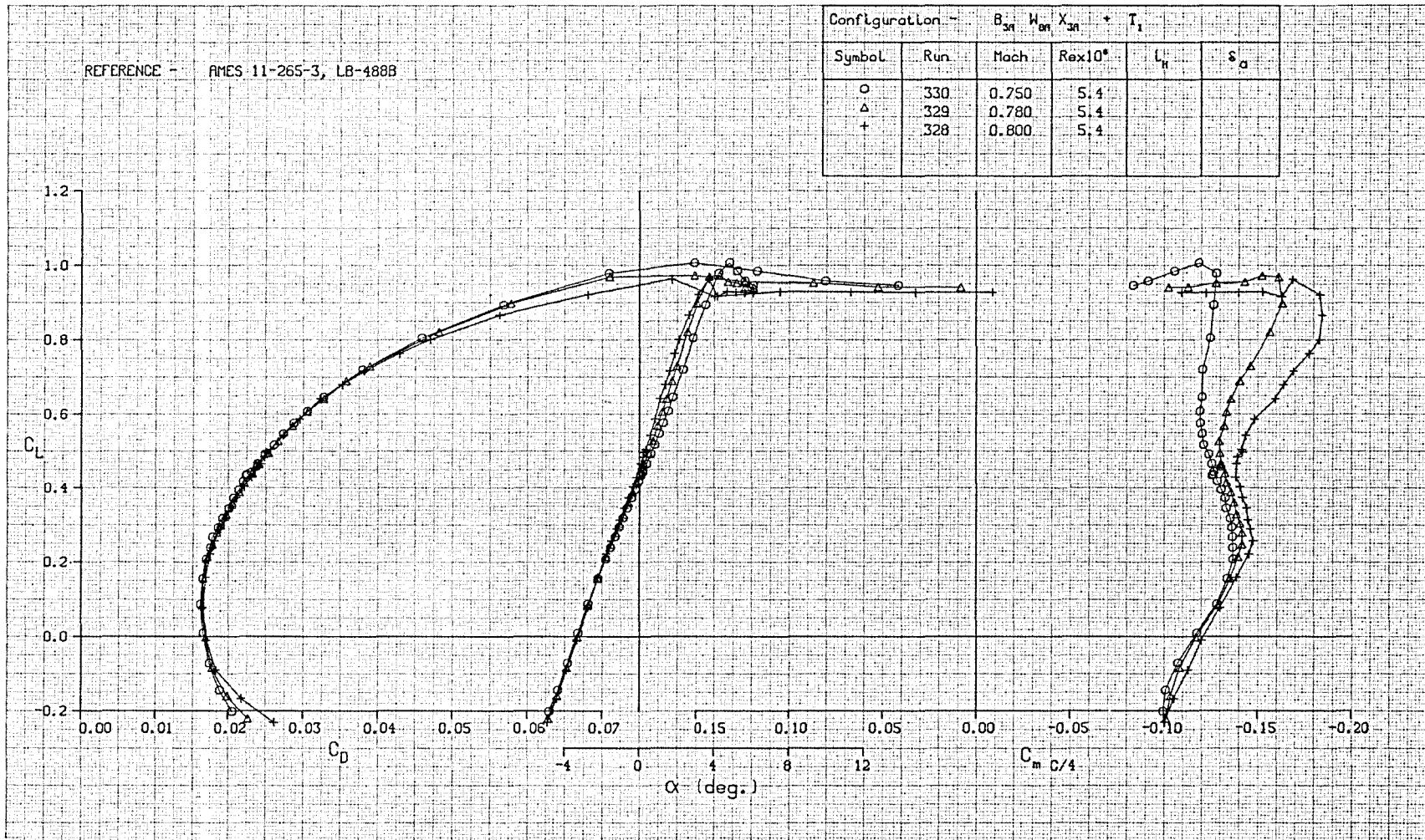


FIGURE A-63. LIFT, DRAG, AND PITCHING MOMENT CHARACTERISTICS OF WING W_{8A} , TRANSITION FREE

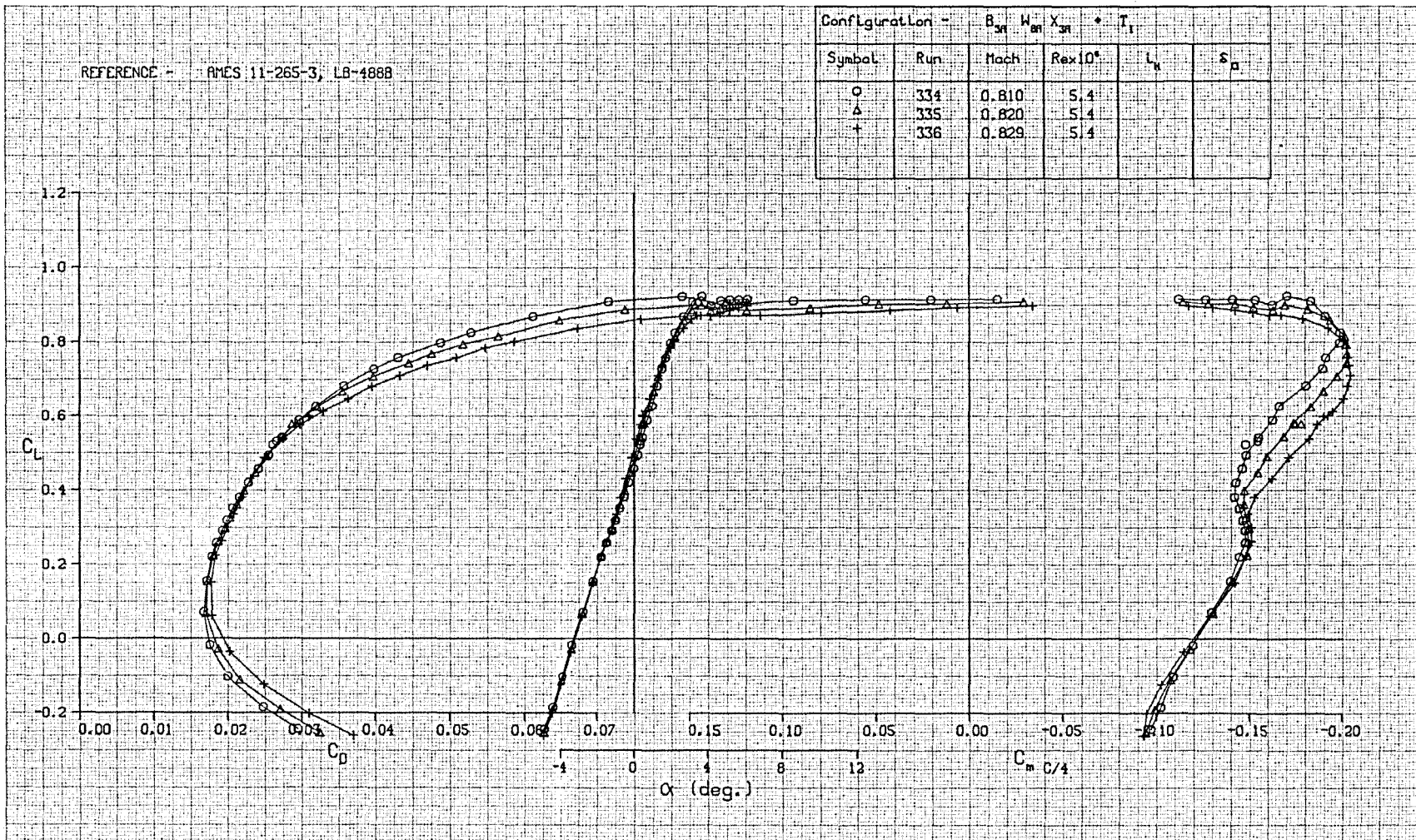


FIGURE A-64. LIFT, DRAG, AND PITCHING MOMENT CHARACTERISTICS OF WING W_{8A} , TRANSITION FREE

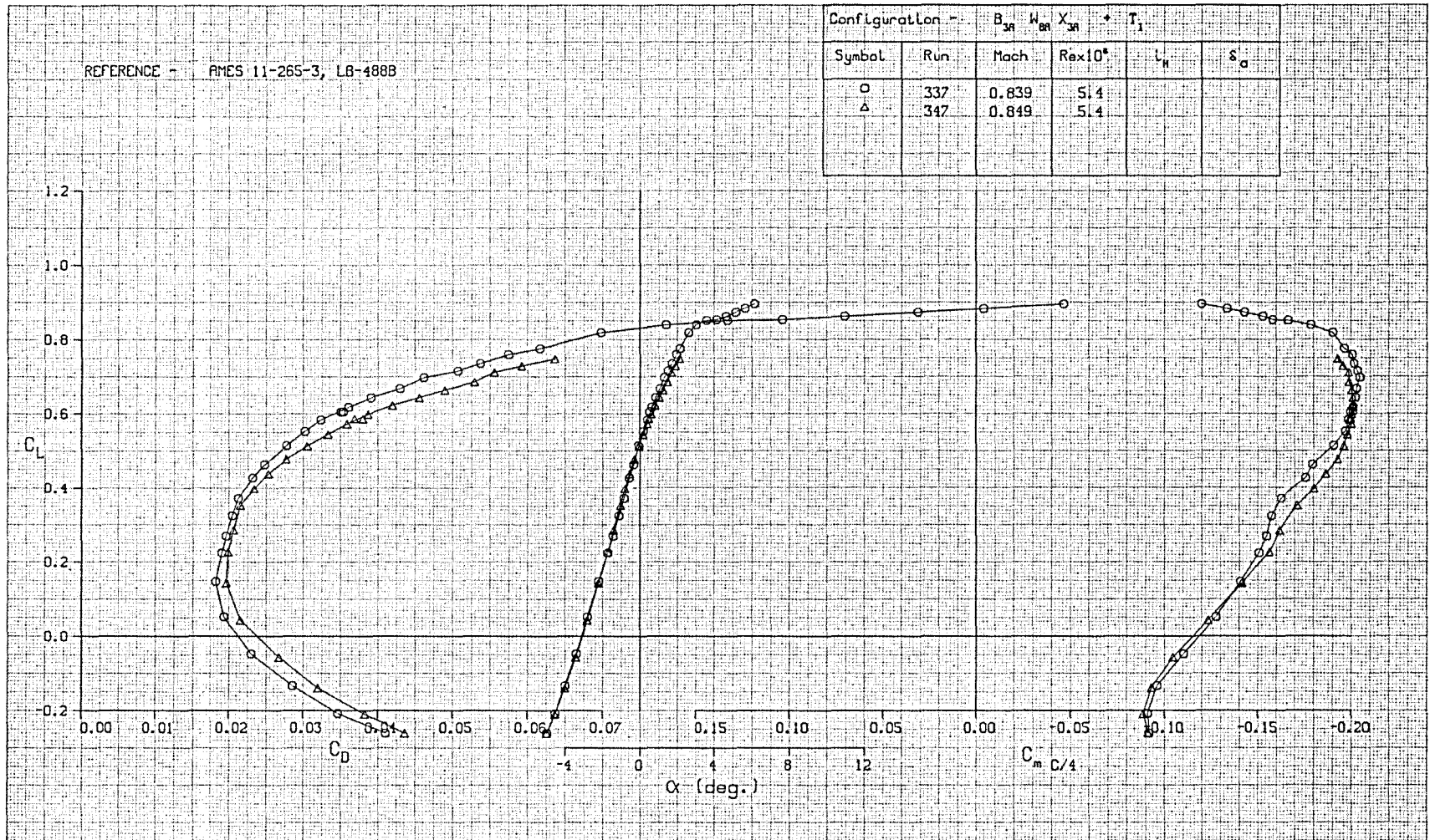


FIGURE A-65. LIFT, DRAG, AND PITCHING MOMENT CHARACTERISTICS OF WING W_{8A} , TRANSITION FREE

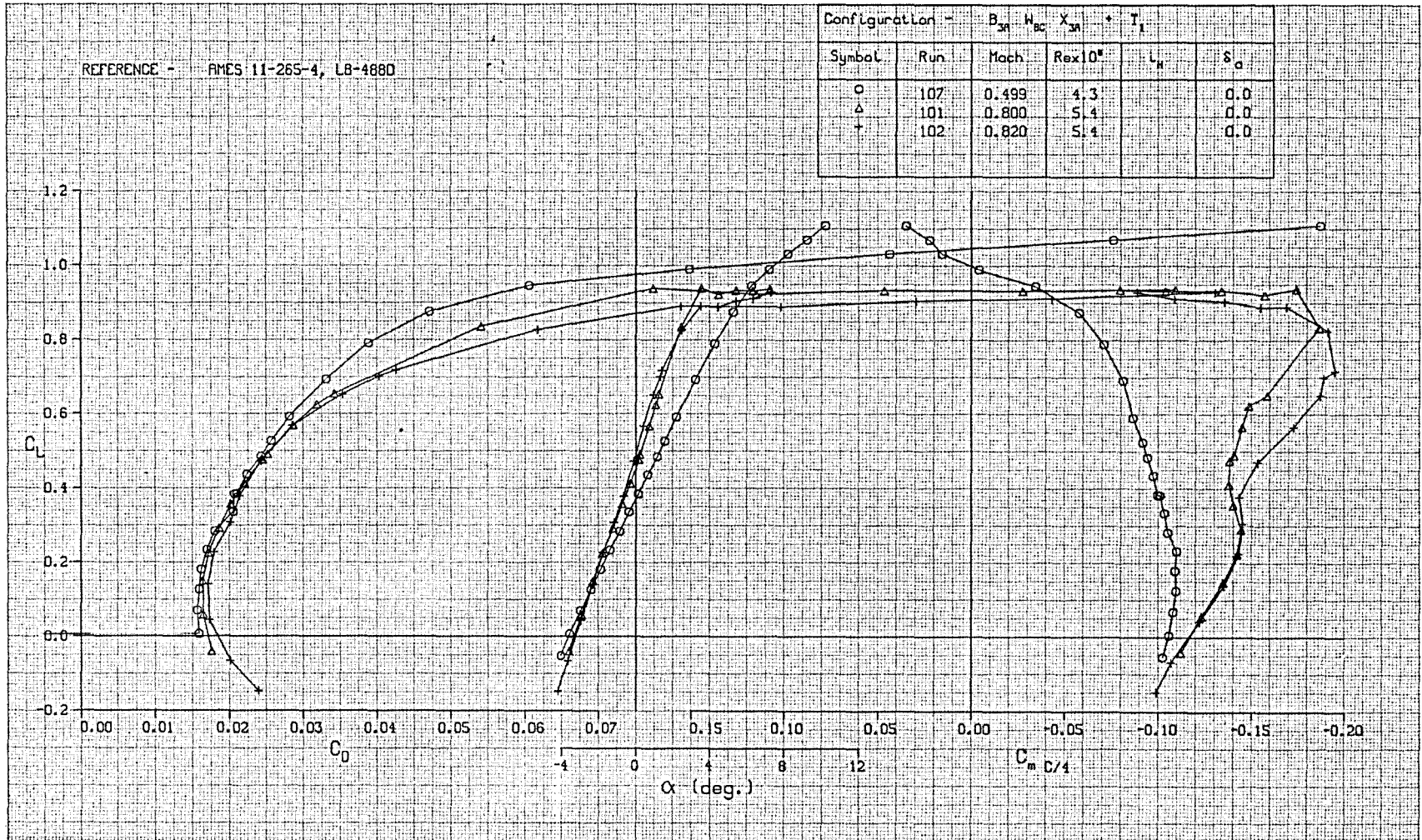


FIGURE A-66. LIFT, DRAG, AND PITCHING MOMENT CHARACTERISTICS OF WING W_{8C} , TRANSITION FREE

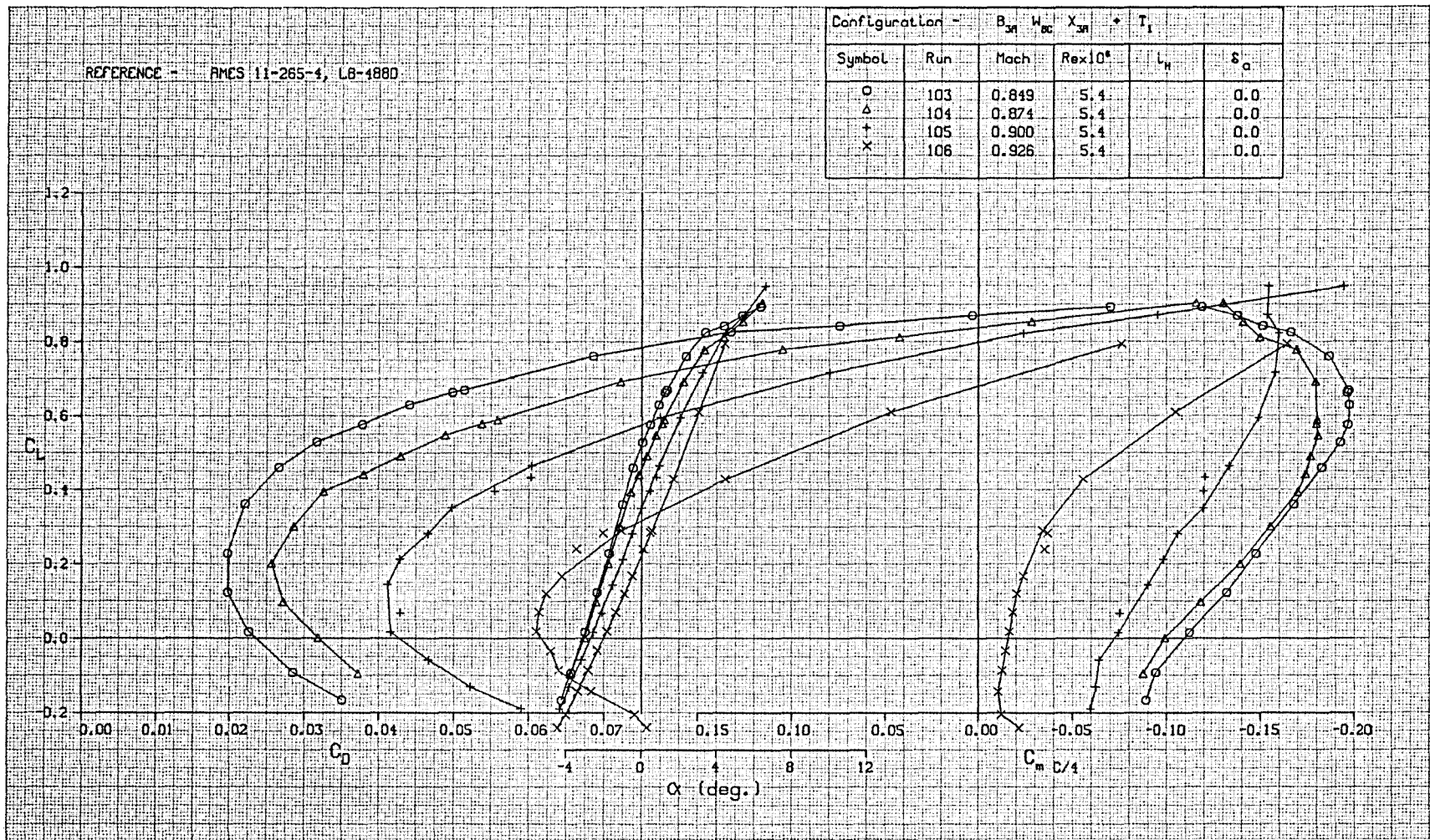


FIGURE A-67. LIFT, DRAG, AND PITCHING MOMENT CHARACTERISTICS OF WING W_{8C} , TRANSITION FREE

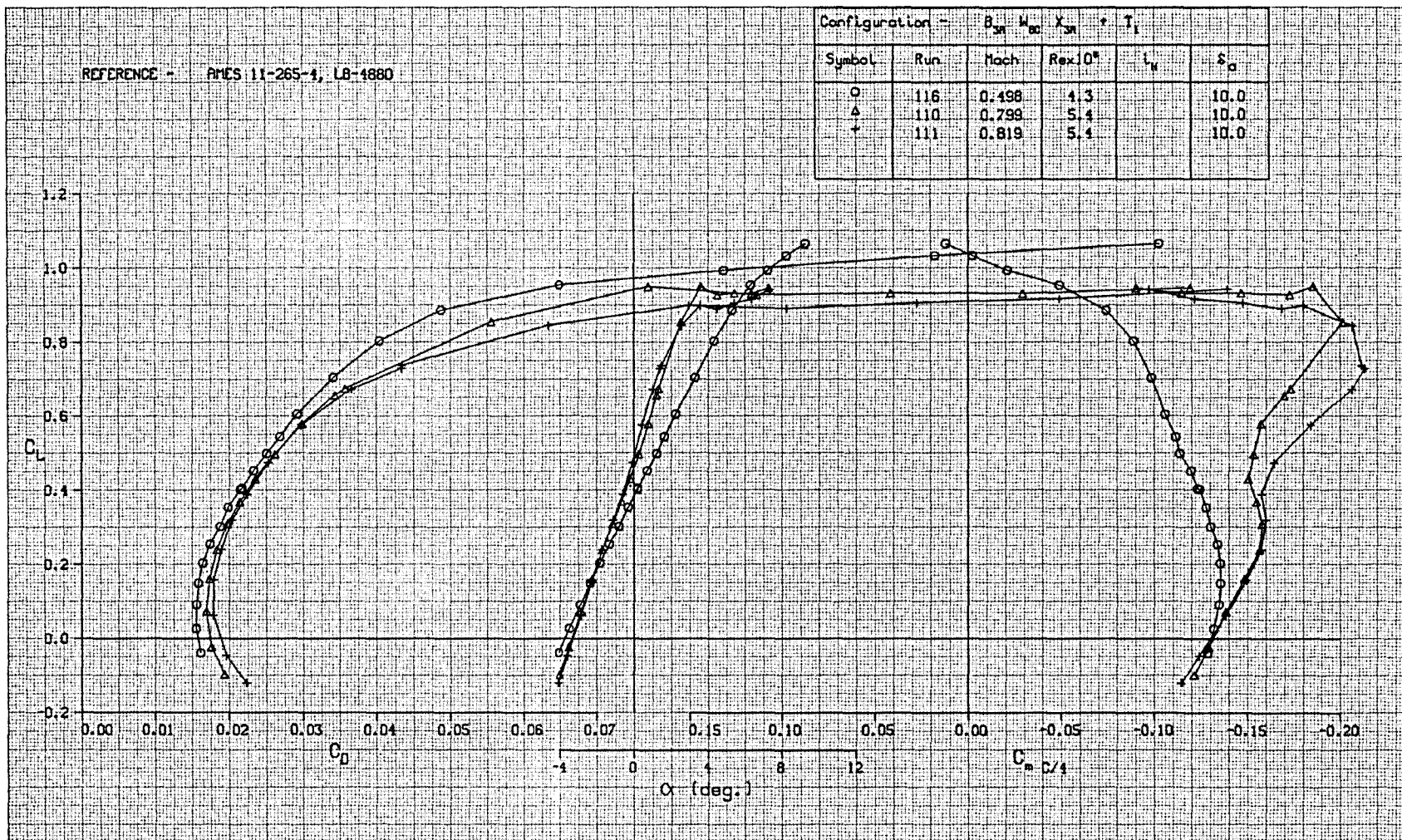


FIGURE A-68. LIFT, DRAG, AND PITCHING MOMENT CHARACTERISTICS OF WING W_{80C} , TRANSITION FREE

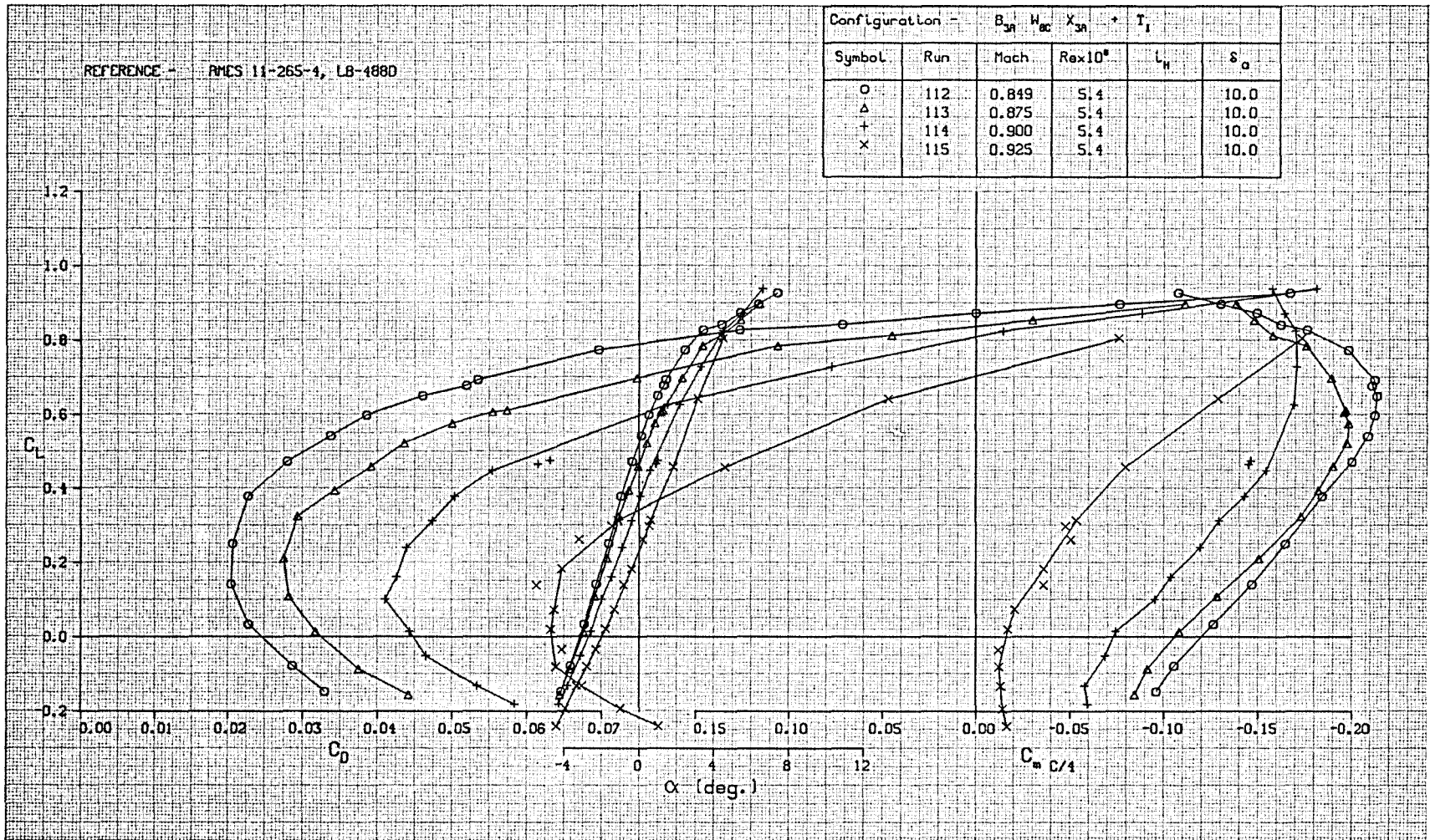


FIGURE A-69. LIFT, DRAG, AND PITCHING MOMENT CHARACTERISTICS OF WING W_{8C} , TRANSITION FREE

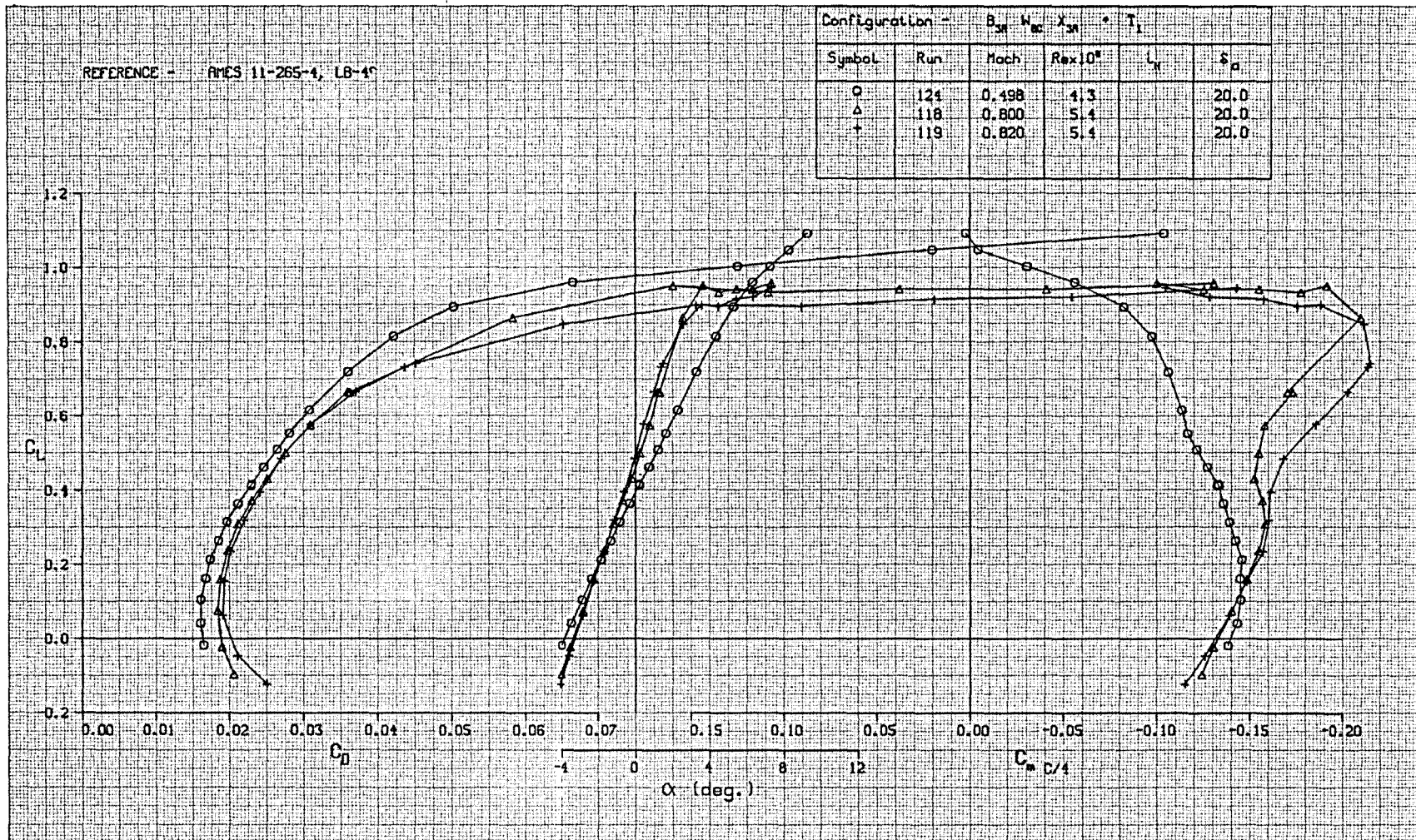


FIGURE A-70. LIFT, DRAG, AND PITCHING MOMENT CHARACTERISTICS OF WING W_{8C} , TRANSITION FREE

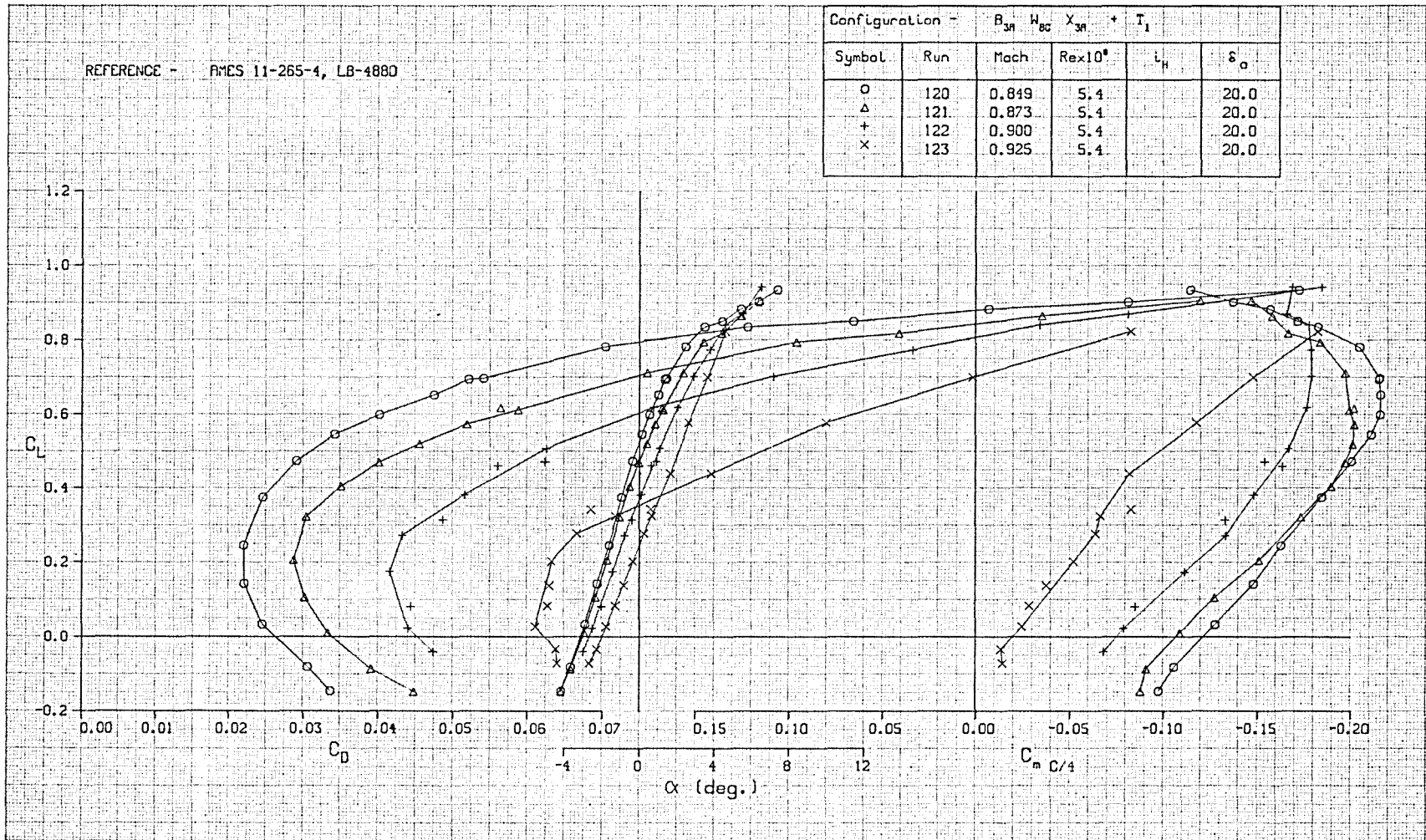


FIGURE A-71. LIFT, DRAG, AND PITCHING MOMENT CHARACTERISTICS OF WING W_{8C} , TRANSITION FREE

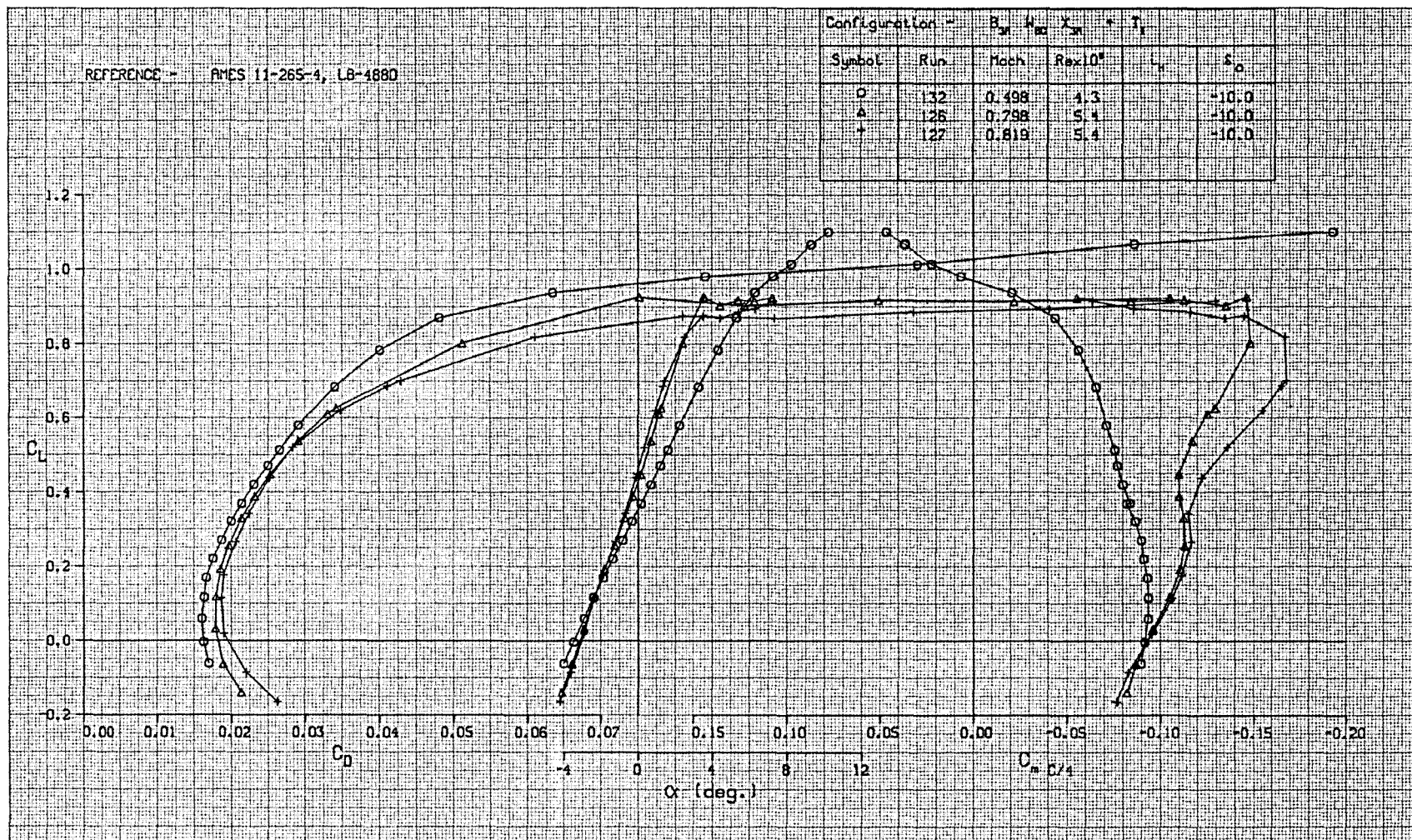


FIGURE A-72. LIFT, DRAG, AND PITCHING MOMENT CHARACTERISTICS OF WING W_{8C} , TRANSITION FREE

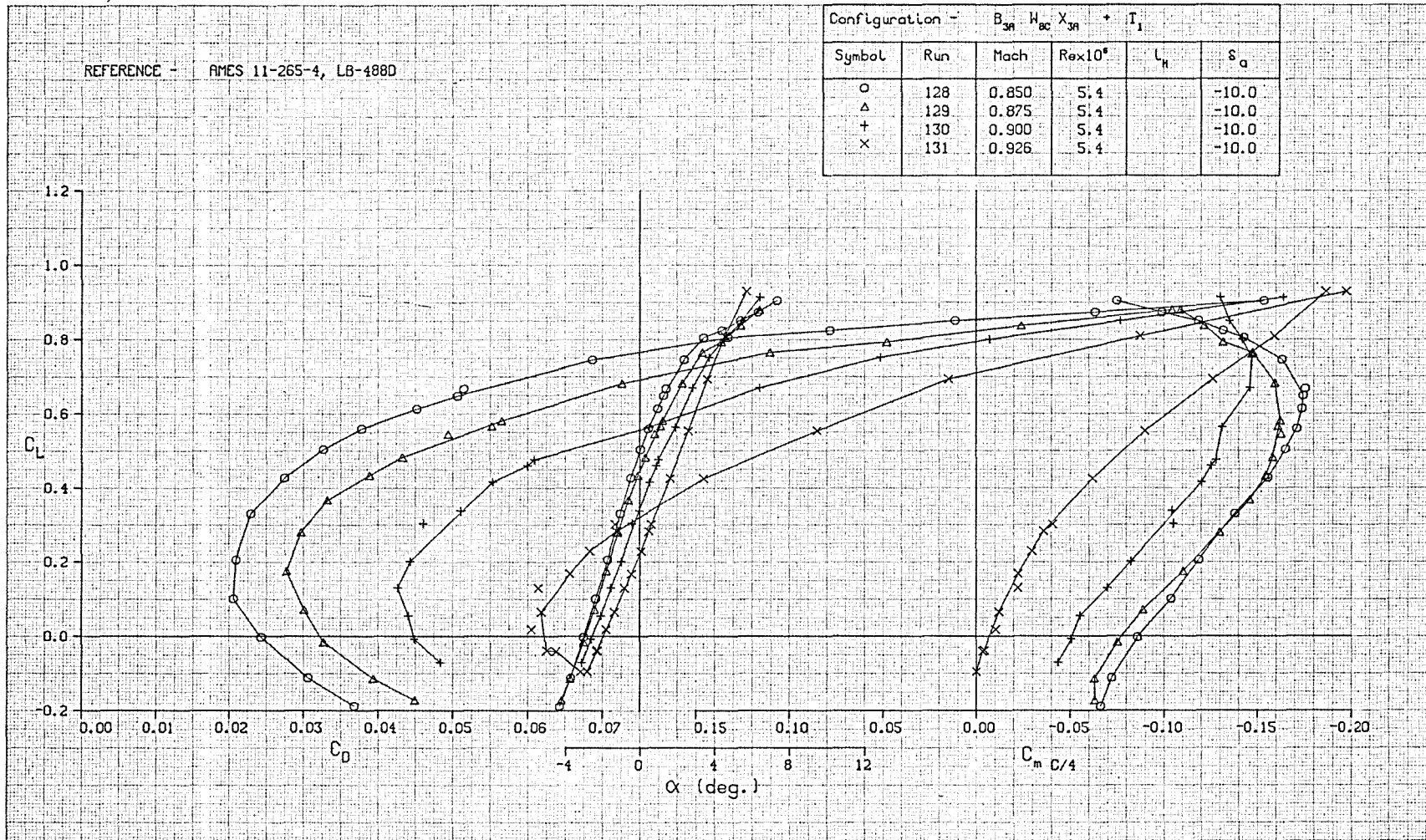


FIGURE A-73. LIFT, DRAG, AND PITCHING MOMENT CHARACTERISTICS OF WING W_{8C} , TRANSITION FREE

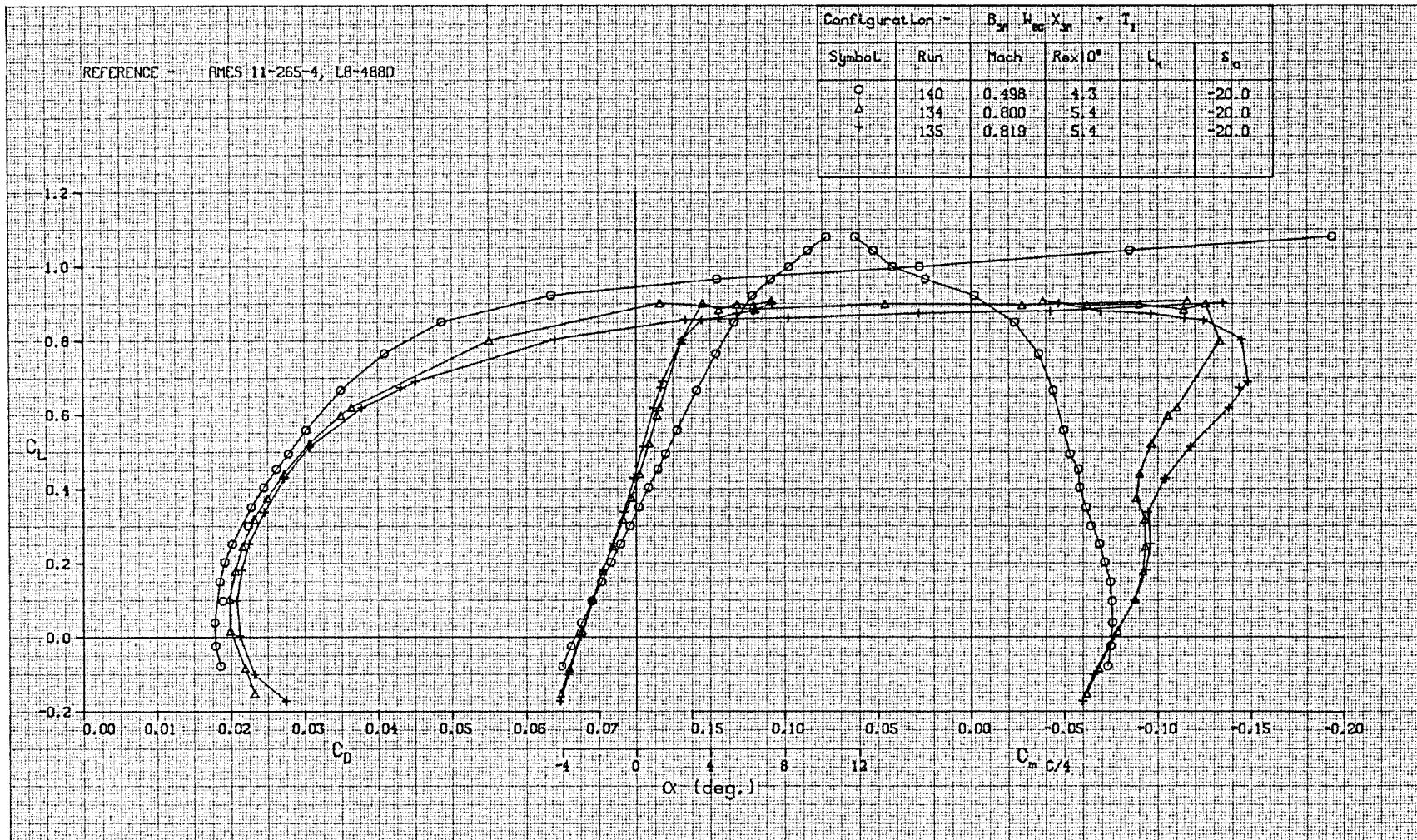


FIGURE A-74. LIFT, DRAG, AND PITCHING MOMENT CHARACTERISTICS OF WING W_{8C} , TRANSITION FREE

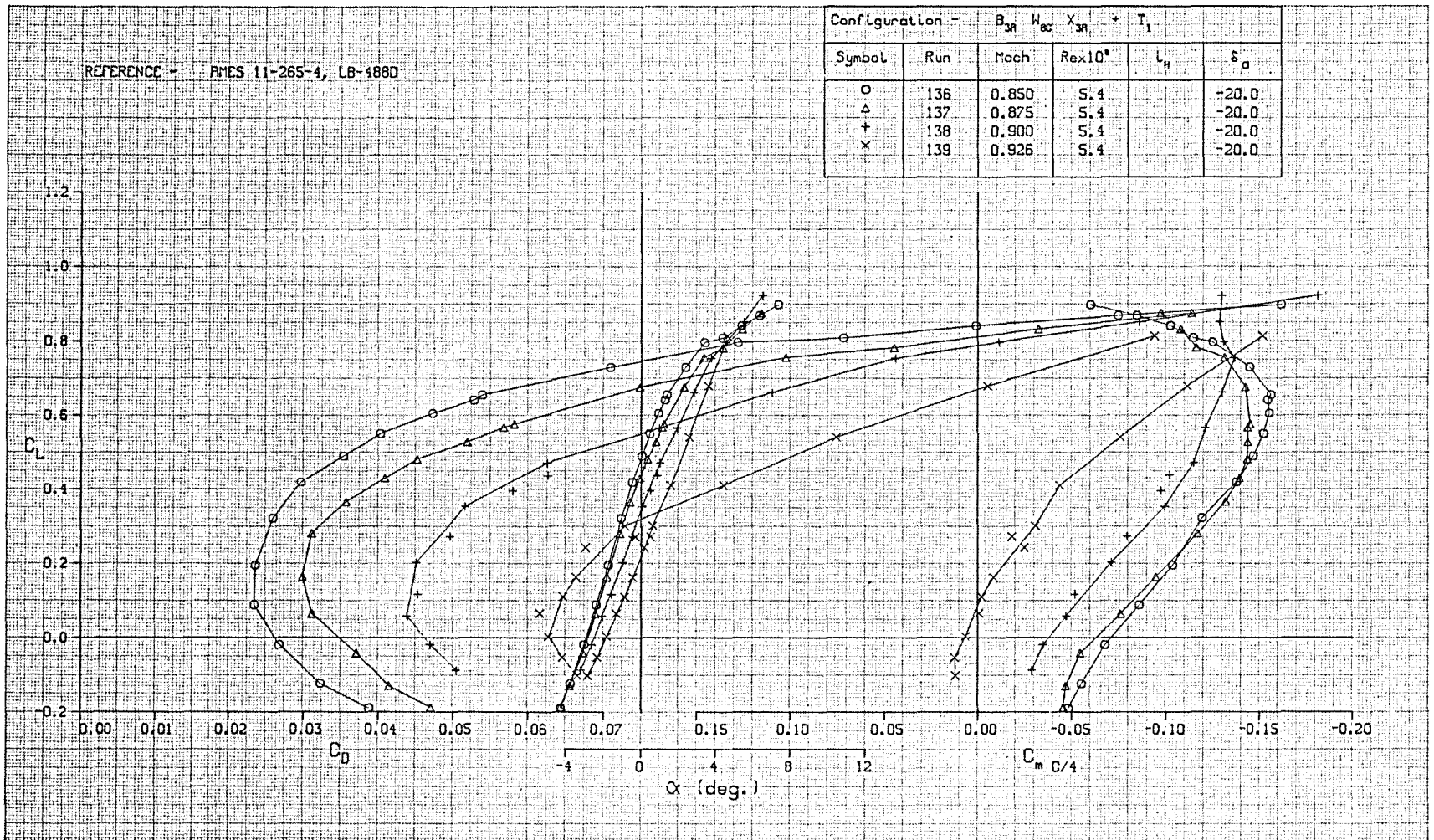


FIGURE A-75. LIFT, DRAG, AND PITCHING MOMENT CHARACTERISTICS OF WING W_{8C} , TRANSITION FREE

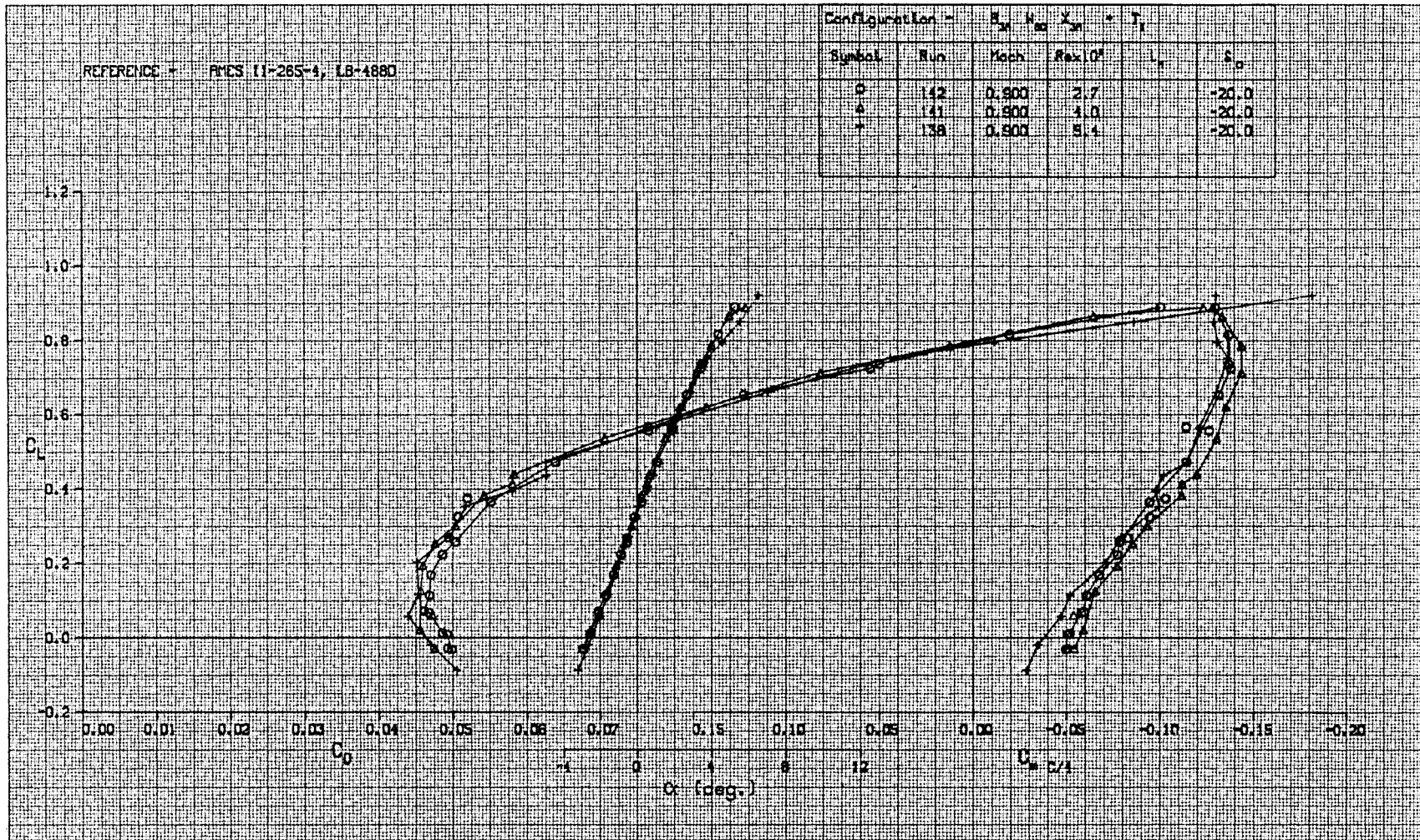


FIGURE A-76. LIFT, DRAG, AND PITCHING MOMENT CHARACTERISTICS OF WING W_{8C} , TRANSITION FREE - REYNOLDS NUMBER EFFECT

1. Report No. NASA CR-159332		2. Government Accession No.		3. Recipient's Catalog No.	
4. Title and Subtitle RESULTS OF DESIGN STUDIES AND WIND TUNNEL TESTS OF HIGH-ASPECT-RATIO SUPERCRITICAL WINGS FOR AN ENERGY EFFICIENT TRANSPORT				5. Report Date	
				6. Performing Organization Code	
7. Author(s) Doris K. Steckel, John A. Dahlin, Preston A. Henne				8. Performing Organization Report No. ACEE-06-FR-9894	
				10. Work Unit No.	
9. Performing Organization Name and Address Douglas Aircraft Company McDonnell Douglas Corporation 3855 Lakewood Boulevard Long Beach, California 90846				11. Contract or Grant No. NAS1-14744	
				13. Type of Report and Period Covered Contractor Report	
12. Sponsoring Agency Name and Address National Aeronautics and Space Administration Washington, D.C. 20546				14. Sponsoring Agency Code	
15. Supplementary Notes Project TRCO, D. L. Maiden Energy Efficient Transport Technology Project NASA Langley Research Center, Hampton, Virginia 23665					
16. Abstract This report presents the results of design studies and wind tunnel tests of high-aspect-ratio supercritical wings suitable for a medium-range, wide-body transport aircraft flying near $M = 0.80$. The basic characteristics of the wings tested were derived from system studies of advanced transport aircraft where detailed structural and aerodynamic tradeoffs were used to determine the most optimum design from the standpoint of fuel usage and direct operating cost. These basic characteristics included wing area, aspect ratio, average thickness, and sweep as well as practical constraints on the planform and thickness near the wing root to allow for the landing gear. Within these constraints, a large matrix of wing designs was studied with spanwise variations in the types of airfoils and distribution of lift as well as some small planform changes. The criteria by which the five candidate wings were chosen for testing were the cruise and buffet characteristics in the transonic regime and the compatibility of the design with low-speed (high-lift) requirements. Five wing-wide-body configurations were tested in the NASA Ames 11-foot transonic wind tunnel over a one-year period starting in May 1978. Nacelles and pylons, flap support fairings, tail surfaces, and an outboard aileron were also tested on selected configurations. Results of these tests showed that the cruise and buffet characteristics used in the system studies could be achieved, and that the high-aspect-ratio supercritical wing can be designed to realize a sizable advantage over today's technology in terms of fuel usage and economics. For the configuration studied, these gains amount to a reduction of over 5 percent in direct operating cost. The results also show that such gains are achievable only when considerable attention is given to the details of the wing design.					
17. Key Words (Suggested by Author(s)) Wings High-Aspect Ratio Span Loading Supercritical Buffet Drag-rise Trim drag Pitching moment Aircraft design				18. Distribution Statement RESTRICTED	
19. Security Classif. (of this report) Unclassified		20. Security Classif. (of this page) Unclassified		21. No. of Pages	22. Price

*Available: NASA's Industrial Applications Centers

End of Document